Overland Flow Scaling Behaviour in a Burned Dry Hillslope

Leila Kasraie

Submitted in total fulfilment of the requirements of
the degree of Doctor of Philosophy

August 2020

Department of Infrastructure Engineering

The University of Melbourne

Abstract

The scale-dependency of overland flow is frequently observed in rainfall runoff measurements, (Wilcox et al., 1997, Wilcox et al., 2003, Van de Giesen et al., 2000, Sheridan et al., 2014), yet largely neglected in rainfall-runoff models (Blöschl and Sivapalan, 1995, Chen et al., 2016a). Overland flow scaling behaviours within a given hillslope have been attributed to the main factors controlling infiltration and runoff processes including spatial variability of soil hydraulic properties (Julien and Moglen, 1990), run-on effect (Wainwright and Parsons, 2002, Langhans et al., 2014), macropore flow (Nyman et al., 2010, Ritsema and Dekker, 1995, Wessolek et al., 2009, Nyman et al., 2014, Stoof et al., 2014a, Ritsema et al., 2005), and rainfall temporal properties (Joel et al., 2002, Li and Sivapalan, 2011, Wainwright and Parsons, 2002). These factors are nonlinear and vary in time and space causing uncertainties when averaging between scales.

Wildfire may introduce higher spatio-temporal variability to the factors controlling soil infiltration by vast alteration in soil and vegetation, and as a result of that scaling effects on hydrological processes may be altered in burned landscapes (Moody et al., 2013). However, the impact of fire on scaling behaviours is poorly investigated and only few practical studies have measured runoffs scaling on burned hillslopes (Sheridan et al., 2014). There are significant knowledge gaps in understanding overland flow scaling effects in relation to post-fire soil, surface factors and rainfall properties (Moody et al., 2013).

This study aimed to investigate overland flow scaling behaviours in relation to soil and rainfall properties on a burnt hillslope by observations, measurements, and simulations. This was obtained by i) collecting rainfall-runoff data from different plot lengths at a eucalyptus hillslope, Southeast Australia burned by wildfire in 2013, ii) quantifying the degree of runoff scale-dependency from empirical rainfall-runoff data, iii) conducting stepwise regression analysis to investigate scaling behaviours of the observed runoffs in relation to the rainfall characteristics, iv) simulating overland flow and scaling effects by coupling traditional infiltration theory, run-on process and rainfall temporal variations, v) investigating macropore flow contribution to runoff scaling behaviour by measuring vertical pathways of activated macropores with a blue dye experiment at the site, modelling macropore flow in relation to runoff depth, and accounting macropore flow into rainfall-runoff simulations.

This is the first study to investigate isolated impact of spatial variability of soil hydraulic conductivity, rainfall parameters, and macropore flow on overland flow scaling behaviour in a

burned hillslope. The outcome of this study was partly obtained from field and laboratory measurements and rainfall-runoff monitoring at the field. These measurements and monitoring data were used for rainfall-runoff models' parametrisation and verifications.

The empirical rainfall-runoff data were collected from multi-scale runoff plots under natural rainfall conditions. The instruments were installed on a severely burned hillslope of eucalyptus forest in southeast Australia. Forty-one rainfall-runoff events were extracted from data collected during the second year following the fire. Strong scaling behaviour was observed for all observed events, seasonally and the whole study period where the rate of runoff declined with increasing plot length.

The data from multi-scale runoff plots were used in the stepwise regression models to investigate runoff scaling behaviour in relation to rainfall volumetric and temporal parameters. Stepwise multiple regression analysis showed that generated runoffs and scaling effects were mainly influenced by annual rainfall depth than other rainfall factors while the impact on runoff productions decreases with increasing plot length.

Measurements and monitoring data were used for model setup, parameterisation, and verifications of rainfall-runoff models to simulate overland flow scaling effects. The rainfall-runoff simulations provided a very weak demonstration of scaling behaviours with underestimated scaling effects. The simulated scaling behaviours did not improve when spatial variability of soil hydraulic conductivity (CV_{Ks}) accounted for the models. This concludes that models with traditional infiltration coupled with run-on process paradigm, and rainfall temporal variability cannot explain the observed scaling behaviour, even where spatially variability of soil hydraulic conductivity (CV_{Ks}) is considered.

Measurement of activated macropores, water repellency strength and soil water content conducted from the top edge of the hill to downslope on one occasion. No systematic evidence was found regarding reduction in soil water repellency, nor an increase in activated macropores, nor higher water content within distance from uphill. The outcome from these measurements did not support the hypothesis of runoff scaling behaviour to be a result of infiltration increase with distance from uphill.

Macropore flow was modelled in relation to runoff depth satisfying pores pressure entry at the point, that is exceeded more frequently with distance downslope due to increased runoff depths. The model consisted of macropore network algorithm, macropore filling when runoff depth

exceeded the macropore entry pressure head based on the Young–Laplace and Bernoulli equations, and gravity-driven vertical flow from fully saturated macropores based on Darcy Law. The macropore flow application was coupled with rainfall-runoff models with traditional infiltration theory, runoff-runon, and rainfall temporal variability. The proportion of simulated macropore flow increased with plot lengths. Simulated scaling effects from models with macropore flow application obtained a better prediction of overland flow scaling behaviour. This concludes that macropore flow is the main factor affecting runoff scaling behaviours in water repellent soil where infiltration mostly occurs through activated macropores and preferential flow.

This study supports the theory that macropore flow is a dominant factor controlling overland flow scaling behaviours in burnt dry hillslopes where the soil is strongly hydrophobic. Young–Laplace and Bernoulli equations were found sufficient to calculate macropores filling process in relation to runoff depth, and Darcy Law equation demonstrated continuous flows from full saturated macropores to underneath soil (Hardie et al., 2013, Buttle and House, 1997, Nimmo, 2012, Podgorney and Fairley, 2008). The simulations showed that higher macropore flow is triggered in the longer distance when runoff depth satisfies pressure entry of activated pores. This also explains why the impact of rainfall parameters on runoff productions and scaling decreases with length. The findings of this study are in agreements with earlier findings (Müller et al., 2018, Stoof et al., 2014a, Jarvis et al., 2008, Jarvis et al., 2016, Nimmo, 2012).

Declaration

This is to certify that:

The thesis comprises only my original work towards the PhD except were otherwise indicated in the acknowledgment section.

Due acknowledgment has been made in the text to all other material used.

The thesis is fewer than 100,000 words in length, exclusive of tables, maps, bibliographies, and appendices.

Leila Kasraie

Acknowledgements

I begin by thanking my supervisor, Professor Andrew William Western for his dedicated support, patience and guidance in the time of writing this thesis. I could not imagine preparing a better dissertation without his insightful comments and encouragement, and all those hard questions that motivated me to refine my results. I would like to thank the rest of my thesis committee: Prof. Patrick Lane and Associate Prof. Gary Sheridan..

Importantly, this PhD would never have happened without funding support. I gratefully acknowledge the funding received from the Australian Federal Government for Postgraduate Award (APA) scholarship. I thank Prof. Gerd Bossinger and Prof. Patrick Lane for providing me with two additional top-up scholarships from Pownall, Irving, Davies Trust during my time in the School of Ecosystem and Forest Sciences.

My sincere thank also goes to Prof. Ian Rutherford for his kind guidance and support during my PhD as advisory committee chair. From School of Ecosystem and Forest Sciences, my special thanks and appreciation goes to Prof. Rodney John Keenan who introduced me to his network from where I pursue my today career. I appreciate the guidance and support I received from Dr. Petter Nyman during my time in the Forest Hydrology Team. I am thankful to my dear friend, Dr. Rene Van Der Sant who kindly shared her fieldwork data and always been an awesome friend and a dear colleague to me.

Finally, I would like to thank my family and colleagues who never gave up on me, persuading me to finish my PhD despite all of the difficulties I faced.

Contents

List of Tables

List of Figure

List of Appendices

Thesis Structure

Chapter I: Literature Review

Chapter 1 includes a literature review of key concepts related to post-fire hydrology, scaling behaviours of infiltration-excess runoff and the research gaps are identified. The research design and main objectives are also set out in this chapter.

Chapter II: Geographic information of the study site

Chapter 2 describes the study site, including geographic and climate information. General weather conditions over the study period are also described.

Chapter III: Measurement of overland flow scale-dependency using multi-length rainfall-runoff plots

Chapter 3 details the rainfall-runoff monitoring set-up and instrumentation, along with descriptions of the measurement techniques, data collection, data quality control and data analysis methods. In this Chapter, event-based and cumulative runoff, runoff ratio, peak flows, and the degree of runoff scale dependency were quantified for the monitored events.

Chapter IV: The role of rainfall properties on overland flow scaling

Chapter 4 investigates the impact of rainfall temporal and volumetric factors on runoff scaling behaviours for the monitored events. Stepwise multiple regression models were set up to examine the contribution of different rainfall characteristics in runoff generation and overland flow scaling.

Chapter V: Modelling scaling effects of overland flow on burned hillslopes using the KINEROS2 model

Chapter 5 investigates the effects of storm temporal patterns on scaling. It contains model set-up for rainfall-runoff simulations, calibration and validation procedures. This Chapter investigates whether a model with traditional infiltration theory coupled with run-on infiltration and temporal rainfall variations can explain runoff scaling behaviours.

Chapter VI: Macropore flow Measurement and Modelling and Its Implication in Capturing Runoff Scaling Behaviour

Chapter 6 includes measurements and macropore modelling approaches to test two hypotheses: i) that soil infiltration increases down the hillslope due to increased soil moisture and weaker water repellency with distance; and ii) that increased infiltration occurs due to greater runoff depth exceeding macropore entry pressure activating macropore flow, and subsequently causing scaling effects.

This Chapter describes measurements of vertical pathways of activated macropores, water repellency strength and soil water content at the site to investigate Hypothesis I. A macropore flow model was developed from conceptualised macropores networks for each runoff plot to simulate macropore flow based on entry pressure of the individual pores in relation to runoff depth. The macropore flow model was combined with a rainfall-runoff model with traditional infiltration theory to calculate direct infiltration, runon, and macropore flow under temporally varied rainfalls. The macropore flow simulations were used to investigate the role macropore flow in controlling runoff scaling behaviour (Hypothesis II).

Chapter VII: Overall Conclusion and Future Study

Chapter 7 discusses overall findings of the study, the conclusion and suggestions for future research direction regarding runoff scaling behaviours and macropore flow modelling.

Chapter 1: Key Concept and Literature Review

This Chapter includes a literature review from which the research gaps that I addressed were identified. The chapter continues to describe the research design, and the main objectives.

The current literature related to post-fire hydro-geomorphology and hydrological processes governing overland flow scaling behaviours was reviewed to develop a comprehensive picture of important fire-induced factors affecting overland flow scaling in burned dry hillslopes.

1.2 Hydrologic Responses in Burned Hillslopes

Wildfire is a disturbance agent impacting hydrologic responses in affected landscapes by altering hydro-geomorphic patterns via destruction of vegetation and changes in soil hydrological properties (Moody et al., 2013, Shakesby and Doerr, 2006, Wohl, 2018, Shakesby, 2011, Santín and Doerr, 2016). Fire-induced soil-surface changes may shift threshold responses of overland flow generation and transport on burned hillslopes depending on burn severity and fire spatial extent (Moody et al., 2013, Sheridan et al., 2007, Neary et al., 1999). The enhancement of overland flow formation in the early rainfall events following fire reported is quite variable between different studies. Lower bound reported impacts include 1.5 to 3-fold more overland flow in burned eucalyptus forest, Southeast Australia (Lane et al., 2006, Sheridan et al., 2007) and 2.1 to 2.5 folds in north-central Portugal (Stoof et al., 2012). Moderate to higher impacts include 2.5-10 times increase in southern California (Kinoshita and Hogue, 2015, Bart, 2016), 7-fold increases in burned chaparral forest, California (Wells, 1981), and 12 to 16 times greater in New Mexico (Wine and Cadol, 2016).

Fire-induced changes contributing to flow initiation and transport include vegetation destruction and litter removal (Stoof et al., 2012, Shakesby, 2011, Cerdá and Doerr, 2005, Cawson et al., 2013), soil-hydraulic property alterations (DeBano et al., 1998, Imeson et al., 1992, Kinner and Moody, 2010, Moody et al., 2009, Ebel and Moody, 2017), fire-induced water repellency (Larsen et al., 2009, Doerr et al., 2003, Doerr et al., 2009, Nyman et al., 2010, White et al., 2017), and enhancement of macropores and preferential infiltration (Stoof et al., 2014b, Nyman et al., 2010, Nyman et al., 2014). Reduction in surface roughness (Stoof et al., 2012, Smith et al., 2011a) and a higher proportion of bare soil patches (Cawson et al., 2012, Cawson et al., 2013, Cerdá and Doerr, 2005) are other fire-induced factors that impact runoff transmission mechanisms. High space-time variability of these hydrological properties after

fire results in larger uncertainties in runoff and erosion predictions (Shakesby, 2011, Moody et al., 2013, Vieira et al., 2015).

1.2.1 Hydrologic Responses to Vegetation Removal after Fire

Depending on fire severity, three forest vegetation storeys can be partly or completely burned: plant roots, understorey shrubs, and overstorey canopies. Loss of vegetation causes both immediate and long-term changes in the hydrological cycle (Shakesby and Doerr, 2006, Lane et al., 2010, Poon and Kinoshita, 2018). Where canopies and litter are burned, less interception of precipitation occurs, resulting in more water reaching the soil surface as throughfall and stemflow (Robichaud et al., 2000, Cerdá and Doerr, 2005, Neary et al., 2005, Poon and Kinoshita, 2018). For example, (Stoof et al., 2012) estimated pre-fire canopy interception was on average 48.7% of total rainfall in dense heathland, Portugal; whereas post-fire canopy interception of the regenerating vegetation is minimal because of the sparseness of the regenerated vegetation cover in the first year following fire. The rate of evapotranspiration, as a major component of the forest hydrological cycle, may also decrease after fire because of combustion of forest biomass (Robichaud, 2000, Shakesby and Doerr, 2006).

There are important impacts of spatial patterns of fire intensity. Various post-fire studies have found strong links between post-fire hydrological responses to proportional areas of burned and unburned patches (bare soil-vegetated mosaics), thickness, arrangements and burn severity (Stoof et al., 2012, Cawson et al., 2012, Cawson et al., 2013, de Dios Benavides-Solorio and MacDonald, 2005). For example, higher connectivity of generated overland flow was observed on burned hillslopes due to a higher proportion of bare soil which also have higher runoff generation compared to unburnt patches (Penman et al., 2007). A threshold of 60–70% of bare soil patches was found to increase overland flow connectivity between bare patches in severely burned pine forest, New Mexico (Johansen et al., 2001).

Reduced amounts of litter on the post-fire ground surface reduces storage capacity in the litter layer; each centimetre thickness of litter has been found to store 0.5 mm of water depth for a pine forest in USA (Neary et al., 2003), and 3 mm for eucalypt forest in Portugal (Leighton-Boyce et al., 2003). Soil without litter cover is also less insulated and more exposed to solar radiation. This alters soil thermal regime, and subsequently decreases soil moisture dynamics via direct evaporation from the bare soil (Shakesby and Doerr, 2006, Wieting et al., 2017).

Depending on burn severity, loss of surface vegetation and litter may shift surface roughness and depression storage (Stoof et al., 2012, Moody et al., 2013, Jordán et al., 2016, Martin et

al., 2008), which are factors controlling flow initiation and transmission. Fire-related alterations in hydraulic roughness impact overland flow hydraulics because velocity, depth, and energy of overland flow are regulated through frictional resistance parameter. A few studies have investigated surface roughness features in post-fire landscapes (Martin et al., 2008, Stoof et al., 2012, Nyman et al., 2011) and more research is demanded to quantify changes in hydrologic responses in response to fire-induced changes in surface roughness. For example, (Nyman et al., 2011) measured flow velocity of burned compared to unburned overland flow using dye tracers and found an increase in velocity which explained an increased flashiness of storm hydrographs of burned plots compared to unburned plots.

1.2.2 Fire Effects on Soil Hydraulic Properties

Soil hydrological properties regulating infiltration, are mostly subject to change by severe wildfire (Ebel and Moody, 2017, Shakesby, 2011). Burned soil is more prone to structural breakdown due to the absence of organic materials and may form a very compact soil with higher bulk density and lower porosity (White et al., 2017, Merino et al., 2018, DeBano et al., 1998, Imeson et al., 1992). The degree of changes in soil physical structure depends on the pre-fire soil moisture conditions, and the temperature soil reaches during the fire (Vieira et al., 2015, Shakesby and Doerr, 2006, Cerdá and Doerr, 2005).

Changes in physical structure of the burned soil alter two soil hydraulic components; sorptivity, and hydraulic conductivity (Wieting et al., 2017, Ebel and Moody, 2017, Kinner and Moody, 2010, Moody et al., 2009). Early in an infiltration event, infiltration rate is a function of sorptivity. Sorptivity is controlled by internal capillary drive, which depends on soil texture and adsorption. After a sufficient depth of water has infiltrated, saturated hydraulic conductivity controls the infiltration rate with gravity being the key driving force. This is illustrated in Philips infiltration relationship: $I(t) = St^{1/2} + K_s t$ (Philip, 1957).

Fire-induced increases in soil water repellency (SWR), particularly on the soil surface (Doerr et al., 2000), is another important change that reduce the rate of infiltration in burned soils (Robichaud et al., 2016, Moody et al., 2013, Shakesby and Doerr, 2006). Water repellency has been shown to reduce soil infiltration rates up to 16-fold (laboratory studies by (Leighton-Boyce et al., 2003), particularly if hydrophobicity occurs on the soil surface.

Water-entry pressure (P_e) of macropores and velocity of preferential flow were found to be controlled by soil hydrophobicity (Bauters et al., 1998). These changes are due to contact angle

between water and hydrophobic soil which is >90 (Letey et al., 2000, Leelamanie et al., 2008, Carrillo et al., 1999).

$$\text{Eq 1.1} \qquad Cos\alpha = (\frac{\gamma_{90°}}{\gamma_w})^{0.5} - 1$$

$$\text{Eq 1.2} \qquad P_e = h\rho g = \frac{-2\sigma Cos\alpha}{r}$$

where α is the contact angle between water and soil calculated from, γ_W is the water–air surface tension (mN m^{-1}), γ_{90} is the water–air surface tension at which the contact angle of the water-air interface and the soil is 90° (47.1 mN m^{-1}) (Moody and Schlossberg, 2010), ρ is the liquid density for water (997 kg/m^3), g is acceleration due to gravity (9.8 ms^{-2}), h is the hydraulic head (m), r is the pore radius (m), μ is the dynamic viscosity of water (1.004 m^2/s at 20ºC), and σ is the surface tension (mN/m) obtained.

The degree of soil water repellency in burned soil is spatially variable, and related to the type of organic compounds on soil particles, the soil moisture and the temperature that the soil reaches during fire (Doerr et al., 2000). The degree of water repellency was found to be negatively controlled by soil water content and probably disappears at saturation point (Rye and Smettem, 2017, Rye and Smettem, 2015, Moody et al., 2013, Ritsema et al., 2005) due to alterations in the chemical properties of the molecules of hydrophobic compounds (Doerr et al., 2000). Both sorptivity and hydraulic conductivity are negatively related to the degree of water repellency due to reduced wettability resulting in a reduced proportion of connected water filled pores (Moody et al., 2009). (Nyman et al., 2014) investigated soil infiltration in relation to fire-induced water repellency, dryness index, and soil moisture in three recent burned sites, southeast Australia. The study showed that infiltration rates into burned soil did not reach saturated hydraulic conductivity (K_s) because fire-induced repellency always remained during the recovery period (>3 years), with different degrees of strength fluctuating seasonally.

The strength of water repellency and its impact on soil infiltration measured at point scales may not be reflected to the same degree at larger scales due to preferential flow taking place through wettable patches, cracks, roots and activated macropores (Nyman et al., 2010, Doerr and Moody, 2004, Stoof et al., 2014b) leading to locally high infiltration. Preferential flow in water repellent soil was found to recur at the same locations during successive rainfall events (Ritsema and Dekker, 2000). Therefore, mosaics of repellent and wettable patches regulate infiltration into water repellent soil at larger scales on burned hillslopes (Doerr et al., 2003).

Ponded infiltration and macropore flow are dominant factors in controlling vertical preferential water movement through water repellent soil where a high portion of the soil surface is in non-infiltration areas (Nyman et al., 2010, Stoof et al., 2014b). In a post-fire hydrophobic soil, macropores ($r > 0.5$ mm) contributed to between 70% and 95% of the field-saturated and ponded hydraulic conductivity, while accounting for just 5% of the soil volume. Ponded infiltration was up to 2.5 times higher in water repellent soil when the hydraulic head increased from 0 to 5 mm (Nyman et al., 2010).

Despite of considerable effects of soil hydrophobicity on infiltration and development of preferential flow, only a few studies have incorporated soil water repellency as a variable in infiltration models (Doerr et al., 2003). This is due to the poor knowledge base relating to preferential flow in water repellent soils. To estimate the infiltration rate in water repellent soil, traditional infiltration theories require adjustment. For example, the uniform sharp wetting front assumption in the Green–Ampt infiltration model is inappropriate in water repellent soil due to preferential water movement leading to a highly irregular wetting front.

Ash is another fire-induced factor affecting soil infiltration rates. Low density ash is easily mobilized and can be blown away by wind or leached into the soil or transported downstream by runoff. Typically an ash layer is wettable and has a relatively large water storage capacity controlled by high sorptivity in an initially dry condition (Kinner and Moody, 2010, Woods and Balfour, 2010, Onda et al., 2008, Moody et al., 2009). After severe burning, a thick layer of ash and burned residue usually remains on the soil surface, creating a two-layer system consisting of an ash bed on top and mineral soil beneath. The thickness of the ash layer is a function of burn severity and quantity of burned material. Thickness usually reduces gradually after fire due to water and wind erosion. The soil and ash layers have different values of hydraulic conductivity and sorptivity resulting in variable infiltration rate with depth (Moody et al., 2013, Kinner and Moody, 2010). Any intense rain following a fire infiltrates into the ash layer but deeper penetration through water repellent soil is limited. Water in the ash layer either turns into saturated overland flow, moves laterally downslope in the subsurface above the fire-induced water repellent soil layer, or infiltrates downward through preferential flow paths (Kinner and Moody, 2008, Kinner and Moody, 2010, Cerdà and Doerr, 2008, Onda et al., 2008). Differences of infiltration rates in ash and repellent soils suggest consideration of a two-layer soil system for infiltration analysis of burned soils (Kinner and Moody, 2010).

1.2.3 Summary of Post-Fire Hydrological Response

Summarising the above discussion, fire-induced changes that may alter overland flow responses are:

1. A higher portion of precipitation reaches the mineral soil surface due to reduced interception on burned canopies and surface litter removal (Cerdá and Doerr, 2005, Neary et al., 2005, Stoof et al., 2012).
2. A reduction in hydraulic conductivity and soil infiltration due to a lower percentage of the soil organics (DeBano et al., 1998, White et al., 2017, Merino et al., 2018), fire-induced water repellency (Nyman et al., 2010, Nyman et al., 2014, Robichaud et al., 2016), and ash clogging and surface sealing (Neary et al., 2005, Woods and Balfour, 2010).
3. Higher velocity and kinetic energy of generated runoff on hillslopes because of reduced roughness and drag forces on the ground surface result in higher total discharge, and shorter time to peak (Kinner and Moody, 2008, Stoof et al., 2012).

1.2.4 Overland Flow Formation

Post-fire studies have shown that the occurrence of overland flow in burned landscapes is more likely to be in the form of infiltration-excess runoff than saturation-excess flow (Shakesby, 2011, Vieira et al., 2015, Moody et al., 2013). This is the result of reduced infiltration capacity in burnt soil, lower surface roughness, and water repellency (Shakesby and Doerr, 2006, Moody et al, 2013, Doerr et al., 2000).

Soil hydraulic properties are important controls on infiltration-excess overland flow as they control infiltration of water input from both rainfall and upstream generated runoff (Chow et al., 1988, Nahar et al., 2004, Corradini et al., 1998). In infiltration-excess flow, some parts of the surface may produce runoff while for other parts infiltration may occur due to spatial variability in soil-surface properties (Gómez et al., 2001, Morbidelli et al., 2006b). When runoff from upslope encounters unsaturated areas downslope and infiltrates in a downslope position, this is referred to as a run-on infiltration process (Wainwright and Parsons, 2002, Morbidelli et al., 2006b, Morbidelli et al., 2008, Govindaraju et al., 2006). Spatial variability of soil hydraulic properties, soil water repellency and patchiness are soil-surface factors contributing to infiltration and run-on are all processes affecting runoff (Sheridan et al., 2014, Gomi et al., 2008a, Van de Giesen et al., 2000, Chen et al., 2016a, Langhans et al., 2016).

Field investigations (Gómez et al., 2001, Govindaraju et al., 1996, Zhang and Govindaraju, 2000, Loague and Gander, 1990) have shown significant spatial heterogeneity in hydraulic properties of natural soil. Hydraulic conductivity (K_s) particularly has been shown to have the most variability among soil hydraulic parameters. For example, (Dagan and Bresler, 1983) showed that residual water content, saturated water content, and capillary head vary in much narrower limits than K_s. (Morbidelli et al., 2006b, Nahar et al., 2004, Saghafian, 1993). Several modelling studies have examined the effect of spatial variability of K_s on generation and transport of infiltration-excess runoff in circumstances where run-on infiltration can have an important impact on overall runoff (Julien et al., 1995, Nahar et al., 2004, Morbidelli et al., 2006b).

Rainfall temporal pattern is another important feature controlling infiltration-excess flow (Gomi et al., 2008b, Reaney et al., 2007, Dunne et al., 1991). The interaction between rainfall intensity and soil infiltration capacity, both spatio-temporal variables, determines the rate of infiltration, run-on, and subsequently runoff generation (Kirkby et al., 2005, Morbidelli et al., 2006b, Wainwright and Parsons, 2002, Reaney et al., 2014). The amount and intensity of rainfall reaching the soil surface regulates connections of generated flow between bare soil patches (Cammeraat, 2002, Mayor et al., 2008), with connectivity affecting time to peak, velocity and total discharge in hydrographs. For example, higher rainfall temporal variability may increase the probability of generated runoff being allocated to run-on infiltration downslope (Wainwright and Parsons, 2002).

Events with the same average and peak intensities can have different intensity patterns, which is also referred as rainfall pattern (Smith, 1972) or event profile (Dunkerley, 2012). Rainfall intensity, in concert with other factors such as infiltration capacity, determines threshold responses of hydrological processes, so that temporal variability of rainfall intensity can change the rate of infiltration, time-to-ponding, (Smith, 1972), peak flow (Julien et al., 1995), flow length and total discharge (Reaney et al., 2007). Thus, hydrological responses to storms with different intensity but similar interval metrics (e.g. total precipitation depth and peak intensity) could be distinctly different (Reaney et al., 2007, Moody et al., 2013).

(Dunkerley, 2012) conducted rainfall simulations in arid and semi-arid areas with low infiltration rate and compared hydrographs from temporally varied and uniform events. The results showed that the varying intensity events produced significantly larger runoff ratios and peak runoff rates (85%–570%), demonstrating the important rule of rainfall temporal

variability on soil infiltration rate and runoff generation in infiltration-excess flow. (Reaney et al., 2007) simulated dynamics of overland flow responses to temporal variability of a single storm event with 1000 realizations of varying intensity (40-90 mm/h) and durations (1- 20 min). The study showed that variation of runoff coefficient is positively related to rainfall intensity, whereas the maximum rainfall intensity only explains 14% of the variability in runoff coefficient. However, the study only isolated the effect of rainfall temporal variability without being integrated with the effect of spatial variability of soil and run-on infiltration on overall infiltration and runoff generation.

Results from (Saghafian and Julien, 1995), (Woolhiser et al., 1996), and (Corradini et al., 1998) examined sensitivity of peak flows and total runoffs to both spatial variability of K_s and rainfall intensity and found the sensitivities directly dependent on the magnitude of the rainfall events. (Wainwright and Parsons, 2002) showed that models using the mean rainfall intensity underpredicted overland flow dramatically.

Preferential flow has been found to have a crucial effect on infiltration-excess overland flow (Gerke et al., 2010, Lin, 2010, Flühler et al., 1996, Free et al., 1940) by controlling infiltration rate as water moves through microporous tubes in the dry soil matrix (Zhang et al., 2016). Soil-surface factors contributing to preferential flow in natural soil are soil bulk density (Reading et al., 2012), soil moisture content (Sanders et al., 2012), soil water repellency (Jarvis, 2007, Doerr et al., 2003, Nyman et al., 2010, Müller et al., 2018), plant roots systems (Stokes et al., 2009), rock fragments (Jomaa et al., 2012) and soil cracks (Zhang et al., 2015), shrink-swell phenomena (Shein, 2010), and activated macropores (Stoof et al., 2014b, Nyman et al., 2014, Nyman et al., 2010, Pascual Granged et al., 2010).

Activated macropores are found to be the dominant routes for preferential flow in soils (Guo and Lin, 2018). Once depth of generated runoff overcomes pressure entry of the macropores; known as breakthrough of the bottleneck, water converges to the pores initiating preferential flow and increasing infiltration rate (Guo and Lin, 2018, Jarvis et al., 2008). Rainfall temporal and volumetric factors are external deriving force by controlling depth of runoff in relation to macropore entry pressure (Guo and Lin, 2018)

1.2.5 Runoff Scaling Behaviour

Factors contributing to runoff generation and transfer may differ with both spatial and temporal scales, leading to overland flow scale-dependency (Gentine et al., 2012, Bergström and Graham, 1998, Blöschl and Sivapalan, 1995). Scale-dependency of infiltration-excess runoff

on hillslopes has been measured previously by several studies, with negative relationships between slope lengths and runoff production found (Wilcox et al., 2003, Wainwright and Parsons, 2002, Bagarello and Ferro, 2010, Delmas et al., 2012, Sheridan et al., 2014, Stomph et al., 2002, Van de Giesen et al., 2000, Xu et al., 2009, Bagarello et al., 2018). Thus, hillslope runoff cannot be considered as the sum of runoffs measured at individual points (Bergström and Graham, 1998, Cerdan et al., 2004). (Xu et al., 2009), (Bagarello and Ferro, 2010) and (Mayor et al., 2011) measured plot scale runoffs under natural rainfall, reporting inverse power relationship between slope length and measured runoff per unit area.

Rainfall total depth (Liu et al., 2000), gradient (Lal, 1983), landscape vegetation coverage (Mayor et al., 2011) and treatments (Lal, 1997, Gomi et al., 2008a, Le Bissonnais et al., 1998, Mayor et al., 2011) have all been found to be important drivers controlling the degree of overland flow scale dependence on hillslopes. (Lal, 1983) studied the effect of hillslope gradient and rainfall depth in controlling scaling effects by measuring plot-scale runoffs at arable hillslopes with different gradients for two consecutive years. The study showed both hillslope gradient and rainfall depth (mm) are influential in controlling scaling effects. However, the greater scaling effects were obtained from the second year with 50% more annual precipitation. (Moreno-de las Heras et al., 2010), (Mayor et al., 2011) and (Gomi et al., 2008a) showed that surface coverage is an important factor in controlling generated runoff and scaling effects and that higher vegetation coverage resulted in lower runoff generation with more pronounced scaling effects. (Le Bissonnais et al., 1998) measured plot-scale overland flow under two different treatments; bare and cultivated land and found higher overland flow scaling effects with cultivated plots. (Sheridan et al., 2014) found considerable scaling effects in runoff measurements during the first and second year following a moderate burn (2005-2006) in eucalyptus forest, southeast Australia.

Scaling behaviours of infiltration-excess overland flow within a given hillslope have been attributed to the main factors controlling infiltration and runoff processes. These factors are spatial variability of soil hydraulic properties (Hopmans et al., 2002, Julien and Moglen, 1990, Li and Sivapalan, 2011, Stomph et al., 2002), run-on effect (Joel et al., 2002, Langhans et al., 2014, Chen et al., 2016a) and rainfall temporal properties (Van de Giesen et al., 2000, Stomph and De Riddern, 2002, Wainwright and Parsons, 2002).

(Wainwright and Parsons, 2002) modelled overland flow routing and showed that scale dependency of the measured runoff coefficients is more sensitive to hydraulic conductivity and

water content, and their relative magnitute rather than to rainfall characteristic. (Chen et al., 2016) reported run-on process as the main cause of scaling, finding that a large fraction of runoff generated from less permeable areas upstream infiltrates in more permeable areas of heterogeneous soil downslope. The study found both rainfall intensity and soil spatial variability impacted scaling effects by influencing the run-on effect.

(Dunne et al., 1991) related scaling effects to the depth of runoff and activated macropores in plot-scale runoff measurement, stating higher infiltration occurs through microrelief and activated macropores when a greater proportion of the surface is inundated. (Wainwright and Parsons, 2002) conducted sensitivity analyses showing conditions with greater mean flow depth resulted in greater scaling effects.

Rainfall temporal properties are another important feature contributing to overland flow scaling effects by influencing the supply of water into the system and interacting with various soil and surface features (Li and Sivapalan, 2011, Reaney et al., 2014, Joel et al., 2002, Kirkby et al., 2005, Wainwright and Parsons, 2002). To further understand the scaling behaviour of overland flow on hillslopes, it is not sufficient to only investigate the effect of soil hydraulic variability on run-on infiltration processes. Space-time variability of rainfall regulates the rate of water supply and is also important (Bracken and Croke, 2007, Miyata et al., 2010b, Corradini et al., 2002). (Stomph and De Riddern, 2002) and (Wainwright and Parsons, 2002) demonstrated scaling effects along homogeneous hillslopes with help of field data and models, where scaling varied significantly according to the rainfall temporal variability. (Bagarello et al., 2018) and (Wainwright and Parsons, 2002) found that high intensity rainfalls reducing scale effects for both runoff and sediment transport. (Stomph and De Riddern, 2002) found scaling effects are more pronounced during short-duration rainfall events.

1.3 Research Gaps

The impact of fire on runoff scaling behaviours across different landscapes is poorly investigated and only a few practical studies (Sheridan et al., 2014) have measured runoff scaling on burned hillslopes. Most post-fire undertaken studies have focused on the role of vegetation patches, arrangement, and thickness in capturing mass and flow (Cawson et al., 2013, Cawson et al., 2012, Cerdá and Doerr, 2005), fire-induced ponding infiltration (Nyman et al., 2014, Nyman et al., 2010, Stoof et al., 2014b), and transport (de Dios Benavides-Solorio and MacDonald, 2005, Smith et al., 2011b, Stoof et al., 2012). Significant knowledge gaps remain in relation to post-fire soil-surface characteristics and their interactions with rainfall

properties contributing to scaling behaviours of infiltration-excess runoff. Further research is required to study the contributions of post-fire soil hydraulic properties, fire-induced water repellency, macropore flow and their interactions with rainfall patterns in controlling overland flow scaling behaviour in burned landscapes.

1.4 Research Objectives

This research aims provide insight and knowledge relevant to scaling behaviours of infiltration-excess overland flow in relation to fire-affected soil hydraulic properties, fire-induced water repellency, rainfall patterns, and macropore flow. More specifically the main objectives are as follows.

a) Quantifying the degree of runoff scale-dependency on a dry eucalyptus hillslope severely burned by wildfire.

b) Developing scaling coefficient indices to demonstrate aggregations of scaling effects at different temporal and spatial scales, and investigating the impact of topographic gradient, soil type, and surface vegetation on runoff scaling with help of these scaling coefficients.

c) Studying the contribution of rainfall temporal and volumetric factors in controlling overland flow generation and runoff scaling.

d) Investigating whether overland flow scale dependency on a burnt dry hillslope can be explained by a physically-based rainfall-runoff model coupling detailed runoff, infiltration and run-on processes with rainfall temporal variations at minute timescales.

e) Testing the impact of spatial variability of saturated hydraulic conductivity (CV_{Ks}) on model performance and scaling effects.

f) Quantifying activated macropores, water repellency and soil moisture in fire-induced hydrophobic soil.

f) Modelling macropore flow in relation to overland flow depth and pressure entry and its implication on capturing scaling effects across different plot length.

1.5 Research Method

This research project was designed to investigate overland flow scaling behaviours in relation to soil and rainfall properties at a burnt hillslope using observations, measurements and

simulations. This was achieved by i) collecting rainfall-runoff data from different plot lengths on a eucalyptus hillslope, southeast Australia burned by wildfire in 2013, ii) quantifying the degree of runoff scale-dependency from the collected rainfall-runoff data, iii) conducting stepwise regression analysis to examine runoff scaling behaviour in relation to the rainfall characteristics, iv) simulating overland flow and scaling effects by coupling traditional infiltration theory, run-on process and rainfall temporal variations, and v) investigating macropore flow contribution to runoff scaling behaviour by measuring vertical pathways of activated macropores with blue dye experiment at the site, water repellency, soil moisture, and by modelling macropore flow in relation to runoff depth, and accounting macropore flow into traditional rainfall-runoff simulations.

A multi-scale rainfall-runoff monitoring compound was built with replicated plots of different lengths to quantify the degree of overland flow scaling on a dry eucalyptus hillslope in southeast Australia, burned by wildfire January 2013. Data collection took place under natural rainfall conditions over ten consecutive months during 2014-2015, from which forty-one individual runoff-generating events were extracted (Chapter 3). The empirical rainfall-runoff data collected from the experimental site was used in a set of regression models to find the contribution of different rainfall characteristics in runoff generation and scaling behaviours at the site (Chapter 4).

An event-based rainfall-runoff model was adopted to simulate post-fire soil and surface conditions and verified against observed runoffs. The simulated runoff scaling was obtained and compared with observations to investigate whether rainfall-runoff models with traditional infiltration theory coupled with rainfall temporal variations and run-on processes can capture overland flow scaling behaviours. The impact of spatial variability of saturated hydraulic conductivity (CV_{Ks}) on model performance and scaling effects was also tested by varying CV_{Ks} in the model (Chapter 5).

Finally, measurements and macropore flow modelling were conducted to test two hypotheses: i) that soil infiltration increases with down slope distance due to increased soil moisture and weaker water repellency with distance and ii) increased infiltration occurs due to greater runoff depth exceeding macropore pressure entry resulting in more activating macropore and higher macropore flow downslope, subsequently causing scaling effects.

Hypothesis I was tested by measuring activated macropores, water repellency and water content at intervals down the longest plot (16 m). The blue dye experiment and soil

measurements were studied to characterise activated macropores patterns at the site. Hypothesis II was investigated by modelling macropore flow in relation to runoff depth satisfying pore entry pressure, with that pressure being exceed more frequently with distance downslope due to increased runoff depths. The macropores simulation was combined with rainfall-runoff models using traditional infiltration theory, runoff-runon, and rainfall temporal variability. Scaling effects captured by models with macropore flow were compared with observed scaling effects (Chapter 6).

Chapter 2: Geographic Information and Climate Classification of the study site

2.1 Geographic Information

The study site is in dry eucalyptus forest, between Aberfeldy (37°41′S 146°22′E) and Walhalla (37°56′S 146°27′E), Victoria, Southeast Australia. The forest is part of Aberfeldy River catchment, located to the east of the Thompson River dam watershed, which supplies Melbourne's drinking water. The catchment was severely burned in January 2013, with fire burning for approximately six weeks to a total area of 86,000 ha (DEPI, 2014). The area has burnt previously, most recently in 2006-2007 by the Great Divide Complex South fire.

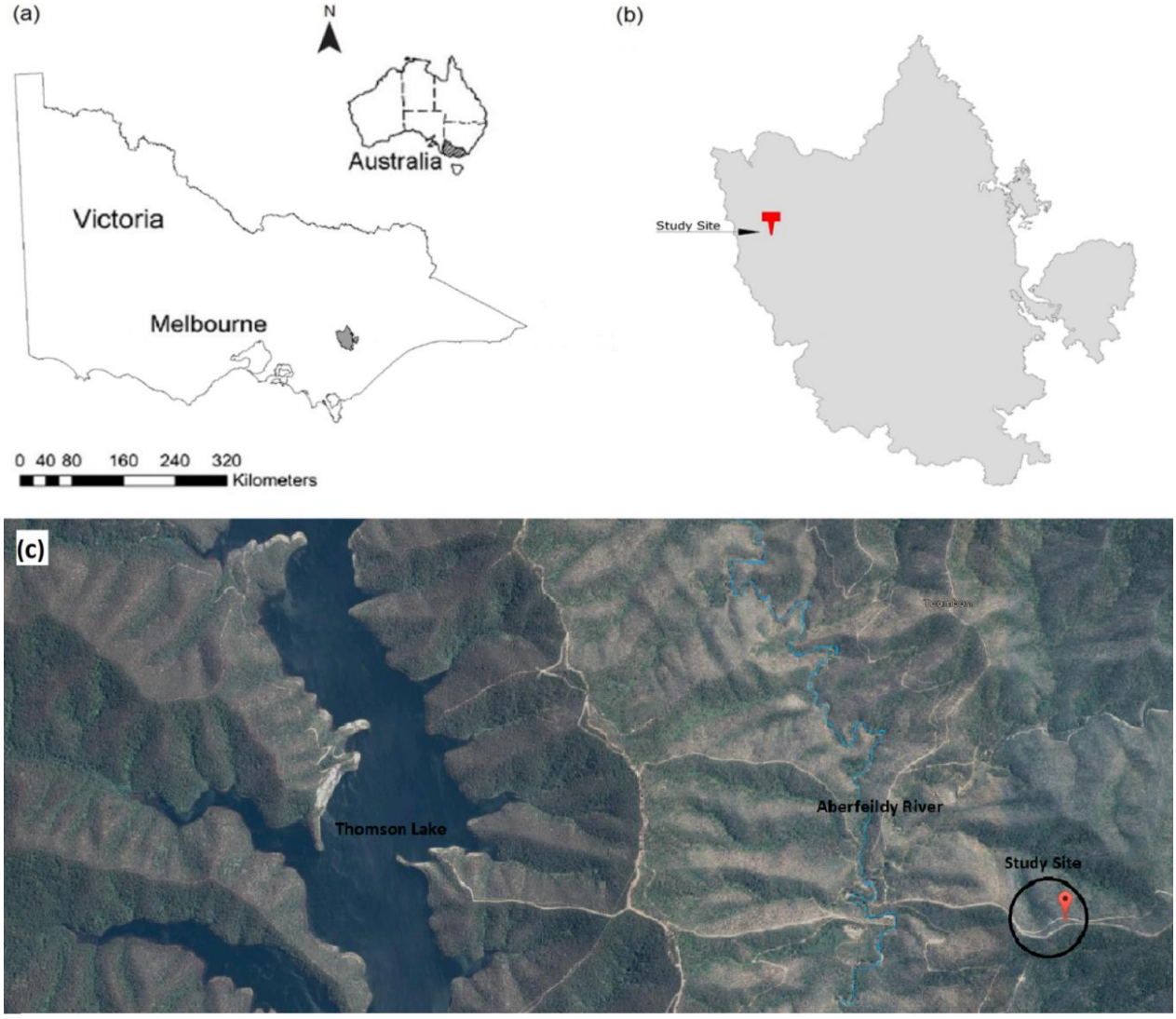

Figure 2. 1 a) East Victoria, Australia b) Experimental sites in West Gippsland Catchment c) Experimental sites in Thomson Dam Watershed.

An instrumented monitoring site was established on a north-facing steep hillslope with the highest aridity index (2.4) (Nyman et al., 2014) and that was subject to high severity fire in 2013 (37° 45' 36.9" E, 146° 25' 9.27" N). The elevation is ~830 m above sea level.

The study area is part of East Victorian uplands (Dissected uplands subdivision), the largest geomorphic subdivision in Victoria. The East Victorian uplands extend from east of Melbourne to the border of New South Wales. Most of the area consists of deep valleys separated by high narrow ridges, covered by native forests (Birch, 2003). The uplift mostly occurred suddenly in restricted periodic patterns during the Cretaceous (Cochrane et al., 1995). Erosion and river down-cutting following the uplifts formed deep and steep valleys separated by narrow ridges (Birch, 2003).

2.2 Climate Classification

Based on the Köppen climate classification, the site climate is classified as temperate with warm summers and cool-wet winters (Peel et al., 2007, Stern et al., 2000). Annual temperature and rainfall are influenced by the El Nino-Southern Oscillation (ENSO) and the tropical Indian Ocean (TIO) during austral spring (September–November), among a range of other influences (Cai et al., 2009).

Southern Australia receives most of its rainfall during the cooler months of the year (BOM, 2020). In autumn and winter (May - September), Victoria weather is determined by cold fronts moving with low pressure systems from west to east, particularly in Gippsland. Rain mostly results from large low-pressure cells originating from southeast coast resulting in long duration, low intensity rainfall events (BOM, 2020). Isohyets in rainfall maps are broadly similar to topographic contours patterns of the state (Berry et al., 2011, Catto et al., 2012). In the austral summer (December-March), the mean El Nino (ENSO) impact is weaker and rainfall mostly occurs due to high moisture content of surface water temperatures in the Pacific Ocean (Murphy and Timbal, 2008). Since the mid-1990s, southeast Australia has experienced declines in precipitation up to 15 percent in late autumn and early winter, with relatively small changes (or an increase) during spring (Murphy and Timbal, 2008, Hennessy et al., 2005, BOM, 2020).

Victoria was relatively warm and dry during the study period in 2014-2015. Annual rainfall averaged across Victoria was 505.2 mm, 23% below the long-term annual mean of 660.2 mm. Except the far east of the state, rainfall was mostly below average to very much below average; October rainfall was the seventh lowest on record for the month since 1900. Maximum

temperature for the whole state was above the long-term mean. Spring 2014 had the second-highest average maximum temperatures on record, with temperatures nearly 3 °C above the long-term mean. In contrast, autumn and winter were cooler than average temperatures, with winter being the coolest since 1989. Many hot days were recorded with the highest temperature (45.0 °C) in December being the warmest on record for this month, well above the long-term mean monthly maximum temperature of 37.8 °C average for December.

There are five weather stations with distance of less than 70 km to the site; Mount Useful, Murderer hills, Walhalla, Baw Baw and Erica. The Aberfeldy weather station (no. 85278) (BOM, 2020) is the closest station to the study site (14 km North) collecting consistent data of rainfall and daily global solar exposure since 1983 until August 2015 which is one month before the end of data collection in the study site (Table 2.1).

Figure 2.2 compares total monthly rainfalls during the study period (2014-2015) to the long-term (1983-2015) maximum, mean, median, and lowest monthly rainfalls collected at Aberfeldy weather station, the closest station to the study site (BOM, 2018). Annual rainfall for years 2014 and 2015 were 892 and 750 mm respectively at this station, lower than long-term annual median (989 mm) and mean (1009 mm) rainfall. Monthly rainfalls from January to August were close to long-term monthly means. This trend changed during spring and early summer for both years, with monthly rainfall below the long-term average and even lower than long-term minimum (September) since 1983.

Table 2. 1 Weather stations nearby the study area (BOM, 2018)

Name	BOM Station no.	Coordinates	Elevation (m)	Operation period
Aberfeldy	85278	37.72° S, 146.39° E	495	1983-Onward
Mount Baw Baw	85291	37.84° S, 146.27° E	1561	1991-onward
Murderers Hill	85289	37.85° S, 146.56° E	720	1989-Onward
Mount Useful	85021	37.70° S, 146.52° E	1440	2002-Onward
Walhalla	85091	37.94° S, 146.45° E	348	1884-Onward
Erica	85026	37.97° S, 146.37° E	445	1931-Onward

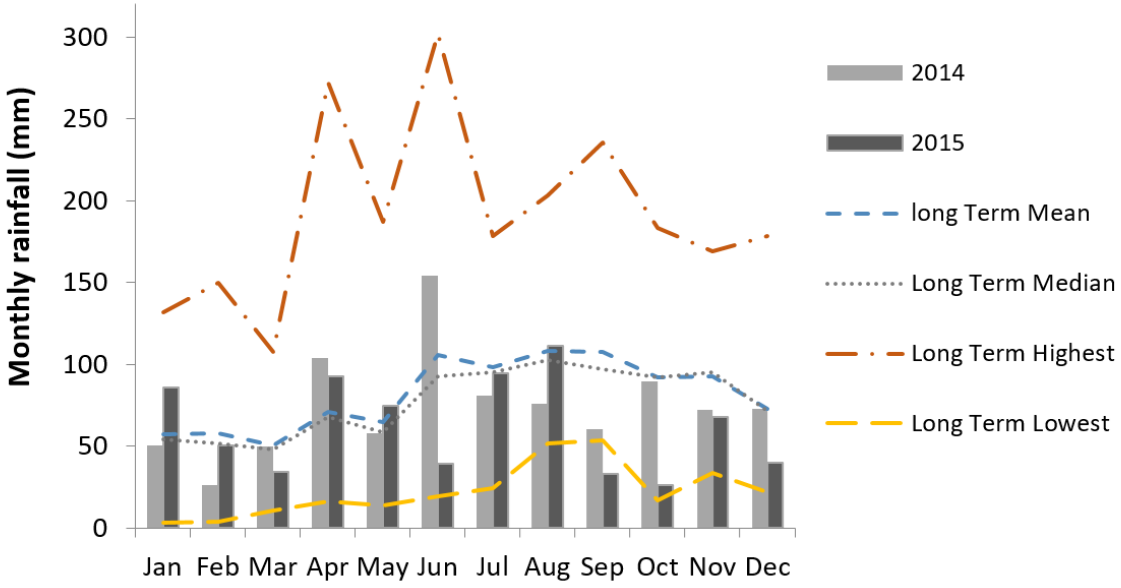

Figure 2. 2 Monthly rainfalls for the study period (2014-2015) and the long-term (1983-2015) data collected at Aberfeldy weather

From five nearby weather stations, only Baw Baw weather station recorded long-term temperature data including study period. The Mt Baw Baw station elevation is 730 m higher than the site, so average temperatures will be different. Data from this station was used to study temperature ranges in the study area for years 2014 and 2015, compared with long term conditions at the site. Monthly mean temperature variations were from 7.8°C to 16.1°C and -1.8°C to 10.8°C respectively in summer and winter at Mt Baw Baw during study period (2014-2015). Compared with the long-term mean temperatures 2.9 °C in winter and 16.1 °C in summer recorded at Baw Baw station, winter 2014 was 3°C cooler while summer was similar to the long-term conditions.

Vegetation in Victoria is classified using Ecological Vegetation Class (EVC) mapping, which is based on detailed interpretation of aerial photograph images and extensive fieldwork (Oates and Taranto, 2001). Based on EVCs, dominant tree species in the study site are mostly narrow-leaved peppermint (Eucalyptus radiata) and stringybark (E. baxteri). Vegetation density for both the upper and lower storeys is influenced by topographic aspect and aridity index in southeast Victoria (Van der Sant et al., 2018, Ossola and Nyman, 2015, Nyman et al., 2015). These studies showed that understorey coverage on northern (equator facing) aspects is not as dense as on southern aspects. The ground surface is sparsely (10-25 %) covered with small

shrubs like silver banksia (Banksia marginata), hakea/needlewood (Hakea spp.), and other grasses with open space in between.

Chapter 3: Measurement of overland flow scale-dependency using multi-length rainfall runoff plots

Abstract

Scale-dependence of overland flow is frequently observed in rainfall runoff datasets, yet largely neglected in models, limiting our capacity to scale up plot-scale runoff measurements to the hillslope scale. The aim of this study was to quantify the scale-dependence of overland flow from hillslopes burned by wildfire, where elevated runoff and erosion rates can be extreme but difficult to predict because rainfall-runoff scale effects are poorly understood (Stoof et al., 2012, Moody et al., 2013, Doerr et al., 2003).

Rainfall and runoff were measured under natural rainfall conditions for five runoff plot lengths varying from 0.5 to 16 m on a severely burned hillslope covered with eucalyptus forest in southeast Australia. Data collection took place over ten consecutive months during 2014-2015; from which forty-one individual runoff-generating events were extracted. For all storm events, there was runoff from replicated plots. Data analysis showed that the rate of runoff declined with increasing plot length. Runoffs from replicates was well correlated for storm events, seasonally and the whole study period.

Two scaling coefficients were defined by correlating runoff depth and runoff ratio with plot length. Regression models related runoff depth and ratio to the natural logarithm of the plot length. They were fitted at event, seasonal and annual time scales. Regression slopes defined runoff depth scaling (SC_1) and runoff ratio scaling (SC_2).

The reliability of the results was investigated in two ways. First, sensitivity testing showed that the treatment of non-rain periods and small rainfall pulses in defining the start and end of events had only a small, statistically insignificant impact on estimating the scaling coefficients; less than 10% for SC_1 and 2% for SC_2. Anomalous behaviour in the total runoff volume collected from 16 m plots was found and appears to be real after careful investigation of field equipment. Excluding the 16 m plots led to larger depth ($|SC_1|$ increased 25%) and runoff ratio ($|SC_2|$ increased 18%) scaling effects.

The impact of rainfall total depth, slope gradient and geomorphology (soil-surface) on runoff scaling were investigated by calculating the scaling coefficients (SC_1 & SC_2) for overland flow studies from the literature. Relationships between the scaling coefficients and annual

rainfall depth, soil hydraulic conductivity, surface vegetation, and slope gradient were investigated graphically. The result showed that annual rainfall depth is a strong driver in controlling overland flow scaling. Both SC_1 and SC_2 were influenced by rainfall depth, with SC_1 being more sensitive. Soil texture and hydraulic conductivity were also found to be important, with higher SC_2 in studies with coarse soil texture and higher hydraulic conductivity. This might be related to the role of runoff-runon processes (downslope re-infiltration) in controlling scaling effects. Runoff generation in specific studies were also influenced by vegetation coverage and slope gradient; however, no systematic trend was found associating scaling coefficients with change in gradient or vegetation in previous studies.

3.1 Introduction

Measurement of overland flow scaling effects have been conducted in several studies, which found negative relationships between slope length and the runoff ratio in semiarid areas throughout the world (Wilcox et al., 2003, Wainwright and Parsons, 2002, Bagarello and Ferro, 2010, Delmas et al., 2012, Sheridan et al., 2014, Stomph et al., 2002, Van de Giesen et al., 2000). The negative relationship has even been detected during periods of continuous runoff in plots with different lengths (Joel et al., 2002). This implies that runoff generated at a point may not reach the outlet boundary. For example, observed runoff coefficients were 30-50% and 4% at point scale (1 m^2) and watershed scale (130 ha) respectively in central Côte d'Ivoire, Africa (Joel et al., 2002, Van de Giesen et al., 2000).

To examine the impact of wildfire on timing and magnitude of extreme hydrologic events, it is essential to quantify the degree of scale-dependency of hydro-geomorphic processes after burns. The enhancement of overland flow formation in early rainfall events after fire has been reported in several studies (e.g. a 3-fold increase in burnt eucalyptus forest, Southeast Australia (Sheridan et al., 2007), a 4-fold increase in burnt pine forest, California (Onda et al., 2008)). Fire as a disturbance can greatly alter connectivity of source areas that results in changes in runoff processes and consequently may impact the relationship between runoff and scale. The degree of scale dependence in overland flow in a burned landscape may vary depending on the degree of soil-surface disturbance. These disturbances include soil properties alterations (Moody et al., 2013), fire-induced water repellency (Sheridan et al., 2007, Doerr et al., 2009), vegetation removal (Wilcox et al., 2003, Moreno-de las Heras et al., 2010, Stoof et al., 2012) and an increase in proportion of bare soil patches (Cawson et al., 2013). In addition, response thresholds for hydrological processes on burned hillslopes may change in response to changes in space-time variability of post-burn hydro-geomorphic conditions (Moody et al., 2013).

Soil-surface spatial variability and rainfall temporal properties have been found to be the main factors in controlling the negative relationship between runoff production and slope length (Sheridan et al., 2014, Wainwright and Parsons, 2002, Van de Giesen et al., 2011, Van de Giesen et al., 2000). At the hillslope scale, one of the main processes causing the scaling effect is runoff-runon process (re-infiltration) due to spatial variability in soil hydraulic properties (Jones et al., 2009, Morbidelli et al., 2006a). There are also thresold dependent processes that may emerge with scale change (Cammeraat, 2002). For example, soil macropores, while only

a small portion of the total soil volume, may contribute considerably to infiltration when flow depth exceeds macropore entry pressures (Nyman et al., 2010, Dunne et al., 1991, Langhans et al., 2013).

The objectives of this chapter are to a) quantify scale-dependency of overland flow from a dry eucalyptus hillslope severely burned by wildfire, b) develop scaling coefficients indices quantifying scaling effects at different temporal and spatial scales, and c) to investigate the impact of annual rainfall, topographic gradient, soil type, and surface vegetation on runoff scaling with help of these scaling coefficients.

3.2 Method

3.2.1 Site set up and Instrumentation

Replicated rainfall-runoff plots with different lengths were installed on a dry eucalyptus hillslope in southeast Australia that was burned by wildfire January 2013. The instrumented area was all on one hillslope and consisted of a rainfall throughfall collector, two replicates of 4x1.5, 8x1.5, 12x1.5, and 16x1.1 m runoff plots, all connected to 0.5 *L* tipping buckets, and three 0.5x0.5 m runoff plots paired with raingauges similar to infiltrometer-rainfall gauges in (Moody and Ebel, 2014). A schematic plan of the instrumented area is illustrated in Figure 3.1 and presented in Table 3.1.

Tipping bucket rain gauges (Model TB3/0.2mm/28cm diameter, Hydrological Services Pty. Ltd., NSW, Australia) were used to measure throughfall. Adjacent to these rain gauges, 0.5x0.5m plots were installed and collected runoff from these plots conveyed by 50 mm pipes to tipping bucket rain gauges (Model TB3/0.2 mm/20 cm diameter). The funnel-shaped collectors of those rain gauges measuring runoff were covered by MDF lid in order to avoid throughfall getting into the funnel (Figure 3.2). These infiltro-rainfall gauges were installed at different locations; the upper right, middle and the lower left corner of the hillslope.

The throughfall collector was built with two parallel galvanised u-shaped gutters (7.0x0.15 m) linked to a T-shaped 80 mm pipe, carrying collected throughfall to the standard collection pipe and then flexible hose connected to a tipping bucket. In order to eliminate the effect of micro-topography on throughfall collection, the troughs were fixed at 0.5 m above ground surface using star pickets and wire (Figure 3.3).

All runoff plots were bound at the top and sides using metal sheet with 200 mm width and either 500- or 1050 mm length, overlapped by 50 mm and hammered into the ground. Pop rivets were used to tie the overlapping metal sheet edges together. The space between overlapping plots was sealed by silicon glue and clamped for 24 hours.

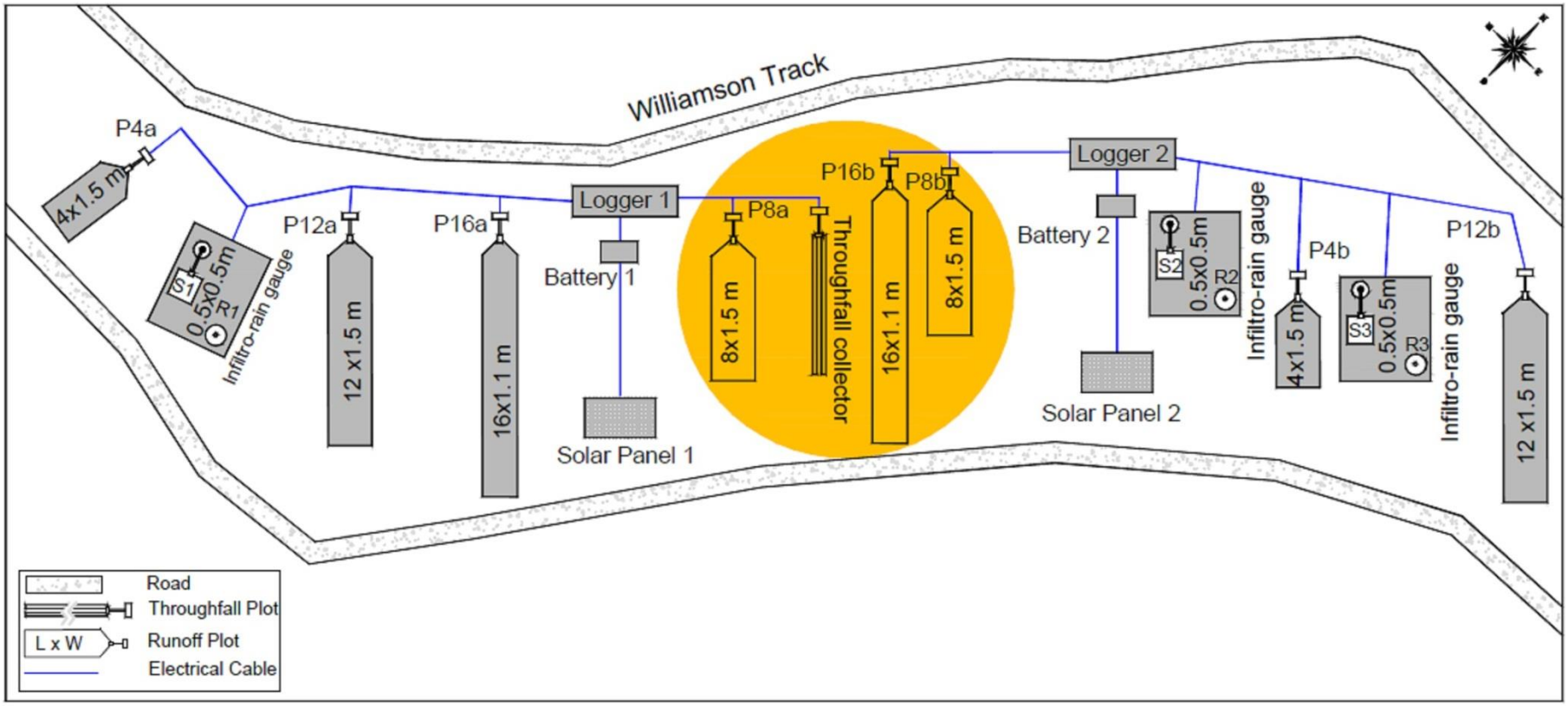

Figure 3.1 Schematic plan of the instrumented compound; throughfall and two 8x1.5 m runoff plots bounded in the yellow circle were operated for previous study (Van der Sant, 2016) from June 2013 to April 2014

Table 3.1 Constructed runoff plots, rain gauges and their connections to loggers

No.	Acronym	Equipment Type	Area			Connected to Logger	Cable no.
			Rectangular	Triangle	Total		
			m²				
1	P4a	Runoff plots	4*1.5	0.9*1.5	7.35	1A	1
2	P12a		12*1.5	0.9*1.5	19.35		2
3	P16a		16*1.1	0.9*1.1	18.59		3
4	P8a		8*1.5	0.9*1.5	13.35		4
5	T	Throughfall	Two gutters, each 7*0.15		1.8		5
6	P16b	Runoff plots	16*1.1	0.9*1.1	18.59	2A	4
7	P8b		8*1.5	0.9*1.5	13.35		3
8	P4b		4*1.5	0.8*1.43	7.15		2
9	P12b		12*1.5	0.8*1.43	19.15		1
10	R1	Raingauge	Diameter: 0.28		0.064	1A	6
11	S1	Runoff plot	0.5x0.45	-	0.225		7
12	R2	Raingauge	Diameter:0.28		0.064		5
13	S2	Runoff plot	0.5x0.45	-	0.225	2A	6
14	R3	Raingauge	Diameter:0.28		0.064		7
15	S2	Runoff plot	0.5x0.45	-	0.225		8

The bottom part of runoff plots was built in triangle shape by installing metal sheets with 10 cm S-bend at the both ends. Inside angle of 135° was created at the plot outlet to fit a pre-made box collector. The downslope edges of the plot and the outlet were sealed with cement to avoid surface runoff leaking through these areas. The box collector was linked to 1m PVC pipe (50 mm diameter) and a piece of flexible hose attached to the tipping bucket. Tipping buckets were screwed to a pre-made concrete slab (40 x 40 cm) levelled on soil cutting area at 1m distance downslope of the plot outlet (Figure 3.4-left).

Figure 3.2 Paired rain gauge-inflitrometer

** Runoff from impermeable concreted area; marked in green circle was deducted from the collected data*

Two data loggers (Model DT80 Intelligent Universal Input Data Logger) with 12 digital channels were installed. Collected data from all tipping buckets and rain gauges was sent to these loggers and recorded in three minutes intervals during study period. Also tipping buckets were equipped with magnetic manual counter which being used to cross-check against the recorded data from the loggers. Two solar panels (Daqo New Energy) were also installed to feed batteries for loggers (Figure 3.4-right).

Figure 3.3 Throughfall gutters to its tipping bucket

Figure 3.4 Runoff plot connected to its tipping bucket (left), Data logger connected to its battery (right)

3.2.2 Data Collection

Rainfall-runoff data were collected at three minutes intervals for 308 consecutive days from 10th October 2014 to next year mid-winter (14th August 2015). Site service and data collection was conducted monthly regardless of total rainfall. During each site visit, standard recording sheets were filled out for data collection and site servicing according to a field protocol. Soil hydraulic properties and saturated water content were not measured before and during data collection period.

Tasks related to data collection were 1) downloading data from loggers, 2) investigating downloaded data for missing or out of range data, 3) recording manual counters, 4) checking data accuracy by cross-checking collected data from loggers and manual counters, and 5) formatting data loggers.

Site servicing and maintenance included 1) checking functionality of instruments, 2) checking plot boundaries for possible water leakage 3) removing debris and sediment from the funnel of rain gauges, plot outlets, collectors and pipes, 4) measuring battery voltage, and 5) calibrating tipping buckets and rain gauges.

Tipping buckets connected to plots, throughfall and rain gauges were calibrated once before installation and then later during operation. Calibrations were conducted by adding a known volume of water continuously and counting numbers of tips in relation to the volume of water added. By obtaining nominal volume per tip, numbers of recorded tips were converted into volume of water (litres) and volume of water per unit area (mm).

Water was applied using hose before installation and ten litre containers with tap were used at the study site after installation as shown in Figure 3.5. A nominal volume of 0.5 litres was calibrated per each tip of the tipping buckets connected to runoff plots and throughfall collectors.

Rain gauges were calibrated using a raingauge calibrator (653 millilitres) and tips were recorded by a data logger both in the laboratory and at the field site (Figure 3.5 & Appendix 3.1). The number of tips divided by the volume of the dripper bottle was used as the volume per tip. The calibration procedure was repeated three to four times for each rain gauge to ensure result consistency.

The nozzles of rain gauge were narrow (~3 mm) and they easily clogged with accumulated fine residue and sediment. To avoid clogging, the funnel-shaped collectors were covered by mesh form fabric wrapped around metal mesh. Accumulated residue was removed manually in each site visit (Figure 3.6).

Figure 3.5 From top to down: Calibration of tipping bucket connected to runoff plots and rain gauges.

Figure 3.6 Metal mesh and fabric mesh form used to capture fine residue

3.2.3 Vegetation Recovery

Canopy and understory vegetation coverage was assessed visually for each plot during each site visit. In addition, a quadrat was used twice, once at the beginning and then at the end of the experiment (Figure 3.7), to estimate the percentage of vegetation coverage and bare soil using field cover charts (McDonald et al., 1998). The outcome of these observations was used to study vegetation recovery; upper storey, understorey and litter recovery, and its impact on the rate of runoff generation. Figure 3.8 shows vegetation recovery at the end of study period.

Figure 3.7 Right to left: Understorey coverage measured with quadrat at the beginning and the end of the study period

Figure 3.8 Upper storey recovery at the end of the study period

3.2.4 Data Quality Control

Measurement errors in throughfall collectors and replicated runoff plots were mainly caused by broken tipping buckets, clogged funnels, and sediment accumulation in buckets. Diagnostic reports were made after downloading data during each site visit to identify invalid data and remove them from the dataset. Regression plots were made between collected data from pairs of replicated plots. These regression analyses were used to infill missing data in the case of faulty equipment.

Two statistical methods were applied in this study to control and refine recorded data: a) Regression analysis of accumulated data (double-mass curves) was used to detect malfunctioning replicates for the whole study period and individual events. For example, double mass curves of accumulated data from three rain gauges against the throughfall collector (Figure 3.9b) showed that R3 pluviometer was out of order for three consecutive months and no data were recorded from R2 pluviometer in the last month due to channel disconnection. b) Correlations of collected data from replicates in three minutes intervals for individual events were also conducted. This method was very helpful to pinpoint errors caused by tipping buckets moving out of calibration over a period of several months. Although, three minutes temporal resolution might be longer than 0.5 m plots response time. This was a limitation of the data loggers storage.

3.2.5 Data Analysis

- **Rainfall Data**

Throughfall data were assumed to be similar to rainfall beneath the canopy and used as rainfall data in data analyses. Rainfall was obtained by area weighed average values of data collected at throughfall troughs and rain gauges for 308 days of the study period (from October 2014 to August 2015). Double mass curve analysis was used to check consistency between collected throughfall at the site and rainfall from the nearby weather stations. Accumulated throughfall volumes at the experimental site (37° 45' 36.9" E, 146° 25' 9.27" N, Elevation: 832 m) were plotted against rainfall data at Aberfeldy (10 km to the south, Bureau No.: 85278, Elevation: 495 m) and Murderer Hill (15 km to the northeast, Bureau No.: 085289, Elevation: 720 m) for the study period. Also, regression analysis was conducted for monthly rainfalls recorded at the site against monthly data at these Bureau weather stations for the same period.

Data from weather station was considered as a representative at seasonal scales and how it relates to longer climate but not events. Local gauges was used for detailed events as the more distant gauges would not be representative at short time scales.

Availability of continuous data at fine temporal scale made it possible to investigate rainfall-runoff trends at different temporal scales from very short storm pulses to the whole 308 days of the study period. Rainfall data were grouped in monthly and daily intervals to identify individual rainfall events that produced overland flow in all operating plots and replicates, from 0.5 to 16 m length. Events were defined a) When the rainfall produced runoff in at least one of the runoff plots within 60 minutes, this was considered to be the start of the event, and b) the event ended when no overland flow was recorded in any of runoff plots for a period of 60 minutes. This definition was also used by (Cawson et al., 2012) and (Van der Sant, 2016) to define rainfall-runoff events. Some events consisted of multiple pluses of rainfall separated by a rainfall hiatus; an inter-storm period with no rainfall. Observations in this study and similar previous studies (Delmas et al., 2012, Mayor et al., 2011, Gomi et al., 2008b) showed that overland flow ended shortly after rain stopped. Thus, a maximum non-rain period of one hour was considered sufficient to separate individual storm events.

Forty-one rainfall-runoff events were selected from the rainfall-runoff data recorded during the study period. For all selected events, there was runoff in all plot lengths, with similar hydrographs characteristics in replicas. The selected storm events have different durations, intensities and patterns, varying from small to large, from dry to wet antecedent conditions. Some pairs of events have similar durations and total rainfalls but with different patterns.

To check whether event selection, definition of event start and end and treatment of non-rain periods within an event impacted the estimates of runoff scaling effects, an alternate set of events was collated consisting of only the main pulses for each event. The scaling effects from this alternate rainfall-runoff set were compared against the scaling effects from the original events.

To describe each storm event, various characteristics of precipitation were calculated including: the rainfall total depth (mm), duration (h), mean and maximum intensity of rainfall pulses (I_{mean} & $I_{max(3mins)}$), rainfall peak (mm/h), and coefficient variability of storm pulses (CV).

Non-rain periods are generally insignificant in runoff production while they can contribute significantly to overall storm duration. Thus, over-estimation of storm duration may occur when storms contain one or multiple dry spells (van Dijk, 2002). To compensate the effect of non-rain periods, depth-weighted rainfall intensity ($\check{R}$) and also storm duration (D_T) were extracted using exponential functions given by (van Dijk, 2002) as additional rainfall characteristics. Depth-weighted intensity represents the average intensity with which the rainfall volume arrives, rather than the temporal mean intensity. Given that more runoff is likely to be generated in high intensity periods, this depth-weighted intensity should be more reflective of runoff volume.

$$\text{Eq 3.1} \qquad \check{R} = \frac{\sum_{i=1}^{n}(R^2\Delta t)_i}{P}$$

For storm duration, a representative duration or time period (D_T) was proposed by van Dijk as:

$$\text{Eq 3.2} \qquad \mathrm{D_{T(<R^*)}} = \frac{\mathrm{P}}{\mathrm{R^*}}\left(1 - \exp\left(-\frac{\mathrm{R^*}}{\check{\mathrm{R}}}\right)\right)$$

$$\text{Eq 3.3} \qquad \mathrm{D_{T(R\geq R^*)}} = \frac{\mathrm{P}}{\check{\mathrm{R}}}\mathrm{E_1}\left(\frac{\mathrm{R^*}}{\check{\mathrm{R}}}\right)$$

$$\text{Eq 3.4} \qquad \mathrm{D_T} = \mathrm{D_{T(<R^*)}} + \mathrm{D_{T(R\geq R^*)}}$$

Where $\check{R}$*:* depth-weighted rainfall intensity, D_T*:* storm duration, R^*: minimum nominal rainfall intensity (mm h^{-1}) calculated from tipping bucket intervals; one tip divided by time step. R^*: 0.06 mm/h, P: rainfall depth (mm), $E1(x)$*:* the exponential integral function known as the Theis well function.

- **Runoff Data**

Total runoff volume (litre), runoff depth (mm), and runoff ratio (%) were calculated on annual, seasonal, and event bases. In addition, hydrographs for forty-one runoff-generating storms were produced along with their associated hyetographs.

Runoff metrics were calculated based on the following procedures:

- Runoff total volume (Q_v): The total volume of collected runoff was estimated by converting number of tips to litre as a volumetric unit. Also, runoff volume in litres was divided by the plot area to obtain runoff depth (Q_d) in millimetres (mm).

$$\text{Eq 3.5} \qquad Q_v = \frac{Recorded\ tips}{Nominal\ volume\ per\ each\ tip}$$

$$\text{Eq 3.6} \qquad Q_d = \frac{Q_v}{Area}$$

- Runoff ratio *(Q_R)*: The total volume of runoff divided by the total volume of rainfall *(P)*, expressed as a percentage.

$$Q_R = \frac{\sum Qv}{\sum P} \quad \text{Eq 3.7}$$

- Runoff peak rate (*P*): The maximum 3-minute runoff rate recorded during the event (mm h^{-1}).

Two scaling metrics were introduced to quantify overland flow scale-dependence for individual events, seasons and the whole study period.

- **Total Runoff Scaling Coefficient (SC_1)**: Total runoff depths (R_d) were plotted against the plot lengths (*x*). The slope of the regression line was considered as scaling coefficient for total runoff.

$$R_d = SC_1 f(x) + \propto \quad \text{Eq 3.8}$$

Where R_d is runoff depth, *x* is plot length, and $\propto$ is the intercept of the regression line representing runoff depth at point scale, *f(x)* is one of a linear, natural logarithms, exponential and power law relation (see below).

- **Runoff Ratio Scaling Coefficient (SC_2):** To compare runoff scaling at different temporal scales; annual, seasonal and event basis, a scaling coefficient independent of storm volume was needed. Thus, the second scaling coefficient (SC_2) was introduced by correlating runoff ratios (R_R) to plot lengths (*x*). The slope of the regression line was considered as the runoff ratio scaling coefficient (SC_2).

$$R_R = SC_2 f(x) + \propto \quad \text{Eq 3.9}$$

The impact of rainfall total depth has been taken into account in this index because $R_R = R_d/P$.

$$SC2 = \frac{SC1}{P} \quad \text{Eq 3.10}$$

Regression lines were modelled in linear, natural logarithm, exponential and power law relations to gain the best regression model with the highest coefficient of determination. It is desirable to predict positive runoff production in very long plots when the rainfall time duration or total is infinite satisfying infiltration at some point.

An assumption was made to have runoff production in very long plots when the rainfall time is infinite. To keep this assumption, runoff production is always between zero and infinity; regression line never meets X representing plot length and Y representing.

Clearly it is desirable for any model to predict positive runoff production in very long plots, so models that remain positive are preferable to those that predict negative depths (e.g. linear model) for long plots.

Soil-surface spatial variability, gradient and rainfall properties have found by others to be the main factors in controlling the negative relationship between runoff production and slope length (Sheridan et al., 2014, Wainwright and Parsons, 2002, Van de Giesen et al., 2011, Van de Giesen et al., 2000). Hence the runoff depth scaling coefficients (SC_1) is assumed to be a function of gradient, geomorphology and precipitation.

$$SC1\ \alpha\ fn(Precipitation.Gradient.Geomorphic(Soil\ Type.Surface\ Coverage))$$

The impact of total rainfall depth has been taken into account in the runoff ratio scaling coefficient (SC_2) because runoff ratio is the product of runoff depth divided by rainfall depth ($R_R=R_d/P_d$). Therefore, SC_2 was considered to be a scaling effect mainly controlled by slope and geomorphology.

$$SC2\ \alpha\ fn(Gradient.Geomorphic(Soil\ Type.Surface\ Coverage))$$

Where R_d = runoff ratio, R_d = runoff depth and P_d = rainfall depth.

3.3 Results

3.3.1 Rainfall Characteristics

Total collected throughfall was 616 mm for the 308 days of the study period from October 2014 to August 2015. Double mass curves between the experimental site and nearby weather stations indicate consistent behaviour with slightly lower throughfall at the site than rainfall at Murderer Hill and Aberfeldy (Figure 3.9 a, b). Ten-month accumulated throughfall at the experimental site was lower than the mean and median values at the nearby weather stations and in fact was in the 10th percentile of the frequency distribution. The regression analysis showed that average monthly rainfall data from experimental site is more correlated with rainfall at Aberfeldy (R^2=0.52) that Murderer Hill (Figure 3.10a). The study period accounted for 29.4% (in 3 months) in and 54% (in 7 months) of the annual rainfall in 2014 and 2015 respectively. The rainfall seasonal allocation for the whole study period is presented in Figure 3.10b.

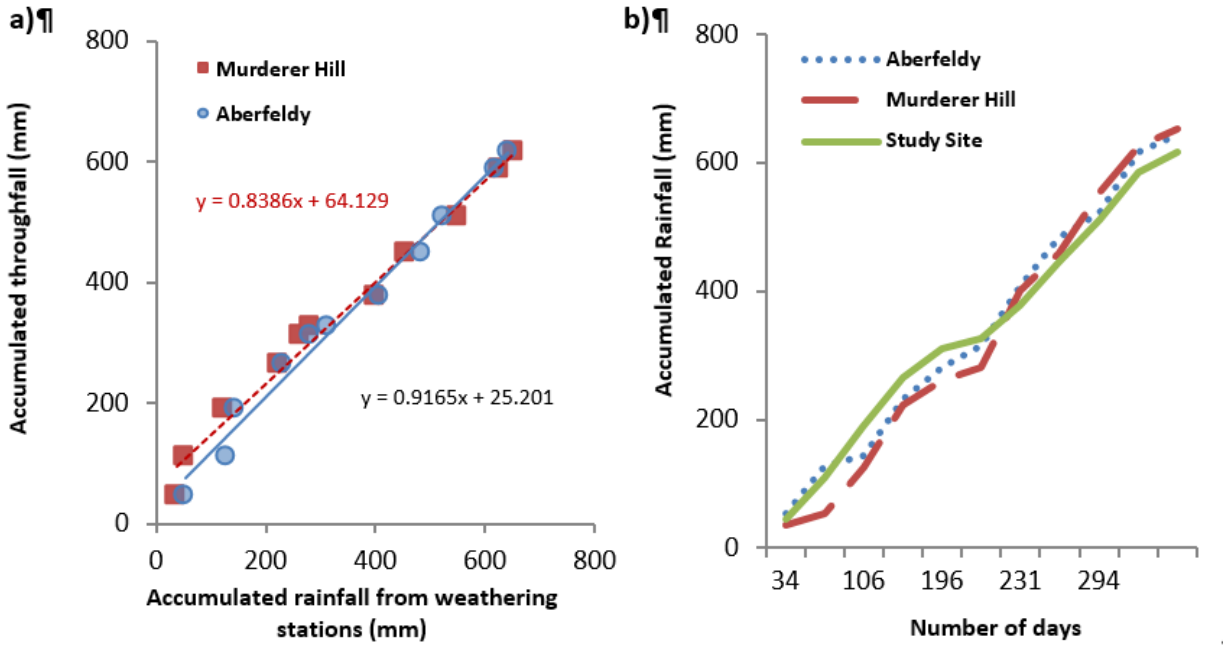

Figure 3.9 a) Double mass curves and b) accumulated linear trends of throughfall recorded at study site in comparison to collected rainfall from Aberfeldy and Murderer Hill weathering stations

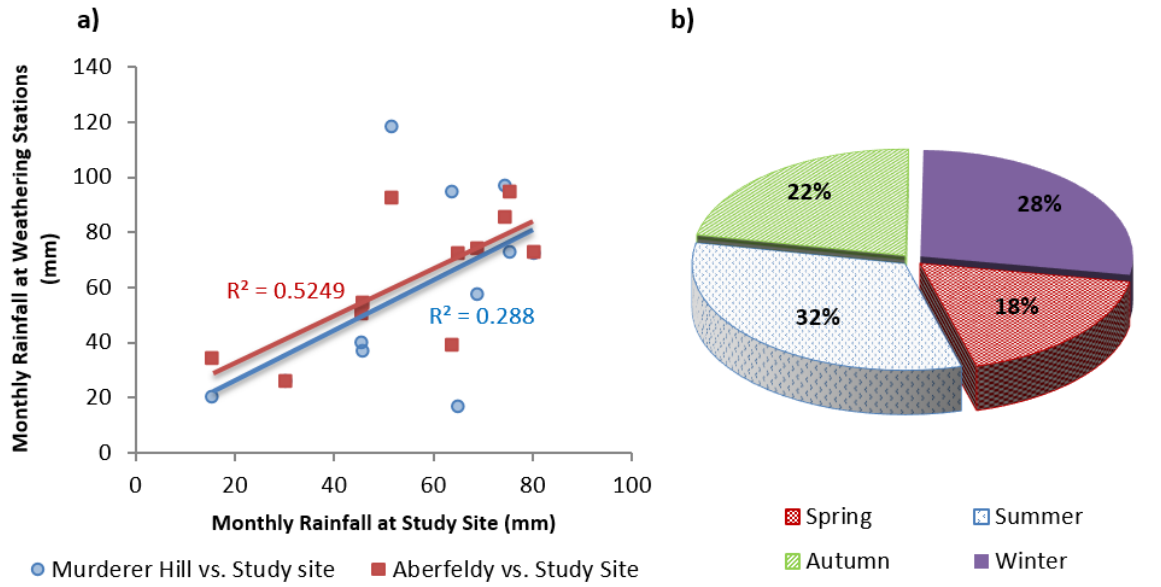

Figure 3.10 (a) Monthly throughfall measured at study site correlated to rainfall data collected at Aberfeldy and Murderer Hill weather stations (BOM), (b) Rainfall seasonal allocation for the whole study period (308 days).

Accumulated rainfall from the raingauges and throughfall collector were plotted (Figure 3.11a) along with double mass curves for the study period (Figure 3.11b) to detect possible problems caused by clogging or other equipment failure. This shows that pluviometer R3 was out of order for three consecutive months, which was detected and rectified during a site visit. The rain gauge was replaced, after several failed repair efforts. There was also no data recorded from pluviometer *R2* in the last month due to disconnection from the data logger. Missing data was infilled using regression, as explained in the Methods section.

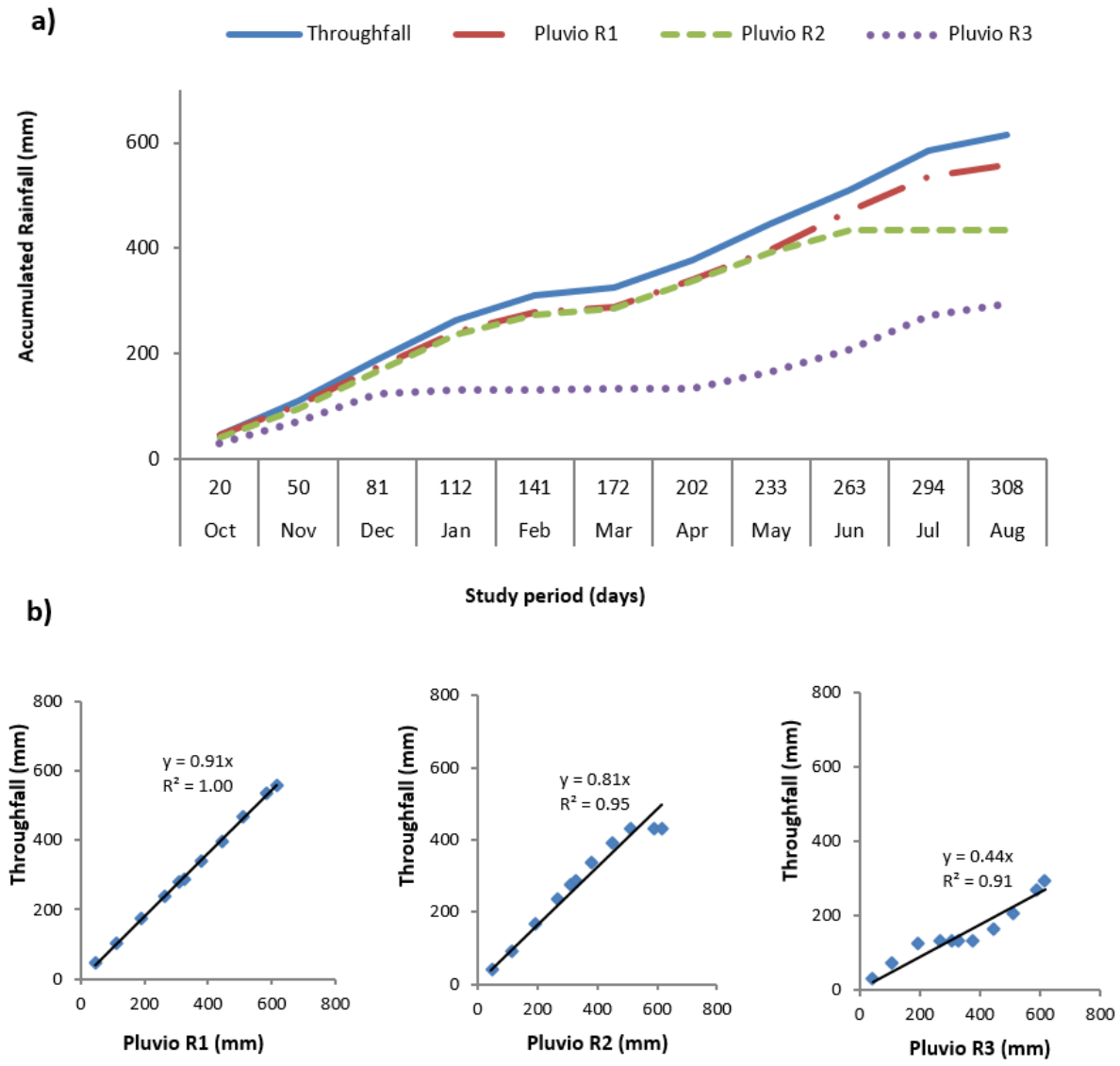

Figure 3.11 (a) Accumulated rainfalls from throughfall collectors and rain gauges; R1, R2, and R3 (b) double mass curves of accumulated data from three rain gauges against the throughfall collector

3.3.2 Runoff-generating Events

Volumetric and temporal indices for forty-one runoff-generating storms and their associated runoff responses are given in Table 3.2 for different plot lengths. Storm hyetographs with associated hydrographs for plot lengths from 0.5 to 16m are also presented in Figure 3.12. No Rilling or flow concentration was observed downslope of the plots.

Table 3.2 Volumetric and temporal indices of rainfall events and their associated runoff productions for plots with different length

Event No.	Start	End	Rainfall							Runoff									
			Duration	Total	Mean	Peak	Ř	DT	CV	0.5 m		%4m		8m		12m		16m	
			hours	mm	mm/h			hours		mm		mm	%	mm	%	mm	%	mm	%
1	13/10/2014 20:15	14/10/2014 6:06	9.9	20.11	3.07	8.84	4.35	6.54	4.93	16.09	80.01	11.83	58.85	8.75	43.49	5.94	29.53	0.61	3.01
2	14/10/2014 10:15	14/10/2014 17:30	7.3	2.23	1.79	4.51	2.53	0.89	21.37	0.79	35.23	0.47	21.04	0.30	13.42	0.31	14.08	0.01	0.60
3	27/10/2014 8:12	27/10/2014 12:36	4.5	17.97	7.81	69.46	25.01	2.15	1.83	6.51	36.22	11.01	61.27	7.38	41.06	5.15	28.64	0.61	3.37
4	1/11/2014 6:30	1/11/2014 10:18	3.9	8.32	3.47	9.28	4.96	2.55	4.64	0.64	7.64	3.38	40.68	1.84	22.06	1.36	16.39	0.16	1.94
5	15/11/2014 19:21	16/11/2014 7:33	12.3	31.11	3.26	8.94	4.26	10.20	3.90	29.07	93.46	23.11	74.29	10.99	35.33	7.40	23.79	0.69	2.20
6	24/11/2014 14:15	24/11/2014 22:00	7.8	16.91	4.63	70.05	21.98	2.20	2.76	10.84	64.11	9.65	57.08	5.39	31.89	4.27	25.22	0.46	2.70
7	5/12/2014 8:03	5/12/2014 11:09	3.2	9.14	4.57	26.16	12.57	1.70	2.94	6.69	73.23	6.43	70.36	3.61	39.56	2.98	32.60	0.15	1.62
8	5/12/2014 20:21	7/12/2014 17:30	45.2	48.76	1.86	7.61	2.96	18.43	8.93	37.78	77.48	30.26	62.07	15.28	31.34	13.05	26.77	1.06	2.18
9	18/12/2014 16:39	18/12/2014 20:12	3.7	4.74	2.11	4.90	3.04	1.77	7.62	2.12	44.64	1.15	24.25	0.71	15.02	0.46	9.60	0.03	0.57
10	8/01/2015 17:30	8/01/2015 18:57	1.5	2.30	9.21	24.44	17.19	0.35	3.78	1.79	77.61	0.98	42.40	0.51	21.97	0.43	18.67	0.03	1.17
11	9/01/2015 15:15	10/01/2015 10:12	19.0	16.44	2.15	20.38	5.54	4.78	8.40	11.49	69.87	9.70	59.00	5.00	30.42	4.31	26.20	0.24	1.47
12	13/01/2015 14:36	13/01/2015 19:48	5.3	4.08	2.15	11.10	4.85	1.26	9.49	2.07	50.74	1.46	35.79	0.58	14.22	0.40	9.83	0.01	0.33
13	13/01/2015 22:27	14/01/2015 7:24	9.0	4.07	2.14	6.43	3.65	1.42	14.63	2.95	72.37	2.44	59.83	0.92	22.53	0.86	21.10	0.05	1.32
14	20/01/2015 23:36	21/01/2015 5:00	5.5	10.38	3.58	8.99	4.89	3.20	5.16	5.77	55.57	4.43	42.63	2.40	23.09	1.83	17.60	0.07	0.65
15	21/01/2015 15:33	21/01/2015 17:36	2.1	5.66	5.96	19.89	12.59	1.05	3.09	2.81	49.64	2.06	36.38	0.96	16.88	0.95	16.77	0.01	0.24
16	29/01/2015 5:09	30/01/2015 8:09	27.1	15.29	2.05	12.74	3.80	5.25	12.60	9.23	60.40	7.19	47.00	4.06	26.58	3.51	22.95	0.20	1.32
17	13/02/2015 21:27	14/02/2015 17:27	20.1	21.56	2.58	31.96	7.89	5.24	6.39	12.52	58.08	11.60	53.80	7.40	34.31	5.37	24.89	0.44	2.06
18	23/02/2015 13:33	23/02/2015 17:18	3.8	4.82	2.29	4.77	3.27	1.76	7.77	2.12	43.90	1.28	26.57	0.71	14.77	0.58	12.07	0.05	1.12
19	28/02/2015 22:30	1/03/2015 5:24	7.0	8.83	3.33	9.10	4.74	2.76	7.01	5.94	67.22	4.33	49.06	2.47	28.00	2.02	22.92	0.11	1.22
20	7/04/2015 5:27	8/04/2015 2:03	20.7	39.36	3.29	12.32	5.13	11.88	5.08	32.23	81.89	26.19	66.55	19.57	49.72	16.12	40.95	1.87	4.75
21	25/04/2015 6:21	26/04/2015 9:54	27.6	8.64	1.56	9.86	3.20	3.18	19.02	6.50	75.17	4.09	47.38	1.91	22.11	1.91	22.16	0.08	0.93
22	5/05/2015 8:21	5/05/2015 16:21	8.1	5.12	2.28	9.05	3.97	1.73	11.58	4.03	78.70	2.59	50.51	1.14	22.30	1.14	22.35	0.05	1.05
23	10/05/2015 4:30	10/05/2015 15:03	10.6	15.66	2.41	9.23	3.90	5.33	6.59	13.47	86.04	10.96	70.01	6.42	41.03	6.07	38.74	0.66	4.21
24	13/05/2015 1:30	14/05/2015 11:48	34.4	12.70	1.54	34.51	6.52	3.41	12.53	8.39	66.02	8.40	66.11	2.92	23.00	2.86	22.54	0.15	1.16
25	21/05/2015 13:12	22/05/2015 8:39	19.5	21.65	1.93	5.55	2.87	8.27	8.79	15.83	73.11	13.61	62.85	7.96	36.76	6.03	27.86	0.32	1.49
26	17/06/2015 17:45	19/06/2015 7:27	37.8	36.64	1.74	6.21	2.57	14.52	10.01	22.28	60.80	2.11	5.76	12.79	34.91	11.44	31.22	1.24	3.38
27	2/07/2015 3:51	2/07/2015 18:51	15.1	7.42	1.77	7.49	2.84	2.85	15.40	5.24	70.60	5.60	75.42	1.85	24.97	1.58	21.34	0.47	6.34
28	11/07/2015 0:12	11/07/2015 11:27	11.3	4.89	1.78	4.27	2.81	1.88	16.73	4.38	89.64	4.25	86.89	1.24	25.27	1.73	35.44	0.40	8.25
29	11/07/2015 14:42	11/07/2015 19:12	4.6	2.41	2.68	8.40	4.67	0.76	12.05	1.82	75.44	1.96	81.25	0.73	30.28	0.74	30.79	0.16	6.69
30	12/07/2015 15:21	13/07/2015 12:00	20.7	12.72	1.96	5.19	2.80	4.90	13.49	8.72	68.54	8.51	66.91	5.71	44.91	4.72	37.11	1.80	14.17
31	13/07/2015 17:36	15/07/2015 8:03	14.5	7.40	1.50	4.63	2.28	3.04	16.37	5.73	77.41	4.02	54.26	2.57	34.65	2.53	34.11	1.06	14.35
32	15/07/2015 21:30	16/07/2015 23:21	25.9	12.31	1.77	6.15	2.75	4.77	15.93	8.99	73.04	10.75	87.36	3.37	27.39	3.19	25.89	1.26	10.27
33	17/07/2015 23:12	18/07/2015 9:45	10.6	2.22	1.31	3.52	2.10	0.94	28.68	2.06	92.43	1.85	83.07	0.45	20.21	0.46	20.75	0.13	6.05
34	22/07/2015 5:45	22/07/2015 10:24	4.7	3.89	2.43	5.46	3.96	1.31	9.89	2.63	67.69	1.35	34.72	0.64	16.38	0.69	17.82	0.44	11.41
35	24/07/2015 17:12	24/07/2015 20:54	3.8	2.03	2.71	5.33	3.91	0.69	12.85	0.90	44.05	0.49	24.03	0.11	5.52	0.12	6.03	0.11	5.29
36	24/07/2015 21:39	25/07/2015 1:27	3.9	1.41	2.56	10.41	5.67	0.41	13.52	1.09	77.45	0.87	61.98	0.41	29.22	0.31	22.09	0.17	12.40

37	25/07/2015 2:39	25/07/2015 8:39	6.1	4.86	2.56	5.33	3.45	1.74	10.58	3.91	80.50	3.32	68.30	1.74	35.81	1.54	31.62	0.91	18.81
38	26/07/2015 1:45	26/07/2015 11:30	9.8	3.06	1.80	4.33	3.06	1.14	19.45	1.98	64.57	1.85	60.39	0.56	18.36	0.37	12.22	0.17	5.71
39	1/08/2015 6:57	1/08/2015 13:45	6.9	5.09	1.72	4.35	2.84	1.95	11.89	3.29	64.60	2.00	39.31	0.96	18.77	1.06	20.77	0.73	14.27
40	3/08/2015 3:09	3/08/2015 18:15	15.2	5.60	1.58	3.95	2.33	2.29	19.78	4.34	77.45	2.68	47.90	1.37	24.40	1.39	24.73	0.77	13.68
41	5/08/2015 3:00	6/08/2015 12:21	33.4	9.69	1.33	4.11	2.22	4.01	23.24	5.63	58.06	4.08	42.12	1.80	18.54	2.18	22.49	1.17	12.07

- *Ř is Depth-weighted rainfall intensity from Van Dijk (2002)*
- *D_T rainfall pulses duration from Van Dijk (2002)*

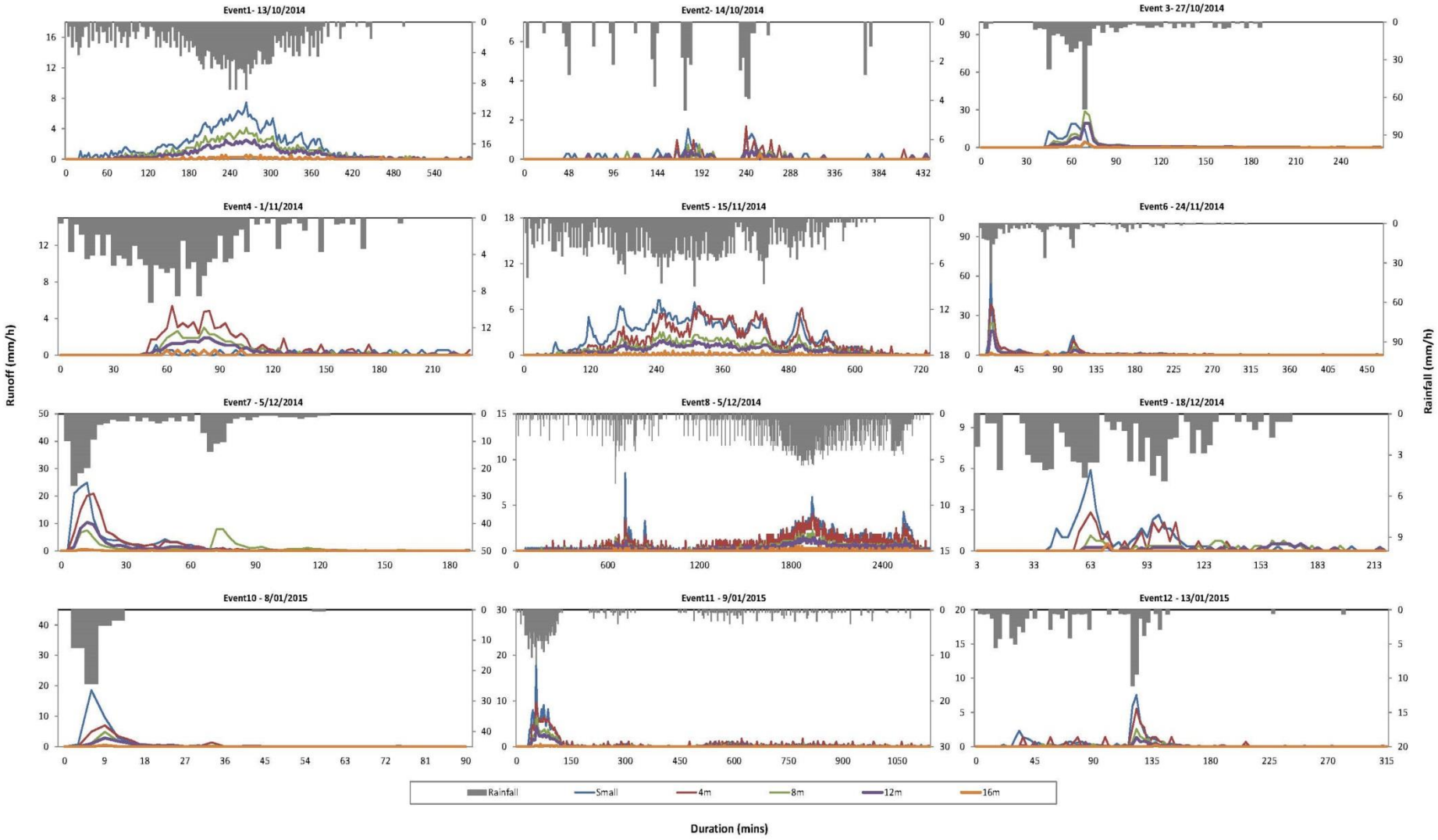

Figure 3.12 Rainfall events and generated runoffs in plots with different length, left vertical axis is the runoff rate, right vertical axis is the rainfall rate and the horizontal axis is the duration of the rainfall-runoff event (min)

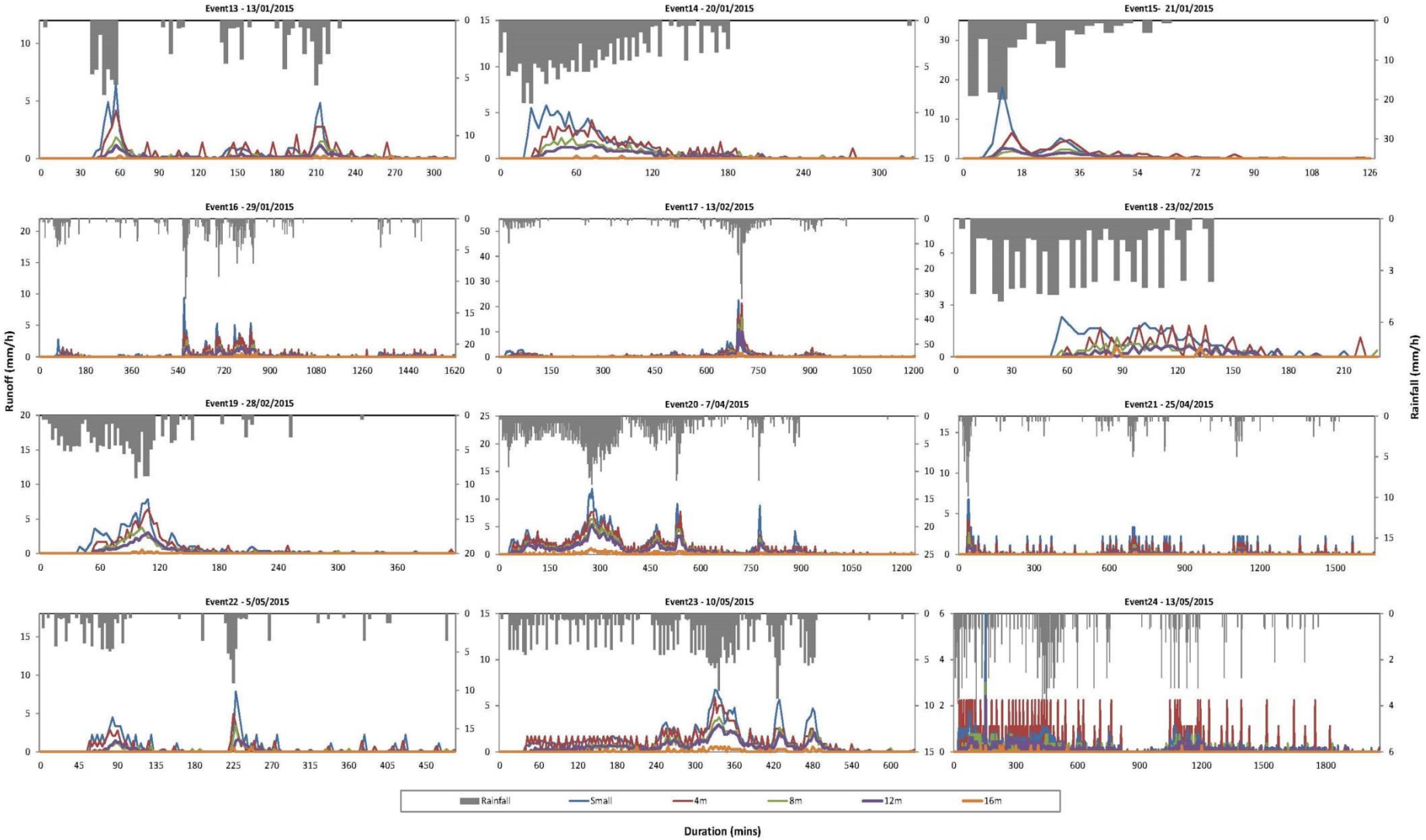

Figure 3.12 Rainfall events and generated runoffs in plots with different length, left vertical axis is the runoff rate, right vertical axis is the rainfall rate and the horizontal axis is the duration of the rainfall-runoff event (min)

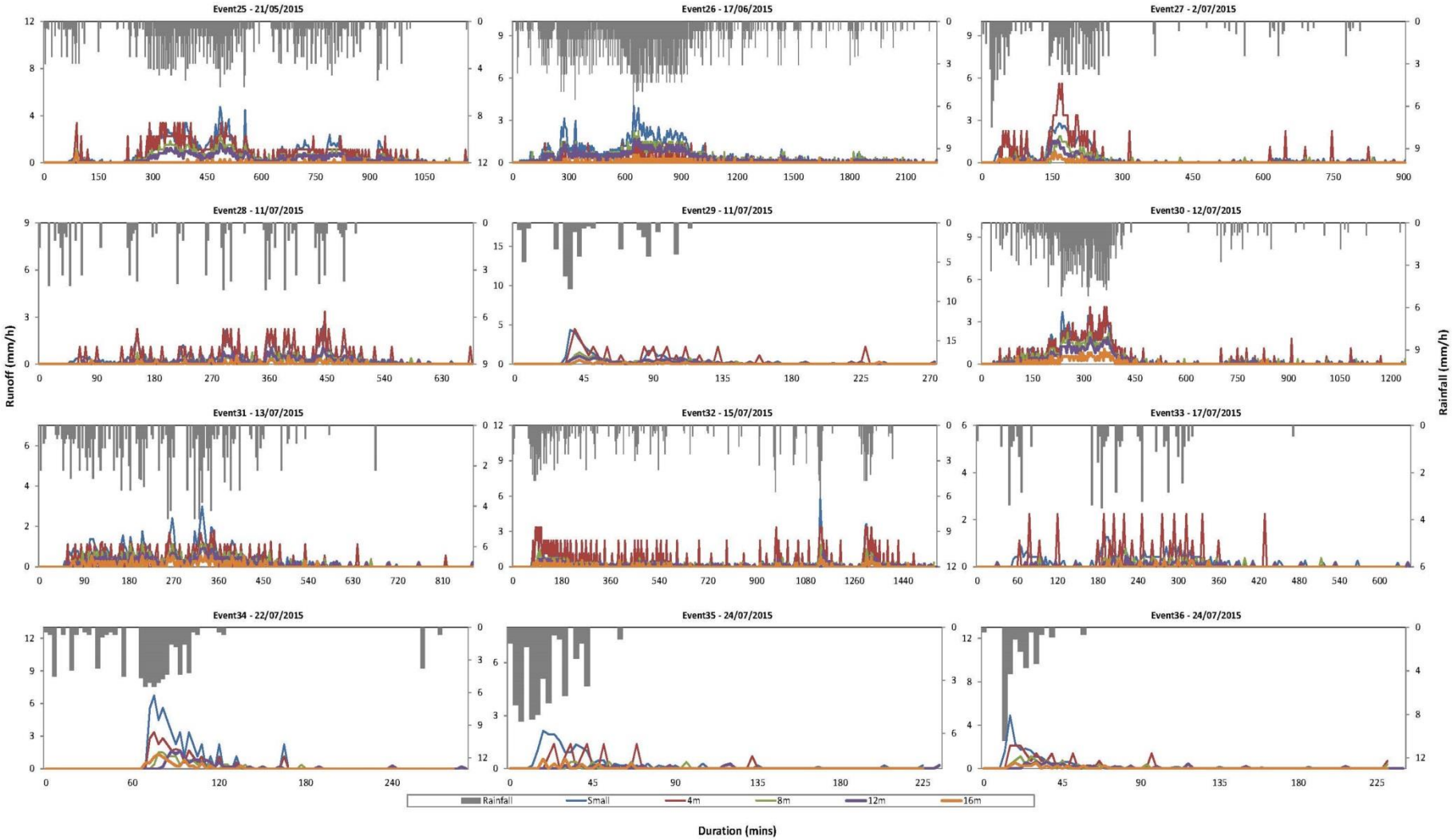

Figure 3.12 Rainfall events and generated runoffs in plots with different length, left vertical axis is the runoff rate, right vertical axis is the rainfall rate and the horizontal axis is the duration of the rainfall-runoff event (min)

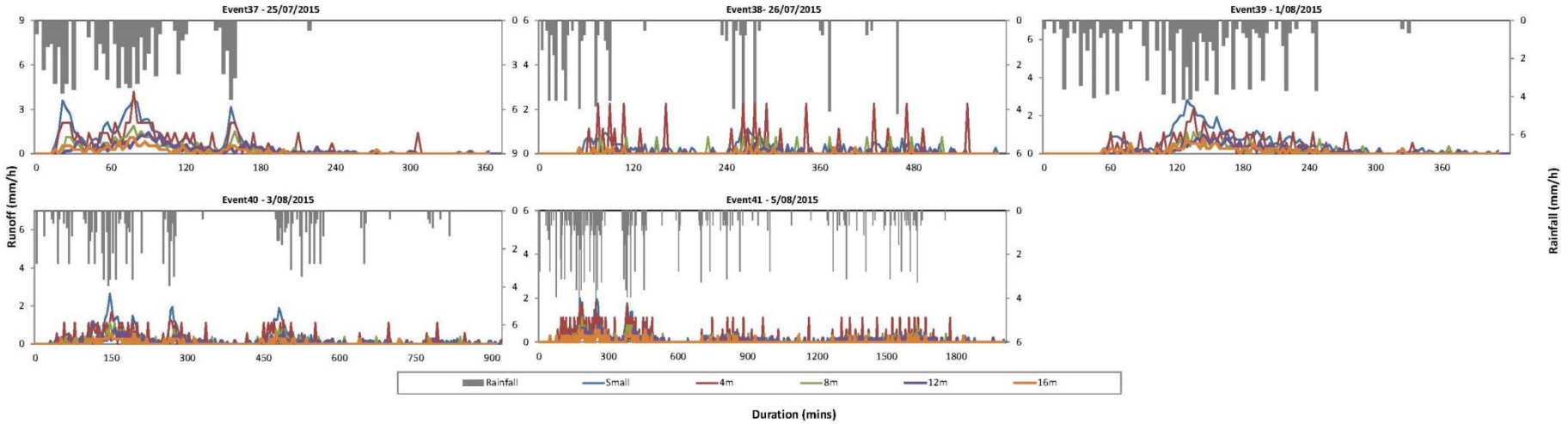

Figure 3.12 Rainfall events and generated runoffs in plots with different length, left vertical axis is the runoff rate, right vertical axis is the rainfall rate and the horizontal axis is the duration of the rainfall-runoff event (min)

Mean and maximum rainfall intensities for durations from 3 (I_{3mins}) to 60 (I_{60mins}) minutes were calculated for individual storms (Appendices 3.2 and 3.3). Statistical summaries of mean and maximum intensities (I_{3mins} to I_{60mins}) for all runoff-generating storms are shown in Figure 3.13. There are slight differences in mean and median values for I_{3mins} that almost disappear for I_{60mins} (Figure 3.13a, b).

Depth-weighted rainfall intensity ($\check{R}$) was calculated following (van Dijk, 2002) to obtain rainfall intensity unaffected by dry spells. The value of $\check{R}$ is higher than mean rainfall intensity calculated both with and without non-rain periods (Figure 3.14).

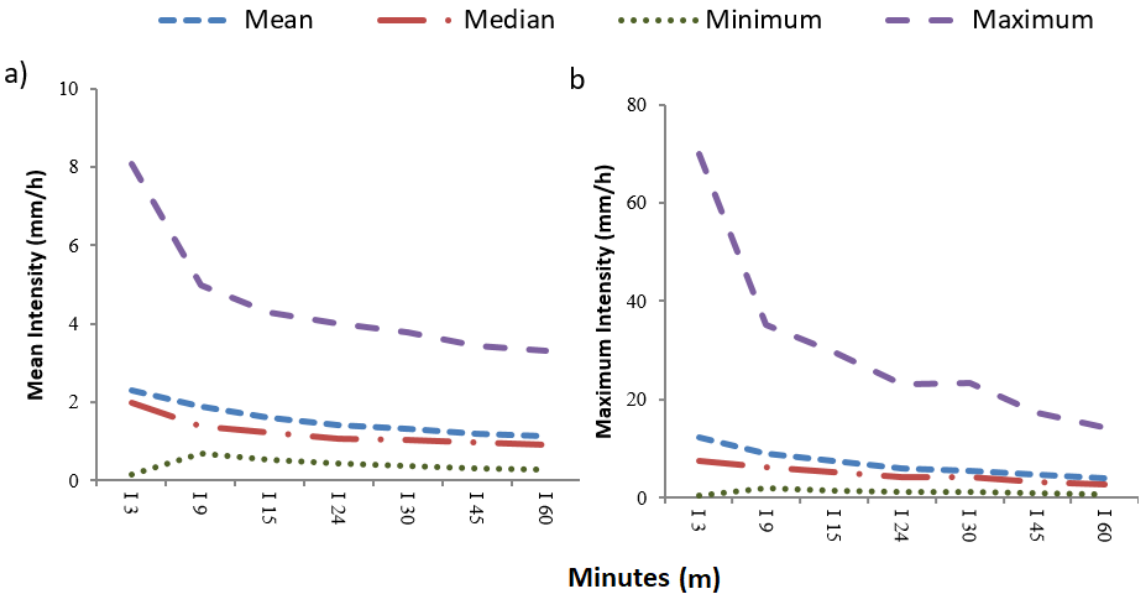

Figure 3.13 Statistical indicators of (a) mean intensities, and (b) maximum intensities of all runoff-generating storms from I3mins to I60mins

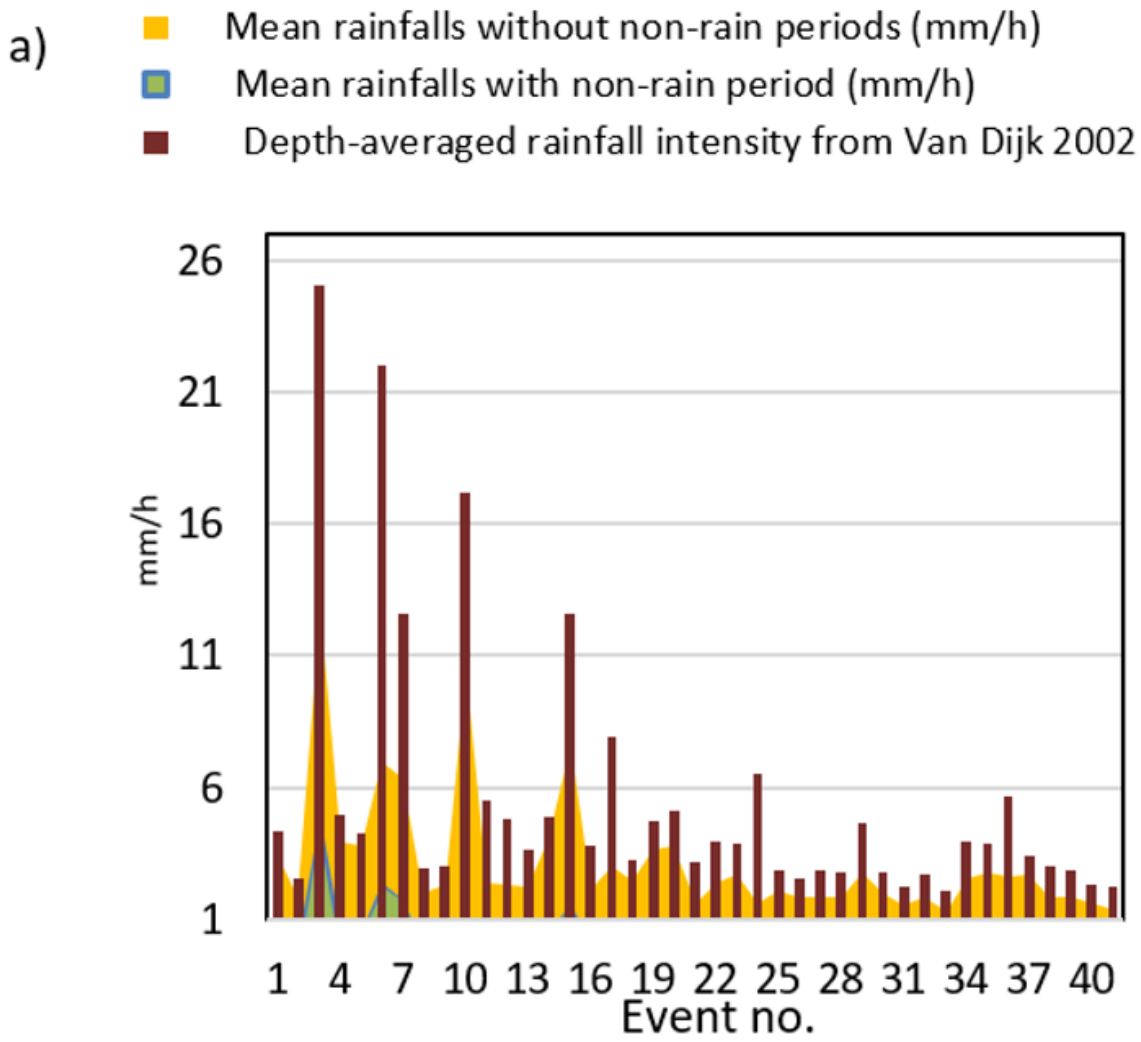

Figure 3.14 Mean rainfalls calculated with and without non-rain periods in comparison to depth-weighted rainfall intensity calculated form Van Dijk A.I.J.M (2002).

The cumulative rainfall and generated runoff for different plot lengths was calculated for the whole study period (Figure 3.15a). The mean runoff coefficient for the whole study period was relatively high (52.6%) in the shortest plots (0.5 m), decreasing to 3.2 % in the largest plot (16 m) as shown in Figure 3.16b. These results show a very clear scaling effect involving a decrease in runoff ratio with slope length (Figure 3.15b).

Runoff volume per unit plot width (*L/m*) was calculated for runoff plots with different lengths. As presented in Figure 3.15c, the collected runoff volume (*L*) increases with plot length, except for both 16m plots. Given the unexpected decline in runoff volume for the 16m plots, the accuracy of collected data from these plots was checked by calibrating the tipping buckets on each replicate plot, and by cross-checking with manual counters. In addition, these plots were investigated for possible leakage at the boundaries, troughs and the outlet pipe. No measurement error was detected associated with recorded runoff at the 16m plots and runoff behaviour was consistent between the two replicate plots.

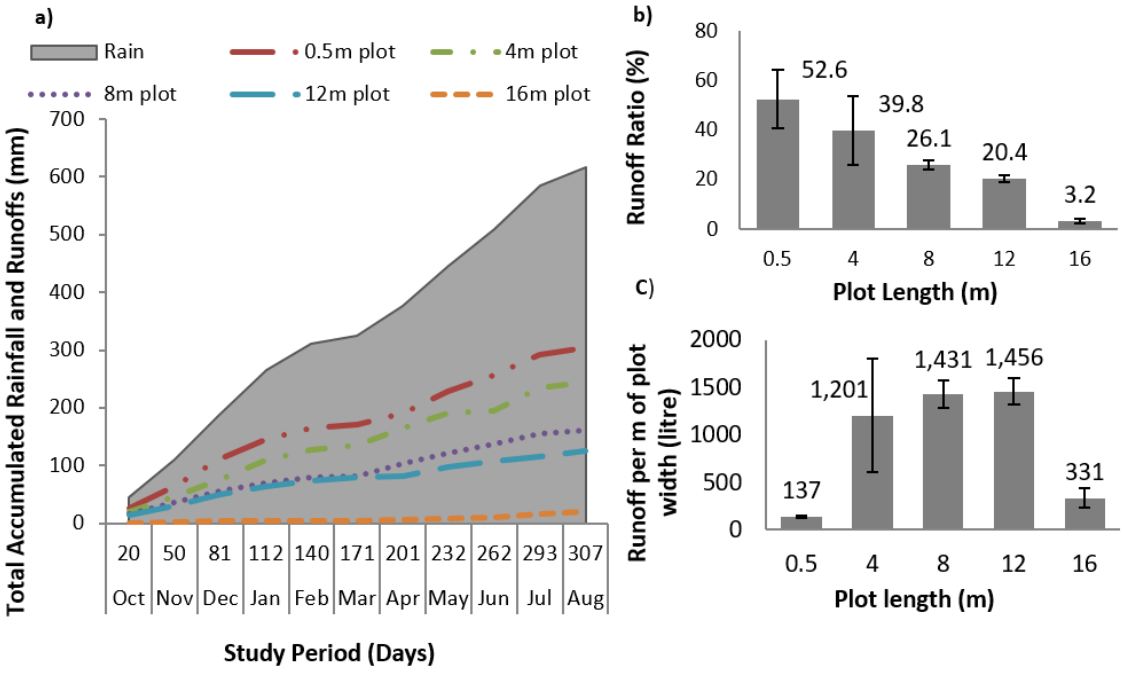

Figure 3.15 (a) Total accumulated rainfall and runoff averaged across measurement replicates, (b) corresponding runoff ratios, and (c) runoff per unit plot width (L/m) from plots with different length for the whole study period

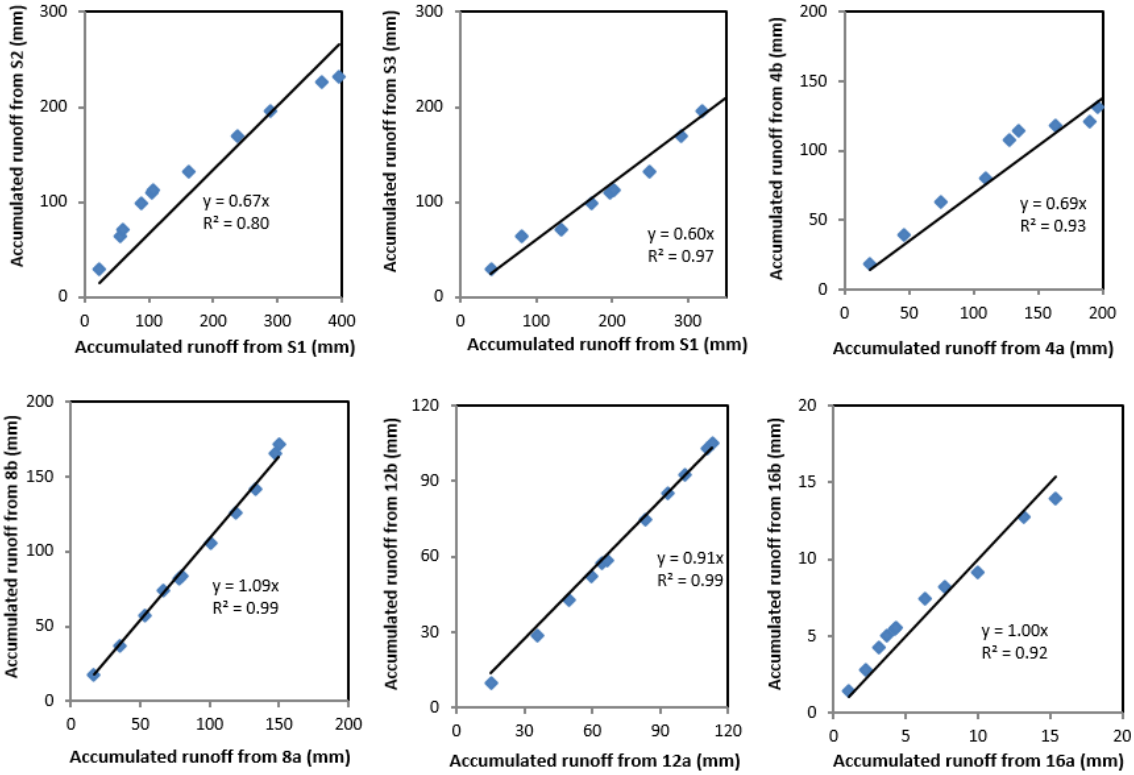

Figure 3.16 Accumulated runoff from 0.5 to 16 m plots against their replicates

Accumulated runoff depths from replicates were compared with double mass plots to investigate deviations in data collected from each plot length. Regression equations were made from one replicate at the other when both replicates were working. These regression analyses were used for identifying malfunctioning equipment and adjusting out of range data that were reported on field visits.

Figure 3.16 shows consistency in collected data from replicates of 8, 12 and 16 m plot lengths. For 0.5 and 4 m plots, some clogging and faults in the tipping bucket occurred during data collection causing skewness.

3.3.3 Runoff Scale Dependence

Total runoff depth (mm) and runoff ratio (%) were plotted against the associated plot length (m) for events, seasonally and for the whole study period. The slope of the regression lines characterises the magnitude of changes in runoff depth and runoff ratio with plot length, standing for SC_1 and SC_2 respectively.

Linear, natural logarithm (ln), exponential and power law models were trialled for regression analysis of all events within the same numerical space (natural) where runoff depth and ratio

plotted against plot lengths. To find the best regression model, average coefficient of determination (R^2) derived from these regression models were compared with one another.

Runoff production estimated by these regression models should be a positive real number in order to conform to the assumption of having runoff in infinite plot length during infinite rainfall. For this reason, the linear form of relationship between plot length and runoff depth was excluded despite of having the highest correlation coefficient (R^2) in this study.

Regression lines derived from the power law models resulted in the lowest coefficient of determination (R^2) among these four regression models. Regression lines from the natural logarithm and exponential models had the second highest R^2 and were almost identical on average (Figure 3.17). The natural logarithm model was chosen over the exponential model for obeying usual laws of logarithm and rule of symmetry.

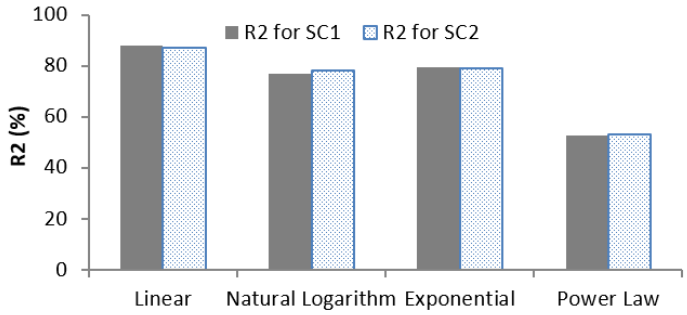

Figure 3.17 Average coefficient of determination for regression relationships of the four regression model forms

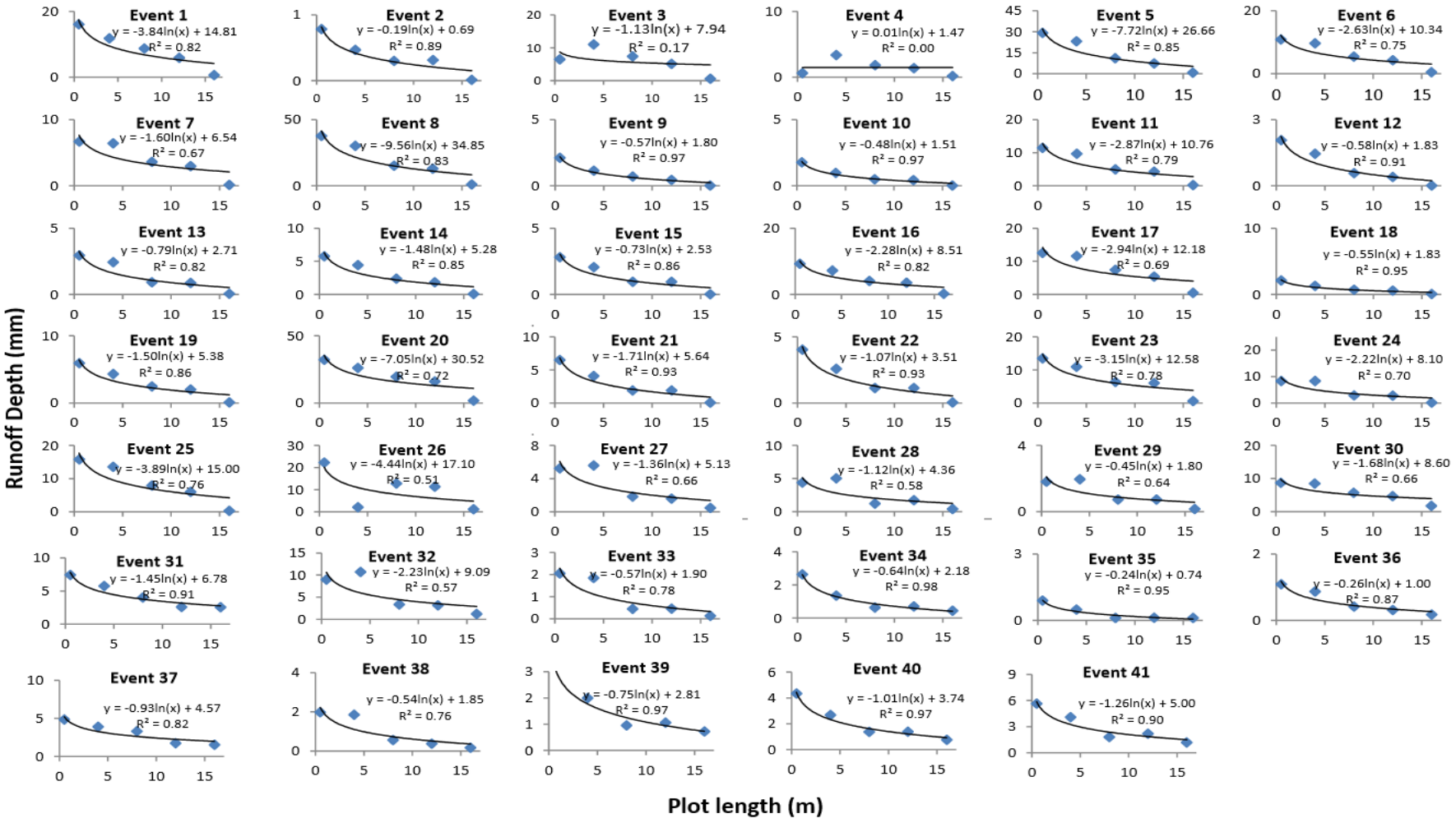

Figure 3.18 Scatter plots of runoff depths (mm) vs. plot lengths (m) showing fitted models for all 41 events representing runoff depth scaling coefficient (SC1)

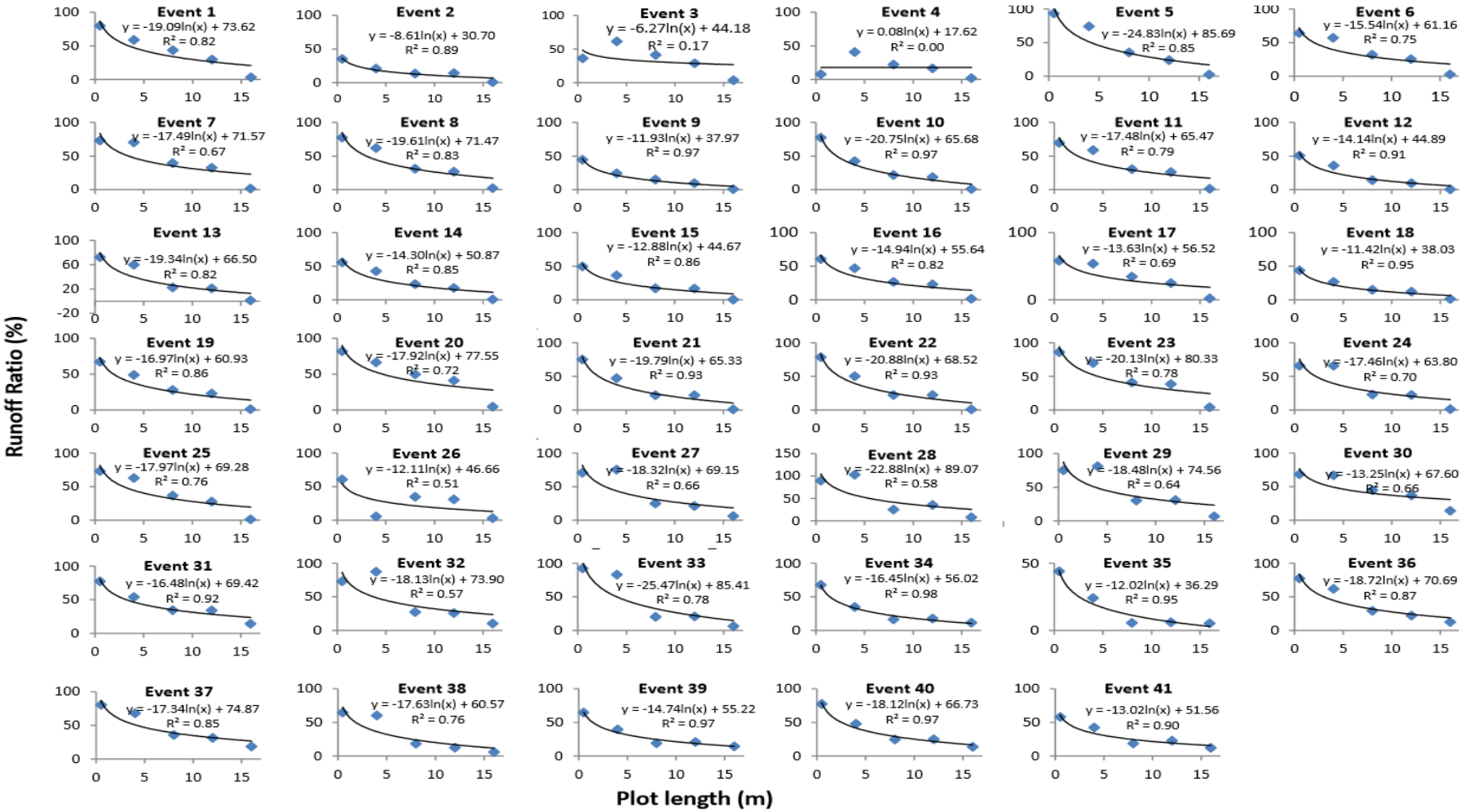

Figure 3.19 Scatter plots of runoff ratio (%) versus plot lengths (m) showing fitted models for all 41 events representing runoff ratio scaling coefficient (SC2)

The regression equations in Figure 3.18 represent runoff depth as a function of plot length where SC_1 stands for the coefficient of these functions. Same relations exist in Figure 3.19 representing runoff ratio as a function of plot length and SC_2 is the coefficient of these functions. Regression lines representing SC_1 and SC_2 have similar correlations coefficients and their correlation equations could be exhibited as multiplications of one another.

Eq 3.11 $$Rd = SC_1 \ln(x) + \propto$$

Eq 3.12 $$RR = SC_2 \ln(x) + \propto$$

Rd is runoff depth, *RR* is runoff ratio, x is plot length, and $\propto$ is the intercept of the regression line representing the rate of runoff from one-meter plot length; ln(x) = 0 when x = 1.

As shown in Figure 3.18 and 3.19, there are negative natural log (ln) relations for both runoff depth and runoff ratio with plot length, with high R^2 for the majority of the events (>70%), with the exception of events 3 and 4. Clogging in tipping buckets was reported for the 0.5m plots on the field visit conducted after these two events.

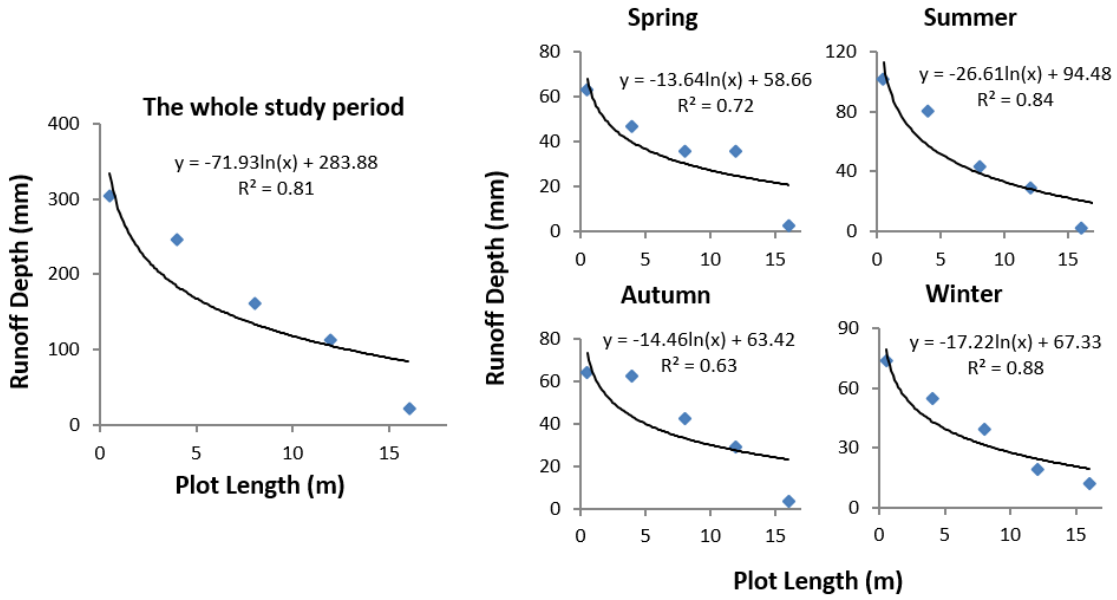

Figure 3.20 Runoff depth scaling coefficient (SC1) for seasons and the whole study period

Logarithmic relationships for runoff depth and plot length were also fitted for each season and the whole study period (Figure 3.20), resulting in estimates of SC_1 for these temporal scales. SC_1 is not suitable for comparing runoff scaling effects at different temporal scales because the value of this indicator for larger scales is summation of SC_1 for events occurred in that time span.

Runoff ratio scaling coefficient (SC_2) was also calculated for seasons and the whole study period (308 days) by correlating runoff ratio and plot length (Figure 3.21). The calculated runoff ratio and plots length are negatively correlated with a strong correlation coefficient. SC_2 for larger time scales is close to average value of SC_2 calculated from 41 events during the period. SC_2 (-10.5) for the whole study period is close to median value of season-based scaling coefficients (SC_2=-11.63) and smaller than median value of event-based scaling coefficients (SC_2 =-16.46).

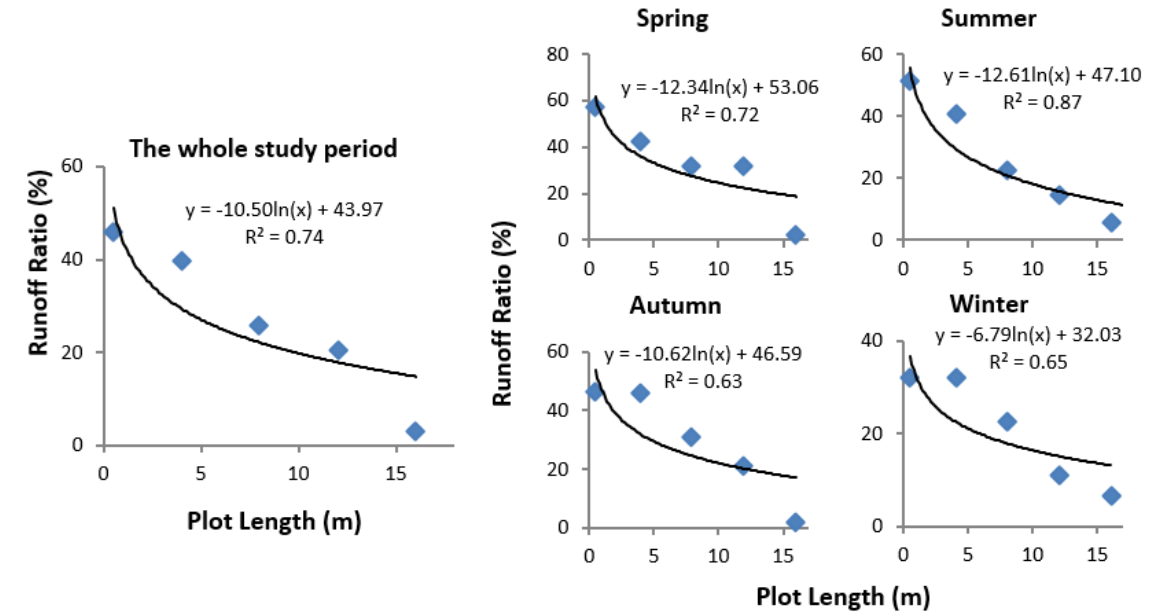

Figure 3.21 Runoff ratio scaling coefficient (SC2) for seasons and the whole study period

3.4 Discussion

The results from both cumulative and event-based rainfall-runoff analysis show a distinctive scaling effect characterised by decreasing runoff delivery with increasing plot length. Similar negative relationships have been reported in previous studies (Lal, 1983, Liu et al., 2000, Sheridan et al., 2007, Sheridan et al., 2014, Van de Giesen et al., 2000).

Total runoff volume (L) increases with length for 0.5 to 12 m plots and then decreases for 16m plots. The quality of the data was investigated carefully, and no measurements error was detected to be associated with recorded runoffs at 16 m plots causing the sudden decline. In addition, collected data from replicas of 16m plots were consistent (Figure 3.16). Less runoff volume (L) for the longest plot was also observed in (Sheridan et al., 2014) and (Lal, 1983) that measured overland flow scaling across different plot lengths.

To measure the impact of low runoff generation in 16 m plots on scaling coefficient estimates, both runoff depth scaling (SC_1) and runoff ratio scaling coefficients (SC_2) were re-calculated excluding runoff measurements from 16 m plots (Appendices 3.4 & 3.5) and then SC_1 and SC_2 with and without 16 m were correlated. As shown in Figure 3.22, by excluding runoff measurements from 16 m plots, SC_1 and SC_2 decrease by 25% and 17% respectively. While the low runoff generations in the 16 m plots impacts the value of the scaling coefficient, the impact is relatively small and does not change the overall pattern of runoff scaling effects in this study.

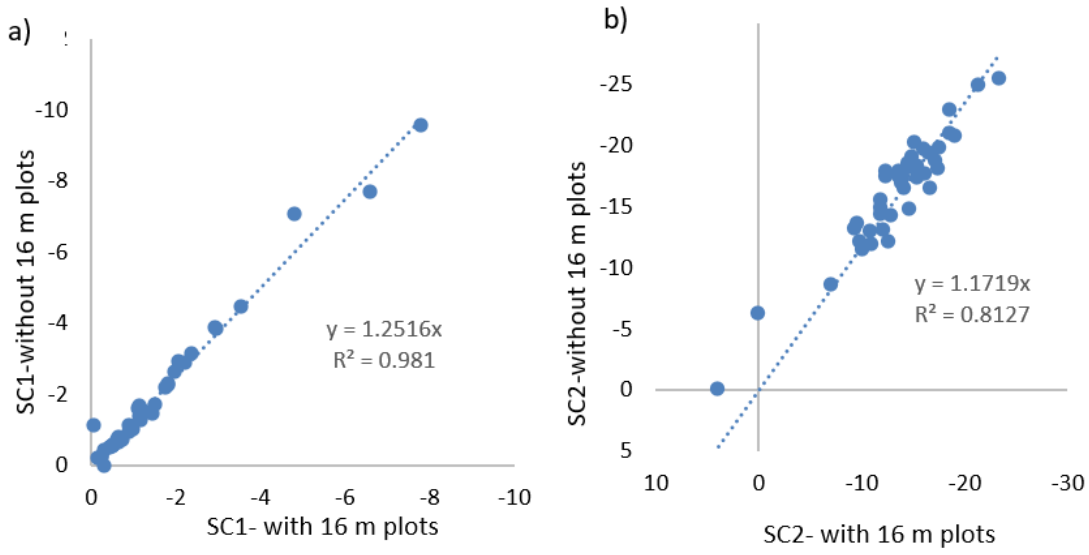

Figure 3.22 a) Correlation of Runoff depth scaling coefficients with and without 16 m plots, b) Correlation of Runoff ratio scaling coefficients with and without 16 m plots

Another important decision was defining the start and end of events. In doing this, non-rain periods and small pulses were included. To check the impact of these decisions on the estimates of scaling effects, a new set of events were made consisting of only main pulses of each events (Appendices 3.6 & 3.7). Both runoff depth scaling coefficient (SC_1) and runoff ratio coefficient (SC_2) were calculated for these main pulses (Appendices 3.8 & 3.9) and compared with the scaling coefficients obtained from the original events. As shown in Figure 3.23, the impact of non-rain periods on the scaling effects is small (less than 10 %), probably because the main rainfall pulses dominate the rainfall volume and runoff generation.

The impact of total annual rainfall, topographic gradient, soil and vegetation cover on runoff scaling were investigated by calculating scaling coefficients (SC_1 & SC_2) using data from relevant literature that has reported scaling studies on hillslopes with different soil type, surface coverage, slope, and annual rainfalls (Table 3.3). Annual runoff depth and runoff ratio were plotted against plot lengths for these studies where the slope of correlations represents SC_1 and SC_2 in Figures 3.24 and Figure 3.25 respectively. The impacts of total annual rainfall, topographic gradient, soil type and vegetation cover on runoff scaling were investigated with these scaling coefficients.

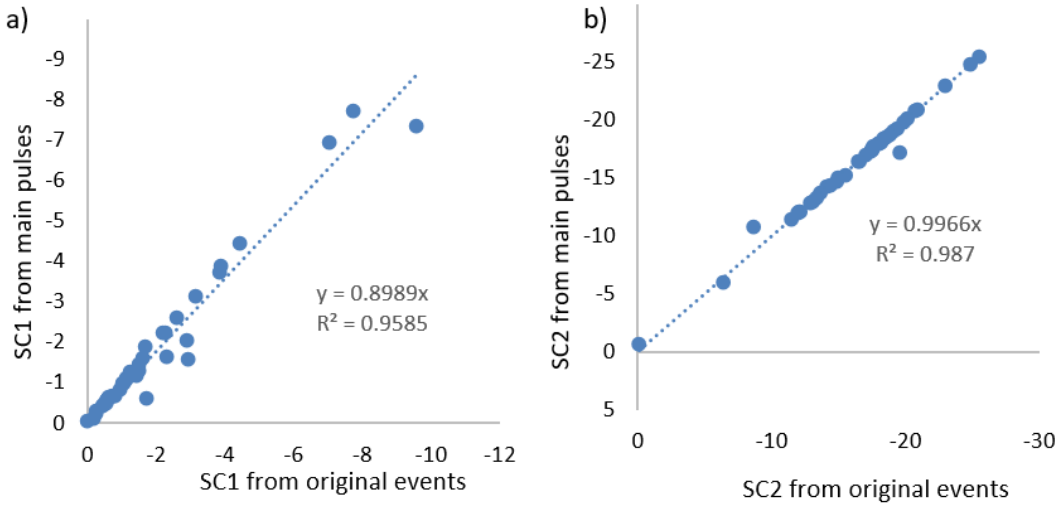

Figure 3.23 Correlation of runoff scaling coefficients of the original events vs. their main pulses a) SC_1, b) SC_2

Table 3.3 Scaling coefficient (SC1 & SC2) calculated for literature previously studied overland flow scale dependency.

Authors	Location	Land condition, treatment and vegetation coverage	Plot length	Slope (degree)	Soil type	K_{sat} (mm/h)	Annual rain (mm)	$\|SC_1\|$	$\|SC_2\|$
This study	Southeast Australia	Burned eucalyptus forest	0.5,4,8,12,16	27	Loam	8.2-47**	616*	78.95	12.82
(Bagarello et al., 2010)	Sicily, Southern Italy	Cultivated	11, 22,33, 44	8.5	Clay	1-3**	700	98.31	8.96
(Gomi et al., 2008a)	South central, Japan	Cypress Forest, sparse understory (~10 veg%)	1.5, 25	41-43	Brown forest soil	500-5000	2500	126.5	5.01
		Hinoki Plantations, Fern and evergreen (<100 veg%)						135	5.41
		Deciduous Forest (~100 veg%)						99.2	3.97
(Lal, 1983)	Western Nigeria, Africa	Cultivated	5,10,15,20	0.6	Sandy loam	22-108**	1st year 792	24.3	3.07
				2.9				72.79	9.18
				5.7				65.67	8.28
				8.5				73.03	9.21
			5,10,15,20	0.6	Sandy loam		2nd year 1215	55.22	4.54
				2.9				295.5	24.32
				5.7				259.8	21.38
				8.5				172.7	14.21
(Van de Giesen et al., 2000)	Ivory Coast, Africa	Bare soil and then rice	1.25, 12	0.8	Loamy sand	50-136**	1075	83.12	7.73
		Weedy fallow and rice						112.2	10.4
(Sheridan et al., 2014)	SE Australia	Burned forest (disturbed)	0.5, 1, 2, 4	20	Silty loams	12-64**	1st year 403	12.72	3.16
							2nd year 809	36.97	4.57
(Sharma et al., 1986)	Jodhpur, India	Compacted fallow	5,7,8.5,11,14.5	0.5, 5 & 10	Sandy loam	22-108**	1200	159.6	13.3
(Xu et al., 2009)	Tibet, China	Roadside slope (disturbed)	1,2,3,4	30	Sand & gravel	93-155**	272	73.56	27.05
(Moreno-de las Heras et al., 2010)	Central Eastern Spain	1.1±2 (veg%)	1, 2, 3, 15	20	Clay loam	4-8**	615	16.91	2.75
		8.2±5.5 (veg%)						10.61	1.72
		27.8±9.9 (veg%)						15.17	2.46
		44.3±16.2 (veg%)						52.22	3.42
		59.4±20.8 (veg%)						32.41	5.27

*10 months throughfall collection at the study site

** Soil hydraulic conductivity calculated from (Rawls et al., 1982)

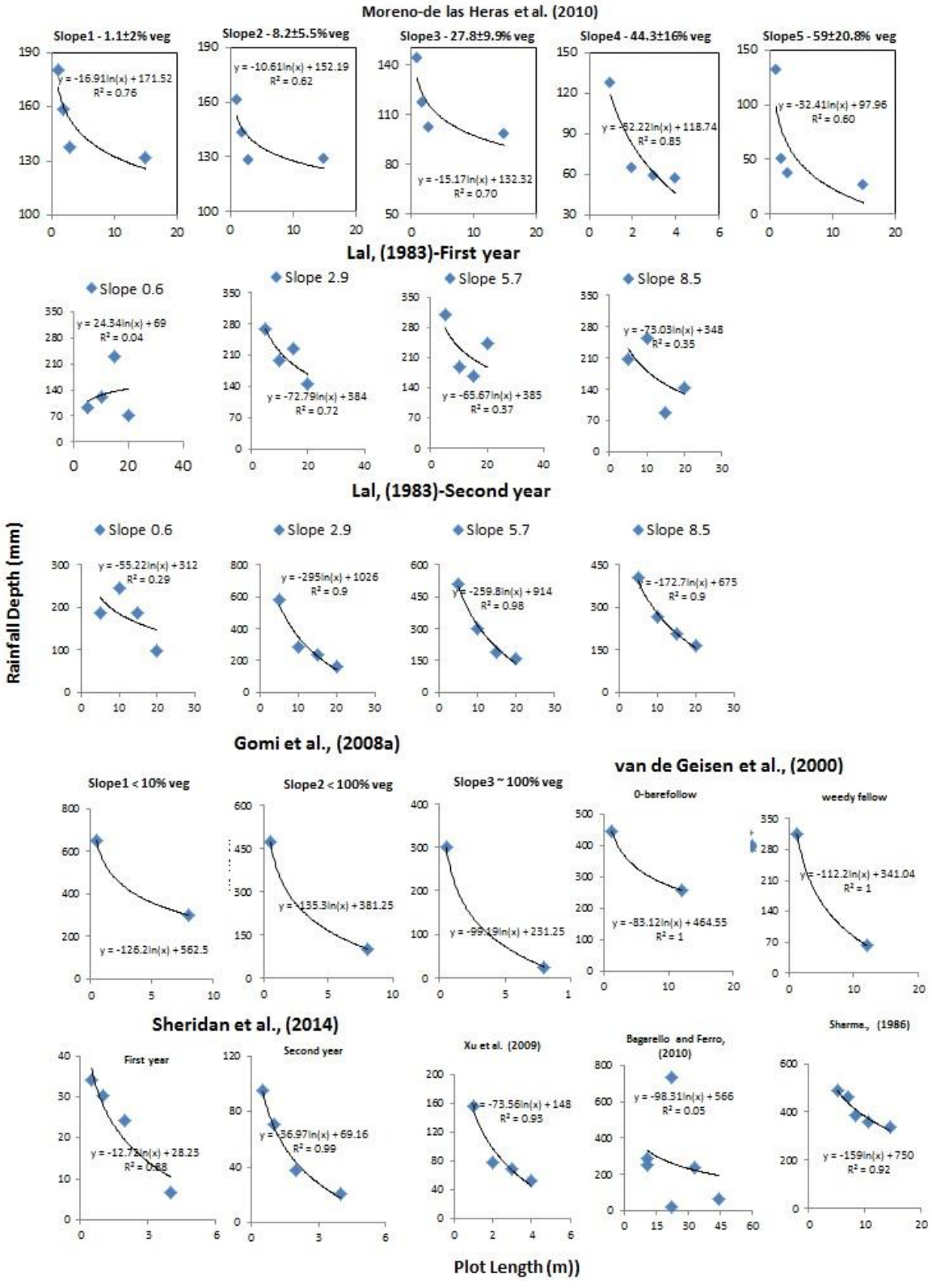

Figure 3.24 Scatter plots of runoff depth against plot lengths representing scaling coefficient (SC1) for literature in Table 3.3

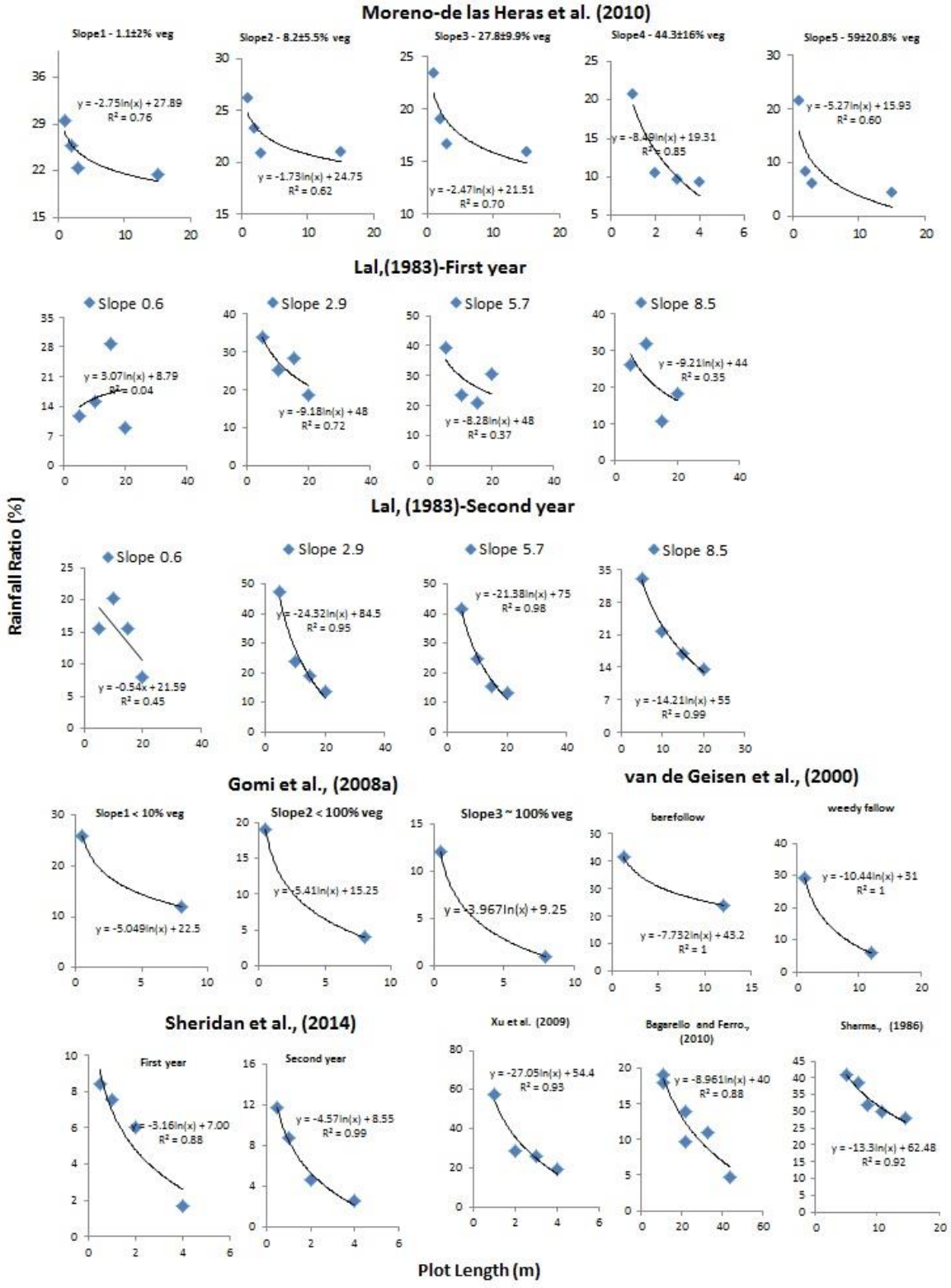

Figure 3.25 Scatter plots of runoff ratio against plot lengths representing scaling coefficient (SC_2) for literature in Table 3.3

(Sheridan et al., 2014) studied post-fire scaling effects by measuring runoff from three replicates of 0.5, 1, 2 and 4 m plots during the first and second year following a moderate burn (2005-2006) in eucalyptus forest, southeast Australia. The result from (Sheridan et al., 2014) showed considerable scaling effects for generated overland flow in the first and second year of data collection (Figure 3.26 a, b, c). There is a significant increase in SC_1 (three times greater) for the second year with twice precipitation while SC_2 increases for 50% (Table 3.3).

(Lal, 1983) measured overland flow scaling across plots with different gradients for two consecutive years. Both scaling coefficients changed with gradient, but the change does not follow any particular pattern (Table 3.3). SC_1 and SC_2 are both two times greater in the second year with 50% more annual precipitation. (Moreno-de las Heras et al., 2010) and (Gomi et al., 2008a) showed that surface coverage is an important factor in controlling generated runoff and scaling effects. In both studies, runoff plots were installed on hillslopes with similar precipitation, slopes and soil type, but different vegetation coverage. Higher vegetation cover resulted in lower runoff generation and also impacted scaling coefficients.

(Gomi et al., 2008a) study has the highest annual rainfall among all the studies (Table 3.3). Given SC_1 and SC_2 are impacted by total runoff, it is expected that the high rainfall in (Gomi et al., 2008a) would lead to the highest SC_1 and SC_2 of all the studies, which is the case. SC_2 obtained from (Gomi et al., 2008a) is smaller than some plots in the second year of (Lal, 1983) and (Xu et al., 2009).

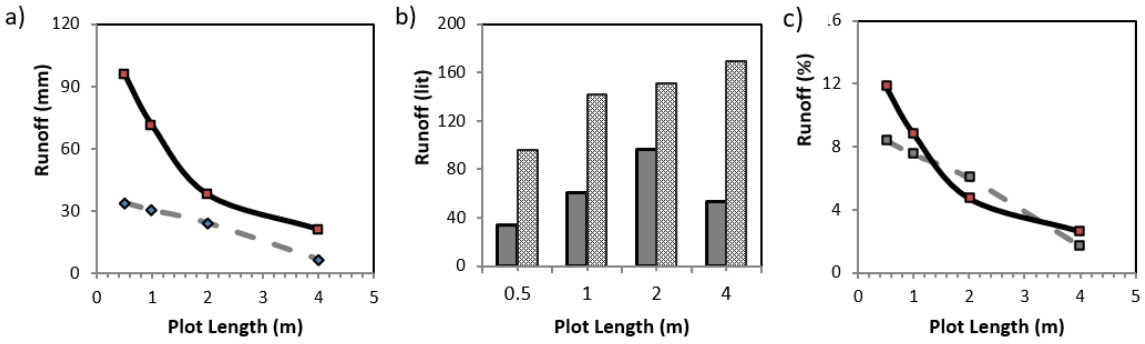

Figure 3.26 a) Total annual runoff (mm) plotted against plots length, b) collected runoffs (litre) presented in stack-bar graph, c) runoff ratio (%) plotted against plot lengths; the first-year data is shown in dashed line and the second year in continues line for left and right graphs. Stack bars are grey for the first-year data and patterned filled for the second year (Sheridan et al., 2014)

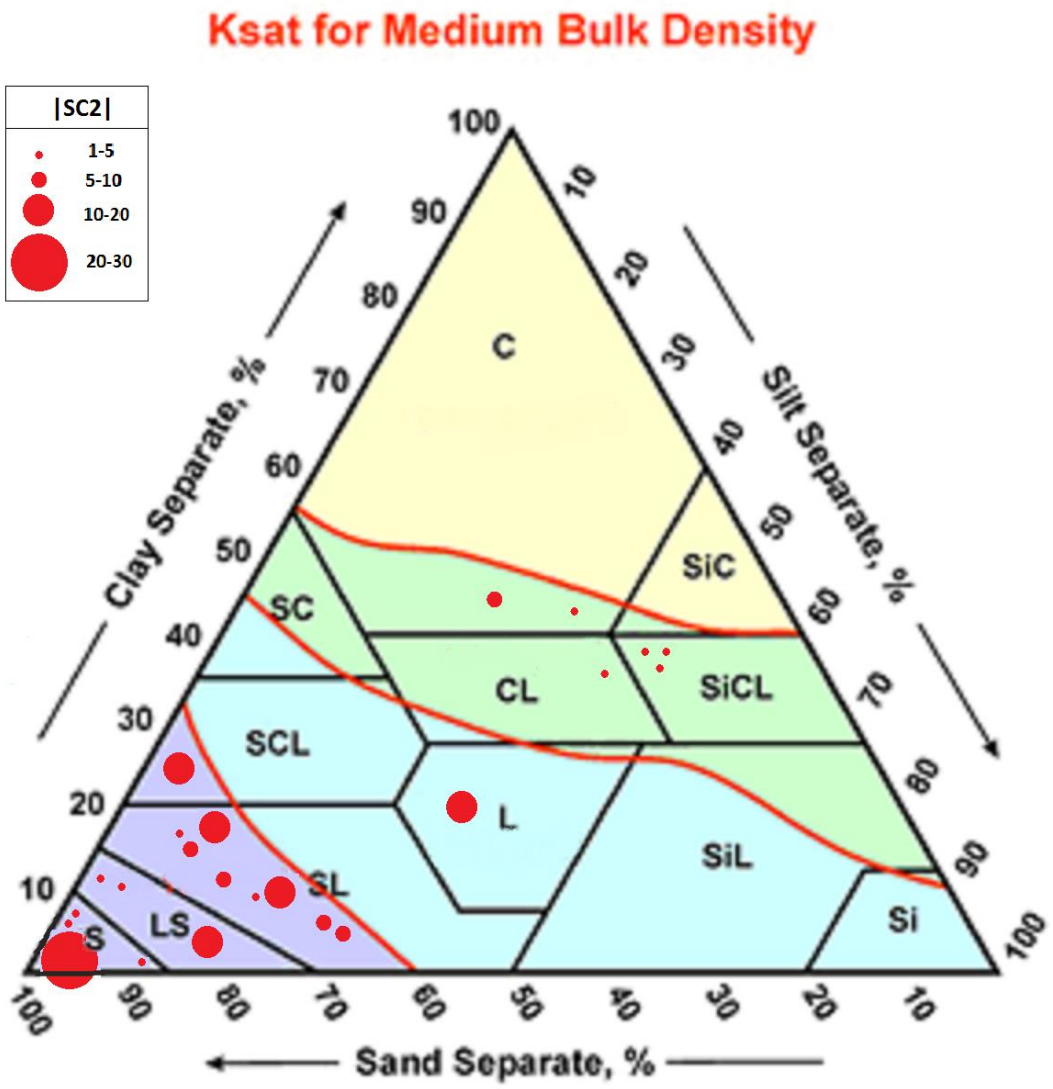

Figure 3.27 Runoff ratio scaling coefficients (SC2) and conductivity mapped in soil texture triangle from (NSSH Part 618-Subpart B, USDA) for literature presented in Table 3.3

To study the impact of soil texture and hydraulic conductivity on scaling effects, runoff ratio scaling coefficients (SC_2) for the literature were mapped onto the soil texture triangle graphs (NSSH Part 618-Subpart B, USDA). Figure 3.27 shows higher (SC_2) are mostly associated with coarse soil texture; however there are some studies with coarse soil type like (Gomi et al., 2008a) obtaining small SC_2. The highest runoff ratio scaling ($|SC_2| = 27.05$) belongs to (Xu et al., 2009) studying road-side plots with sandy gravel soil texture having the lowest precipitation among literature listed in Table 3.3.

The above examples show that rainfall total depth, gradient, soil texture, and vegetation coverage are important drivers controlling scaling effects in high extend. However, these

might not be only drivers controlling scaling effects and other factors like rainfall temporal variability, soil-surface spatial variability, and macropore flow might be influential in overland flow scaling. With a given hillslope length, spatial variability of soil hydraulic properties, vegetation, surface depressions, and patchiness are factors contributing to run-on process impacting scaling effects (Sheridan et al., 2014, Gomi et al., 2008a, Van de Giesen et al., 2000, Langhans et al., 2016). Rainfall temporal variability may also increase the probability of generated runoff allocate to run-on infiltration downslope when infiltration is higher than rainfall rate (Wainwright and Parsons, 2002).

3.5 Conclusion

Overland flow scaling effects were investigated using rainfall-runoff data from multi-length plots; 0.5, 4, 8, 12 and 16 m, installed on a severely burned hillslope in dry eucalyptus forest, southeast Australia. Data collection took place under natural rainfall conditions over ten consecutive months during 2014-2015, from which forty-one individual runoff-generating events were extracted.

The rate of overland flow per unit area decreased with plot length for all storm events, seasons and the whole study period showing a strong overland flow scaling effect at this study site. Collected runoff from replicated plots showed good agreement for all storm events, seasonally and the whole study period. No Rilling or flow concentration was observed downslope of the plots.

Two scaling coefficients were defined by relating runoff depths and runoff ratio with plot lengths. The coefficients of the fitted logarithmic regression lines were used as runoff depth scaling coefficient (SC_1) and runoff ratio scaling coefficient (SC_2). Negative natural logarithm relationships with high (R^2>90%) correlation coefficients were found for the majority of individual events, seasons and the whole study period. SC_2 for larger temporal scales can be predicted as the average of SC_2 from finer temporal scales while SC_1 for a larger temporal scale is the summation of SC_1 for smaller time scales within the period.

Total runoff volume per unit plot width (L/m) increased from 0.5 to 12 m plots and then declined significantly for the 16 m plots. Detailed checking revealed no breakages or measurement error associated with recorded runoffs at 16m plots and the two plots behaved consistently. Scaling coefficients were recalculated without the 16m plots, given this change in behaviour and SC_1 and SC_2 were increase by 25% and 18% respectively.

A sensitivity analysis showed that excluding non-rain periods, and small pulses early and late in the event led to only small changes in SC_1 and SC_2 of less than 10% and 2% respectively. This indicates that scaling coefficient indexes are not sensitive to the details of the event definition.

SC_1 and SC_2 were also calculated for previous literature that studied overland flow scaling in different geomorphic conditions (soil texture, surface coverage, and treatment), slope gradient, and annual precipitation. The results show that scaling is influenced by rainfall depth, soil hydraulic conductivity, surface vegetation, and slope gradient. The impact of

rainfall on runoff scaling was isolated by studies that measured scaling for two consecutive years (Sheridan et al., 2014, Lal, 1983) where geomorphic conditions were almost constant, and rainfall was the only changing drivers. Both $|SC_1|$ and $|SC_2|$ were increased with rainfall depth; however, SC_1 is more sensitive to this driver. Soil texture was found to be an important driver that influences $|SC_2|$. Runoff generation is negatively controlled by surface vegetation and positively impacted by slope gradient results in changes in runoff scaling, however, no specific trend in the scaling effects was found to be associated with systematic change in gradient or vegetation. Soil hydraulic properties and saturated water content were not measured before and during data collection period. Therefore, the role soil spatial variability, rainfall temporal factors and macropore flow were not accounted in defining scaling coefficients that may also cause errors in representing scaling effects.

Chapter 4: The role of rainfall properties on overland flow scaling

Abstract

In this chapter the main focus is to examine whether the scale dependency of infiltration-excess runoff on a burned dry hillslope is related to event rainfall volumetric and temporal parameters. Stepwise multiple regression analysis was conducted to find the contribution of different rainfall characteristics i) to runoff generation at different plot lengths, and ii) to overland flow scaling behaviour on a burned hillslope.

The empirical data used in the stepwise regression models were collected from multi-scale runoff plots under natural rainfall conditions (Chapter 3). The instruments were installed on a severely burned hillslope with eucalyptus forest in southeast Australia. Forty-one rainfall-runoff events were extracted from 10 months of data and two scaling coefficient indices (SC_1 and SC_2) determined by fitting runoff depth and runoff ratio to plots' length. Details of the site instrumentation, data collection, rainfall-runoff event definition, and development of scaling indices were explained in chapter 3.

Stepwise multiple regression was performed in Minitab 17 to analyse the contribution of different event rainfall characteristics to events runoff generation at different plot lengths and to the runoff scaling behaviour. Rainfall parameters used as predictors in the regression models are total depth, duration, peak intensity, mean intensity, and coefficient variation of 3 minutes rainfall, plus depth-averaged rainfall intensity ($\check{R}$) and modified duration (D_T) calculated following (van Dijk, 2002). The correlation matrix and variance inflation factors (*VIFs*) were used to characterise and control for multicollinearity. Stepwise multiple regression analyses were conducted using predictor variables selected to ensure sufficiently low multicollinearity (*VIF*>5).

The regression analysis showed that rainfall total depth (mm) was the dominant factor; obtaining the highest contribution percentage in controlling event runoff generation at each plot length. Rainfall duration was the second most important predictor and it negatively impacting runoff generation; however, this was not consistent for all plots; and only appeared in the regression models for the 0.5 and 8m plots. Weak correlations (R^2 <38%) were found between rainfall parameters and runoff ratio, with no consistency in the importance order of predictors changing with plot lengths.

In terms of runoff scaling behaviour, total rainfall depth (mm) was the dominant parameter positively affecting SC_1, explaining 89% of the variability. Mean rainfall intensity was the second most important predictor impacting $|SC_1|$ with higher intensity reducing the scaling effect, but it only explained a further 2.4% of the variation. Rainfall total and mean intensity jointly explain 92% of the overland flow scaling effect.

The regression analysis showed that the impact of rainfall parameters on runoff generation decreases with plot length. The same conclusion was obtained when the relative impact of rainfall factors and soil properties on overland flow scaling for the forty-one rainfall events in this study was investigated with the help of previous models and parameters representing soil and rainfall impact on overland flow scaling (Van de Giesen et al., 2000).

4.1 Introduction

Rainfall volumetric and temporal properties regulate the rate of water reaching ground surface, which in turn determines the type of overland flow and connection of generated flow between soil patches (Bracken and Croke, 2007, Moody et al., 2013). This influences volumetric and temporal characteristics of overland flow hydrographs which are linked to hydrologic responses at the watershed outlet (Moody et al., 2013, Miyata et al., 2010a, Bracken and Croke, 2007).

The relative roles of soil-surface factors and rainfall properties in controlling overland flow scaling in arid and semiarid landscape have been explored by field-based studies (Wainwright and Parsons, 2002, Bagarello et al., 2010, Gomi et al., 2008a, Lal, 1983, Lal, 1997, Sheridan et al., 2014) and modelling (Julien and Moglen, 1990, Van de Giesen et al., 2000, van de Giesen et al., 2005, Van de Giesen et al., 2011). Studies showed that rainfall properties are important domains in runoff scaling (Sheridan et al., 2014), even in the absence of soil-surface spatial variability (Reaney et al., 2007, van de Giesen et al., 2005).

Storms with similar average and peak intensities have variable patterns of rainfall intensity, often referred to as the rainfall pattern (Smith, 1972) or event profile (Dunkerley, 2012). Rainfall volumetric and temporal characteristics determine threshold responses of hydrological processes by influencing the rate of infiltration, time-to-ponding, (Smith, 1972), peak flow (Julien and Moglen, 1990), and total discharge (Reaney et al., 2007). Rainfall temporal variability may increase the probability of generated runoff allocating to run-on infiltration downslope (Wainwright and Parsons, 2002). Thus hydrological responses to storms with similar event characteristics (e.g. total precipitation depth, peak intensity) can differ in the same basin (Reaney et al., 2007, Moody et al., 2013). This implies that to study scaling behaviour, investigation on soil-surface factors and run-on process are not sufficient, and that it is important to consider storm volumetric and temporal patterns that regulate the rate of water supply (Corradini et al., 2002, Bracken and Croke, 2007, Miyata et al., 2010a).

Rainfall properties and their interactions with post-fire spatial factors have been found to be more influential in runoff initiation and hydrological responses following fire (Moody et al., 2013). Post–fire floods are usually initiated with high intensity, more frequent (2-5 yr), and short duration (<30 min) rainfalls that act as transfer agent for readily mobilized material on burned ground surface (Nyman et al., 2010). For example after fire, soil erosion rate corresponded to ten minute rainfall maximum intensity (I_{max10}) in (Spigel and Robichaud,

2007), peak flow to I_{max30} in (Moody, 2012) and debris flow initiation to I_{15min} in (Kean et al., 2011) and I_{max30} in (Nyman et al., 2011). (Moody and Ebel, 2014) showed that time-to-peak of overland flow on a burned hillslope was mostly controlled by storm profile and soil moisture deficit than soil hydraulic properties.

The objective of this chapter is to study the contribution of rainfall temporal and volumetric factors in controlling overland flow generation and runoff scaling across different plot lengths.

4.2 Method

Stepwise multiple regressions analysis was chosen to investigate a range of possible correlations, and to find the best explanatory rainfall characteristics to explain runoff generation behaviour (both depth and runoff ratio) for different plot lengths, as well as runoff scaling behaviour.

The empirical data used in this analysis was collected from rainfall-runoff plots of 0.5m, 4m, 8m, 12m, and 16m lengths measuring overland flow during the second year following wildfire in southeast Australia. Forty-one runoff generated events were extracted from 10 months of rainfall and runoff data and two scaling coefficient indices (SC_1 and SC_2) were defined by correlating runoff depth and runoff ratio with plot lengths. Details of the site instrumentation, data collection, rainfall-runoff event definition, and development of scaling indexes were explained in chapter 3.

Four different types of regression models were developed using stepwise multiple regression analysis. The prediction variables for these four regressions were the runoff depth and runoff ratio (for each plot length), and the two runoff scaling coefficients ($|SC_1|$ and $|SC_2|$). The explanatory variables were the volumetric and temporal storm characteristics. Storm parameters used in the stepwise multiple regressions are total, duration, peak, mean, and coefficient variation of pulses (*CVs*), plus depth-averaged rainfall intensity ($\check{R}$) and modified duration (D_T) calculated following (van Dijk, 2002).

Depth- weighted average rainfall intensity ($\check{R}$) and adjusted storm duration (D_T) calculated from (van Dijk, 2002) are functions of mean intensity and total rainfall and also correlated to one another. This could cause problems with multicollinearity effects, or mathematical error in multiple regression models that occur when two or more explanatory variables are highly correlated. Multicollinearity inflates the standard errors of some coefficients resulting in underestimation of the significance of the contribution of those predictors in the regression model.

Two methods were used to deal with multicollinearity. First, the correlation matrix was calculated for all seven predictor variables. Second, the variance inflation factor (*VIF*) was calculated to measure the effect of multicollinearity of each independent variable with all other independent variables. No formal cut-off value exists to determine when a *VIF* is too large. However, if the *VIF* = 1, there is no multicollinearity, for 1<VIF <5, the predictor is

moderately correlated with others, and when the *VIF* is above 5, the regression coefficients are poorly estimated and multicollinearity considered to be severing (Graham, 2003).

VIF values were calculated for the explanatory variables in each regression and the predictor with the largest VIF was removed each time. This procedure repeated until the largest *VIF* was smaller than 5 (Zuur et al., 2010). Multiple regression analyses were then conducted with the remaining set of variables (*VIF*>5).

Minitab 17 standard stepwise regression was performed in which regression models systematically add the most significant variables and remove the least significant variables at each step. After adding a variable, all candidate variables in the model are checked to see if their significance (P-value) has been reduced below the specified tolerance levels (α). The procedure goes on until all non-significant variables are found and removed from the model and entering new variables does not increase regression coefficient (Nathans et al., 2012). Acronyms used in the interpretations of stepwise regression analysis are presented in Table 4.1.

Table 4. 1 Acronyms used in the result interpretations of stepwise regression analysis

No.	Acronym	Result interpretation
1	β	Coefficient of regression analysis for predicting the dependent variable from the independent variable.
2	**t-value**	The relative difference of a given coefficient from mean coefficient in sample data, represented in units of standard error.
3	**2-tailed p-values**	The probability of very unlikely observations in the both sides of bell-shaped probability curve.
4	**A**	The specified tolerance levels are used as threshold for significance of independent variables (P value) for entering and removing. In Minitab, variables with p-values greater than the specified Alpha-to-Enter value are removed from the model and those with p-values less than or equal to the specified Alpha-to-Remove value are kept into the model.
5	**95% Confidence Limit for B**	95% confidence intervals for the coefficients (B) representing how much the value could vary.
6	**Std. Error**	Standard errors associated with the coefficients.
7	**VIF**	Variance inflation factor derived from is the coefficient of determination of the regression equation ($\frac{1}{1-R^2}$)

4.3 Results

The correlation matrix of rainfall parameters was calculated and parameters with coefficient of determination above 0.3 were considered highly correlated (Table 4.2). The correlation matrix shows strong relations between rainfall properties. Mean, peak and Ř are positively correlated to one another with high R^2. D_T, rainfall total and duration are also positively and strongly correlated to one another with p-value = 0.000. To avoid multicollinearity, stepwise analyses were repeated and each time parameter with the largest *VIF* was removed until the largest *VIF* is below threshold (*VIF*<5).

As shown in Table 4.3, depth-averaged rainfall intensity ($\check{R}$) and non-rain storm duration (D_T) calculated from (van Dijk, 2002) obtained the largest VIFs. Therefore, these two parameters were removed from regression analyses.

Table 4. 2 Pearson's correlation matrix of predictors in multiple regression analyses

Predictors	Duration (D)	Total	Mean ($\bar{I}$)	Peak (I_{max})	$\check{R}$	D_T
Duration (D)						
Total	0.65 (0.000)					
Mean ($\bar{I}$)	-0.28 (0.071)	0.12 (0.460)				
Peak (I_{max})	-0.08 (0.598)	0.17 (0.295)	0.84 (0.000)			
$\check{R}$	-0.31 (0.052)	0.04 (0.788)	0.92 (0.000)	0.92 (0.000)		
D_T	0.73 (0.000)	0.96 (0.000)	-0.11 (0.496)	-0.09 (0.584)	-0.19 (0.227)	
CV	0.27 (0.08)	-0.37 (0.017)	-0.54 (0.000)	-0.49 (0.001)	-0.57 (0.00)	-0.21 (0.182)

Table 4. 3 Variance inflation factors (VIFs) of rainfall parameters (predictors) in stepwise regression analyses for runoff depth (mm) as dependent

Predictors	VIFs		
	Repetition 1	Repetition 2	Repetition 3
Total	96.47	4.7	4.40
Duration (D)	7.33	4.61	4.61
Mean ($\bar{I}$)	7.95	7.92	4.77
Peak I_{max})	22.78	8.62	4.39
CV	3.41	3.36	3.05
$\check{R}$	18.97	16.67	
D_T	111.97		

4.3.1 Rainfall Properties Correlated with Runoff Depths

A set of stepwise multiple regression analysis was conducted to study the contribution of storm parameters (total, duration (D), mean ($\bar{I}$), peak (I_{max}), CV, and $\check{R}$ and D_T) in controlling total runoff depth across different plot lengths (Table 4.4).

Table 4. 4 Model 1- Summary of multiple regression analyses of rainfall five parameters (total, CV, duration, peak, mean) with runoff depth (mm) in different plot length.

Plot 0.5 m								
Model Summary	SE=1.78, R-sq= 96.14%, R-sq(adj) = 95.71%, R-sq(pred)= 95.71%							
Variable	**β**	**Std Error**	***VIF***	**t value***	**p value***	**Contribution**	**95% CI***	
Total	0.89	0.28	3.96	17.39	0.000	56.53%	7.49	8.63
Duration (*D*)	-0.14	0.05	3.76	-2.84	0.007	37.63%	-0.24	-0.04
Mean ($\bar{I}$)	-1.28	0.38	1.46	-3.35	0.002	1.74%	-2.06	-0.50
CV	0.11	0.075	2.75	1.49	0.144	0.24%	-0.04	0.26
Regression Equation = -1.13 + 0.89 Total - 0.14 D - 1.28 $\bar{I}$ + 0.11 *CV*								
Plot 4 m								
Model Summary	SE=3.39, R-sq= 76.22%, R-sq(adj) = 75.61%, R-sq(pred)= 75.35%							
Variable	**β**	**Std Error**	***VIF***	**t value***	**p value***	**Contribution**	**95% CI***	
Total	0.55	0.049	1	11.18	0.000	76.22%	0.45	0.65
Regression Equation = 0.046 + 0.55 Total								
Plot 8 m								
Model Summary	SE=1.02, R-sq= 95.26%, R-sq(adj) = 94.87%, R-sq(pred)= 91.93%							
Variable	**β**	**Std Error**	***VIF***	**t value***	**p value***	**Contribution**	**95% CI***	
Total	0.47	0.03	3.94	19.77	0.000	66.21%	0.41	0.53
Duration (D)	-0.10	0.03	3.68	-2.52	0.001	28.57%	-0.16	-0.04
CV	0.078	0.04	2.48	-1.81	0.059	0.49%	-0.003	0.16
Regression Equation = -1.23 + 0.47 Total - 0.104 D + 0.078 *CV*								
Plot 12 m								
Model Summary	SE=0.96, R-sq= 92.92%, R-sq(adj) = 92.92%, R-sq(pred)= 90.10%							
Variable	**β**	**Std Error**	***VIF***	**t value***	**p value***	**Contribution**	**95% CI***	
Total	0.32	0.02	1.00	22.63	0.000	91.00%	0.28	0.35
Regression Equation = -0.52 + 0.32 Total								
Plot 16 m								
Model Summary	SE=0.39, R-sq= 39.79%, R-sq(adj) = 36.62%, R-sq(pred)= 27.46%							
Variable	**β**	**Std Error**	***VIF***	**t value***	**p value***	**Contribution**	**95% CI***	
Total	0.02	0.006	0.24	5.00	0.000	32.13%	0.35	0.59
CV	0.22	0.106	0.54	2.2	0.034	7.65%	0.002	0.045
Regression Equation = -0.14 + 0.030 Total + 0.023 *CV*								
***α* to enter and remove = 0.15**								

Contribution percentage, coefficients, and p-values were used to find the importance order of rainfall parameters in runoff depth generation. Total rainfall depth (mm) impacted generated runoff depth positively with the highest coefficient of determination (R^2) and the

lowest p-value for all plot lengths indicating strong contribution of this parameter in runoff production at all plot lengths.

In the shortest plot lengths, rainfall total depth (mm) and runoff generation obtained strong positive relationship (R^2=0.94). The coefficient of determination (R^2) fluctuated in a range of 96% to 76% for plots 0.5 to 12 m and then dropped to 39% for 16 m plots. The slopes of trendlines (β) for total rainfall steadily declined with length. The weakest correlation (R^2=39%) and the smallest contribution of rainfall parameters in runoff generation were observed for 16 m plots. The isolated univariate relationship of runoff depth to rainfall depth (Figure 4.1) had similar trends to stepwise multiple regression models.

In the regression models, rainfall duration was the second most important predictor negatively impacting runoff generation; with less runoff generation for long events when other parameters are constant. However, this result was not consistent for all plots and only appeared in the regression analyses for 0.5 and 8 m plots.

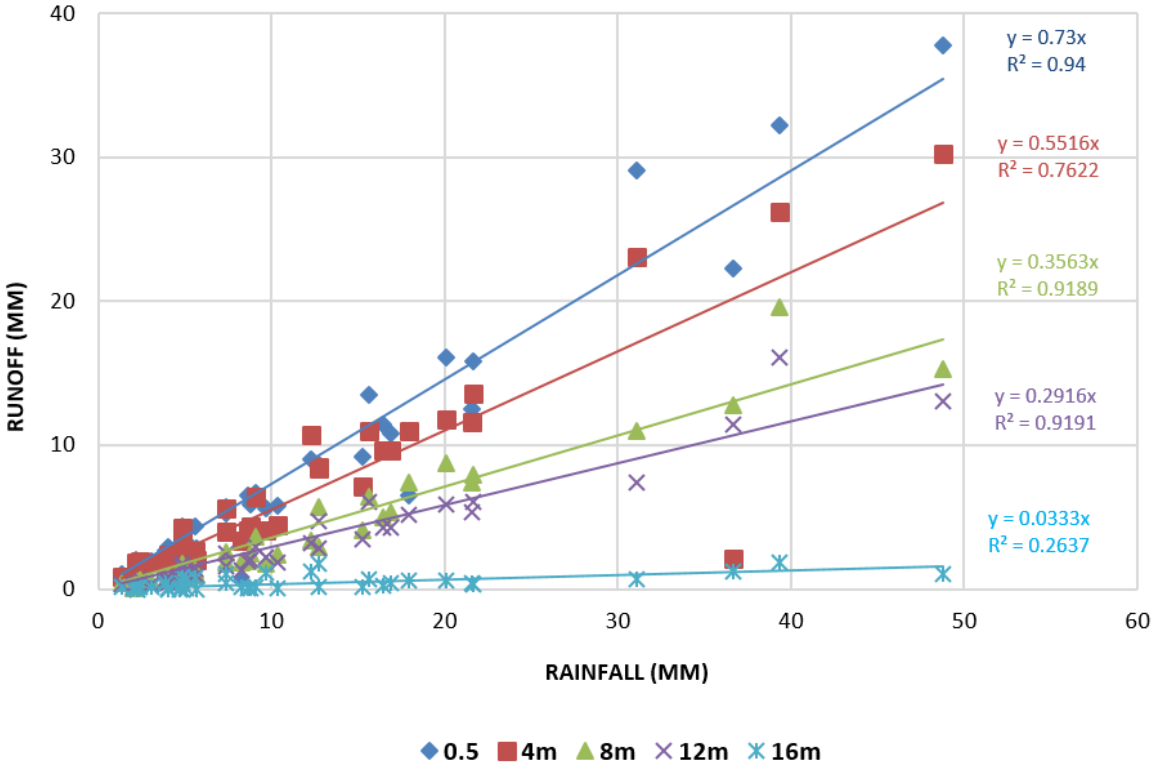

Figure 4.1 Scatter plot of rainfall total depth (mm) versus associated runoff (mm) for all runoff generating storms recorded during the study period

As presented in multiple regression analysis, total rainfall depth (mm) is the dominant factor in controlling runoff that faded the impact of other four parameters. To study the importance order of remaining rainfall indices in controlling runoff depth at different plot length, this dominant factor was excluded. The remaining four parameters; duration (D), mean ($\bar{I}$), peak (I_{max}), CV plus $\check{R}$ and D_T were put into another multiple regression analysis. The same procedure was conducted for detecting multicollinearity based on $VIFs$ and stepwise regression analysis repeated for each plot length as shown in Table 4.5.

In the absence of rainfall total, D_T is the most influential predictors obtaining the highest contribution percentage and the lowest p-value (0.000) in all plot length. Trendline slope of this parameter follows a decreasing trend with plot length increase, stating decrease in its impacts with travel distance as shown in Table 4.5. The regression model obtains high coefficient of determinations (R^2) fluctuated in a range of 92% to 68% for plots 0.5 to 12 m and then dropped to 33% for 16 m plots. This result was predictable because D_T is a function of rainfall total. The univariable regression analysis of D_T and total runoff depth also follows similar trends to stepwise multiple regression models (Figure 4.2).

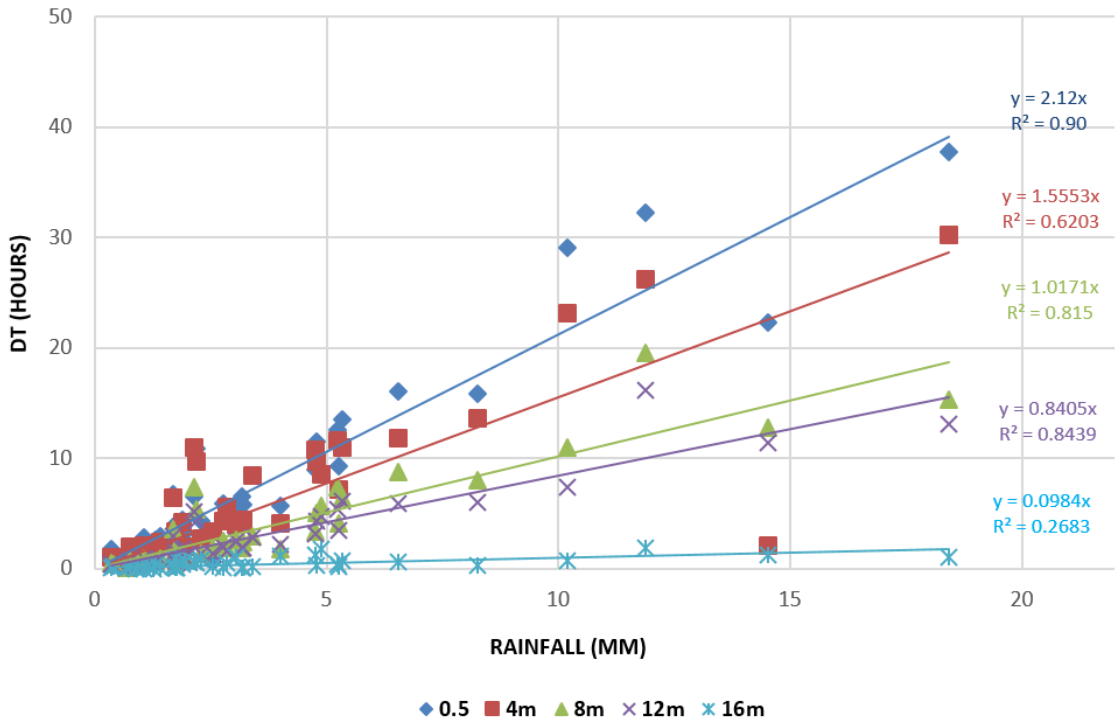

Figure 4.2 Scatter plot of DT (hours) correlated to rainfall depths (mm) for all runoff generating storms at different plot lengths recorded during the study period

Table 4.5 Model 2- Summary of stepwise multiple regression analyses of six rainfall parameters (*CV*, duration (*D*), peak (I_{max}), mean ($\bar{I}$), $\check{R}$ and D_T) and runoff productions (mm) in different plot length

Plot 0.5 m								
Model Summary	SE=2.29, R-sq= 93.66%, R-sq(adj) = 92.96%, R-sq(pred)= 90.93%							
Variable	**β**	**Std Error**	***VIF***	**t value***	**p value***	**Contribution**	**95% CI***	
D_T	2.48	0.14	2.43	17.05	0.000	51.15%	2.18	2.77
Duration (D)	-0.18	0.05	2.89	-3.11	0.004	37.63%	-0.29	-0.061
Peak (I_{max})	0.16	0.05	4.36	3.18	0.003	1.20%	0.058	0.26
Mean ($\bar{I}$)	-0.163	0.89	4.81	-1.82	0.076	3.67%	-3.43	0.18
Regression Equation = -0.25 +2.48 D_T- 0.17 D+ 0.16 I_{max} - 1.63 $\bar{I}$								
Plot 4 m								
Model Summary	SE=3.84, R-sq= 70.24%, R-sq(adj) = 68.67%, R-sq(pred)= 54.92%							
Variable	**β**	**Std Error**	***VIF***	**t value***	**p value***	**Contribution**	**95% CI***	
D_T	1.45	0.16	1.01	9.23	0.000	66.68 %	1.13	1.76
Peak (I_{max})	0.12	0.04	1.01	2.94	0.006	3.56 %	0.038	0.20
Regression Equation = -0.54 +1.45 D_T + 0.12 I_{max}								
Plot 8 m								
Model Summary	S=1.4, R-sq= 90.69%, R-sq(adj) = 89.93%, R-sq(pred)= 85.20%							
Variable	**β**	**Std Error**	***VIF***	**t value***	**p value***	**Contribution**	**95% CI***	
D_T	1.26	0.08	2.12	15.11	0.000	57.45%	1.09	1.42
Duration (D)	-0.1	0.029	2.12	-3.39	0.000	28.57%	-0.16	-0.04
Peak (I_{max})	0.072	0.015	1.01	4.89	0.000	4.67%	0.0425	0.120
Regression Equation = -0.54 - 1.26 D_T -0.1 D + 0.072 I_{max}								
Plot 12 m								
Model Summary	S=1.17, R-sq= 90.05%, R-sq(adj) = 89.24%, R-sq(pred)= 84.88%							
Variable	**β**	**Std Error**	***VIF***	**t value***	**p value***	**Contribution**	**95% CI***	
D_T	0.95	0.59	2.12	13.83	0.000	51.43%	0.82	1.1
Duration (*D*)	-0.04	0.031	2.12	-1.96	0.057	35.22%	-0.09	0.0016
Peak (I_{max})	0.05	0.027	1.01	4.08	0.000	3.39%	0.0254	0.075
Regression Equation = -0.47 + 0.96 D_T - 0.049 D + 0.05 I_{max}								
Plot 16 m								
Model Summary	S=0.46, R-sq= 34.57%, R-sq(adj) = 32.89%, R-sq(pred)= 24.85%							
Variable	**β**	**Std Error**	***VIF***	**t value***	**p value***	**Contribution**	**95% CI***	
D_T	0.074	0.016	1.00	-2.31	0.000	34.57%	0.041	0.106
Regression Equation = 0.188 + 0.074 D_T								

α to enter and remove = 0.15

Another set of multicollinearity detections and stepwise multiple regression analysis conducted (Model3) to study rainfall parameters in relation to runoff ratio. Total rainfall depth (mm) was excluded from the regression analyses because runoff ratio is calculated by dividing by rainfall depth meaning that runoff ratio and rainfall depth are dependent.

Rainfall average-depth intensity ($\check{R}$) and duration were excluded from the stepwise regression analyses for having the highest VIF in first and second repetitions. Stepwise regression analyses (Model3) of runoff ratio against the remaining four parameters (Mean ($\bar{I}$), Peak (I_{max}), *CV*, and D_T) for different plot lengths are presented in Table 4.6.

Table 4.6 Variance inflation factors (*VIFs*) of rainfall parameters (predictors) in stepwise regression analyses with runoff ratio (dependent)

Predictors	VIFs		
	Repetition1	**Repetition2**	**Repetition3**
Duration (*D*)	5.84	5.81	---
Mean ($\bar{I}$)	7.82	4.91	3.90
Peak (I_{max})	9.51	5.63	3.55
CV	3.40	3.20	1.59
D_T	5.45	5.30	1.13
$\check{R}$	16.09	---	---

Table 4.7 Model 3- Summary of stepwise multiple regression analyses of rainfall parameters with runoff ratio (%) in different plot length.

Plot 0.5 m								
Model Summary	S=16.08, R-sq= 7.24%, R-sq(adj) = 4.48%, R-sq(pred)= 0.00%							
Variable	β	Std Error	VIF	t value*	p value*	Contribution	95% CI*	
Mean	-5.19	2.97	1.00	-1.75	0.089	7.24	-11.2	0.82
Regression Equation = 68.71 – 5.19 Mean								
Plot 4 m								
Model Summary	No terms enter the model for α to enter and remove = 0.15							
Plot 8 m								
Model Summary	S=7.98, R-sq= 37.71%, R-sq(adj) = 34.43%, R-sq(pred)= 21.87%							
Variable	β	Std Error	VIF	t value*	p value*	Contribution	95% CI*	
Mean	3.76	1.43	1.01	2.63	0.012	7.80%	0.87	6.65
D_T	1.39	0.326	1.13	4.26	0.00	29.91%	0.734	2.055
Regression Equation = 20.13 + 3.76 Mean + 1.39 D_T								
Plot 12 m								
Model Summary	S=7.36 R-sq= 18.61%, R-sq(adj) = 16.52%, R-sq(pred)= 5.99%							
Variable	β	Std Error	VIF	t value*	p value*	Contribution	95% CI*	
D_T	0.894	0.30	1.00	2.99	0.005	18.61%	0.288	1.5
Regression Equation = 20.26 + 0.89 DT								
Plot 16 m								
Model Summary	S=4.66, R-sq= 16.91%, R-sq(adj) = 14.78%, R-sq(pred)= 8.53%							
Variable	β	Std Error	VIF	t value*	p value*	Contribution	95% CI*	
CV	0.33	0.11	1.00	2.82	0.008	16.91%	0.094	0.57
Regression Equation = 1.36 + 0.33 CV								

α to enter and remove = 0.15

The result of regression analysis in Model 3 shows weak correlations (R^2 <38%) between rainfall parameters and runoff ratio with no consistency in the importance order of predictors

which change with plot length (Table 4.7). Runoff ratio is a proportional indicator derived from total runoff depth divided by total rainfall depth. The impact of rainfall total depth which is the strongest predictor for generated runoff depth (mm) is removed from the regression analyses, which explain weak correlations of the remaining rainfall parameters with runoff ratio.

4.3.2 Rainfall Properties Controlling Scaling Effect

Multicollinearity detection and stepwise multiple regression analyses were conducted to find key factors and their order of importance in controlling scale-dependency of generated runoff. Rainfall volumetric and temporal parameters; Total depth, Duration, Peaks, Mean, *CV*s and $\check{R}$ and D_T from (van Dijk, 2002) were set as predictors and overland flow scaling effect indexes ($|SC_1|$, $|SC_2|$) were dependents in the regression analyses. The calculated VIFs for rainfall parameters in relation to $|SC_1|$ and $|SC_2|$ were the same as *VIF*s calculated for runoff depth and runoff ratio respectively.

Table 4.8 Summary of stepwise multiple regression analyses of rainfall parameters in relation to runoff depth scaling coefficients ($|SC_1|$), and runoff ratio scaling coefficient ($|SC_2|$)

Model 4- SC_1								
Model Summary	S=0.62, R-sq= 92.00%, R-sq(adj) = 91.34%, R-sq(pred)= 87.71%							
Variable	**β**	**Std Error**	***VIF***	**t value***	**p value***	**Contribution**	**95% CI***	
Total	0.21	0.013	2.08	15.68	0.00	89.54%	0.17	0.22
Duration	-0.025	0.013	2.23	-1.89	0.067	0.02%	-0.052	0.002
Mean	-0.41	0.125	1.31	-3.35	0.002	2.43%	-0.67	-0.165
Regression Equation = 0.12 + 0.21 Total - 0.025 Duration - 0.42 Mean								
Model 5- SC_2								
Model Summary	S=4.53, R-sq= 9.62%, R-sq(adj) = 7.30%, R-sq(pred)= 0.00%							
Variable	**β**	**Std Error**	***VIF***	**t value***	**p value***	**Contribution**	**95% CI***	
Mean	-1.63	0.8	1	-2.04	0.048	9.62%	-3.26	-0.012
Regression Equation = 17 - 1.63 Mean								
α to enter and remove = 0.15								

As shown in Table 4.8, total rainfall is the dominant parameter positively affecting $|SC_1|$ with 89.5% contribution and P-value of zero. Thus, rainfall total depth can explain 89% of the variability in runoff depth scaling effect (SC_1). Rainfall mean intensity is the second most important predictor negatively impacting SC_1 with less than 3% contribution. The regression analyses showed that these two parameters (rainfall total and mean) can explain 92% of overland flow scaling for a single event.

The univariate regression analysis was also conducted to isolate relationships of these parameters and runoff depth-scaling coefficient ($|SC_1|$). As shown in Figure 4.3, only univariate regression analysis between total rainfall depth and $|SC_1|$ is similar to stepwise multiple regression analysis in Model 4. The result of univariate regression analysis for the rest of rainfall parameters and $|SC_1|$ are different from stepwise multiple regression analysis in Model 4.

Similar multicollinearity detection and stepwise regression analyses were conducted to relate rainfall parameters to runoff ratio scaling coefficient ($|SC_2|$). The result showed minor contributions of rainfall parameters correlating with runoff ratio scaling coefficient ($|SC_2|$) as shown in Table 4.7. Similar results were obtained from univariable regression analysis as shown in Figure 4.4.

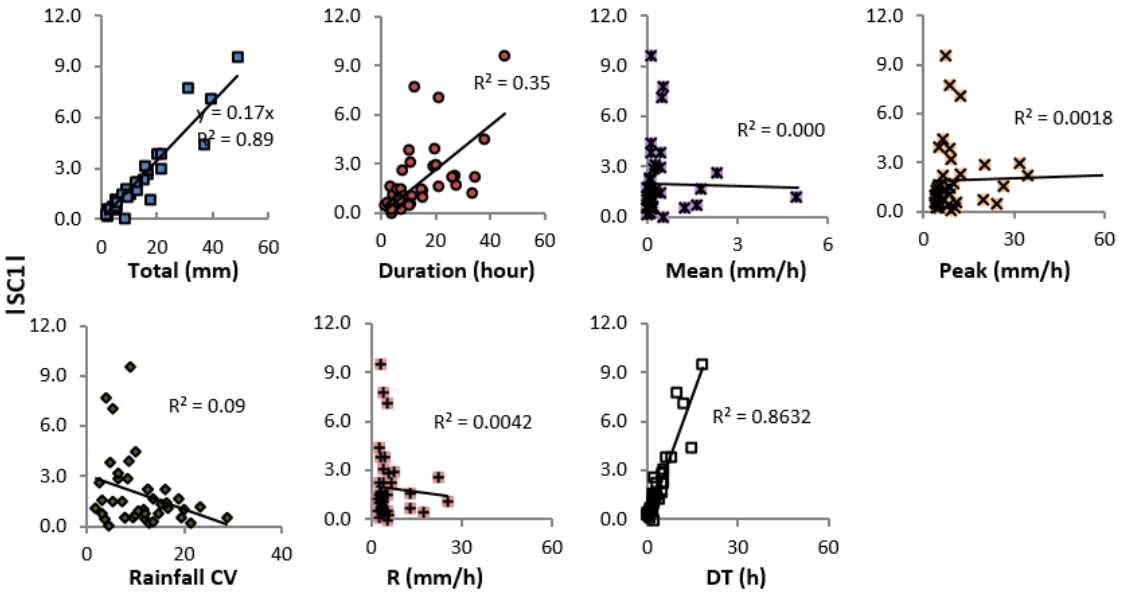

Figure 4.3 Runoff depth scaling coefficients (SC_1) correlated with rainfall indices

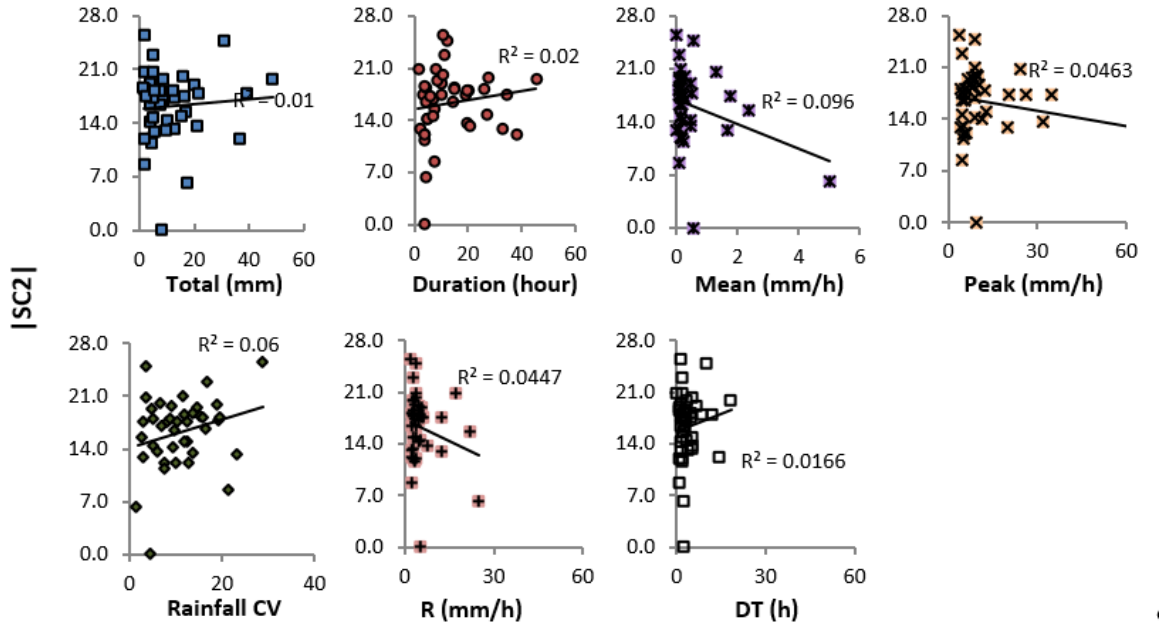

Figure 4.4 Runoff ratio scaling coefficients (*SC₂*) correlated with rainfall indices

4.4 Discussion

4.4.1 Rainfall Properties Controlling Runoff Production

From stepwise multiple regression analysis of generated runoff in relation to storm characteristics, rainfall total depth (mm) was the dominant factor positively impacting runoff depth at different plot lengths; with high coefficient of determination (R^2= 0.96-0.76), except 16m plot (R^2 = 0.39). (Gomi et al., 2008a) also found that total storm depths were positively correlated with total runoff depth in plots 1.6x0.5 m and 24.5x8 m in steep forested hillslope. Similarly, rainfall total depth had the best correlation positively impacting runoff depth at plot scale measurements in (Mayor et al., 2011).

The depth of generated runoff in relation to rainfall parameters also was investigated for 14 rainfall-runoff data collected by (Van der Sant, 2016) during the first year after fire (2013-2014) from 8m plots at the same study site. The stepwise regression analysis shows positive strong correlation (R^2 = 0.85, p=0.000) between total rainfall depth (mm) and collected runoff (mm) at the 8 m plots (Appendix 4.1).

Correlation coefficients (β) of the regression analysis had a decreasing trend with plot length showing their degree of influence on runoff depth decline with plot length. Therefore, the role of rainfall factors in controlling runoff depth decreases with length. This trend conforms

to the result of univariable regression analysis, obtained from isolated relationships of these parameters with generated runoff depth (Figure 4.2).

(Reaney et al., 2007) simulated dynamics of overland flow responses to temporal variability of a single storm event with varying intensity (40-90 mm/h) and duration (1- 20 min). Their study showed that variation of runoff ratio is positively related to *CV*s of rainfall intensity (64%), whereas the maximum rainfall intensity only explains 14% of the variability. In this multiple regression analysis, runoff ratio was not significantly correlated with rainfall parameters in both multiple and univariable regression analysis ($R^2 < 0.39$). Gome et al., 2001 studied the relationship between rainfall *CV* and mean runoff volume (mm) per event and found a power law relationship. (Dunkerley, 2012) operated rainfall simulations in arid and semi-arid areas with low infiltration rate to compare hydrographs of discharge derived from temporally varied and uniform events. The result showed that the varying intensity runs produced significantly larger runoff ratios and peak runoff rates (85%–570%), implicating important rule of rainfall temporal variability on soil infiltration rate and runoff in dry condition.

In this study, rainfall *CV* was only correlated with runoff ratio at 16m plot length; positively and weakly (16%). Similarly, rainfall mean, and maximum intensities weakly correlated to depth (mm) and ratio (%) of the generated runoffs in this study (Appendices 4.2, 4.3, 4.4 & 4.5).

4.4.2 Rainfall Properties Controlling Runoff Scaling

From stepwise multiple regression analysis, runoff depth scaling coefficient ($|SC_1|$) was found positively correlated with total rainfall (mm) with high coefficient of determination ($R^2 = 0.89$). Therefore, higher scaling effects was found associated with runoffs generated by larger storms (Figure 4.3). (Van de Giesen et al., 2000) and (Mayor et al., 2011) also found higher scaling effects associated with higher total rainfall depth. This is in agreement with (Dunne et al., 1991) that argue higher run-on infiltration occurs through micro-relief when inundation depth increases with runoff travel distance which is plot length in this study.

Rainfall *CV* and duration were found important in controlling runoff scaling in previous studies (Van de Giesen et al., 2000, Stomph et al., 2002, Wainwright and Parsons, 2002). For example, (Wainwright and Parsons, 2002) found that temporal variability of rainfalls can increase scaling effects mainly due to re-infiltration of generated runoff when infiltration

exceed rainfall input throughout the events. In this study, rainfall mean has the second most influential (but very minor) factor with 2% contribution to runoff depth scaling effects (SC_1). Rainfall depth and mean together explained almost 92% of SC_1 of a single event.

(Liu et al., 2000) found scaling effect decreases when maximum intensity of I_{30mins}>15 mm h^{-1} and there would be no scaling effects when maximum storm intensities of I_{30mins} exceed 45 mm h^{-1}. (Cammeraat, 2004) also stated rainfall intensity above approximately 20 mm h^{-1} in 30 min is a critical threshold to obtain runoff in longer travel distance while the impact increases with longer durations. In this study, all storms except event 3 obtain maximum intensity of I_{30mins} below 15 mm/h (Appendix 4.3); however, the scaling effects for event 3 are not the lowest (Figure 3.20). (Chen et al., 2016) stated the scaling effect was more significant for rainfall events with lower intensity; however, no strong relationship was found between rainfall intensities and runoff scaling coefficient in this study.

4.4.3 Examining Runoff Scaling with Previous Metrics

(Sheridan et al., 2014) developed a scaling equation to define runoff ratio reaching downslope as a function of runoff ratio at point scale in relation to precipitation, and soil-surface spatial factor.

$$\text{Eq 4.1} \qquad Q_h(\lambda) = \frac{\beta\mu}{\mu+\lambda}$$

Where λ: slope length ($\lambda \geq 0$), $Q_h(\lambda)$: runoff ratio at distance λ, β: a parameter related to annual-average point-scale runoff ratio (a fraction of precipitation, $0 \leq \beta \leq 1$), μ: a parameter related to travel distance before reinfiltrating (soil-surface spatial factor; $\mu > 0$).

In (Sheridan et al., 2014), the above equation was fitted into multi-length plot-scale datasets of published international literature to parameterizing β and μ suitable for different landscape conditions; bare soil, forested, tilled, shrublands, and burned. The same procedure was used to examine whether the equation fits scaling patterns in this study. Total runoff ratio for plots with different length from 0.5 m to 16 m at the study site was predicted by calibrating two parameters of the scaling equation proposed by (Sheridan et al., 2014). Parameters were allowed to range within $0 < \mu < 200$ and $0 \leq \beta \leq 1$ and acceptable ranges were found based on predicted runoff ratios being within the range of averaged observed runoff ratio ± 1 standard deviations of the replicates.

This resulted in acceptable bounds of $0.5 \leq \beta \leq 0.7$ and $5 < \mu < 8.5$ for all plot lengths, except the 16 m plots. The best fit of predations was obtained with β=0.56 and μ=8.5 (Figure 4.5b). High correlation (R^2 = 0.83) was obtained when the predicted runoff ratios from the optimum parameters were plotted against total observed runoff ratio for the study period as shown in Figure 4.5a.

Sheridan et al., 2014 proposed β and μ to be a function of the complex interaction between the temporal variability of precipitation and the spatial variability of the infiltration capacity of the soil for the period of observation. The aim was to predict the parameter values for different landscape and climate combinations allowing the application of the model in the absence of field runoff plot data. Values for β and μ in this study are similar to values calculated for the second year of the steepest site in (Lal, 1983). The site obtains 15% steepness (8.5 degree), sandy clay loam soil, and cultivated treatment with 1215 mm of annual precipitation. Despite of similarity in β and μ, only soil type is common landscape condition for the steepest site in (Lal, 1983) and this study. Therefore, having a good fit model for this scaling equation with similar β and μ does not necessarily represent similarities in all landscape factors (gradient, treatments) and precipitation patterns.

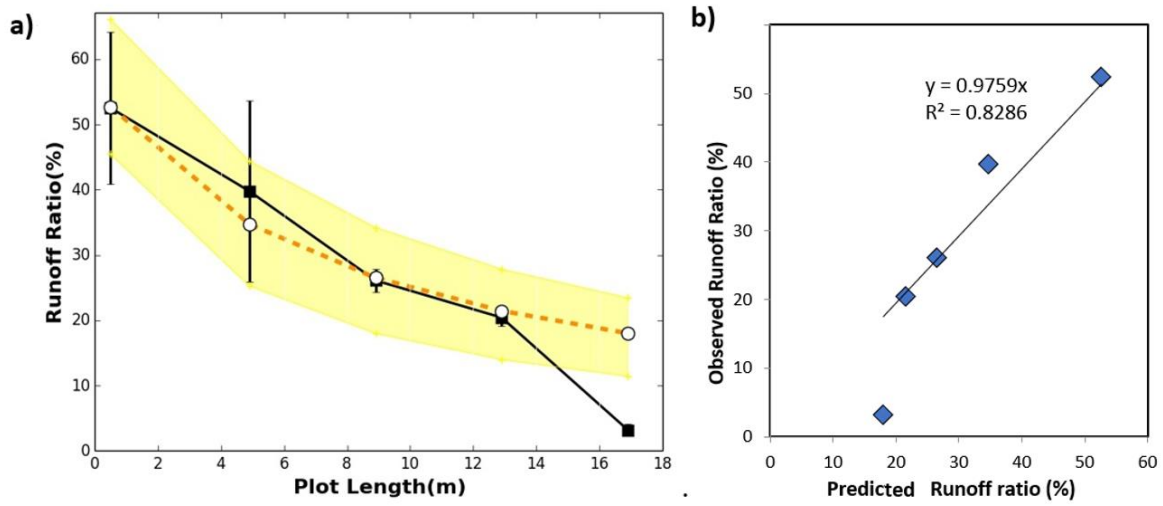

Figure 4.5 a) Boundary of accepted values for predicted runoff ratio with parameters in range of $0.5 \leq \beta \leq 0.7$ and $5 < \mu < 8.5$ and optimum fit (dashed orange line) derived from β=0.56 and μ=8.5, b) Total observed runoff ratio for the whole 308 days of study period plotted against predicted runoff ratio from the model by Sheridan et al., 2014.

In (Van de Giesen et al., 2000), an indicator was introduced to measure scaling effects from observed runoff coefficient in 12 m plot divided by runoff coefficient in 1.25 m plot ($FR = \frac{RR_{long}}{RR_{short}}$) where FR is scaling indicator. The outcome of their study was summarized as:

- Scaling effects exist when this indicator is below one ($FR < 1$)
- Soil-surface retention factors are dominant when the value of this indicator is less than their plot length ratio ($FR < \frac{L_{short}}{L_{long}}$); where L is the plot's length in long and short plots.

This indicator was used in this study to investigate at what degree scaling effects are controlled by rainfall parameters at different lengths. Ten combinations of short and long plots were set for $\frac{RR_{long}}{RR_{short}}$ and $\frac{L_{short}}{L_{long}}$ calculations for each event. As shown in Figure 4.6, there are some events with FR above or close to one when plots 0.5 and 4 m were put into the test. This states that scaling effect is not significant in short travel distance. However, this trend changed when FR was calculated for longer plots. FR obtained from division of runoff ratio of longer plots is below one for the majority of events and below the threshold line ($\frac{L_{short}}{L_{long}}$) when the longer plot is 16 m. This could be concluded that run-on runoff is more pronounced with increasing travel distance when generated runoff travels downslope. This agrees with the earlier regression analysis showing that the impact of all rainfall parameters on runoff productions decreases with plot length.

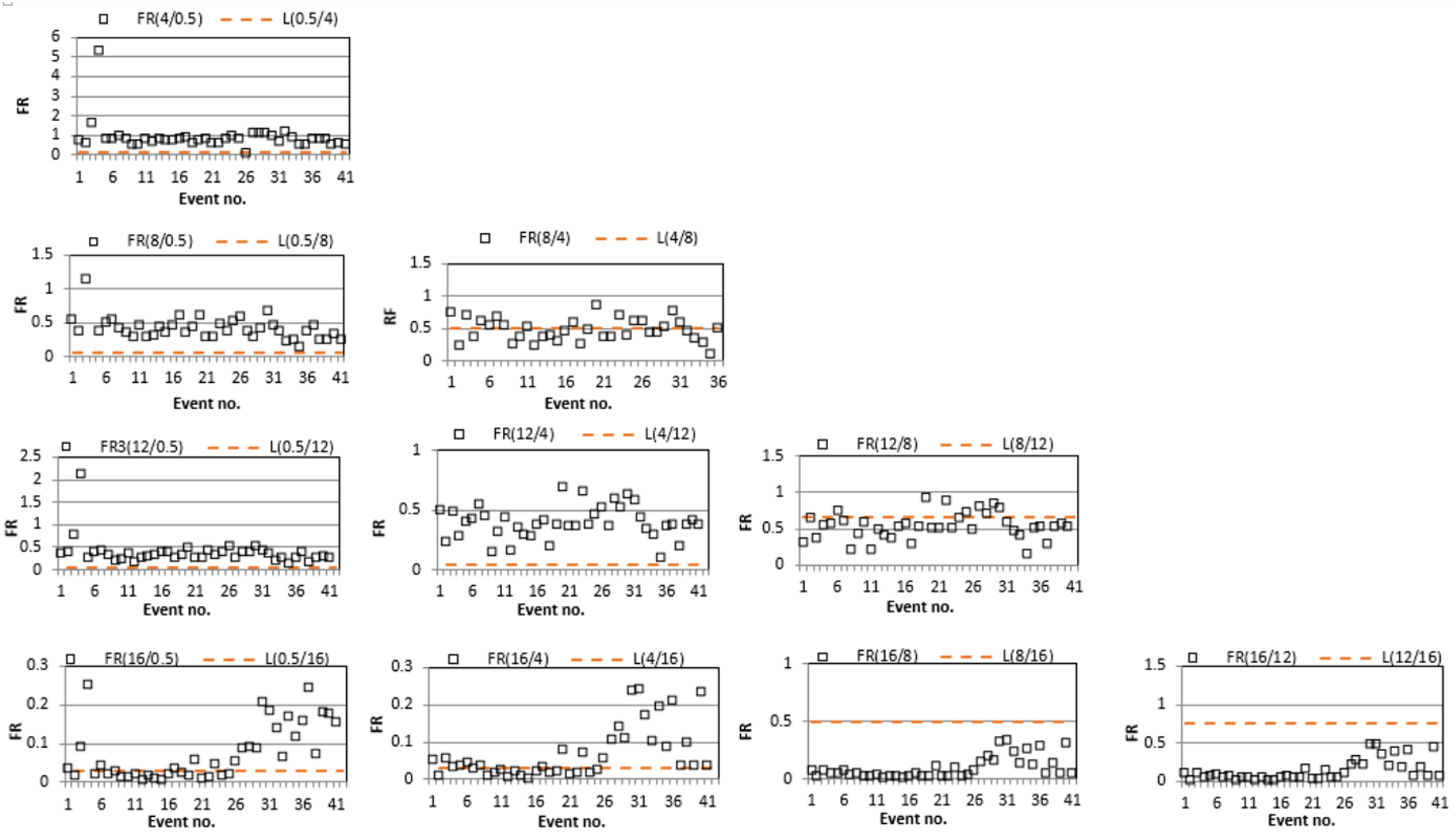

Figure 4.6 Scaling effect from observed runoff coefficient in large plots divided by runoff coefficient in short plots ($FR = \frac{RR_{long}}{RR_{short}}$). Red line shows $FR < \frac{L_{short}}{L_{long}}$

4.5 Conclusion

Stepwise multiple regression models were fitted to study the contribution of rainfall volumetric and temporal factors in controlling overland flow generation and scaling on a burned dry hillslope. Rainfall parameters were used as predictors in the stepwise multiple regressions. The correlation matrix and variance inflation factors (*VIF*s) were used to avoid multicollinearity. Multiple regression analyses were conducted with a set of variables with sufficiently low multicollinearity.

The result of regression analysis showed that rainfall total depth (mm) was the dominant factor in controlling runoff generation depth at different plot lengths; obtaining the highest contribution percentage. Rainfall duration was the second most important, but minor, predictor negatively impacting runoff generation in the regression analysis for 0.5 and 8m plots.

Total rainfall depth is the dominant parameter positively affecting $|SC_1|$ with 89.5% contribution (P-value = 0.00) indicating rainfall total depth can explain 89% of the variability in runoff depth scaling effect (SC_1). Rainfall mean is the second most important, but again minor, predictor; negatively impacting $|SC_1|$ with 2.4% contribution. These two parameters explain 92% of overland flow scaling for a single event.

Similar multicollinearity detection and stepwise regression analyses were conducted to relate rainfall parameters to runoff ratio and $|SC_2|$. Rainfall predictors were weakly correlated (R^2 <38%) with runoff ratio with no consistency in the importance order of predictors, which changed between plot lengths. Only a minor contribution of rainfall parameters was found for runoff ratio and $|SC_2|$.

Result from both multiple and univariate regression analysis showed that rainfall total depth (mm) is the most dominant factor in both overland flow generation and scaling effects; obtaining the highest contribution percentage. However, contribution of rainfall total depth and other rainfall parameters in generated runoff depth (mm) and their regression coefficient decreased with plot length reaching the lowest values at the longest plots. Thus, the influence of rainfall properties on runoff production and scaling declines with plot length. This could be due to macropore flow being more pronounced with increasing length when generated runoff travels downslope. Similar conclusions were obtained when the scaling indicator from (Van de Giesen et al., 2000) was used for the

events in this study. The scaling effect was smaller for short travel distance and became more pronounced with plot length while less impacted by rainfall factors. This suggests that rainfall properties regulate runoff production at shorter plot length, while runoff-runon processes become more pronounced at longer plot length when generated runoff travels downslope.

Chapter 5: Modelling Runoff scaling behaviours on burned hillslopes using the KINEROS2 model

Abstract

This chapter investigates whether traditional rainfall-runoff models; coupling rainfall temporal variations with soil infiltration and runon process, can predict overland flow scaling behaviour on a burnt eucalypt forested hillslope. Overland flow simulations using KINEROS2 were calibrated for the 8 m plot length. Calibration outcome showed the model was able to represent runoff hydrographs well for a subset of events ($NSE > 0.5$), which were then examined further. Weak model performance ($NSE < 0.5$) was obtained for small events with total runoff depth < 4 mm. The model was then applied to 0.5, 4, 12 and 16 m plot lengths to investigate whether models with traditional infiltration theories and runon process coupled with rainfall temporal pattern are capable of simulating scaling behaviours. These simulations were used to investigate whether the representing spatial variability of saturated hydraulic conductivity (CV_{Ks}) could explain observed runoff scaling effects.

Soil infiltration parameters (hydraulic conductivity, net capillary, porosity, and pore index) and soil water content were considered to vary from event to event with the aim of representing changes in post-fire water repellency. Surface roughness was assumed to be constant for the whole study period given that vegetation growth was insignificant during the study period.

The key properties impacting simulated hydrographs were identified to be soil hydraulic conductivity (K_s), net capillary drive (G) and surface roughness respectively. The dynamics of simulated hydrographs were found to be less sensitive to variations of porosity, pore index and initial water content; which led to < 5% variation in model efficiencies and error indicators. Increasing CV_{Ks} (from 0 to 2) resulted in a slight increase in total runoff depth and peak flow (up to 3%) for the majority of the events (> 95%) and slightly higher R-squared (R^2) (up to 5%).

Weak scaling effects were demonstrated by the model and were <10% of those observed. Changing the spatial variability of saturated hydraulic conductivity (CV_{Ks} = 0.5, 1 and 2) did not help in capturing scaling effects, resulting only in minor changes (< 3%). The results show that a) rainfall-runoff models with traditional infiltration theories, and runoff

processes were inadequate in capturing the observed overland flow scaling effects, and b) accounting CV_{Ks} in the models did not help to capture scaling behaviour on a burnt dry environment with extremely water repellent soil.

5.1 Introduction

Scale-dependence of overland flow is frequently observed under natural rainfall runoff datasets (Sheridan et al., 2014, Van de Giesen et al., 2000, Lal, 1997, Moreno-de las Heras et al., 2010), yet largely neglected in models (Chen et al., 2016b, Blöschl and Sivapalan, 1995), limiting our capacity to scale up plot-scale runoff measurements (Moody et al., 2013). Scaling behaviours of overland flow have been attributed to spatial variability of soil physical properties (Julien and Moglen, 1990), the run-on effect (Wainwright and Parsons, 2002, Langhans et al., 2016) and rainfall temporal properties (Li and Sivapalan, 2011, Joel et al., 2002, Wainwright and Parsons, 2002) due to their sustantial roles in infiltration excess runoff processes.

Field investigations (Gómez et al., 2001, Govindaraju et al., 2001, Sivapalan and Wood, 1986) showed significant spatial heterogeneity in hydraulic properties of natural soil, with hydraulic conductivity (*Ks*) being the most variable. Several modeling studies have examined the effect of spatial variability of hydraulic conductivity (CV_{Ks}) on generation and transport of infiltration-excess runoffs through infiltration and run-on (Morbidelli et al., 2006a, Woolhiser et al., 1996, Nahar et al., 2004, Saghafian et al., 1995). Excluding CV_{Ks} in rainfall-runoff modlling resulted in underestimation of total depth and peak flow in (Morbidelli et al., 2006) and (Nahar et al., 2004), and weak demonstration of overland flow scaling in (Wainwright and Parsons, 2002).

During a Hortonian rainfall-runoff event, some parts of surface may have infiltration-excess runoff while for other surface parts infiltration capacities are unsatisfied due to spatial variability in soil-surface properties, particularly soil hydraulic conductivity(CV_{Ks}) (Gómez et al., 2001, Morbidelli et al., 2006a). Runoff from upslope encounters unsaturated areas downslope providing more water for infiltration, known as runoff-runon process (Wainwright and Parsons, 2002, Morbidelli et al., 2006a, Jones et al., 2009). In (Chen et al., 2016), the run-on process was identified as the main factor causing scaling effects in a cell-based Rainfall-Infiltration-Runoff Model.

Rainfall intensity determines threshold responses of hydrological processes by shifting the rate of infiltration and time-to-ponding (Smith, 1972), peak flow (Julien and Moglen, 1990), and total discharge (Reaney et al., 2007). Thus hydrological responses to storms with similar interval metrics (e.g. total precipitation depth, peak intensity) and different tempral variabilities could be distinctly different in the same basin (Reaney et al., 2007,

Moody et al., 2013). Results from (Julien and Moglen, 1990, Woolhiser et al., 1996, Corradini et al., 1998, Saghafian et al., 1995) examined sensitivity of peak flows and total runoffs to both CV_{Ks} and rainfall intensity and found them directly dependents on the magnitude of rainfall events. In (Wainwright and Parsons, 2002), runoff depth was significantly underpredicted in overland flow simulations using mean rainfall intensities. Scale dependence of overland flow was captured in the same model by accounting for temporal variations of rainfall intensity, even in the absence of CV_{Ks}.

Fire may impact runoff scaling effects by altering spatial variability of soil-surface features such soil property alterations (Moody et al., 2013), fire-induced water repellency (Sheridan et al., 2007, Doerr et al., 2009), and macropore infiltration (Nyman et al., 2010). Alterations in soil-surface factors may last several years, depending on the degree of burn severity and the capacity of the burnt forest ecosystem to recover (Neary et al., 2005, Shakesby and Doerr, 2006, Sheridan et al., 2007). Considerable scaling effects have been observed at the study site during the first- and second year following fire (Chapter 3). Similarly, Sheridan et al., 2014 measured scaling behaviours for two consecutive years following fire at plot-scale study in NE Victoria, Australia.

Physical process-based models incorporate CV_{Ks}, runon-runoff, and rainfall temporal variabilities in rainfall-runoff simulations at hillslope scale. These models are built based on classical infiltration theories coupled with overland flow hydraulics, and run at high temporal resolutions (Sitterson et al., 2017). This chapter investigates whether overland flow scale dependence on a burnt dry forest can be explained by a process-based rainfall-runoff model coupling temporal rainfall variations at minute timescales with detailed overland flow, infiltration and runon processes. The objectives addressed in this chapter were:

a) Modelling plot-scale runoff on a burnt dry hillslope under post-fire surface condition with extremely water repellent soil
b) Comparing scaling effects obtained from simulations to measurements
c) Testing the impact of spatial variability of saturated hydraulic conductivity (CV_{Ks}) on model performance and scaling effects

5.2 Method

The event-based physically-oriented rainfall-runoff model, KINEROS2 (Woolhiser et al., 1996) was used to simulate infiltration excess overland dynamics. Due to strong water repellency, shallow soil profile, and the absence of base flow in the study area, only infiltration-excess flow, which is the dominant flow type in dry forest (Moody et al., 2013), was considered. Four sets of rainfall-runoff simulations were developed in this study:

First, a primary rainfall-runoff model was calibrated to simulate runoff from 8 m plots for forty-one events that occurred during the second year following fire. The rainfall-runoff simulations for the events were calibrated with the help of observed data collected from 8 m plots. Events with calibration NSE > 0.5 were then selected.

Second, the calibrated parameters obtained from simulations of 8 m plots were used to model runoff from 0.5, 4, 12, and 16 m plots. Simulated scaling effects were compared with observations.

Third, a sensitivity analysis was conducted to study the impact of spatial variability (Coefficient of Variation, *CV*) of soil hydraulic conductivity (K_s) on the model performance and simulated scaling effects by systematic increase of this factor from zero to 0.5, 1 and 2 in the simulations, while the remaining soil and surface parameters were kept as measured or calibrated.

Rainfall-runoff data and soil and surface measurements used in the simulations collected during the first and second year on a dry eucalyptus hillslope, southeast Australia that was burned by bushfire 2013. Forty-one rainfall-runoff events were measure using multi-length plots during the second year (2014-2015) following fire. Instrumentation of rainfall-runoff plots, data collection, and event selection were explained in Chapter 3.

5.2.1 KINEROS2

KINEROS was originally developed by the USDA Agricultural Research Service (ARS) in the late 1960s and has been further developed over the last four decades for hydrological modelling in small (<100 km^2) arid and semi-arid (Al-Qurashi et al., 2008) catchments. It has also been used to model surface runoff response in burned forests (Canfield et al., 2005, McLin et al., 2001, Chen et al., 2016a, Langhans et al., 2016, Chen et al., 2013). Currently KINEROS2 is part of the Automated Geospatial Watershed

Assessment (AGWA) tool, an application for watershed hydrological analysis using readily available spatial data sets in ArcGIS (Goodrich et al., 2012).

Contributing areas in KINEROS2 are modelled using a cascade form of rectangular planes representing hillslopes feeding straight channels. Runoff is calculated by starting at the top of the slope and then moving to each subsequent plane or channel using 1-D kinematic wave equations. Parameters can vary between planes and channel lines but are homogeneous for each plane and channel. An approach has been developed to represent the plane scale effect of sub-plane scale spatial variability of soil hydraulic conductivity (K_s). In this study, only the planar slope units are used, and each plot is represented by a single plane.

Infiltration characteristics, slope length and gradient, depression storage and micro-topography, hydraulic resistance, and rainfall intensity are factors controlling runoff responses in KINEROS2. Either Manning hydraulic resistance or Chezy law may be used for roughness relationships. A general one-layer model is used for infiltrability, f_c, as a function of infiltrated depth, I, is (Parlange et al., 1978).

$$\text{Eq 5.1} \qquad f_c = K_s[1 + \frac{\alpha}{exp(\frac{\alpha I}{\beta})-1})]$$

where B is a parameter representing the effects of net capillary drive, α represents the soil type with near 0 for a sand, for the Green-Ampt relation; and near 1 for a well-mixed loam, in for the Smith-Parlange infiltration equation.

The primary soil infiltration model in KINEROS was set based on infiltration equations of (Smith and Parlange, 1978), modified later by (Parlange et al., 1981, Parlange et al., 1982) with four basic parameters representing soil infiltration properties: effective saturated hydraulic conductivity (*Ks*); effective net capillary drive (*G*) derived from soil texture class; initial soil moisture, and soil porosity (Φ). Another parameter; the pore size distribution index (λ) was added later to the next version (KINEROS2) from the statistical study of soils texture by (Rawls et al., 1982), affecting water retention calculations (Woolhiser et al., 1990).

An extension was added to the infiltration model by (Smith et al., 1993) and modified by (Corradini et al., 1994, Corradini et al., 1997) to account for arbitrary patterns of a given rainfall event by using an analytical solution considering pre and post-hiatus infiltration

while accounting for a continuous infiltration process in both pre-ponding and post-ponding conditions.

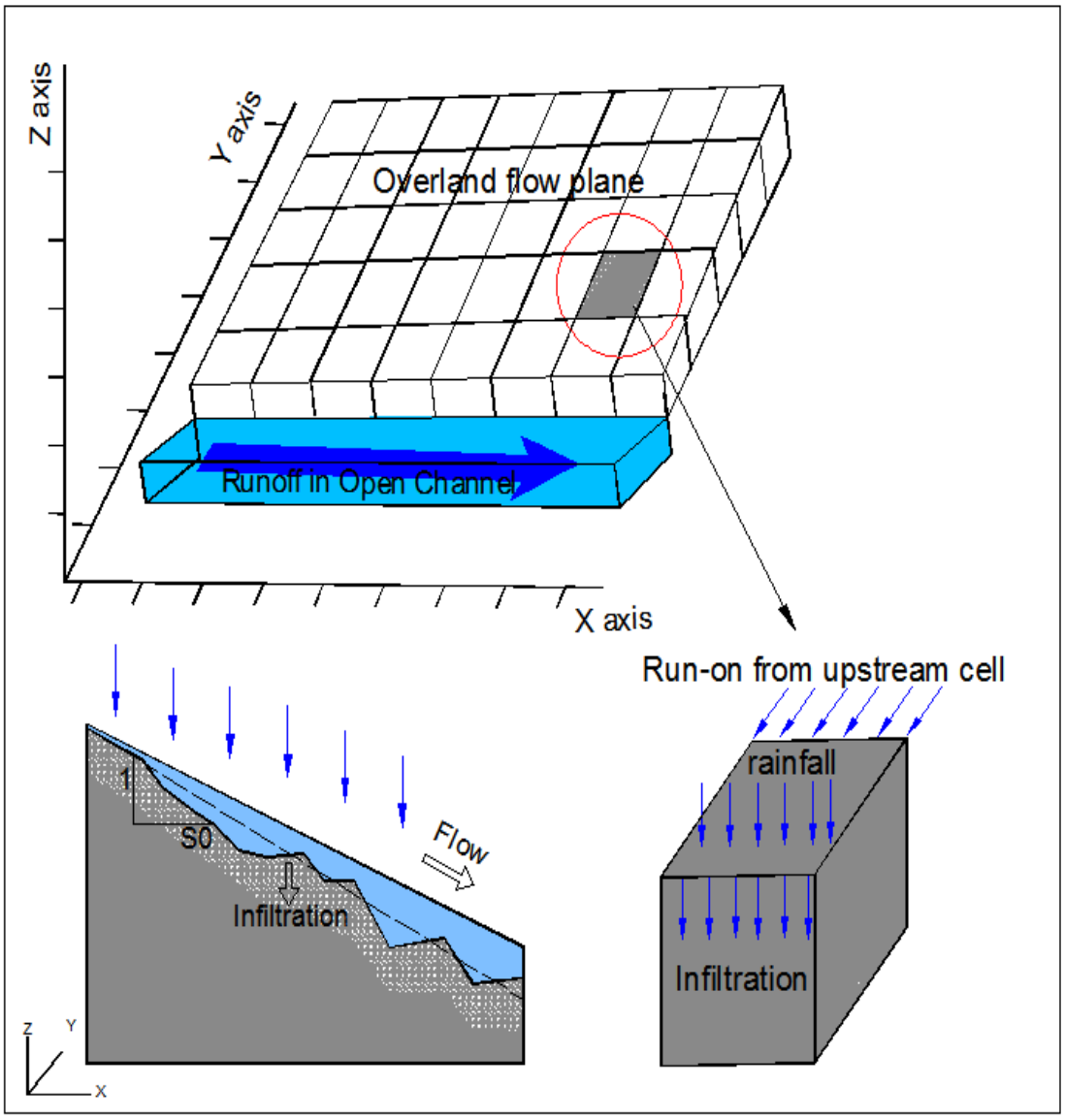

Figure 5. 1 Schematic of plane and channels in KINEROS2

5.2.2 Soil Physical Properties

Detail descriptions of vegetation type, fire severity, climate of the study area and soil hydraulic property measurements were given in Chapter 2. Both field-based and laboratory measurement of soil properties and water repellency were carried out at the study site during the first and second year after fire. The first year (2013-2014) measurements were conducted by (Van der Sant et al., 2018) to study post-fire hydro-geomorphic responses in relation to aridity index. Field measurement of soil moisture, water repellency and blue dye experiment were repeated in one occasion in the second year (2014-2015). Table 5.1 is a summary of soil hydraulic properties measurements that being used as input data in the simulations.

Table 5.1 Study site soil properties

Soil property	**Measurement Method**	**Result**
Saturated hydraulic conductivity (Ks)	Tension infiltrometer	39.5 mm/h (SD 30.8)
	ponded infiltrometer	74.1 mm/h (SD 40.4, n: 2)
Soil texture and particle size (%)	Sieving and particle size analyzer	15% Clay, 44% Silt, 41%Sand Course fraction (>2 mm) 45%
	Texture triangle class	Silty loam
Porosity	Tension table	38.5% (SD 0.04, n: 3) corrected for gravel (porosity of <2mm fraction)
Soil Water Content	Oven drying	Average 5.1% (SD 3.8, n: 52)
Potential Soil Water Repellency	Critical Surface Tension	Average Air-dry CST 60.3 mN/m2 (SD13.0, n: 24)
Bulk density (g/cm3)	Total	1.19 (std 0.08, n: 9)
	Fine fraction (<2 mm) (gravel corrected)	0.86(std 0.46, n: 9)

**SD: Standard deviation, CST: Critical Surface Tension (mN/m2)*

5.2.3 Model Setup for Post-fire Conditions

Observation after severe wildfire 2013 showed that only skeleton of trees remained in the study site. Frequent site visits during the first- and second year following fire reported insignificant vegetation recovery; <5% canopy recovery and <10% surface revegetation at the end of the second year. Therefore, no interception storage was considered for canopies and shrub in the rainfall-runoff simulations. Moreover, rain gauges were installed at 40 centimetres above the ground surface, collecting throughfall data which also justifies the exclusion of the upper storey and under storey interceptions in the model. Details of rain gauges' instrumentation and data collections were explained in Chapter 3.

Distinctly varied hydraulic characteristics of burned residue on top and water repellent mineral soil underneath resulted in a sudden shift in the rate of infiltration at a depth of around 20 mm in the soil profile in the first and second year. Burn debris were more woody debris than ash remaining at the site for the entire study period. For this reason, they were considered immobile layer for the entire period of study. For this reason, 20 mm abstraction was considered for surface interception compartment for burned woody layer before infiltration process taking place in water repellent soil underneath (Figure 5.2). Details of soil hydraulic properties were explained in Chapter 2.

To model soil infiltration process in water repellent dry soil, traditional infiltration theories require adjustment due to different patterns of vertical water movement comparing to non-repellent soils. For example, the wetting front assumption of uniform distributed wet soil above dry soil in Green–Ampt infiltration model is rejected in water repellent soil due to preferential water movement through soil depth.

To adjust infiltration model with the fire-induced water repellent soil in the study area, a two-layer system was applied; strongly water repellent soil with low hydraulic conductivity for the eight cm top layer. This is the depth of water repellent soil measured at the field by 2 M ethanol test (McDonald et al., 1998) and underneath silt loamy soil with average hydraulic conductivity of 80 mm/h based on laboratory measurements of soil sample collected from the study site.

Hydrophobicity promotes lateral preferential flow at the interface between water repellent soil layer and the mineral layer beneath (Stoof et al., 2014a, Leelamanie and Karube, 2009, Gerke et al., 2015). Lateral flow between these two layers was not accounted for in the simulations which may result into the model uncertainties.

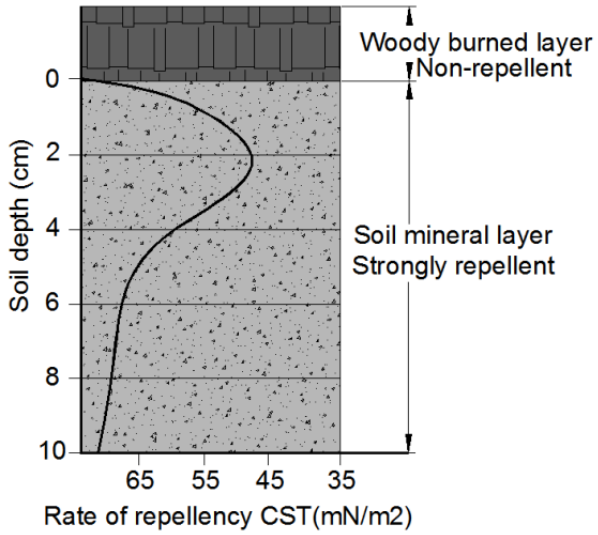

Figure 5.2 Cross-section profile illustration of the severely burned soil in the study site

Field observation showed slow recovery and insignificant surface vegetation change during the study period. Therefore, a single Manning's value was appointed as a valid effective hydraulic roughness for the whole study period. Only soil particle size; as resistance factor on the flow bed (D_{50}, *and* D_{90}), was accounted for primary estimation of overland flow effective friction factor (Manning's n). Other factors contributing to boundary source roughness (e.g. relative roughness), form roughness (surface irregularities in cross-section, and flow obstruction) and sediment load roughness were not included in primary value of effective friction factor.

Based on field observation, average particle size of debris, gravels and boulders were approximately $d_{50\%}$=50 mm, $d_{90\%}$=30 mm. Three empirical equations (Strickler, 1923, Maynord, 1991, Wong and Parker, 2006) were used to estimate hydraulic roughness based on particle size. An average value of 0.085 was used for Manning' n as an effective friction factor in for the initial parameter value.

Investigator	**Equations**	**values**
Strickler (1923)	$n = 0.0474\, d_{50}^{1/6}$	0.091
Maynord (1991)	$n = 0.0439\, d_{90}^{1/6}$	0.0812
Wong and Parker (2006)	$n = 0.0431\, d_{90}^{1/6}$	0.08

Other soil-surface parameters were taken either from field and laboratory measurements from previous study (Van der Sant et al., 2018) at the study site as presented in Table 5.2. These parameters were used in primary rainfall-runoff model set up and one simulation operated per each event for plot 8 m.

Table 5.2 Kineros2 parameters and values for initial modelling set-up

Parameter	Symbol	Units	Range	Source
Saturated hydraulic conductivity	Ks	mm/h	2	Extremely water repellence soil
Effective net capillary drive	G	mm	20	G for Silt loam soil from Kineros2 table
Variation of K_s	CV	--	0	Assuming hydraulic conductivity did not change during the event
Soil layer thickness	Th	mm	80	Field observation
Initial Saturation	sat	--	0.1-0.03	Oven dried analysis for GWC (3%-10%)
Pore size distribution index (DIST)	λ		0.15	Laboratory measurement (varied in range of 0.15-0.65)
Porosity	θ	--	0.35	Laboratory analysis (varied in range of 0.25-0.35)
Rock	Ro		0	Laboratory measurement (<0.46%)
Slope factor	sl	degree	27	Field observation
Interception depth	i		1	Water storage capacity in burned layer
Canopy coverage	p		1	100% coverage of woody burned layer
Manning's coefficient	n	$sm^{-1/3}$	0.085	Hydraulic roughness based on particle size
Relief (microtopography)	re	mm	3	Field observation
Relief spacing	rs	m	0.05	Field observation

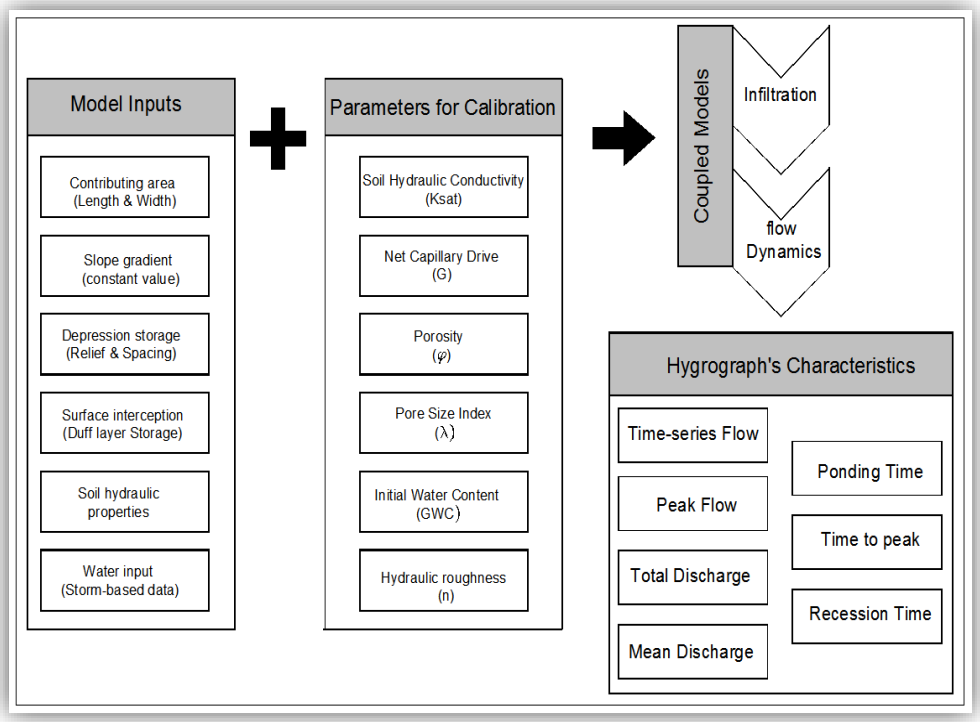

Figure 5.3 Rainfall-runoff Model inputs and outputs

5.3 Calibration

The focus in the calibration procedure was to obtain optimum values for parameters representing post-fire surface and soil infiltration during recovery period after fire. To reduce errors associated with over-parameterization, parameters for calibration were categorized in two groups and an automated stepwise calibration was conducted for each group separately. Variable soil hydraulic properties were selected for the events to represent variation between events in soil water repellency.

First, parameters that presumed to have a highly influential role in soil infiltration and overland flow including saturated hydraulic conductivity (*Ks*), effective net capillary drive (*G*), and hydraulic roughness (Manning's n) were calibrated together. Because the surface condition at the study site did not change markedly during the study period, a constant hydraulic roughness was used for the whole simulation period. Other parameters varied between events. That is K_s and *G* varied between events while Manning's n was calibrated for the whole study period. An exhaustive grid search was used with simulated hydrographs for all parameter combinations compared against observed hydrographs. Optimum values of these parameters were assigned for the next round of calibration.

The second round of calibration considered a new set of soil hydraulic properties consisting of porosity (ϕ) in the range 0.25-0.55 based on laboratory analysis, and pore size distribution index (λ) in the range 0.15-0.85 based on soil texture class in (Corradini et al., 1994). There were no soil moisture sensors co-located with the plots to measure pre-storm soil moisture. Initial water content for each event was approximated within upper and lower limits of gravimetric water content (*GWC*) measurements (3%-15%). The same calibration method and objective function were used for both calibration rounds.

Table 5.3 Soil and surface parameters for calibrations

no.	Calibration	Parameter	Symbol	Range value	Unit	Stepwise	Status
1	First round	Hydraulic conductivity	K_s	1-20	mm/h	1	variable
2		effective net capillary drive	G	0-20	mm	1	variable
3		Manning's hydraulic roughness	n	0.01-0.9	$sm^{-1/3}$	0.01	constant
4	Second round	Porosity	ϕ	0.25-0.55	%	0.01	variable
5		pore size distribution index	λ	0.15-0.85	--	0.1	variable
6		gravimetric water content	GWC	15-3	%	1	variable

Model performance quantified using the Nash-Sutcliffe (1970) coefficient of efficiency (NSE) (Goodrich et al., 2012, Krause et al., 2005) between simulated and observed runoff at three minute time steps.

$$\text{Eq 5.2} \qquad \text{NSE} = 1 - \frac{\sum(\text{Observed}-\text{Simulated})^2}{\sum(\text{Observed}-\overline{\text{Obsereved}})^2}$$

Additional statistical metrics were calculated from the simulated and observed hydrographs, as follows:

$$\text{Eq 5.3} \qquad R^2 = \left(\frac{\sum_{i=1}^{n}(\text{obs}-\overline{\text{obs}})(\text{sim}-\overline{\text{sim}})}{n\sqrt{\sum(\text{obs}-\overline{\text{obs}})^2}\sqrt{\sum(\text{sim}-\overline{\text{sim}})^2}}\right)^2$$

$$\text{Eq 5.4} \qquad \text{Volume error (Res)} = \frac{\text{Total runoff depth}_{\text{Obs}} - \text{Total runoff depth}_{\text{Sim}}}{\text{Total runoff depth}_{\text{Obs}}} \text{x}100$$

$$\text{Eq 5.5} \qquad \text{Peak volume error} = \frac{\text{Peak flow}_{\text{Obs}} - \text{Peak flow}_{\text{Sim}}}{\text{Peak flow}_{\text{Obs}}} \times 100$$

5.2.4 Scaling Simulations

Calibrated parameters from 8 m plots were applied to plots with lengths of 0.5, 4, 12 and 16 m. One overland flow simulation was conducted per each event for each of these plot lengths. Observed and simulated total runoff depth (mm) and runoff ratio (%) were plotted against the associated plot length (m) to examine how the scaling effects from simulated hydrographs compared with observations. The slope of the regression lines for these plots characterises the magnitude of changes in runoff depth and runoff ratio with plot length, standing for runoff depth and runoff ratio scaling coefficients (SC_1 *and* SC_2)

respectively. The scaling coefficients (SC_1 *and* SC_2) derived from down- and up-scaled runoffs represented scaling effects from models and compared to observations.

5.2.5 Contribution of Hydraulic Conductivity CV on Scaling

The impact of spatial variability of hydraulic conductivity (CV_{Ks}) on scaling behaviours was investigated by assigning a range of CVs (0.5, 1, and 2) for hydraulic conductivity (K_s) and conducting one runoff simulation per each event for all plot length (0.5, 4, 8, 12 and 16 m). The scaling effects from simulated hydrographs with different CV_{Ks} were plotted against observations. Both runoff depth and runoff ratio scaling coefficients (SC_1 and SC_2) were calculated from simulations with parameterized CV_{Ks} and compared to observations.

5.3 Results

5.3.1 Model Calibration

Calibration outcome showed that simulated hydrographs with higher roughness values obtain lower errors in peak and mean value. From the range of calibrated Manning's n of the accepted runs for all events, average value of 0.65 was chosen for Manning's n for the whole study period (Figure 5.4). The calibrated value of hydraulic roughness is eight times higher than the initial value. This was expected because only bed particle size was accounted in the primary model, and other resistance factors were excluded from the hydraulic roughness estimation.

The weak point of considering Manning's coefficient for overland flow hydraulic calculation is the assumption of being independent from flow hydraulics and Reynolds number in the empirical equation. However, the coefficient (Manning's n) has been found to be very sensitive to flow depth in relation to bed particle size in shallow overland flows; increasing dramatically when inundation ratio (the inverse of relative roughness) was below ten and not applicable if the ratio was below three (Smith et al., 2007).

For this reason, the whole calibration procedure was repeated after replacing Manning's n with Chezy friction coefficient (C) with a range of 0.2-22.5; in which slope factor (S), hydraulic radius (R, flow depth), and mean velocity (V) are taken into account ($\overline{V} = C\sqrt{RS}$). Calibrations with Chezy (C) resistance factor followed the same trends of those were operated by Manning's n and the best simulation performances were allocated to 0.2<C<0.6 that is almost equivalent to the calibrated range of Manning's n ($C = \frac{1}{n}R^{\frac{1}{6}}$).

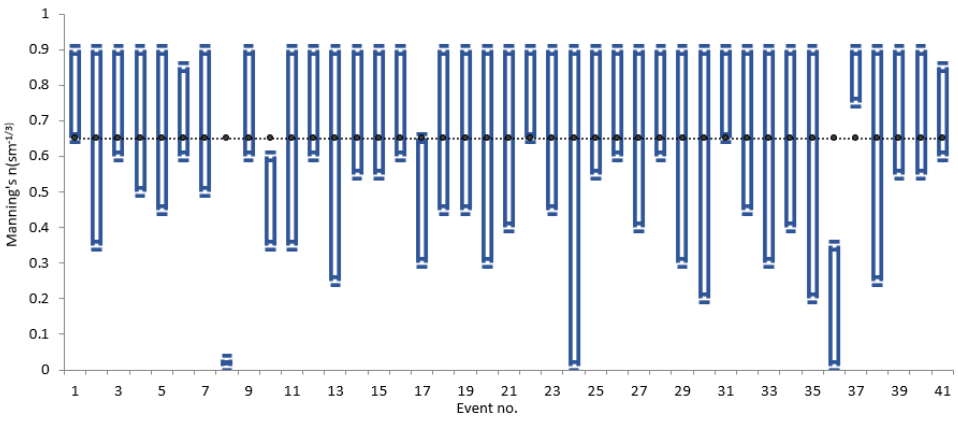

Figure 5.4 Value range of calibrated Manning's n in blue hanged bars and optimum value (n=0.65) in dotted black line

Variant values were calibrated for saturated hydraulic conductivity (K_s) and effective net capillary drive (G) for the individual events. Similar parameter values were found for K_s and G compared with previous modelling studies conducted in arid and semi-arid forest with hydrophobic soil (Langhans et al., 2016, Chen et al., 2013).

A combination of single Manning's coefficient (n=0.65) for the whole study period and varied K_s and G from event to event were assembled for the second round of calibration where porosity, pore index and initial water content were added to calibration. Soil water content (*GWC*) values varied from event to event, however appointed values of this parameter for each event were constrained within the range of measured *GWC* values (3 to 15%) measured during the first and second year. The entire range of considered values for both soil porosity and distribution index (*DIS*) were found to be adequate in some of the events and changes in these two parameters only caused slight alterations in simulated hydrographs for most of the events (90%).

The optimum values of parameters in the calibration were chosen by accepting the best fit simulation with the highest *NSE* as summarized in Table 5.6. The majority of events (~70%) obtain R^2> 50% (Figure 5.5 a) and Nash-Sutcliffe (*NSE*) larger than zero indicating model predictions are more accurate than the observed mean (Figure 5.5b). Total runoff depth of the calibrated hydrographs was underestimated for the majority of the events (90%, Figure 5.5c) while peak flow was overestimated for almost 70% of the simulated hydrographs (Figure 5.5d). Considering all events together, high correlations (R^2> 90%) were obtained between simulated and observed runoff depth and peakflow (Figure 5.5e, f).

Optimum values of the calibrated parameters and model performance of the accepted hydrographs were summarized in Table 5.4. Simulated hydrographs derived from the optimum values of the six parameters (hydraulic conductivity, effective net capillary porosity, roughness, pore index and water content) were plotted against observation as shown in Figure 5.6. Only events with high model performance (NSE> 0.5) were considered for analysing scaling effects and CV_{Ks} impact on scaling. Weak model performance was obtained for small events with total runoff depth < 4 mm, marked with red X in Figure 5.6.

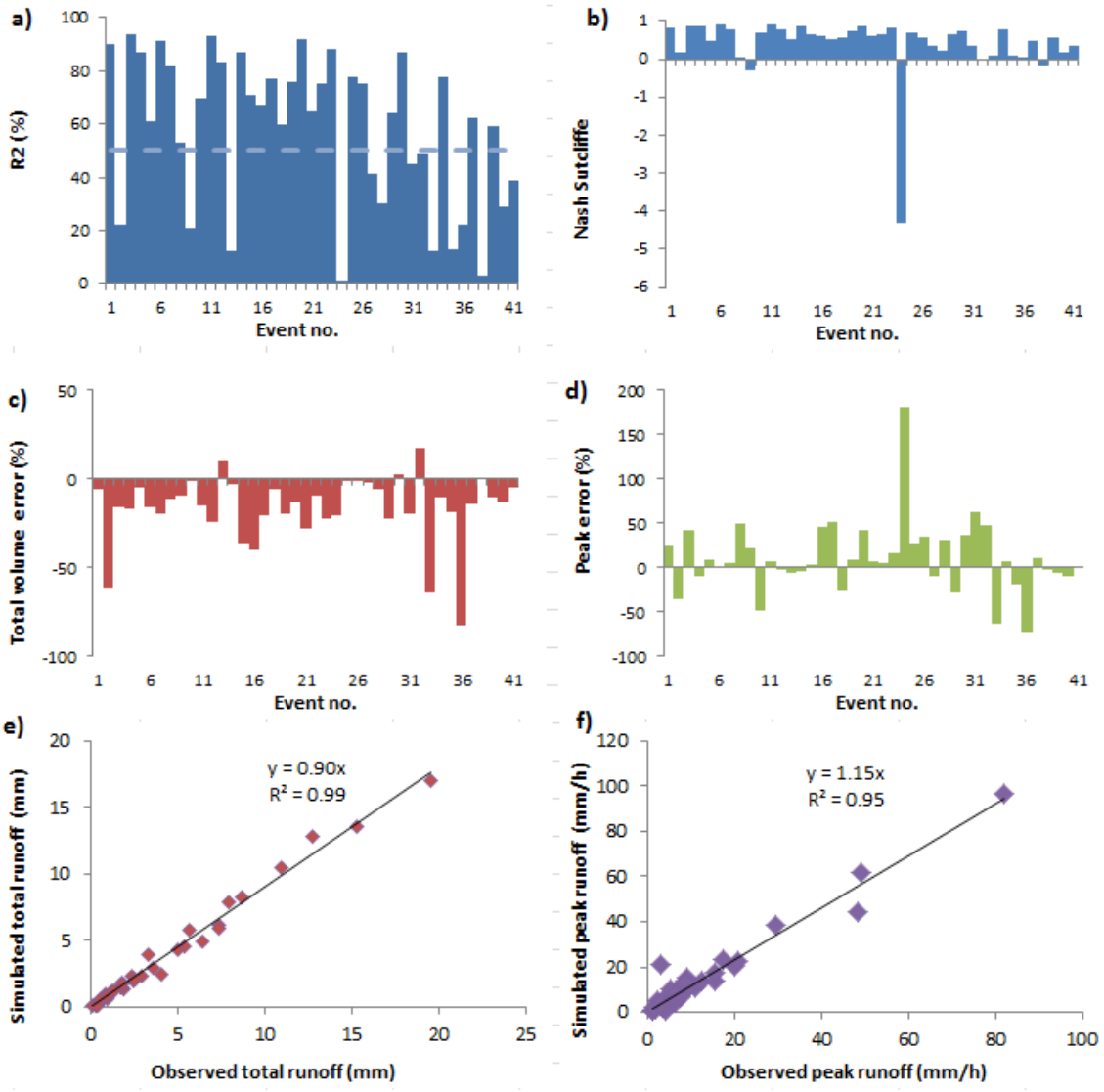

Figure 5.5 Model performance indicators: a) Coefficient of determination between simulated events and observations (R^2), b) Nash–Sutcliffe model efficiency coefficients (NSE), c) Volume errors (%), d) Peak errors (%), e) Simulated total runoffs depth vs. observations f) Simulated peak flow vs. observed peak flow

Table 5.4 Optimum values of calibrated parameters and model efficiencies

Event	Ks (mm/h)	G	DIS	Porosity	Soil Moisture (GWC)	Total runoff depth(mm)		Runoff ratio (%)		NSE	R^2	Total error	Peak error
						Observation	Simulation	Observation	Simulation				
												%	
1	2	2	0.65	0.25	9	8.75	8.28	43.51	41.17	0.80	0.9	5.38	25.68
2	1	4	0.15	0.30	9	0.30	0.12	13.45	5.38	0.19*	0.22	61.07	-34.94
3	7	5	0.75	0.45	9	7.38	6.19	41.07	34.45	0.88	0.94	16.14	41.85
4	3	6	0.4	0.30	8	1.84	1.53	22.12	18.39	0.86	0.87	16.01	-8.80
5	3	1	0.2	0.30	8	10.99	10.44	35.33	33.56	0.5	0.61	5.06	9.33
6	5	8	0.35	0.45	8	5.39	4.54	31.87	26.85	0.91	0.91	15.74	1.51
7	2	8	0.75	0.50	7	3.61	2.90	39.50	31.73	0.78	0.82	19.76	5.14
8	2	9	0.80	0.55	7	15.28	13.62	31.34	27.93	0.5	0.68	10.86	49.12
9	2	1	0.2	0.45	7	0.71	0.64	14.98	13.50	-0.32*	0.21	9.65	21.77
10	1	4	0.75	0.40	6	0.51	0.50	22.17	21.74	0.70	0.7	0.37	-48.49
11	2	7	0.75	0.50	6	5.00	4.27	30.41	25.97	0.90	0.93	14.52	6.42
12	4	3	0.75	0.20	6	0.58	0.44	14.22	10.78	0.80	0.83	23.73	-1.44
13	1	1	0.3	0.50	6	0.92	1.01	22.60	24.82	-0.24*	0.12	-9.76	-5.04
14	2	8	0.7	0.40	4	2.40	2.33	23.12	22.45	0.86	0.87	2.72	-4.83
15	3	8	0.75	0.50	4	0.96	0.61	16.96	10.78	0.63	0.71	36.15	3.62
16	2	10	0.8	0.50	3	4.06	2.42	26.55	15.83	0.63	0.67	39.55	45.16
17	3	6	0.75	0.50	3	7.40	5.91	34.32	27.41	0.51	0.77	20.13	51.13
18	1	8	0.75	0.40	4	0.71	0.65	14.73	13.49	0.60	0.6	6.11	-26.76
19	3	1	0.75	0.30	6	2.47	2.00	27.97	22.65	0.74	0.76	19.18	8.23
20	2	3	0.75	0.50	8	19.57	17.05	49.72	43.32	0.87	0.92	12.86	41.62
21	2	3	0.75	0.10	8	1.91	1.37	22.11	15.86	0.61	0.65	28.33	6.39
22	2	7	0.65	0.10	10	1.14	1.04	22.27	20.31	0.67	0.75	8.31	5.83
23	2	1	0.75	0.30	10	6.42	4.96	41.00	31.67	0.82	0.88	22.72	17.13
24	1	9	0.80	0.55	10	2.92	2.32	22.99	18.27	-4.30*	0.01	20.42	180.46
25	1	8	0.75	0.50	10	7.96	7.89	36.77	36.44	0.71	0.78	0.92	27.01
26	1	9	0.80	0.55	10	12.79	12.79	34.91	34.91	0.55	0.75	0.02	35.52
27	1	3	0.75	0.40	10	1.85	1.82	24.93	24.53	0.35*	0.41	1.88	-10.35
28	1	1	0.75	0.50	10	1.24	1.17	25.36	23.93	0.20*	0.3	5.58	31.68
29	1	1	0.75	0.10	10	0.73	0.57	30.29	23.65	0.63	0.64	21.94	-28.23
30	1	1	0.75	0.10	10	5.71	5.84	44.89	45.91	0.76	0.87	-2.66	36.15
31	1	1	0.7	0.10	10	2.57	2.05	34.73	27.70	0.35*	0.45	19.97	62.71
32	1	2	0.55	0.25	10	3.37	3.93	27.38	31.93	-0.01*	0.49	-17.13	47.39
33	1	1	0.75	0.10	10	0.45	0.16	20.27	7.21	0.07*	0.12	64.19	-63.84
34	2	2	0.75	0.50	10	0.64	0.57	16.45	14.65	0.77	0.78	11.02	7.34
35	2	1	0.75	0.30	10	0.11	0.09	5.42	4.43	0.08*	0.13	18.95	-18.94
36	1	1	0.75	0.10	10	0.41	0.07	29.08	4.96	0.05*	0.22	82.39	-72.30
37	1	2	0.75	0.45	10	1.74	1.50	35.80	30.86	0.48	0.62	13.75	10.81
38	1	1	0.75	0.50	10	0.56	0.56	18.30	18.30	-0.19*	0.03	-0.03	-2.45
39	1	6	0.6	0.35	10	0.96	0.86	18.86	16.90	0.58	0.59	10.28	-4.89
40	1	1	0.75	0.45	10	1.37	1.19	24.46	21.25	0.17*	0.29	12.76	-9.05
41	1	3	0.25	0.40	10	1.80	1.72	18.58	17.75	0.33*	0.39	4.53	0.30

* The closest fits were obtained by accepting runs with NSE smaller than 0.5

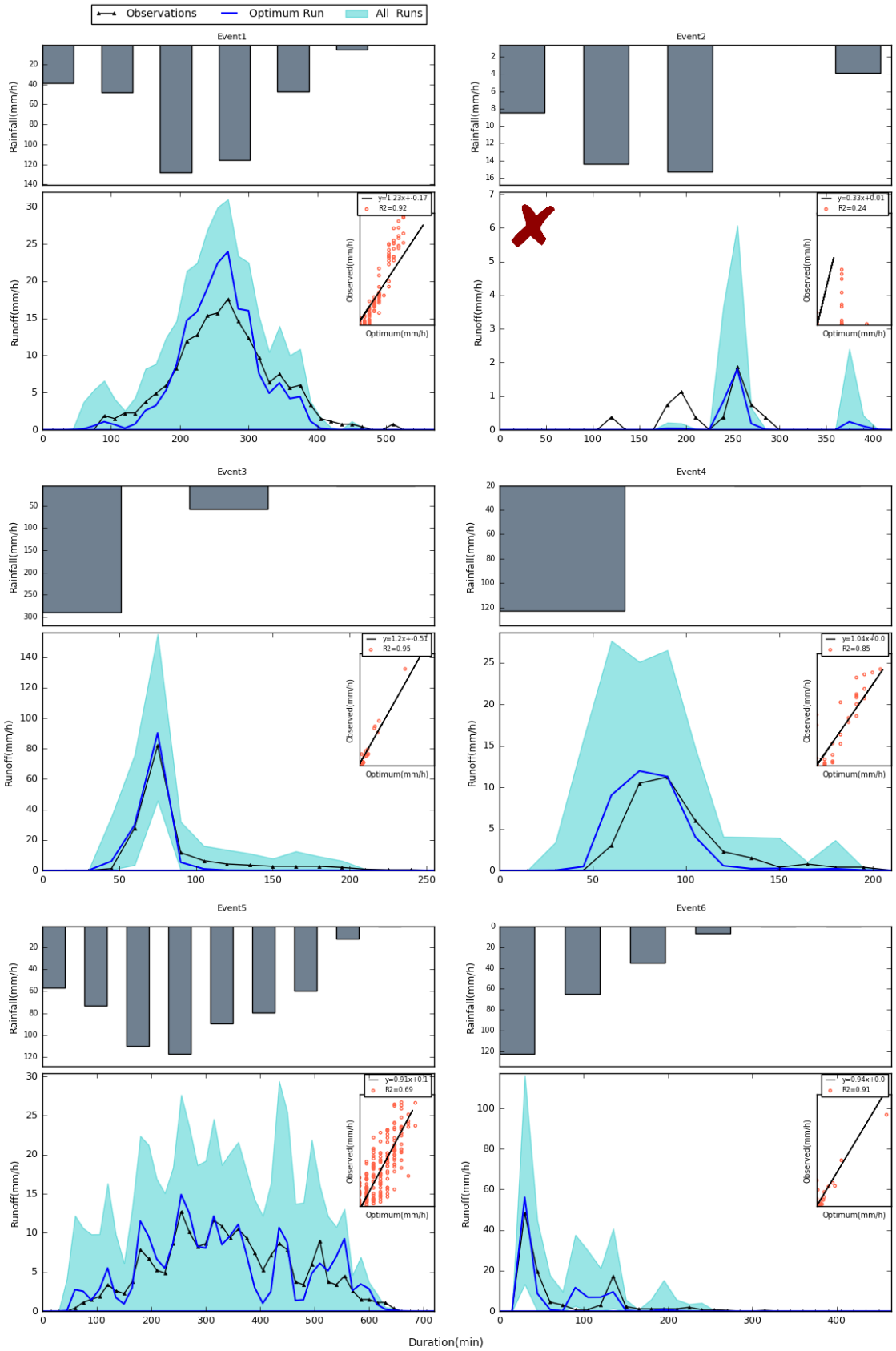

Figure 5.6 Hyetograph-hydrograph for events 1 to 6 presenting all simulations (cyan band), optimum run (blue line) and observation (black line). Events with weak model performance (NSE< 0.5) marked with red X.

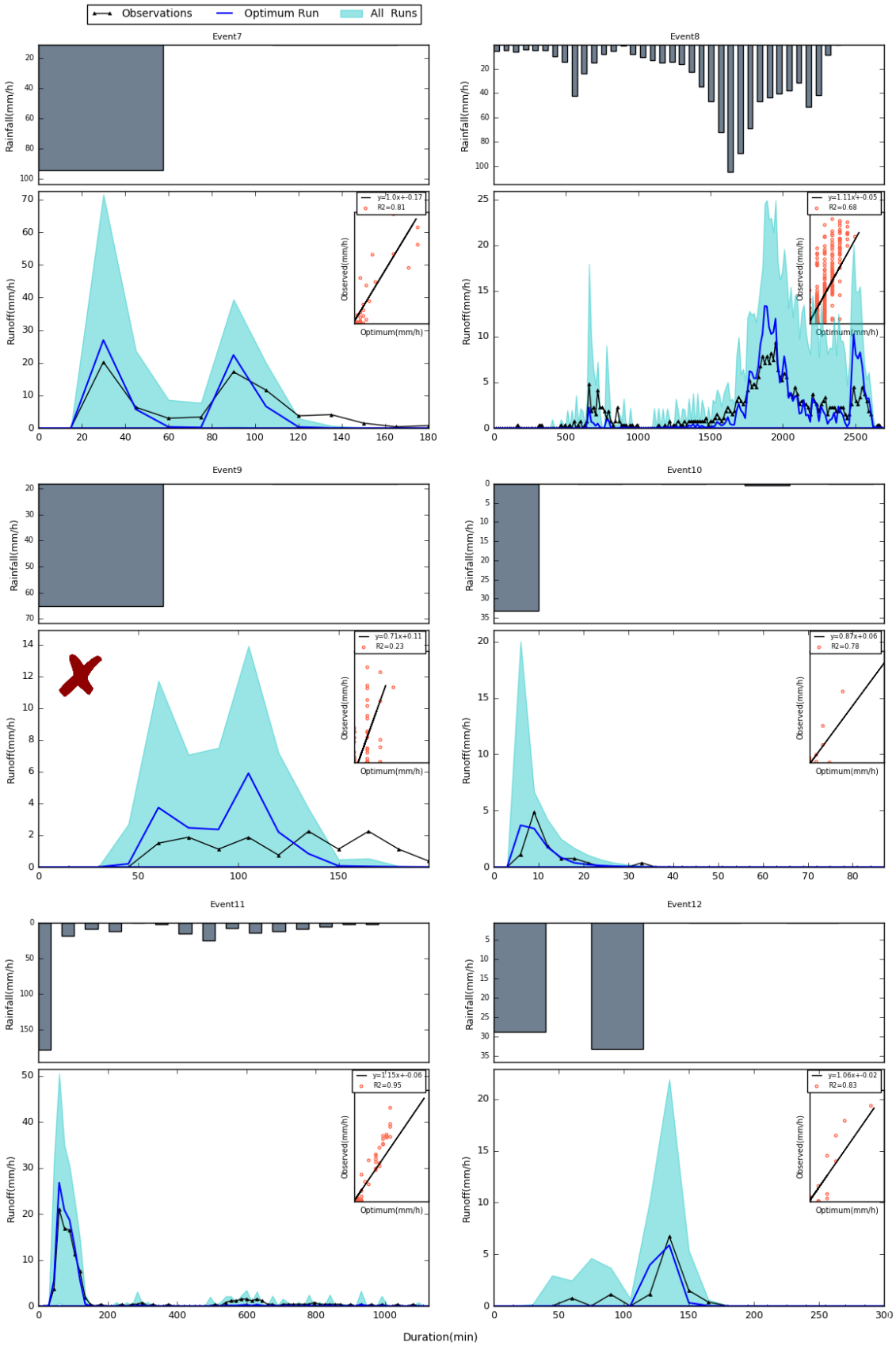

Figure 5.6 Hyetograph-hydrograph for events 7 to 12, presenting all simulations (cyan band), optimum run (blue line) and observation (black line). Events with weak model performance (NSE< 0.5) marked with red X.

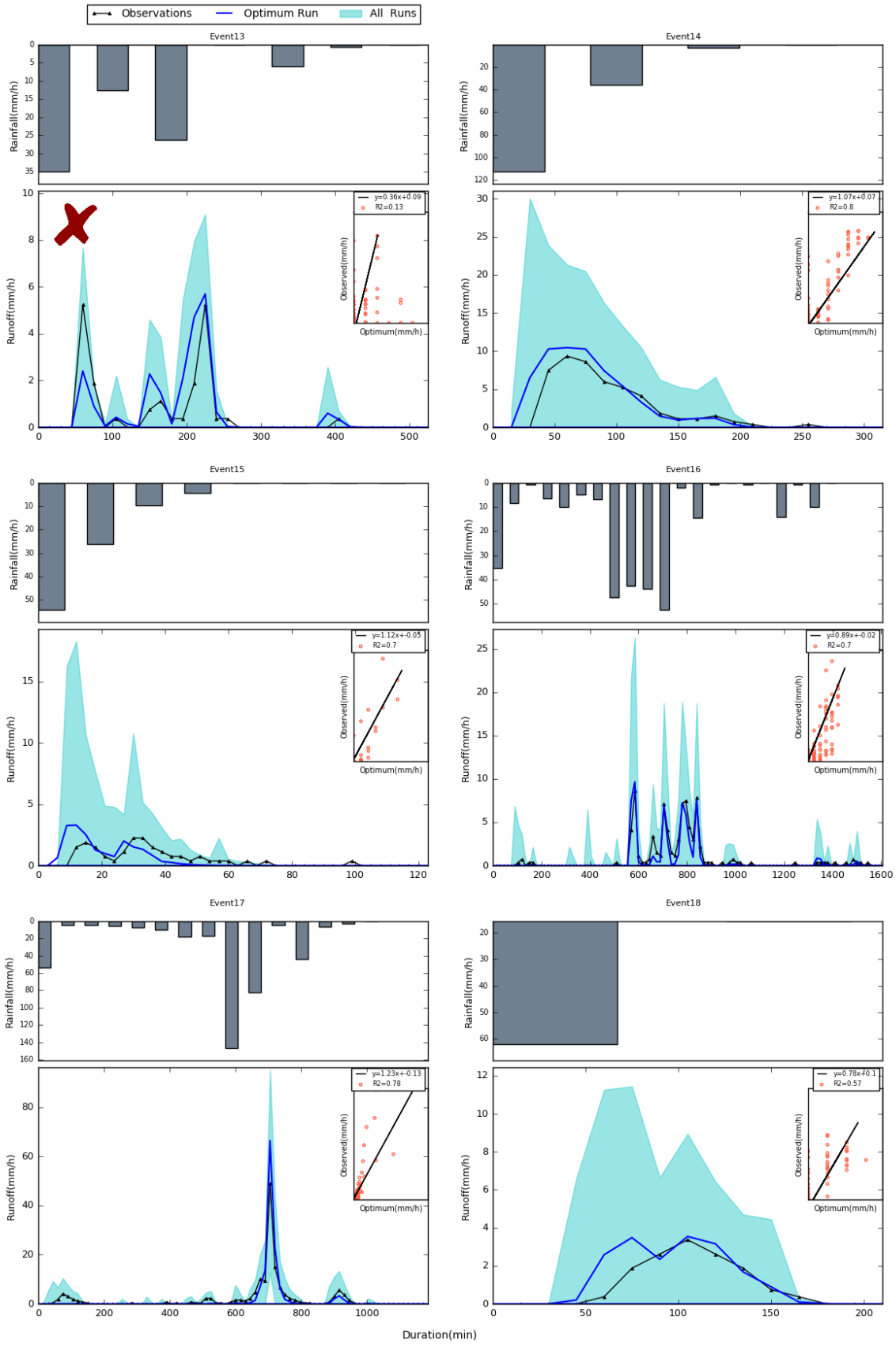

Figure 5.6 Hyetograph-hydrograph for events 13 to 18, presenting all simulations (cyan band), optimum run (blue line) and observation (black line). Events with weak model performance (NSE< 0.5) marked with red X.

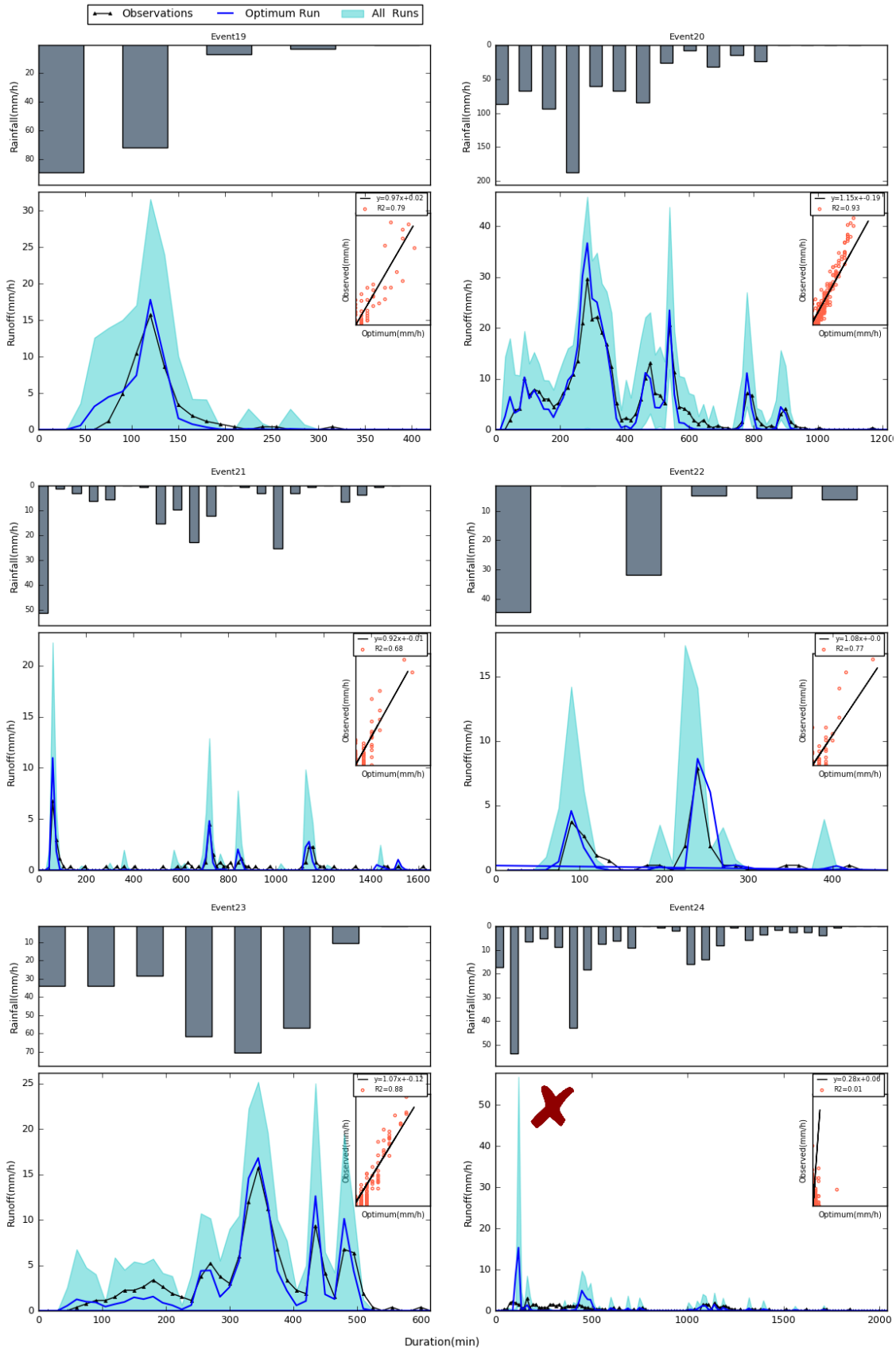

Figure 5.6 Hyetograph-hydrograph for events 19 to 24, presenting all simulations (cyan band), optimum run (blue line) and observation (black line). Events with weak model performance (NSE< 0.5) marked with red X.

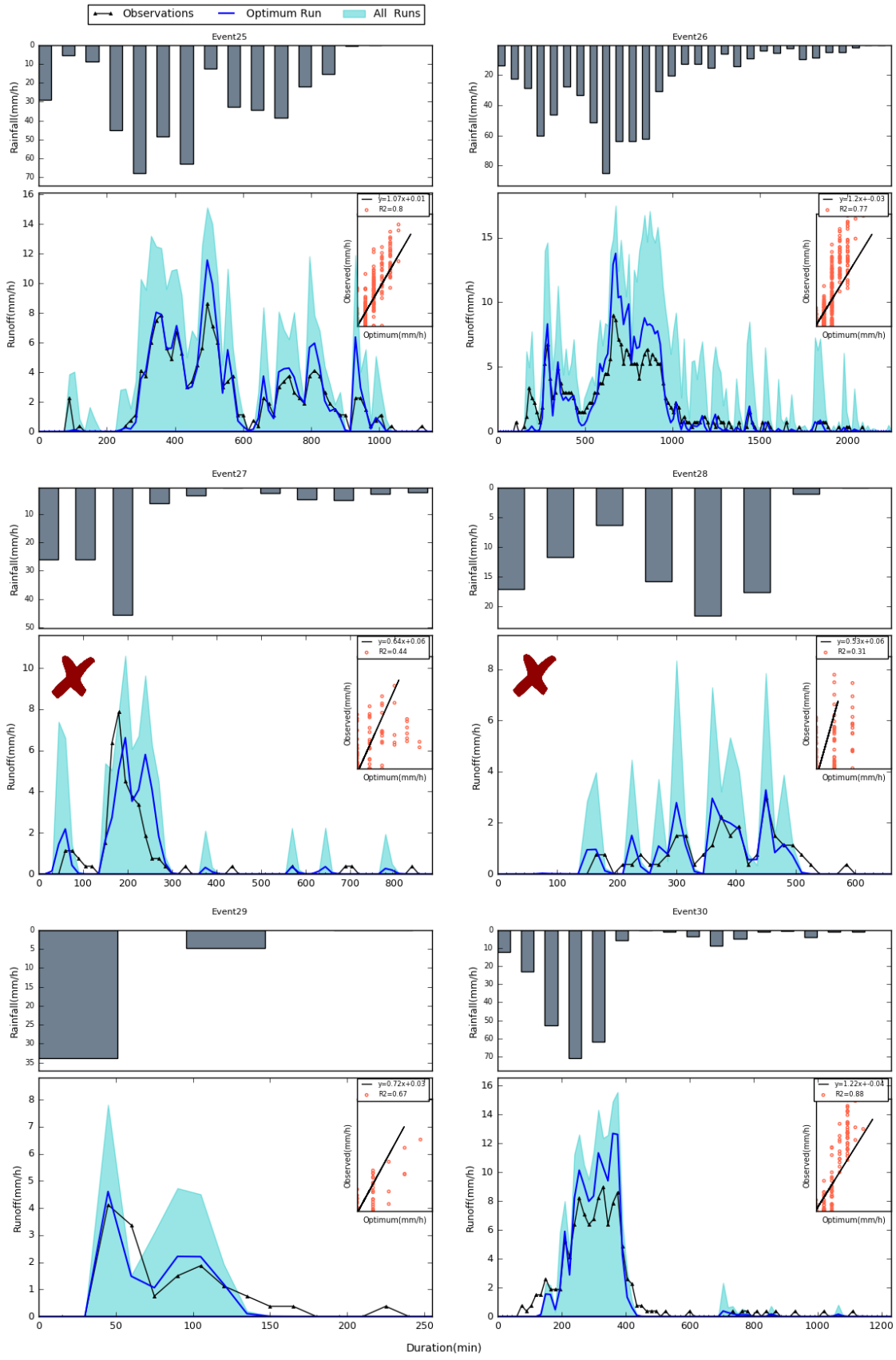

Figure 5.6 Hyetograph-hydrograph for events 25 to 30, presenting all simulations (cyan band), optimum run (blue line) and observation (black line). Events with weak model performance (NSE< 0.5) marked with red X.

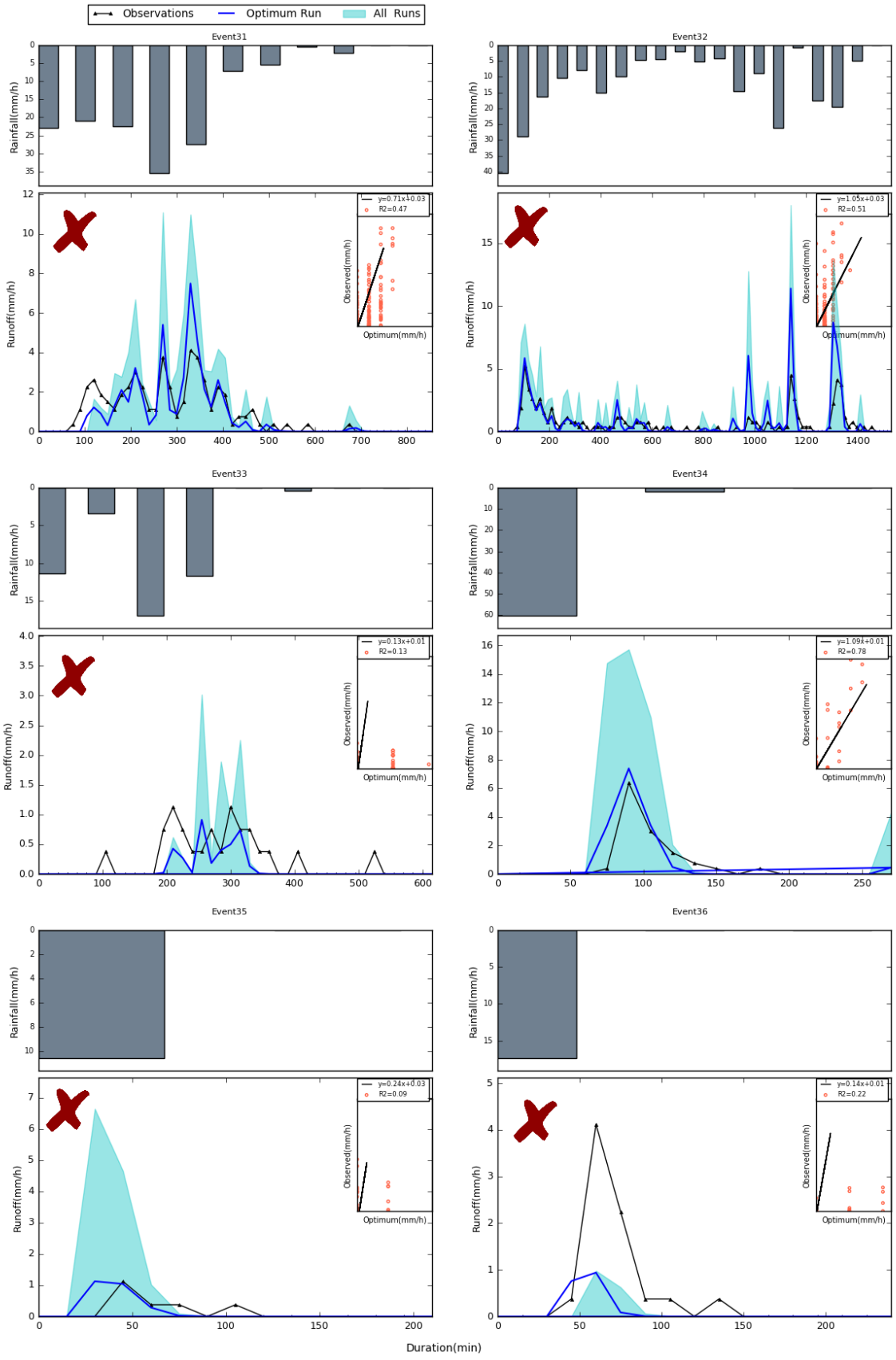

Figure 5.6 Hyetograph-hydrograph for events 31 to 36, presenting all simulations (cyan band), optimum run (blue line) and observation (black line). Events with weak model performance (NSE< 0.5) marked with red X.

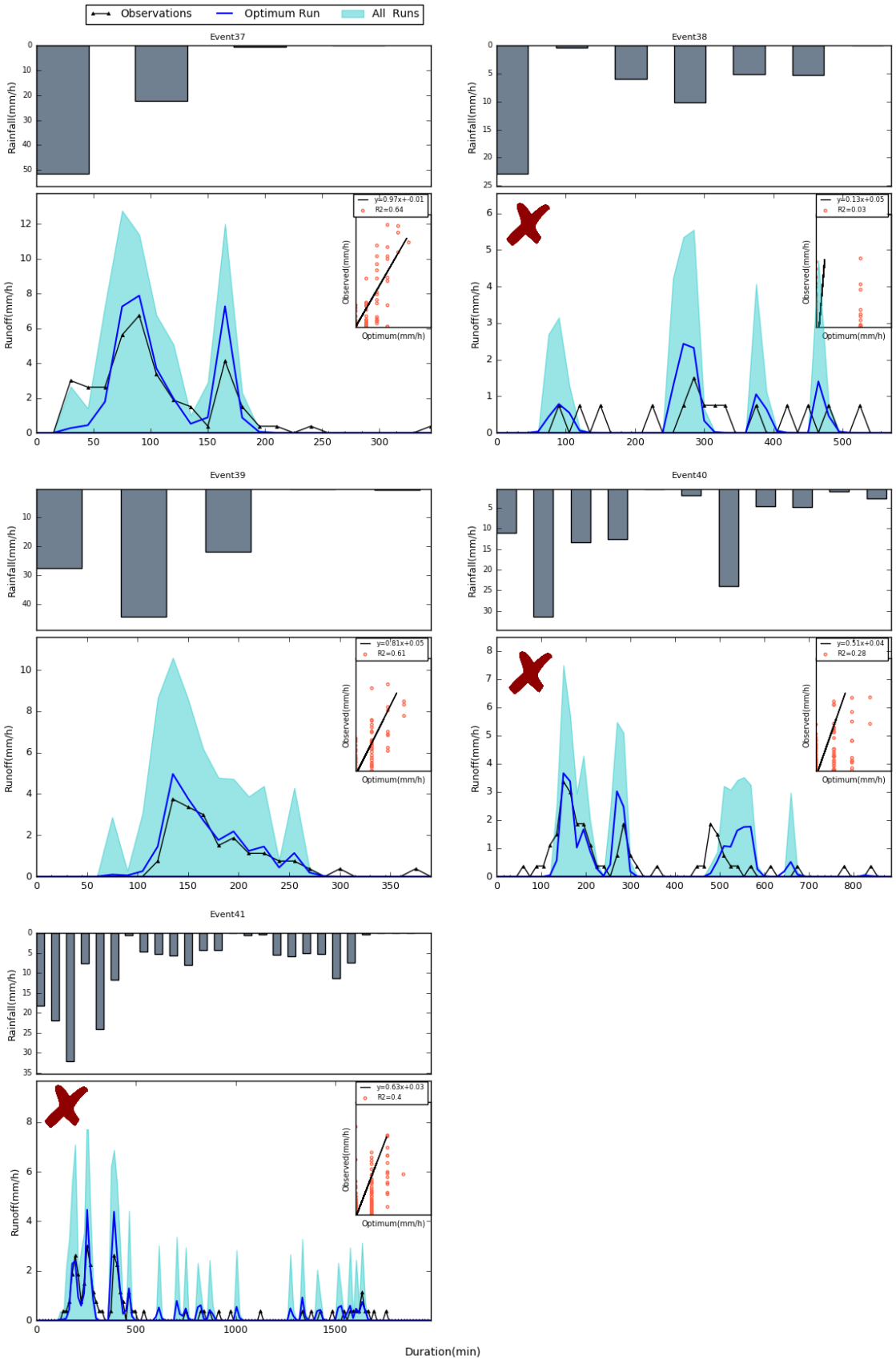

Figure 5.6 Hyetograph-hydrograph for events 37 to 41, presenting all simulations (cyan band), optimum run (blue line) and observation (black line). Events with weak model performance (NSE< 0.5) marked with red X.

Events were then re-simulated for the 8 m plots with the parameterized CV_{Ks}. Increasing CV_{Ks} from zero to 0.5, 1 and 2 resulted in small to moderate systematic increases in total runoff depth for all events (~20% for CV_{Ks} =2) as shown in Figure 5.7 and slightly higher peak flow (<3%) for the majority of events (>95%). The R-Squared of the simulated hydrographs improved slightly (<5%) as CV_{Ks} increased.

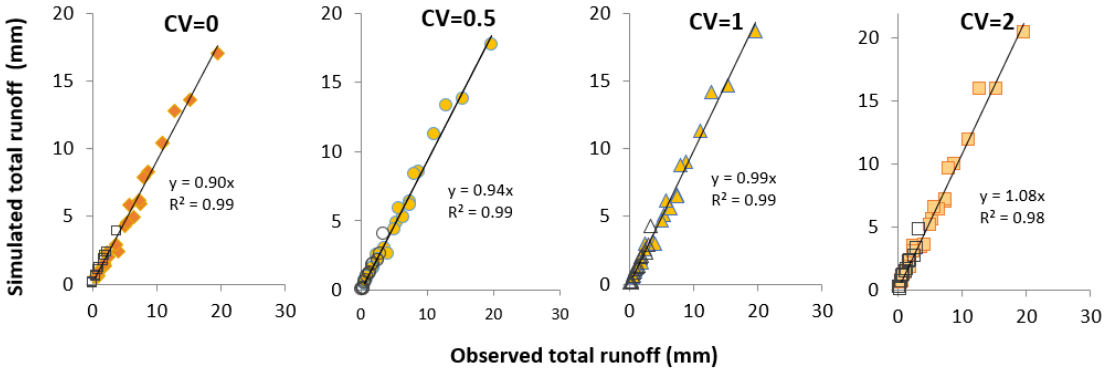

Figure 5.7 Total runoffs depth for 8 m plots from simulations with parameterized CV_{Ks} vs. observations. Event with NSE < 0.5 are shown in grey hollow markers

5.3.2 Scaling Behaviour

To characterise the scaling behaviour captured in the model, the calibrated models from the 8 m plots were used to simulate runoff from the other existing plot lengths; 0.5, 4, 12 and 16 m plots. Simulations generally resulted in underestimation of total runoff depth for shorter plots (0.5 and 4 m) and overestimation for longer plots (12 and 16 m) for the majority of events (up to 90%; Figure 5.8). Hydrographs of down-scaled runoffs for plots 0.5 and 4 m and up-scaled runoffs for plots 12 and 16 m were plotted against observation and presented in Appendices 5.3, 5.4, 5.5, and 5.6.

For completeness, the scaling behaviours were demonstrated by plotting total runoff depth (mm) against the associated plot length for both simulations and observations, and the scaling coefficients (SC_1, SC_2) were also calculated from these plots as defined in Chapter 3. As shown in Figure 5.9, the scaling effects presented by the simulations were much weaker than the observations and as a result, the simulated scaling coefficients ($|SC_1|$, $|SC_2|$) were underestimated considerably (10 to 20 times less) for the all events (Figure 5.10 a, b).

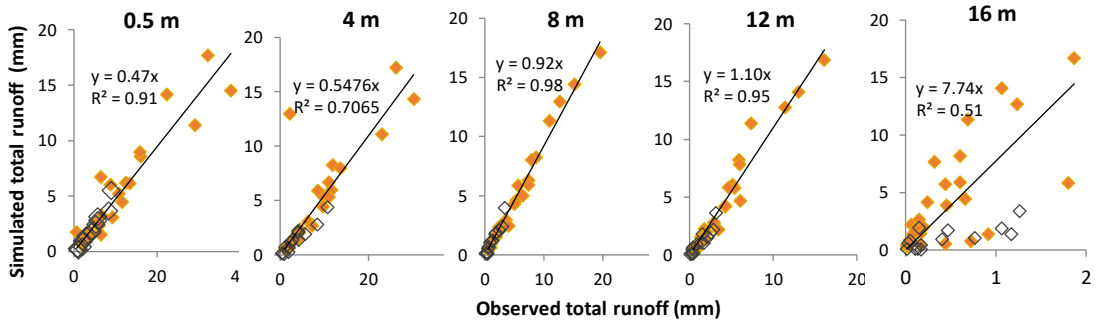

Figure 5.8 Down-scaled and up-scaled simulated total runoffs vs. observations. Event with NSE<0.5 are shown in grey hollow markers

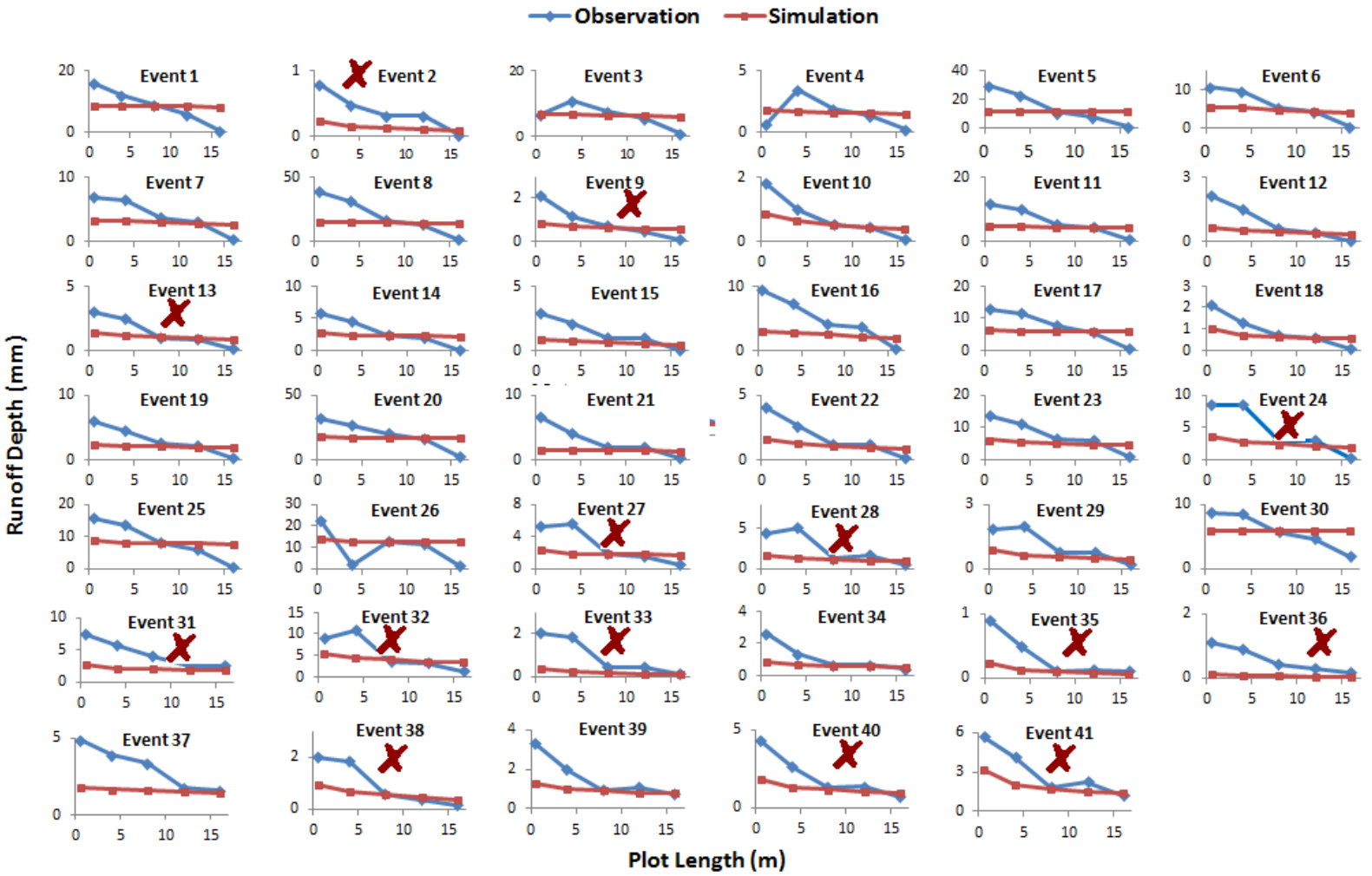

Figure 5.9 Observed and simulated runoff depths (mm) vs. plot lengths (m) for the all 41 events; events with weak model performance (NSE<0.5) marked with red X

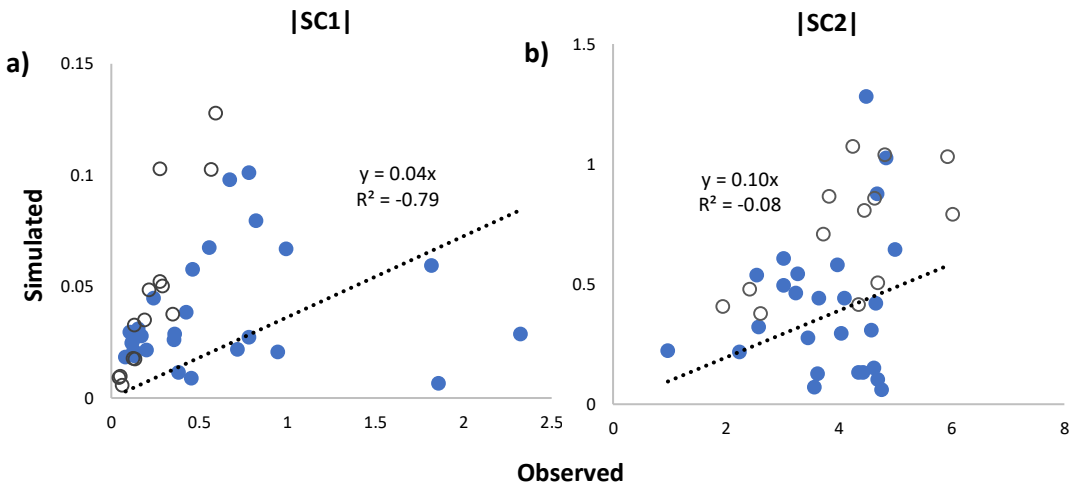

Figure 5.10 a) Observed and simulated runoffs depth scaling coefficient ($|SC_1|$), and b) Observed and simulated runoff ratio scaling coefficient ($|SC_2|$). Event with NSE<0.5 are shown in grey hollow markers

The role of CV_{Ks} in capturing scaling behaviours derived from models was also investigated by repeating simulations with CV_{Ks} (0.5, 1, and 2). Figure 5.11 shows simulated runoff depth (mm) with parameterized CV_{Ks} and observations, plotted against their associated plot length for some events. The events in the figure were selected to have different hydrograph patterns from small to large duration, early and late peak, and dry to wet conditions. As shown in Figure 5.11, the scaling behaviour is almost completely insensitive to CV_{Ks}; SC_1 changing by less than 3% as CV_{Ks} increase from 0 to 2.

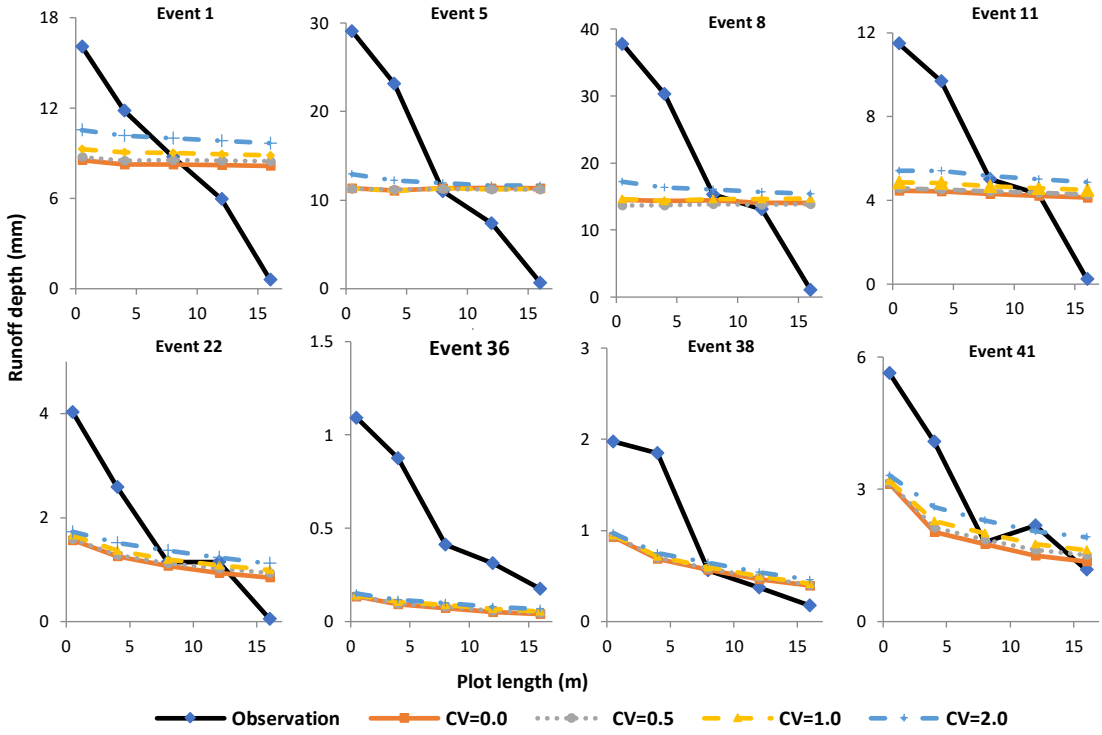

Figure 5.11 simulated runoff depth (mm) from models with different CV and observations vs. plot lengths (m) for the selected events

5.4 Discussion

The calibration outcome showed that dominant factors in controlling infiltration and overland flow models were parameterised properly for water repellent soil and burnt conditions at the study site. Model efficiencies of the optimum simulations were greater than 50% for these events.

From calibration output, the most influential parameters governing soil infiltration and infiltration-excess flow were soil hydraulic conductivity (Ks), net capillary drive (G) and surface roughness (Manning's n) respectively. This was expected from theory and conforms to similar studies (Yatheendradas et al., 2008, Al-Qurashi et al., 2008) using KINEROS2 model for rainfall-runoff modellings. Calibrated K_s was low (2 mm/h) for the first event and varied from 1 to 7 mm/h from event to event. A range value of 2 to 9 mm was found for the net capillary drive (G) parameter. The low values of capillary drive (G) could be result of the large contact angle (> 90) between liquid-solid interfaces in these water repellent soils (Bachmann et al., 2002, 2007).

Hydraulic roughness was modelled with Manning's n and Chezy (C) coefficients. In both cases, simulated hydrographs with higher roughness values resulted in lower errors in peak flow and total runoff depth. The initial roughness factor estimated based on bed particle sizes was an order of magnitude lower than the calibrated value. Similarly, large Manning's n values compared with those based on particle sizer were found by Chen et al. (2013) and Langham et al. (2016) studying rainfall-runoff modelling in fire affected watersheds. In Chen et al. (2013), the calibrated value of Manning's n was five times higher than the value based on particle size. The dynamics of the simulated hydrographs were found to be less sensitive to porosity, pore index and initial water content; with <5% variation in model efficiencies and other error indicators.

The role of soil heterogeneity on model simulations was examined by varying CV_{Ks} (0.5, 1, and 2). Increasing CV_{Ks} led to a slight rise (up to 5%) in total depth and peak flow for the majority of the events (> 90%). This is similar to previous studies stating that ignoring spatial variability of soil hydraulic conductivity (*Ks*) results in underestimation of peak discharge and total hydrograph volumes at both field (Morbidelli et al., 2006a, Nahar et al., 2004) and watershed scales (32.2 km^2, (Saghafian et al., 1995)). Model performance (R-squared) improved when CV_{Ks} increased from 0 to 2 for the majority of the simulated events (> 90%).

The scaling effects were grossly underestimated, with overestimated runoff at larger scales (smaller scaling effects), similar to (Lesschen et al. 2009) where soil infiltration was considered as the only sink (their no vegetation scenario). Scaling coefficients (SC_1, SC_2) derived from simulation presented less than 10% of the scaling coefficients from the observations. Scaling coefficients ($|SC_1|$, $|SC_2|$) obtained from simulations were underestimated; more than 10 times smaller than the observations.

To examine the possible role of CV_{Ks} on scaling behaviour, the variability of soil hydraulic conductivity (CV_{Ks}) was varied from zero to 0.5, 1, and 2 and down and up-scaling simulations were repeated accounting CV_{Ks}. Simulated scaling coefficients (SC1 and SC2) were found insignificantly (< 3%) responsive to the systematic changes of CV_{Ks}. Given that in KINEROS, Ks only varies in a cross-slope direction only, the model cannot capture down or upslope variation of Ks along the slope. Therefore, the model was not designed to capture these trends and as a result accounting CV_{Ks} was not influential in capturing approximate scaling behaviour in the rainfall-runoff model.

5.5 Conclusion

Process-based rainfall-runoff simulations were conducted using KINEROS2 to investigate whether a model with traditional infiltration theory coupled with overland flow hydraulics and temporal rainfall variations can explain the overland flow scaling effects observed on a dry burned hillslope. The study site is a dry eucalyptus hillslope located in West Gippsland, Victoria, Australia that was severely burnt by bushfire in January 2013. Soils at the site showed strong hydrophobicity and insignificant surface vegetation recovery during the study period.

The model input data were imported from measurements of post-fire soil-surface characteristics and forty-one individual runoff-generating storms from rainfall-runoff monitoring data collected during the second year following fire (Chapter 3). Field and laboratory measurements of soil and surface properties were used to successfully calibrate for post-fire soil-surface factors in rainfall-runoff simulations for the 8 m plot length.

The key parameters governing soil infiltration and infiltration excess flow in the model were soil hydraulic conductivity (K_s), net capillary drive (G) and surface roughness. Other soil hydraulic properties (porosity, pore index and initial water content) were less influential. Model performance (NSE) was above 0.5 for the majority of events (70%). Weak model performance was obtained for small events with total runoff depth < 4 mm. Only events with adequate model performance (NSE > 0.5) were considered when investigating scaling behaviours derived from simulations.

Simulations with spatially uniform soils (CV_{Ks}=0) and spatially variable soils (CV_{Ks} = 0.5, 1& 2), indicated low sensitivity to spatial variability in K_s. Scaling behaviour was investigated in the model by simulating runoff for 0.5, 4, 12 and 16 m plots using calibrated parameters from the 8 m plots. These simulations resulted in very weak scaling behaviour. Underestimated scaling coefficients *($|SC_1|$, $|SC_2|$)* derived from simulations further indicates weak demonstration of scaling behaviours by the rainfall-runoff model. The simulated scaling behaviour did not improve when variability in soil hydraulic conductivity (CV_{Ks}) was included in the model; with only slight changes in simulated scaling coefficients (<3%). Together, these results suggest that models with traditional infiltration coupled with runon process and rainfall temporal variability cannot explain the observed scaling behaviour, even where spatially variability of soil hydraulic conductivity (CV_{Ks}) is considered.

Chapter 6: Macropore flow Measurement and Modelling and Its Implication in Capturing Runoff Scaling Behaviour

Abstract

A set of experiments were conducted to measure vertical pathways of activated macropores, soil water repellency and water content from the edge of hillslope downwards. A Brilliant Blue dye tracer experiment, measurements of water repellency under field conditions and measurements of soil water content were conducted across one meter transects from top edge to the bottom of the two 16 m runoff plots. The experiments involved destructive sampling of the runoff plots and therefore was carried out only once at the end of the rainfall-runoff monitoring period; the second year following fire. The motivation for conducting these experiments was the observed dramatic reduction of runoff volume per unit length (L/m) from the 16m plots.

Two hypotheses were developed to explain runoff scaling behaviour and the dramatic reduction of runoff volume per unit length (L/m) from the 16m plots, compared with the shorter plots; Hypothesis I - soil infiltration increases from the hillslope edge towards the downhill due to increased soil moisture and weaker water repellency with distance from the top of the plot, Hypothesis II - increased infiltration occurs due to greater runoff depth exceeding macropore entry pressure thereby activating macropore flow.

The experimental results were used to investigate the hypothesis I. A tracer experiment using Brilliant Blue dye showed no increasing trend in macropore activation and breakthroughs down the plots. Soil water repellency and water content measurements showed no systematic evidence of infiltration increases with distance downslope, and thereby did not support the Hypothesis I.

To test the Hypothesis II, a model was developed to simulate macropore flow in relation to runoff depth. The model consists of i) macropore network generator using Shuffled Complex Evolution (SCE) algorithm, ii) macropore filling ($Mac_{filling}$) when runoff depth exceeded the entry pressure head of the individual pores based on the Young–Laplace and Bernoulli equations, and iii) gravity-driven vertical flow ($Mac_{seeping}$) from fully saturated macropores to the underneath soil based on Darcy's Law. The point-scale macropore model was coupled with KINEROS2 overland flow model. The model input data was from measurements partly

done in this study and partly collected from the previous similar studies (Beven and Germann, 2013, Nyman et al., 2010, Van der Sant et al., 2018).

Rainfall-runoff models with and without macropore flow application were used to simulate runoff at 0.5, 4, 8, 12 and 16 m plot lengths. Simulated runoff without macropore flow exhibited overestimated peakflows and total runoff for all events. These trends were pronounced more in longer plot lengths. Models with macropore flow calculations obtained a better agreement to observations for both total flow and peak flow with high model performance. The proportion of macropore flow increased with plot lengths for models with macropore flow.

The simulated scaling effects from models with and without macropore flow simulation were obtained and plotted against the observations. Simulations with macropore flow obtained a better predictions of overland flow scaling behaviour, but still 2.5 times higher.

The assumptions made for macropores network and geometry may contribute to the model uncertainty causing errors in the simulation results. The macropore network for different plot length was generated with no connection between macropores. However, actual macropore geometry and flow in natural soil rarely correspond to the assumed geometry. The impact of soil internal air entrapment under ponding condition and lateral preferential flow were also ignored in the macropore flow simulations.

In summary, results from runoff-rainfall simulations with macropore flow application showed that macropore flow partly demonstrates runoff scaling behaviours in water repellent soil where infiltration mostly occurs through macropores and preferential flow. This conclusion supports Hypothesis II stating higher macropore flow is obtained where runoff depth provides pressure entry, and subsequently results in higher macropores flow with distance downslope.

6.1 Introduction

Ponded infiltration and macropore flow are found to be dominant factors in controlling vertical preferential flow through water repellent soil (Nyman et al., 2010, Jarvis et al., 2008, Stoof et al., 2014a, Nyman et al., 2014, Nimmo, 2012, Hardie et al., 2013, Granged et al., 2011) Studies in S.E. Australian forests (Nyman et al., 2010, Nyman et al., 2014), Portugal and Spain (Granged et al., 2011) showed that fire-induced soil infiltration and surface runoff response are strongly influenced by preferential flow paths through activated macropores. For example, (Nyman et al., 2010) showed macropores control field-saturated and ponded hydraulic conductivity up to 95% while just includes small portion (<5%) of the whole volume of post-fire hydrophobic soil. (Stoof et al., 2014a) studied fire-induced finger flow in burnt soils and found that finger flows were more distinct, wetter, and slightly narrower compared with unburned soil in north-central Portugal. Therefore, a deeper flow downslope results in higher positive pore pressures, overcoming the water repellence of the soil and increasing macropore flow in the water repellent layer. This layer then becomes less repellent, resulting in higher infiltration in the following rainfall events, which in turn reduces the water repellence (Ritsema et al., 2001).

Flow in a macropore initiates when its water-entry pressure is satisfied by water pressure. This is directly related to contact angle between soil-water and water surface tension while inversely proportional to macropores radius as expressed in the Laplace equation (Beven and Germann, 2013, Podgorney and Fairley, 2008, Jarvis et al., 2008). Soil water repellecny elevates macropores pressure entry by increasing contact angle between water and soil surface (Bauters et al., 1998). For strongly water repellent soil, measured contact angle is above 90 degrees (Letey et al., 2000, Leelamanie et al., 2008). Darcy's law was used previously to model gravity driven (vertical) flow movement from fully saturated macropores when the depth of runoff overcomes capillary force of the saturated pore in unsaturated water repellent soil (Podgorney and Fairley, 2008, Hardie et al., 2013, Nimmo, 2012, Buttle and House, 1997). The method was found acceptable as an empirical model despite simplifying assumption (Jarvis et al., 2008).

Applying blue dye tracer followed by excavation has provided high quality images of flow pathways, activated macroporosity and patchiness in both vertical and horizontal levels of hydrophobic soil suggesting pores with equivalent diameters larger than 0.3-20 mm can allow rapid flow (Flury and Flühler, 1995, Flury and Flühler, 1994, Beven and Germann, 2013, Jarvis et al., 2008, Beven and Germann, 1982, Müller et al., 2018). Computed

tomography (CT) X-ray scanning images showed macropore structure as a complex network with a power law distribution of the number of pores against soil pore size (Samec et al., 2013, Sammartino et al., 2015, Robinet et al., 2012).

Runoff volume per unit width (L/m) at 0.5, 4, 8, 12 and 16 m plots was calculated for the whole study period as explained in Chapter 3. As presented in Figure 3.16c, total runoff volume per unit width (L/m) increases with plot lengths from 0.5 to 12 m plots and then decreases significantly for the 16 m plots. Given the unexpected decline in runoff volume per width (L/m) for the 16m plots, the quality of the data was investigated carefully, and no measurement error was detected. Runoff behaviour was consistent between the two 16 m replicate plots. Less runoff volume per width (L/m) for the longest plot was also observed in (Sheridan et al., 2014) and (Lal, 1983), who also measured overland flow scaling across different plot lengths.

The following two hypotheses were developed to explain the dramatic reduction of runoff volume per unit length (L/m) from the 16m plots, compared with the shorter plots:

> Hypothesis I: Changes in soil infiltration rate with distance from the hillslope crest due to reduced soil water repellency and higher water content with distance from downslope.
>
> Hypothesis II: Increasing runoff depth leads to macropores entry pressure being exceeded, activating macropore flow, and subsequently causing runoff scaling effects.

6.2 Methodology

6.2.1 Field and Laboratory Measurements

To examine Hypothesis I, a set of experiments were designed to measure vertical flow pathways of activated macropores (Bouma et al., 1981), actual water repellency content under field conditions (Dekker and Ritsema, 1994), and soil water content across the 16 m plots on one occasion at the end of the second year following fire (2014-2015). Two lines, perpendicular to the hillslope contours (redline shown in Figure 6.1) were chosen passing through both 16 m runoff plots from uphill to downhill. Sixteen parallel transects were appointed across the intersects within each plot perpendicular to the slope. Blue dye experiment was conducted across these transects. Soil samples for laboratory measurement

of soil water content were collected from the intact corner of these transects opposite to the trenches dug for water repellency test (Figure 6.1).

The blue dye experiment was designed to investigate vertical patterns of macropores population, distribution and breakthroughs within 10 cm depth across each transect. Brilliant Blue FCF dye powder that has a relatively low toxicity, (Germán-Heins and Flury, 2000, Flury and Flühler, 1995) was used to trace preferential flow paths during infiltration (Müller et al., 2018, Allaire-Leung et al., 2000) by measuring the area and patterns of stained from unstained soil patches across the soil profile (Persson, 2005).

Uniform dilution of > 4 grams blue dye per one litre water is required to obtain visible blue stains in soil profile (Anderson et al., 2008, Weiler and Flühler, 2004, Germán-Heins and Flury, 2000). Solution of 960 grams of Brilliant Blue FCF dye powder in 10 litre water was prepared in laboratory from which 400 millilitres was diluted with 10 litre water at the field. Prior to blue dye application, surface litter and vegetation were removed without disturbing the soil surface. Watering can (capacity 9 L) with rose nozzles (Figure 2) was used to pour diluted dye mixture (4 gr/lit) until ponding occurs on the transect and then left to drain overnight (24 hours).

A vertical soil face was excavated the day after applying blue dye, using a mattock and shovel, and then cleaned by hand scraper and brush to expose the top 10 cm of the soil profile. Manual measurement of activated pores was conducted using a measuring tape at the bottom section of the cuts and a fold-up ruler. Breakthroughs / finger flows were defined where blue dye stains exceeded beneath 10 mm vertical soil profile. Depth of dye penetration and presence/absence of finger flow was recorded along the transect (Figure 6.3). The exposed soil profile was also photographed to enable estimation of the extent and percentage coverage of blue dye stains using digital image processing. This provided an estimate of the total area of the activated pores (wetted area) within the upper 10 cm soil layer.

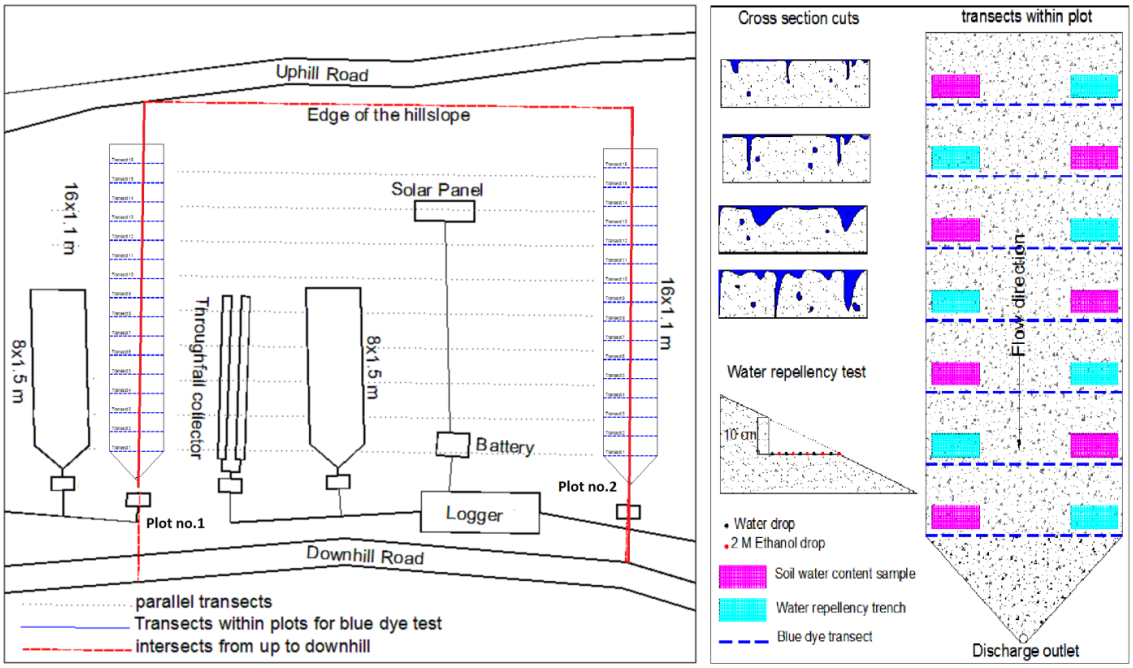

Figure 6.1 Experiment design and sample collections

Figure 6.2 Applying blue dye solution across the transects

Figure 6.3 Manual measurements of preferential flow path and wetted area within vertical soil profile

Actual soil water repellency was measured under field conditions, in situ at 1 cm depth intervals from 0-3 cm depth along a small trench transect similar to the method outlined in (Van der Sant, 2016) and (Cawson et al., 2012). The water drop penetration time (WDPT) method was used to measure water repellency (McDonald et al., 1998). The trenches were dug at the upper edge of the blue dye transects, opposite to the locations that soil samples were collected for gravimetric water content measurements (Figure 6.1). Critical surface tension (CST) was calculated from both the water drop penetration test (Letey et al., 2000) and 2 M ethanol test (McDonald et al., 1998) to measure water repellency as a function of soil depth, average and proportions of repellent and non-repellent soil. Actual water repellency was classified into three levels based on (McDonald et al., 1998):

1. Non-repellent: water is absorbed into the soil in 10 seconds or less
2. Repellent: water is absorbed in >10 seconds and 2 Molar ethanol is absorbed in <10 seconds
3. Strongly repellent: 2 Molar ethanol is absorbed in >10 seconds

To measure soil water content, soil samples were collected from 10 cm soil depth at the upper corners of the transects, opposite to the trenches dug for water repellency test, and then transported to the laboratory in sealed plastic bags. These samples were weighed before and after being oven dried at 105°C for 24 hours. The gravimetric water content (*GWC*) was calculated based on the method outlined in (Gregorich and Carter, 2007):

$$\text{Eq 6.1} \qquad GWC(\%) = \left(\frac{m_{wet} - m_{dry}}{m_{dry}}\right) \times 100$$

where m_{wet} is mass of soil before being dried, m_{dry} is mass of soil after being oven dried.

During the first year following fire, (Van der Sant, 2016) conducted both field-based and laboratory measurements to investigate soil hydraulic properties, water repellency and macropore flow paths at the study site. Soil hydraulic properties were studied by taking soil samples to a depth of 10 cm along transects, adjacent to the 8 m runoff plots. The laboratory measurements of these samples included soil texture, porosity, bulk density, air dry/background water repellency, and saturated hydraulic conductivity to a depth of 10 cm (Table 6.1).

Field-based measurements of soil water repellency were also carried out under field condition on six separate occasions during the first year after fire; from early October 2013 to March 2014. (Van der Sant, 2016) conducted similar blue dye experiment to measure horizontal distribution of macropores and infiltration patterns at 3 cm, 5 cm, and 10 cm depths.

Table 6.1 Soil hydraulic properties measurement from (Van der Sant, 2016)

Soil property	**Measurement method**	**Result**
Soil hydraulic conductivity (*Ks*)	Tension infltrometer	39.5 mm/h (SD: 30.8, n: 4)
	ponded infltrometer	74.1 mm/h (SD: 40.4, n: 2)
Soil texture and particle size	Sieving and particle size analyser	15% Clay, 44% Silt, 41% Sand Course fraction (>2 mm) 45%
	Texture triangle class (USDA)	Silty loam
Porosity	Tension table	0.385 (SD 0.04, n =3) corrected for gravel (porosity of <2mm fraction)
Gravimetric Soil Water Content	Oven drying	Average 5.1% (SD: 3.8, n: 52)
Potential Soil Water Repellency	Critical Surface Tension	Average Air-dry CST 60.3 mN/m² (SD: 13.0, n: 24)
Bulk density	Total	1.19 g/cm³ (SD: 0.08, n: 9)
	Fine fraction (<2 mm) (gravel corrected)	0.86 g/cm³ (SD: 0.46, n: 9)

**SD: Standard deviation, CST: Critical Surface Tension (mN/m²)*

6.2.2 Pore-scale Flow Modelling

To test Hypothesis II, a pore-scale model was built to simulate macropore flow in water repellent soil layer. Macropore flow was modelled based on pressure entry of the existing pores in relation to the runoff depth at the point, that are exceeded more frequently with distance downslope due to increasing runoff depths. Therefore, longer plots should have higher macropore flow during longer events that explains higher scaling coefficients for these events.

A conceptualization of flow patterns in soils with water repellent top layer was shaped based on observations of the activated macropores, breakthroughs (finger flow) in this study and similar studies (Nyman et al., 2010, Ritsema and Dekker, 1995, Wessolek et al., 2009, Nyman et al., 2014). In this model, infiltration in water repellent soils happens in four different stages as followed (Figure 6.4):

i) Pre-ponding stage when only K_s contributes to infiltration; $f(t)=K_s$

ii) Filling stage during ponding when runoff depth overcomes pressure entry of pores and macropores filling takes place; $f(t)= K_s+ Mac_{filling}$

iii) Seeping stage when macropores are full of water and a continuous flow initiates from pores to underneath non-water repellent soil while filling continues for pores that their pressure entry is satisfied; $f(t)= K_s+ Mac_{filling} + Mac_{seeping}$

iv) Seeping continues as long as rain continues when all pores are filled; $f(t)= K_s+ Mac_{seeping}$

Figure 6.5 shows conceptual scheme of macropore flow simulation coupled with traditional rainfall-runoff model

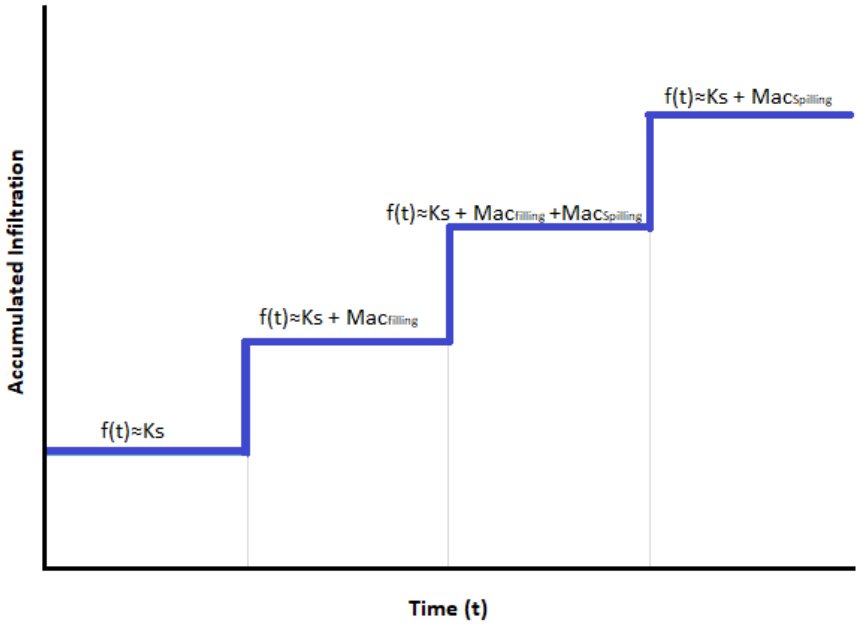

Figure 6.4 Schematic representation of four-stage infiltration in a soil with a water-repellent toplayer modified from (Tofteng et al., 2002, Podgorney and Fairley, 2008)

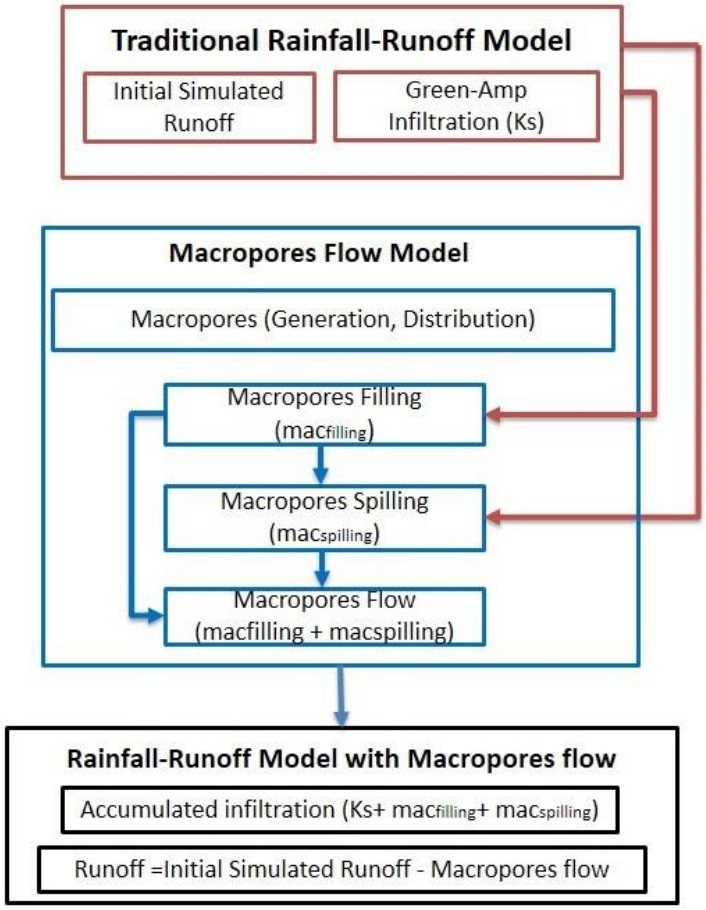

Figure 6.5 Conceptual scheme of macropore flow simulation coupled with traditional rainfall-runoff model

6.2.3 Macropore Flow Model Coupled with KINEROS Rainfall-Runoff Model

The rainfall-runoff simulations were set in three minutes time intervals and at each time interval, below steps were conducted:

- Pre-ponding stage:
  - Only matrix infiltration occurs during pre-ponding stage which was simulated by matrix infiltration modelling approach.
- Macropore flow after runoff initiation
  - When runoff initiation occurs at a time interval, depth of water at each pore was calculated based on their location within the plot.
  - Macropore filling was calculated based on pressure entry of the individual pores in relation to flow depth, if satisfied then filling process took place.
  - The total amount of water filling pores was deducted from the initial runoff discharge at the time interval.
  - At the next time interval, if pores were already filled from the previous time intervals and water depth pressure was available at the pore, then discharge from the pores would take place.
- Macropores seeping flow
  - Total amount of water flowing from pores to below mineral soil was deducted from the initial runoff discharge at the time interval.
  - **Macropore Network Generation**

A macropore network was generated with pores conceptualised as permeable capillary pipes with variable diameters and no connection between pores. Pore diameters, depth and their distributions across the plot plane were obtained from classical power law distributions (Samec et al., 2013, Nimmo, 2004) where smaller pores obtained smaller depth and higher populations. Two assumptions were made in building the macropore network:

- Generated macropores are assumed to have static characteristics and their population remains constant during simulation.
- Generated macropores are assumed to behave independently from each other and individually drain to the underneath mineral soil.

Shuffled Complex Evolution (SCE) optimization algorithm was used to generate a random set of individual pores distributed in all direction within the feasible space. SPOTPY-Statistical Parameter Optimization Tool, (Houska et al., 2015), an open source python package has been used for SCE algorithm based Griewank function ((Griewank, 1981)-Appendix 6.1).

There were major regions of attraction into which an optimization search strategy needed convergence. If any of the convergence criteria is satisfied, the process is terminated. These regions are radius, depth, and distribution of macropores in water repellent soils obtained from measurements in both laboratory (Nyman et al., 2010, Sammartino et al., 2012, Sammartino et al., 2015, Jarvis, 2007, Allaire et al., 2009, Zhang et al., 2016) and field-based experiments (Nyquist et al., 2018, Jarvis et al., 2008, Weiler and Flühler, 2004, Beven and Germann, 2013, Flühler et al., 1996, Anderson et al., 2008, Jarvis, 2007, Ritsema and Dekker, 1995).These major regions of attraction for optimization searches are as follow:

- Macropores with equivalent radius ranged from 0.5 to 10 mm to allow rapid flow (Beven and Germann, 1982, Jarvis, 2007).
- Macropores with equivalent depth ranged from 10 to 100 mm.
- Macropores distribution based on classical power law distributions; possibility of having pores with smaller radius and shorter depth was much higher than larger pores based on previous laboratory measurement (Samec et al., 2013, Nimmo, 2004, Beven and Germann, 1982).
- Total macropores volume was assumed to be approximately 5% of the total volume of 10 cm topsoil layer based on laboratory measurement undertaken by (Nyman et al., 2010) for dry eucalyptus burned site with strong water repellent soil.

The steps in SCE algorithms for pores network optimization is given below:

1) Generate N number of points randomly placed in the given space representing macropores.
2) Give a certain diameter to each generated point within a given range. The diameter of the points from the complexes are combined into a single sample population.
3) Give a certain depth to each generated point within a given range. The pores depth from the complexes are combined into a single sample population.
4) Use SCE optimisation to populate macropores network within a certain range of depth and radios.
    a. Total volume of generated pores is less than 5% of total volume of 10 cm topsoil and,
    b. Pores radius size and depth distribution follows power law distribution

Source python code functions used for the macropore network generation are presented in Appendix 6.2.

- **Pre-ponding infiltration**

The Green-Ampt relation with spatially uniform soil properties was assumed for estimating the infiltration pattern during the pre-ponding period. The KINEROS2 event-based rainfall-runoff model (Chapter 5) was used to solve infiltration model derived from

(Parlange and Haverkamp, 1989) and a kinematic wave solution represented sheet flow as a one-dimensional laminar flow:

$$\text{Eq 6.2} \qquad Q = \propto h^{m}$$

$$\text{Eq 6.3} \qquad \propto = 1.49\frac{S^{\frac{1}{2}}}{n} \text{ and } m = \frac{5}{3} \text{ for Manning hydraulic resistance law}$$

$$\text{Eq 6.4} \qquad \propto = CS^{\frac{1}{2}} \text{ and } m = 3/2 \text{ for Chezy law}$$

where *Q* is discharge per unit width, h is depth of water per unit area, and m are parameters related to slope, friction slope (*Sf=h.f/L*) equal to hillslope gradient (S_0, bed slope) for laminar flow, *C* is Chezy friction coefficient, and *n* is manning coefficient. Source python code for pre-ponding infiltration is presented in Appendix 6.3.

- **Macropore Filling**

Macropore filling (Mac_{filing}) starts when the entry pressure (P_e) of the individual pore is satisfied by flow depth (Young–Laplace equation).

$$\text{Eq 6.5} \qquad P_e = h\rho g = \frac{-2\sigma Cos\alpha}{r} \rightarrow h = \frac{2\sigma Cos\alpha}{r\rho g}$$

where ρ is the liquid density for water (997 kg/m^3), g is acceleration due to gravity (9.8 m/s), h is the hydraulic head (m), r is the pore radius (m), σ is the surface tension (*mN/m*) obtained, α is contact angle between water and soil.

Soil water repellency controls water-entry pressure by increasing the contact angle between water and soil surface (Bauters et al., 1998). The contact angle was calculated from (Carrillo et al., 1999) as a function of critical surface tension from the Molarity of an ethanol droplet (MED) test (Doerr, 1998) used for water repellency measurement. This method has been found to be suitable for strongly water repellent soil with contact angle > 90 (Letey et al., 2000, Leelamanie et al., 2008).

$$\text{Eq 6.6} \qquad Cos\alpha = \left(\frac{\gamma_{90^\circ}}{\gamma_w}\right)^{0.5} - 1$$

where γ_W is the water–air surface tension (*mN/m*), γ_{90} is the water–air surface tension at which the contact angle made on the soil is 90° (47.1 *mN/ m*) from (Moody and Schlossberg, 2010). Source Python code for Pressure Entry calculation at Individual Pores is presented in Appendix 6.4.

For each single pore, water pressure at the point (P_x) is comparable to the pore's pressure entry (P_e). If $P_x \geq P_e$, the pore would either fill up or remain empty. Water pressure on

individual pores (P_x) is calculated in relation to distance of the pore to ΔP at the outlet as shown in Figure 6.6.

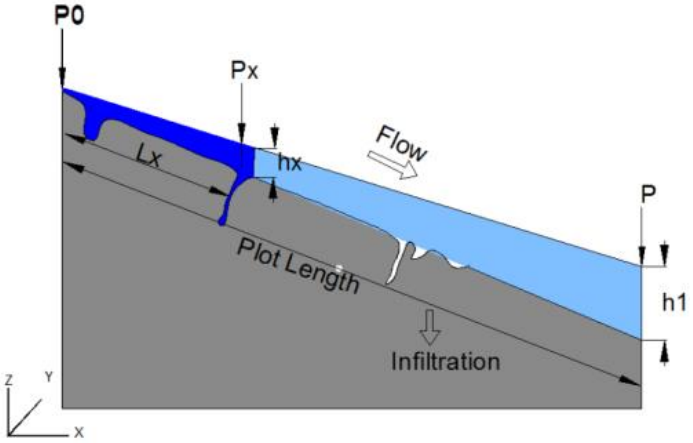

Figure 6.6 Bernoulli equation across plots with different length

Eq 6.7 $$\frac{1}{2}\rho V_0^2 + \rho g h_0 + P_0 = \frac{1}{2}\rho V_1^2 + \rho g h_1 + P_1$$

Eq 6.8 $$\Delta P = \rho(g\Delta h + \frac{1}{2}(V_1^2 - V_0^2)) \; or \; \Delta P = \rho(g\Delta h + \frac{1}{2}(Q/Area)\text{^}2)$$

Eq 6.9 $$P_x = \Delta P(\frac{L_x}{Plot\ length})\ (\mathrm{N/m^2})$$

where ΔP is pressure gradient between two ends of the plot length (N/m^2), g is acceleration due to gravity (9.8 m/s^2), Q is simulated flow (m^3/s), ρ is the liquid density for water (997 kg/m^3), and V is velocity (m/s). Python source code used for macropores filling module is presented in Appendix 6.5.

- **Macropore Seeping**

Gravity-driven (vertical) flow in activated macropores was modelled to happen only from fully saturated macropores when the depth of runoff overcomes capillary force of the saturated pore in unsaturated water repellent soil (Podgorney and Fairley, 2008, Nimmo, 2012). Darcy Law was assumed to calculate vertical flow passing through cylindrical-shaped pores similar to (Podgorney and Fairley, 2008). From Darcy Law, saturated hydraulic conductivity of macropores is obtained from vertical flow exiting the saturated macropores ($K_{seeping}$) in relation to runoff depth (h) similar to the method was outlined (Hardie et al., 2013, Buttle and House, 1997). The impact of soil internal air pressure (air entrapment) under ponding condition and lateral preferential flow at the interface between water repellent soil layer and the mineral layer beneath (Stoof et al., 2014a, Gerke et al., 2010, Gerke et al., 2015) were ignored in this model.

Eq 6.10 $$Q_{spilling} = AV = \frac{\pi r^2 L}{t} K_{spilling} = Q\Delta Z/Ah$$

where $Q_{seeping}$ (m^3/s) is vertical flow in pores network, $K_{seeping}$ (m/s) saturated hydraulic conductivity of macropores, ΔZ is the length of the water repellent soil (m), L is depth of pore, t is time interval (3 minutes), A is surface area (m^2), h is applied hydraulic head (m) by runoff depth. Python source code used for macropores seeping module is presented in Appendix 6.6.

6.2.4 Scaling in Runoff Simulations with Macropore flow

Rainfall-runoff model parameters were calibrated for the shortest plot lengths (0.5 m) assuming zero macropore flow and thereby assumed matrix infiltration properties were obtained. The calibrated parameters from the shortest plot length then used to simulate runoff from 0.5, 4, 8, 12 and 16 m length plots. Two sets of simulations were conducted assuming: a) only matrix infiltration, and b) matrix infiltration plus macropore flow. The scaling behaviour from these simulations were then plotted against those from the observations to determine whether macropore flow could explain the overland flow scaling effects.

6.3 Result

6.3.1 Experiment

Image processing of the photographed blue dye stains on the excavated soil profiles provided an estimate of the total area of the activated pores (wetted area) within the upper 10 cm soil layer. The results of the photographed soil profiles showed that the percentage of the blue dyed area on the vertical soil profile fluctuated between 9 and 32%, with average values of 17% (std=6, n=16) and 15% (std=4, n=16) for 16 m plots. No trend was found in the proportion of dyed areas from top to down the plots (Figure 6.7). Previous blue dye measurements conducted by (Van der Sant, 2016) at the site during the first year following fire showed that the proportion of active infiltration regions (blue dyed areas) of the horizontal soil profiles (50 x 50 cm) was 36.1%.

On average, 1.46 breakthroughs were observed at each transect across plots, mostly in the lower transects. The depth of breakthroughs varied between 12 to 70 mm following no trend down the plots (Figure 6.8 a, b).

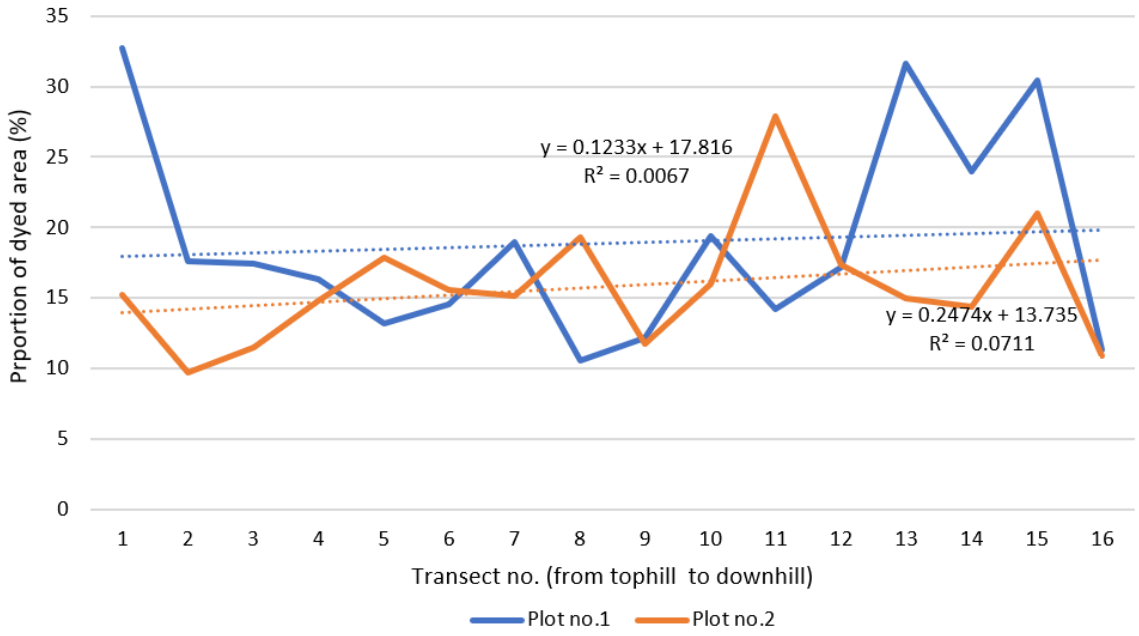

Figure 6.7 Area of blue dyed soil as a proportion of the total area of the vertical soil profile

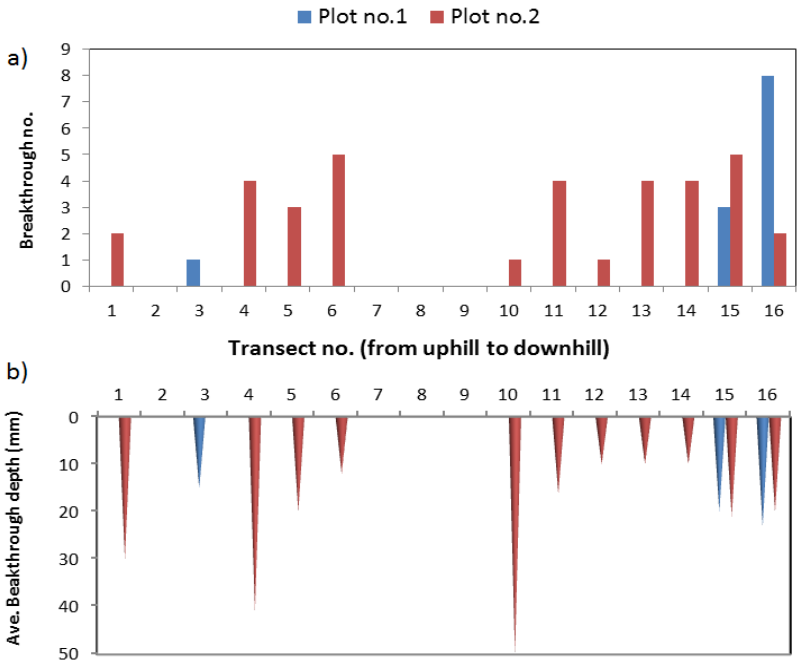

Figure 6.8 a) The number of breakthroughs observed within each transect, b) Average depth of breakthroughs at each transect

Field-based investigation was conducted to examine the possibility of infiltration toward the transects' edges. Blue dye proportions were investigated from the centre of the transects towards the both edges to observe the propensity of higher blue dye patterns towards the plots' side as sign of seepage from these areas. No increase pattern of blue dye stains was found to prove infiltration increase from the centre of 16 m plots towards the edges.

Figure 6.9 shows water repellence at the depth of 1, 2 and 3 cm of the vertical soil profile categories based on (Leighton-Boyce et al., 2005). As shown in the Figure, the mineral soil at the ground surface is not hydrophobic but it becomes strongly repellent at depths of 1, 2 and 3 cm for more than 50% of the tested area. The measurements also show that Plot no.1 is more water repellent in the downhill sections while Plot no.2 obtains strong water repellency in the uphill transects.

Figure 6.10 demonstrates laboratory measurements of water repellency strength from the ground surface to the depth of 10 cm during the first year (Van der Sant, 2016), and field-based measurement within 4 cm soil profile conducted at the end of the second year. Both the field-based and laboratory measurements showed that the strength of hydrophobicity steadily weakened from 4 cm depth downward, becoming non-repellent below 8 cm.

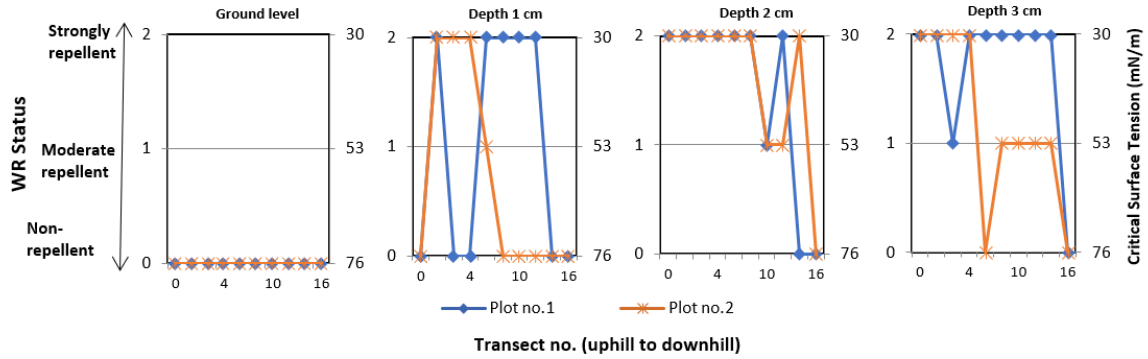

Figure 6.9 Soil water repellency measurements within 3 cm depth with categories from (Leighton-Boyce et al., 2005)

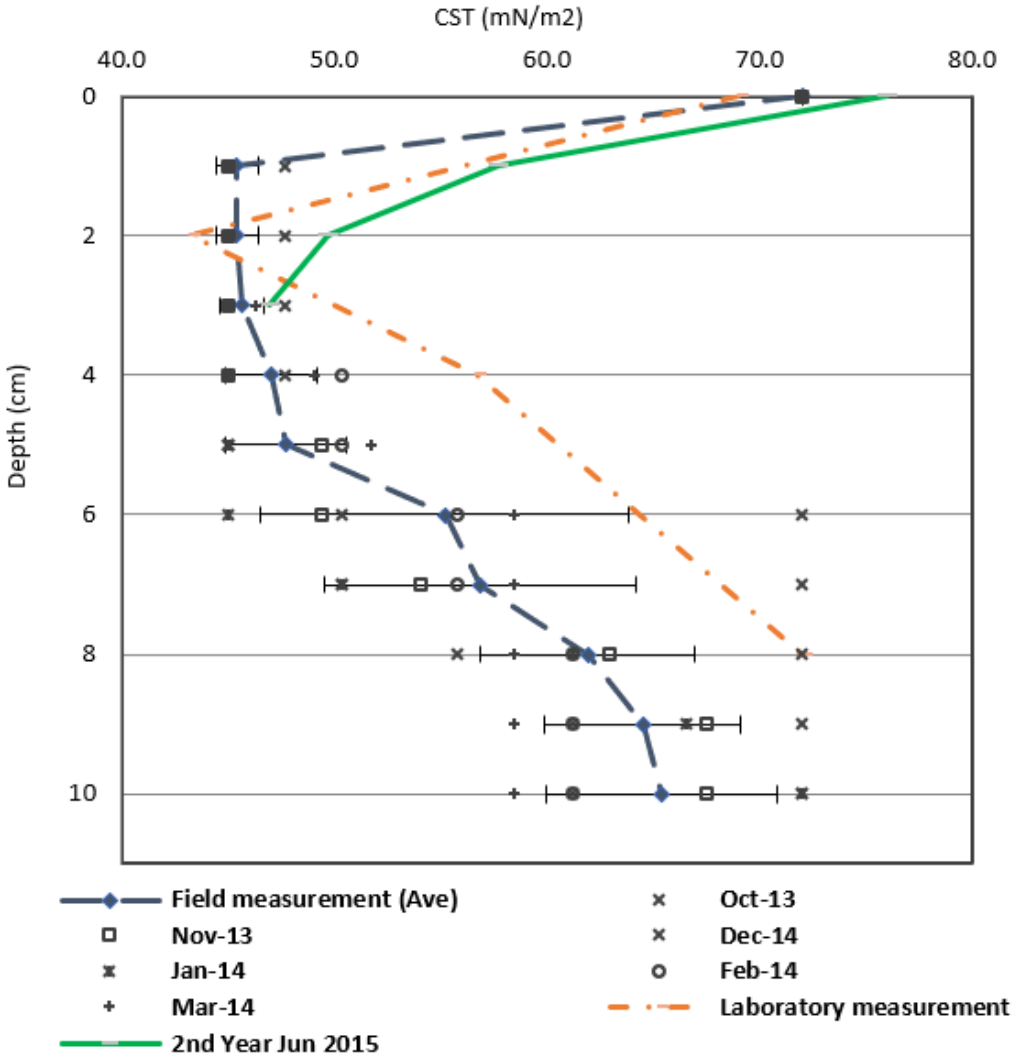

Figure 6.10 Field based and laboratory measurement of water repellency within 10 cm soil profile, during the first year following fire (Van der Sant, 2016) and at the end of the second year. Corresponding CST values for water repellency categories; Non-repellent > 72 mN/m2, Repellent 72-45 mN/m2, Strongly Repellent <45 mN/m2 from (Leighton-Boyce et al., 2005)

Gravimetric water content (GWC) of the soil samples, collected from 10 cm top-soil layer at the adjacent of each transect is between 7 and 17%, with the mean value of ~11% (std= 6, n= 16). As shown in Figure 6.11, lower GWC was found within the bottom half of transects with moderate R-squared (R^2~0.30) between soil GWC and distance down the plots.

Combining the data from the first (Van der Sant, 2016) and second (this study) years after the fire, a negative relationship was obtained between soil water content and soil water repellency averaged across the study area (Figure 6.12). For example, a 20% increase was observed in the proportional occurrence of strong water repellence when gravimetric water content decreased from 8 % to 4 % in the summer of 2014 (326 days since fire). Similar studies in dry eucalyptus forest have indicated that the degree of water repellency is negatively related to soil water content and probably disappears at saturation point (Sheridan et al., 2007, Nyman et al., 2010, Nyman et al., 2014). Monitoring seasonal water repellency showed a continuation of strong water repellency during the first winter following fire. This indicates fire-induced water repellency did not follow the seasonal oscillations typical of naturally water-repellent soil in which hydrophobicity breaks down in winter and forms during spring and summer. A similar trend has been observed by (Sheridan et al., 2007), who showed continuous water repellency which resulted in higher rates of runoff in the first winter following fire.

As discussed above, weaker soil hydrophobicity was observed to be associated with higher *GWC.* Thus, a higher proportion of blue dyed soil; representing higher infiltration was expected for those transects with higher water content (*GWC*). However, comparing soil water content and proportion of blue dyed areas shows no correlation between soil water content and proportion of blue dyed areas in this study (Figure 6.13).

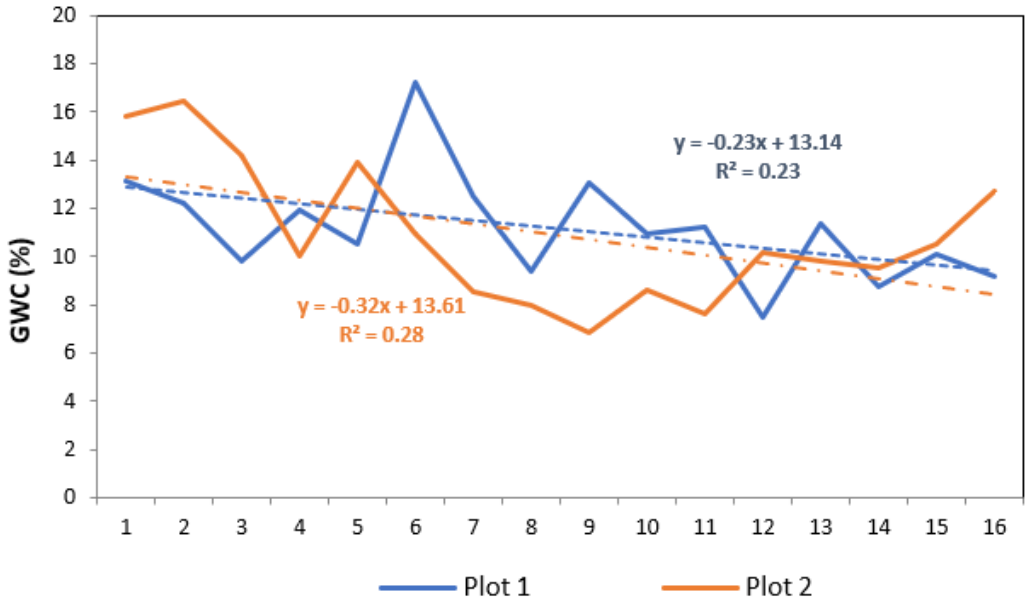

Figure 6.11 Gravimetric water content (GWC %)

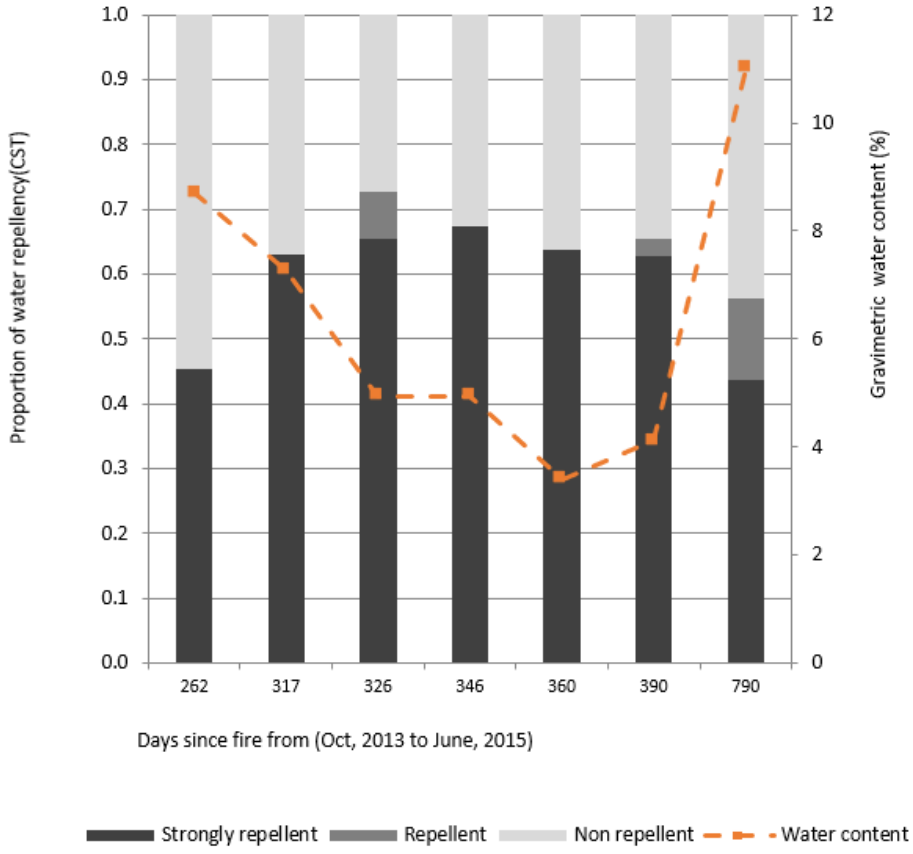

Figure 6.12 Proportional of water repellence strength and gravimetric soil water content measured on the six occasions during the first year following fire by Van der Sant (2016) and once at the end of the second year in this study

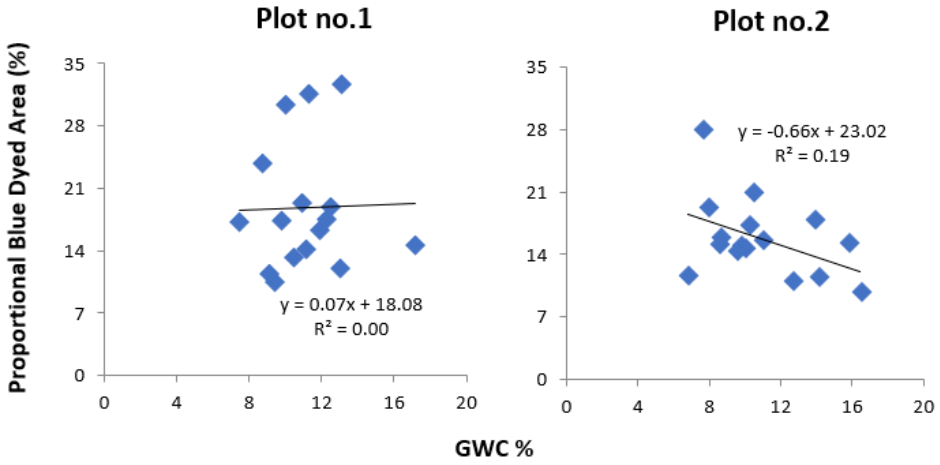

Figure 6.13 Soil water content vs. blue dyed proportion areas

6.3.2 Macropores Network Model

Macropores network was generated for 0.5, 4, 8, 12 and 16 m plot lengths with help of Shuffled Complex Evolution (SCE) algorithm based on Griewank function (Griewank, 1981). A SCE search model was conducted to optimise pores population with a certain range of depth and radios while obtaining certain proportion of total soil volume and certain proportion of soil surface area, randomly distributed within the plot (6.15).

Input data for modelling pores network was obtained from measurements partly done in this study and partly collected from previous similar studies (Van der Sant et al., 2018, Nyman et al., 2010). Pores are considered as individual tubes with various radius in a range of 0.5-10 mm plus, responsible for quick macrospores flow (Beven and Germann, 1982). Depth of the generated pores are in range of 15 to 50 mm in accordance to the depth of stained soil and breakthroughs. The total volume of pores at depth of 10cm soil is around 5% (±0.5) or under and the total pores area is less than 15% of the plot area. Summary of the generated pores for different plot lengths are in Table 6.2. The search model was to converge small radius with shorter depth. Figure 6.14 shows probability distribution of pores' radius in one square metre area generated by SCE, Griewank function. As shown in the Figure, the majority of generated macropores (>75%) have radius under 2 mm.

Table 6.2 Pores generation for different plot length

Plot Area	Radius	Depth	Population	Volume	Proportional Area (Pores / Plot)	Proportional Volume (Pores/ Total Soil at 10 cm depth)
m²	mm			Litre	%	
0.5x0.45	0.5 – 20	15 – 70	4080	1.15	12.8	5.11
1x1			12150	4.06	9.7	4.06
4x1.5			31680	37.28	11.74	5.07
8x1.5			62937	56.12	15.04	4.90
12x1.5			86256	96.95	10.35	5.01
16x1.1			98128	94.42	12.52	5.10

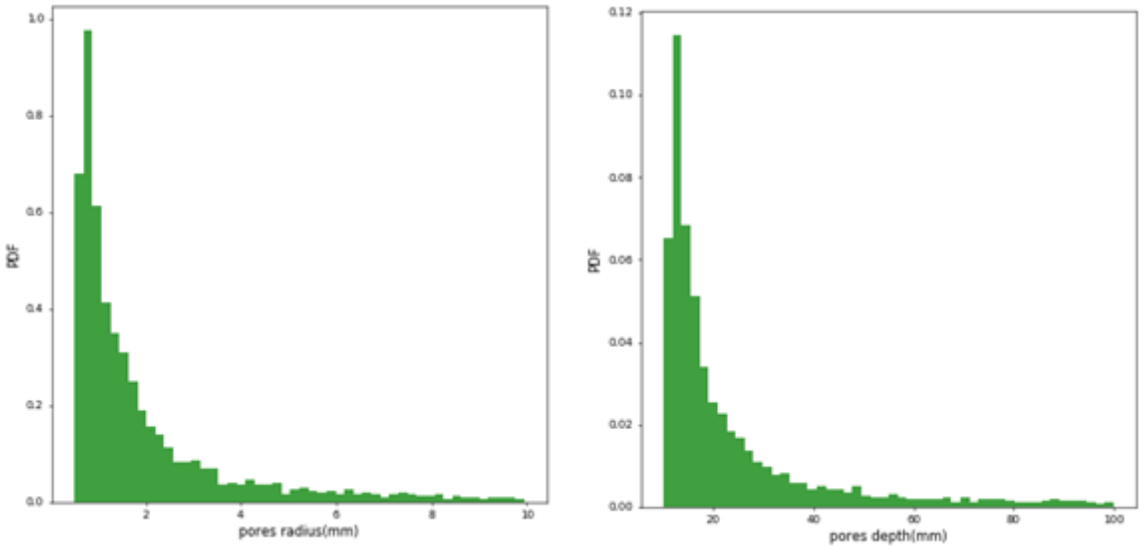

Figure 6.14 PDF of macropores' radius and depth sizes in one square metre area generated by SCE, Griewank function

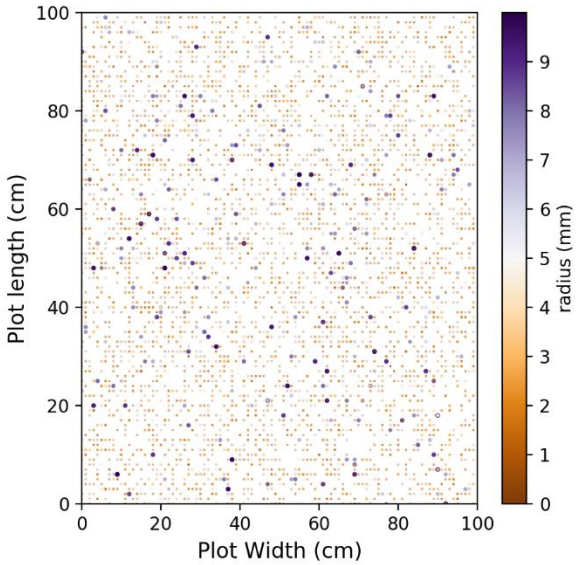

Figure 6. 15 Pores coordinates (x, y) within 1x1 m plot

6.3.3 Runoff Simulations with Macropore flow

Forty-one rainfall-runoff events were selected from the data collected during the second year following fire. The KINEROS2 model was used to simulate overland flow at the shortest plot lengths plot length (0.5 m) based on matrix soil infiltration, assuming no macropore flow. Calibrated soil-surface parameters are obtained with the same method described in Chapter 5 and summarised in Table 6.3. Soil moisture were varied from 3 to 10%.

Table 6.4 presents a summary of calibrated parameters for runoff simulation at the shortest plot.

Table 6.3 Summary of calibrated Soil parameters for runoff simulation

Parameter	Symbol	Units	Value	Source
Effective net capillary drive	*G*	mm	5	G for Silt loam soil from Kineros2 table
Hydraulic Conductivity	K_s	mm/h	0.5	Obtained from model calibration
Variation of K_s	*CV*	--	0	Assuming hydraulic conductivity did not change during the event
Soil layer thickness	*Th*	mm	80	Field observation
Pore size distribution index (DIST)	λ		0.6	Laboratory measurement (varied in range of 0.15-0.65)
Porosity	θ	--	0.5	Laboratory analysis (varied in range of 0.25-0.35)
Rock	*Ro*		0	Laboratory measurement (<0.46%)
Slope factor	*sl*	degree	27	Field observation
Interception depth	*i*		1	Water storage capacity in burned layer
Canopy coverage	*p*		1	100% coverage of woody burned layer
Manning's coefficient	*n*	$sm^{-1/3}$	0.065	Hydraulic roughness based on particle size
Relief (microtopography)	*re*	mm	3	Field observation
Relief spacing	*Rs*	m	0.05	Field observation

Table 6.4 Runoff simulations versus observations and model efficiencies

Event no.	Soil Moisture (GWC)	Total runoff depth (mm)		NSE	R^2
		Observation	Simulation		
1	9	16.09	16.02	0.80	0.82
2	9	0.79	0.62	0.20	0.17
3	9	6.51	9.24	-0.95	0.53
4	8	0.64	2.51	-5.94	0.00
5	8	29.07	25.42	0.48	0.56
6	8	10.84	13.07	0.5	0.84
7	7	6.69	7.55	0.74	0.72
8	7	37.78	33.57	-0.16	0.31
9	7	2.12	2.82	0.48	0.55
10	6	1.79	1.59	0.88	0.92
11	6	11.49	11.45	0.82	0.85
12	6	2.07	2.31	0.47	0.73
13	6	2.95	2.29	0.44	0.51
14	4	5.77	8.25	0.26	0.61
15	4	2.81	4.21	0.28	0.68
16	3	9.23	10.58	0.07	0.39
17	3	12.52	14.10	-0.49	0.33
18	4	2.12	2.87	-1.41	0.06
19	6	5.94	5.79	0.64	0.64
20	8	32.23	32.34	0.72	0.78
21	8	6.49	4.97	0.82	0.22
22	10	4.03	3.17	0.63	0.18
23	10	13.47	11.23	0.34	0.56
24	10	8.39	7.39	-8.52	0.06
25	10	15.83	14.65	-0.08	0.39
26	10	22.28	23.75	0.14	0.54
27	10	5.24	3.25	0.22	0.25
28	10	4.38	2.54	-1.35	0.13
29	10	1.82	1.21	0.03	0.40
30	10	8.72	8.37	0.74	0.73
31	10	5.73	4.00	-0.34	0.26
32	10	8.99	7.68	-0.10	0.39
33	10	2.06	0.70	-0.36	0.05
34	10	2.63	2.49	0.87	0.50
35	10	0.90	0.91	-0.03	0.43
36	10	1.09	0.31	0.23	0.08
37	10	3.91	3.06	0.25	0.48
38	10	1.98	1.43	-2.68	0.06
39	10	3.29	2.76	-0.73	0.25
40	10	4.34	2.91	-0.59	0.17
41	10	5.63	4.64	-0.90	0.16

*The closest fits were obtained by accepting runs with NSE > 0.5, shown in grey

Ten simulated events with high Nash–Sutcliffe model efficiency coefficient (NSE>0.50) were selected to conduct macropores simulations at longer plot lengths. The calibrated parameters obtained from simulations at the 0.5 plots were used to simulate rainfall-runoff for 4, 8, 12 and 16 m plot lengths. Two sets of simulations were conducted with:

a) Only soil infiltration model at 0.5, 4, 8, 12 and 16 m plot lengths,

b) Soil infiltration and macropores filling-seeping model at 4, 8, 12 and 16 m plot lengths.

Hydrographs of simulated runoffs with and without macropore flow were plotted against observations (Figure 6.16).

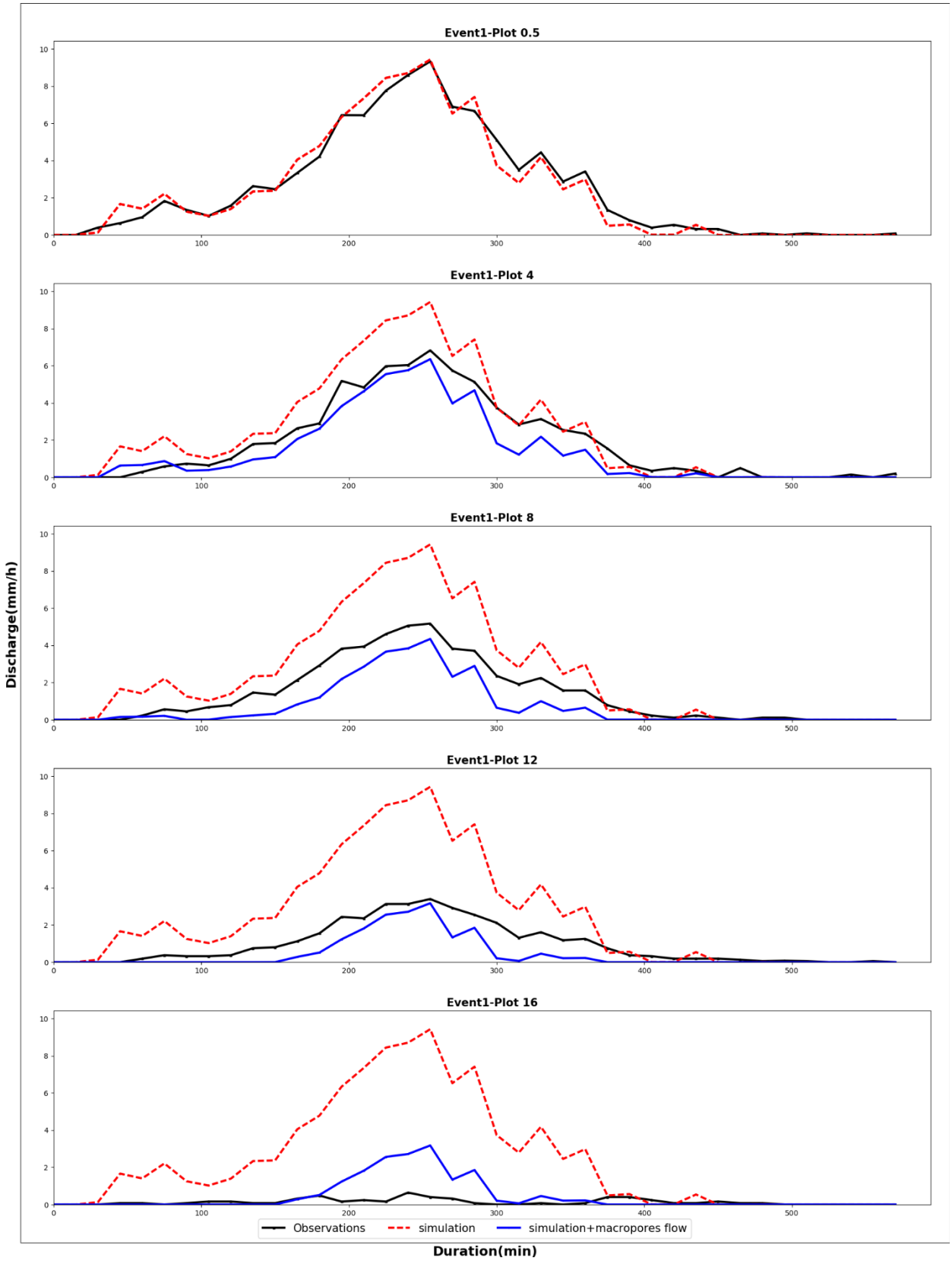

Figure 6.16 Rainfall-runoff simulations at different plot lengths with a) only soil infiltration model (red line) and b) soil infiltration and macropores filling-seeping models (blue line)

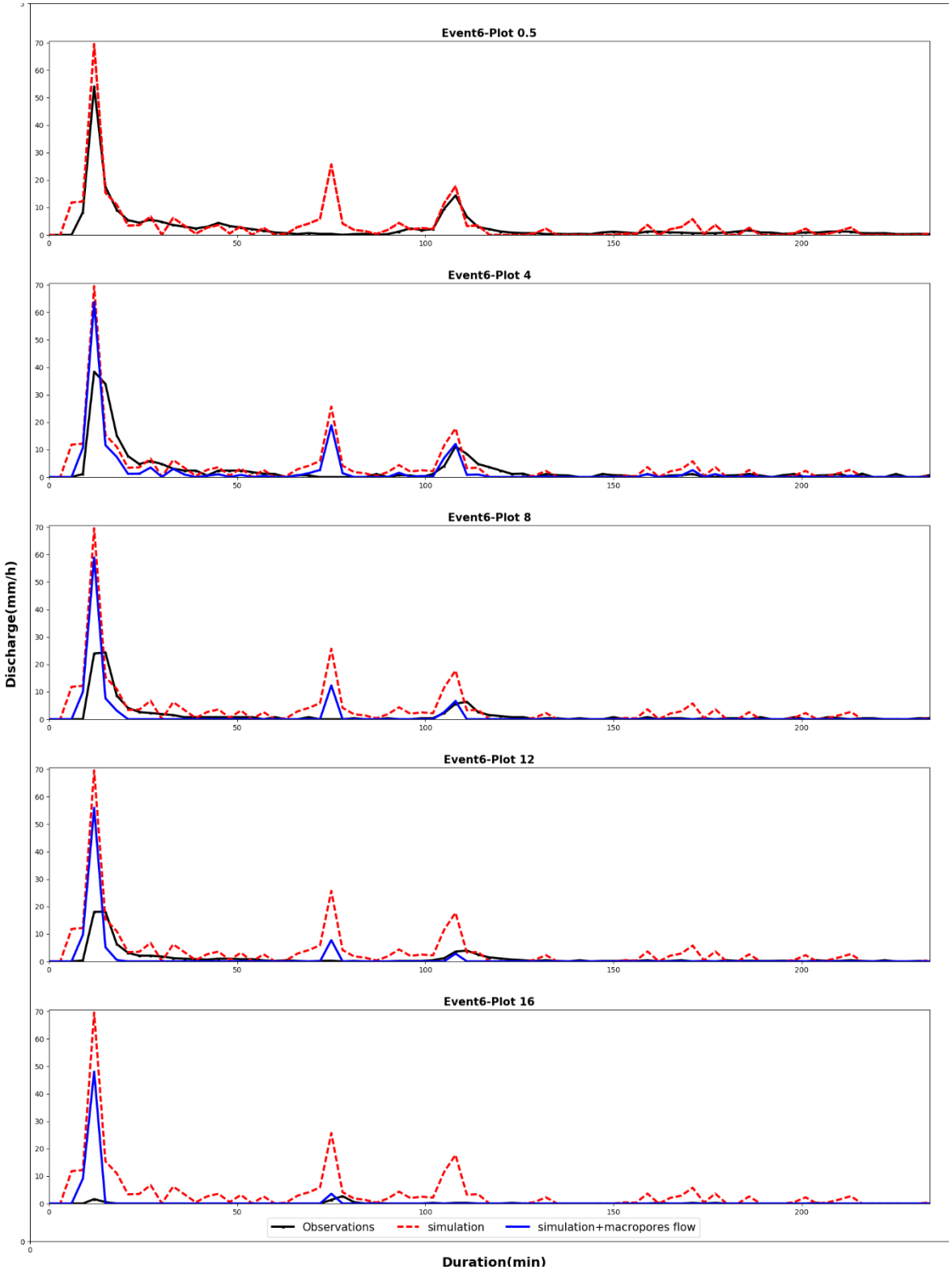

Figure 6.16 Rainfall-runoff simulations at different plot lengths with a) only soil infiltration model (red line) and b) soil infiltration and macropores filling-seeping models (blue line)

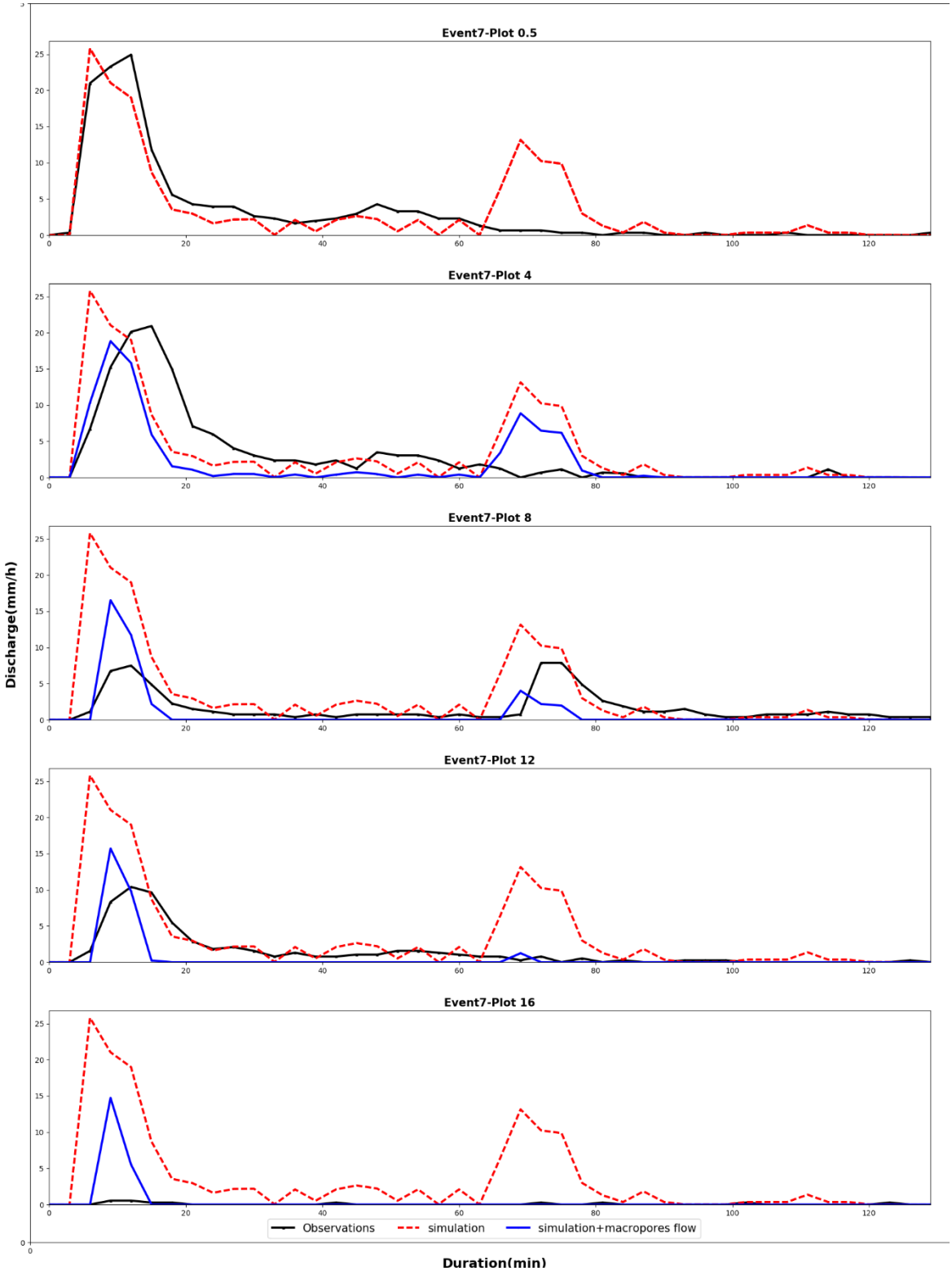

Figure 6.16 Rainfall-runoff simulations at different plot lengths with a) only soil infiltration model (red line) and b) soil infiltration and macropores filling-seeping models (blue line)

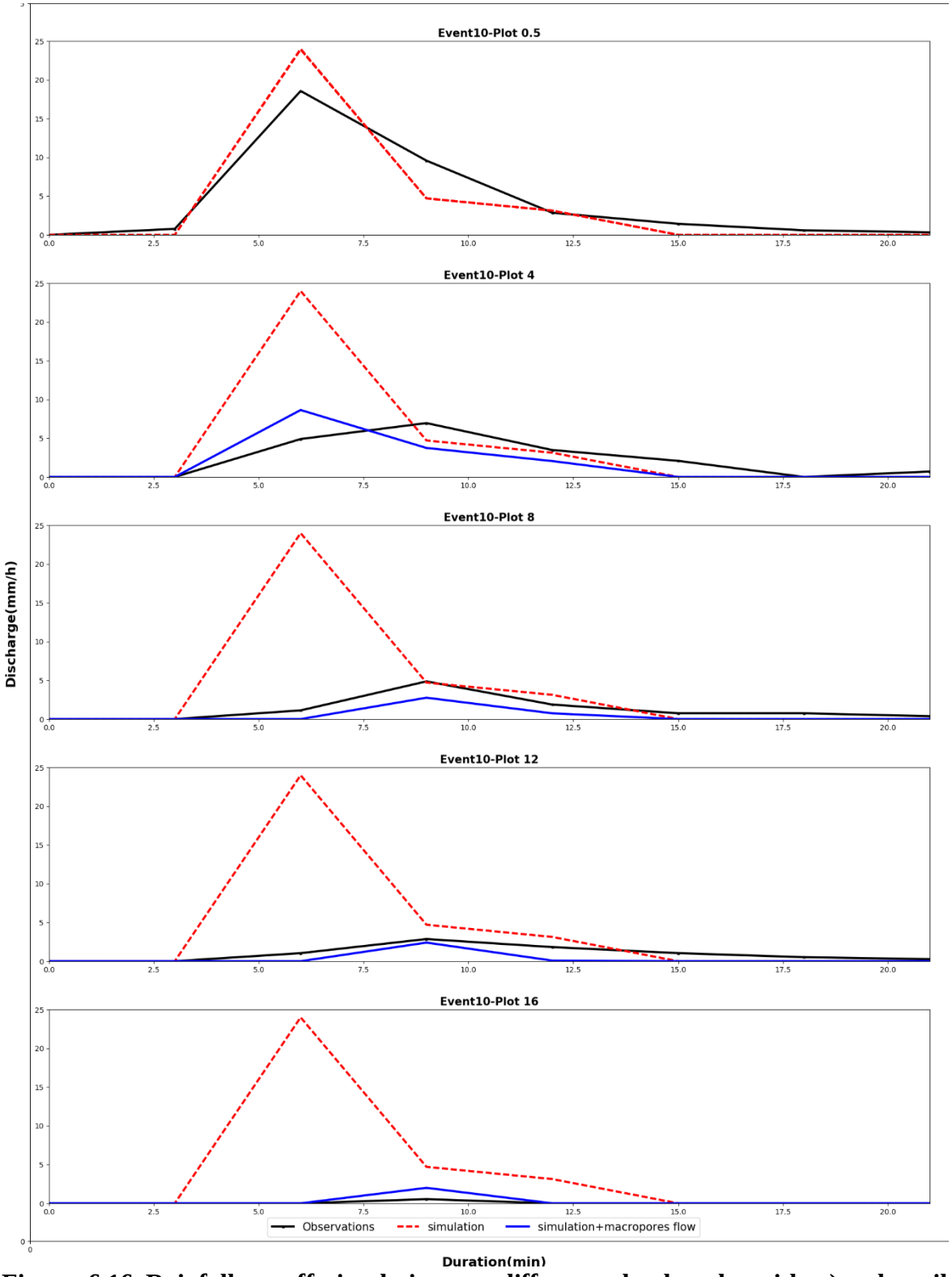

Figure 6.16 Rainfall-runoff simulations at different plot lengths with a) only soil infiltration model (red line) and b) soil infiltration and macropores filling-seeping models (blue line)

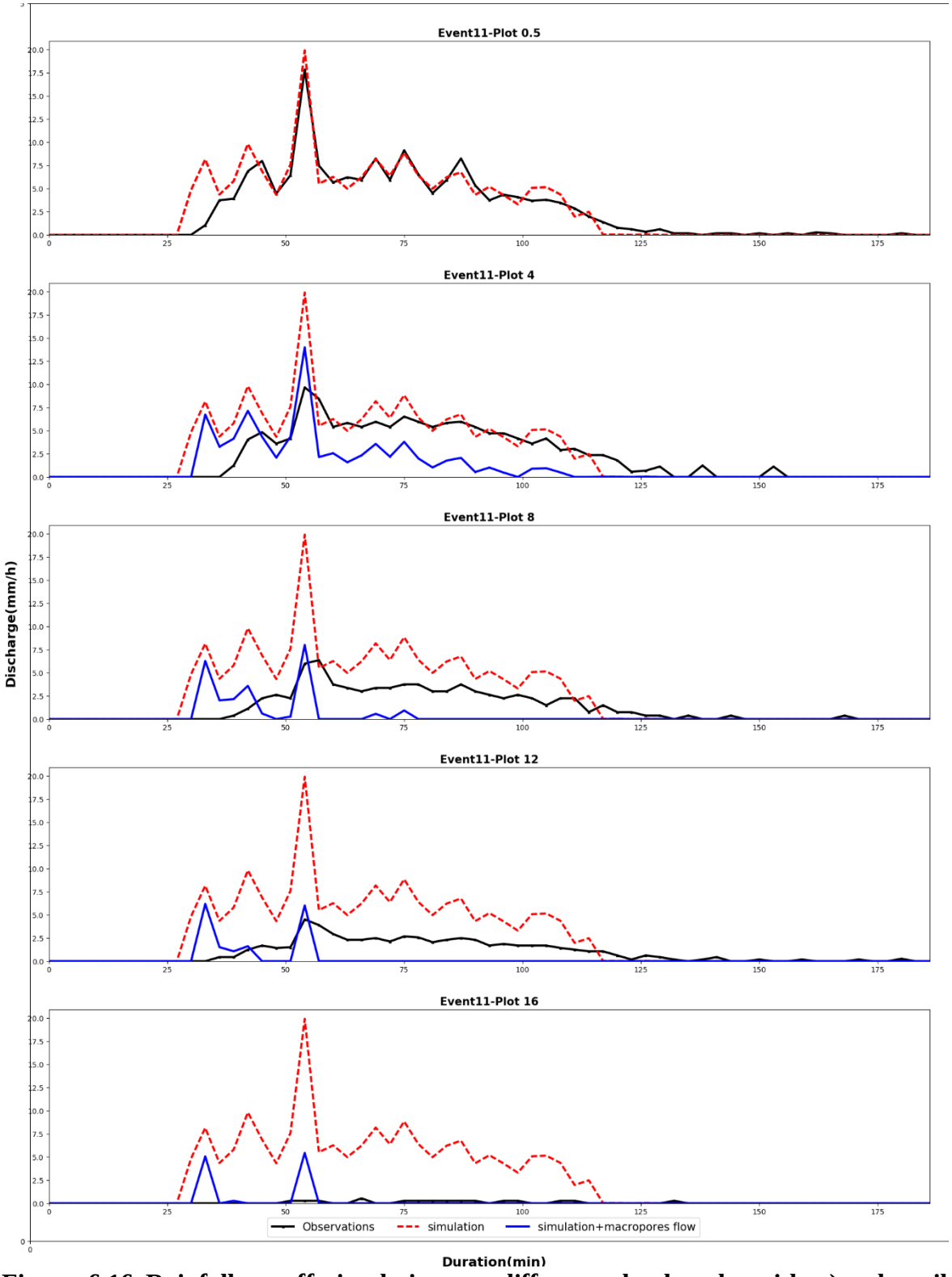

Figure 6.16 Rainfall-runoff simulations at different plot lengths with a) only soil infiltration model (red line) and b) soil infiltration and macropores filling-seeping models (blue line)

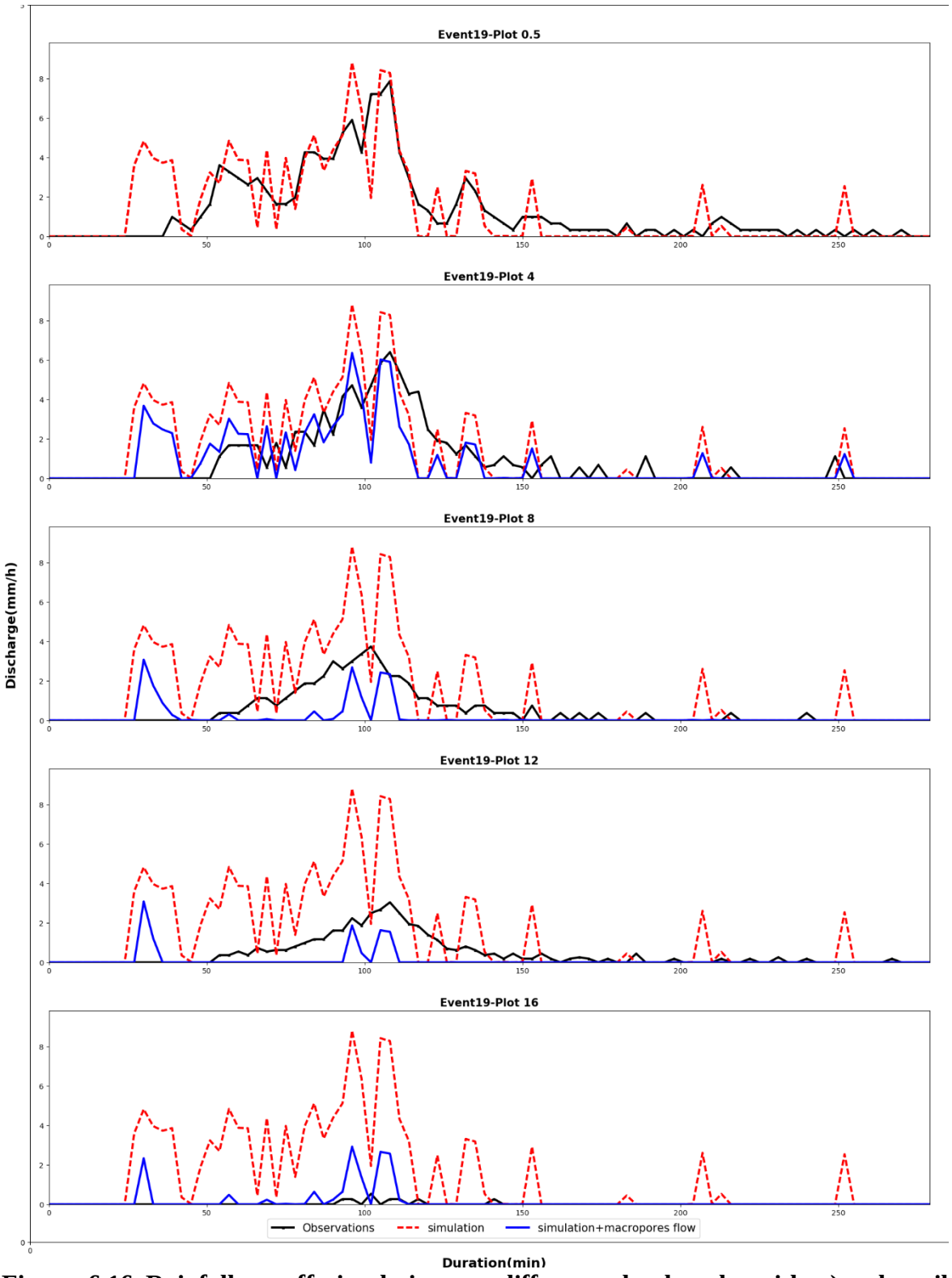

Figure 6.16 Rainfall-runoff simulations at different plot lengths with a) only soil infiltration model (red line) and b) soil infiltration and macropores filling-seeping models (blue line)

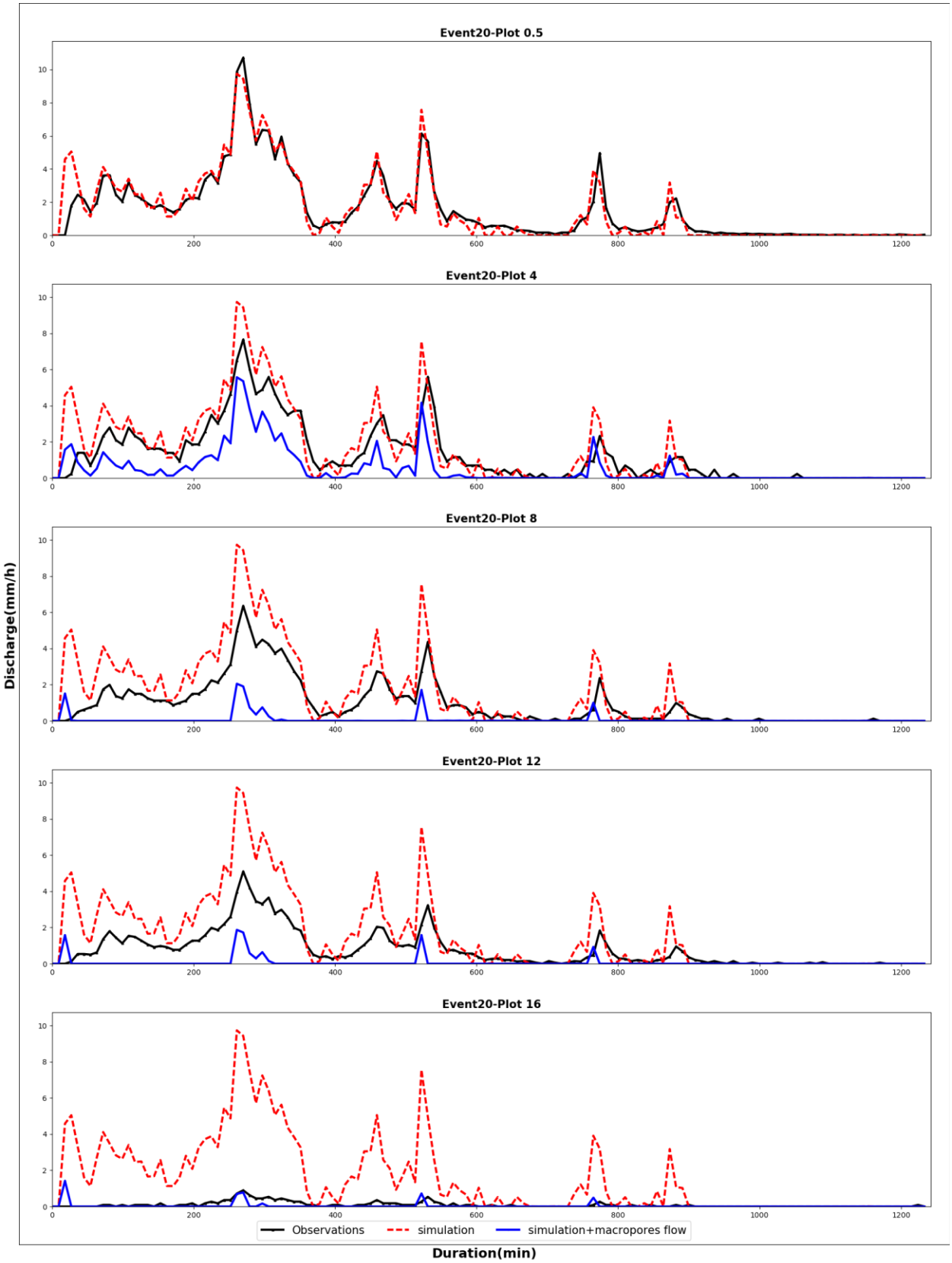

Figure 6.16 Rainfall-runoff simulations at different plot lengths with a) only soil infiltration model (red line) and b) soil infiltration and macropores filling-seeping models (blue line)

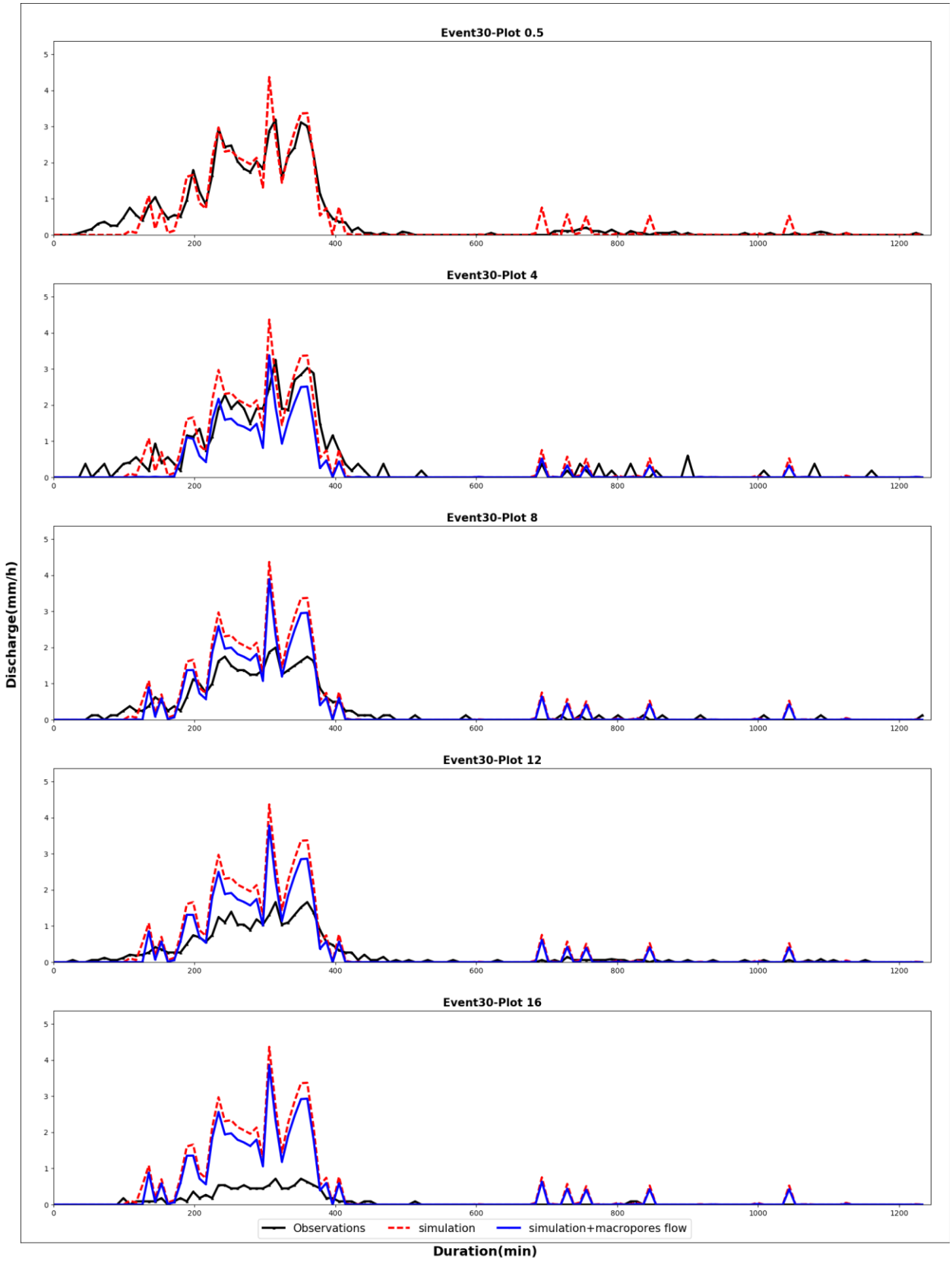

Figure 6.16 Rainfall-runoff simulations at different plot lengths with a) only soil infiltration model (red line) and b) soil infiltration and macropores filling-seeping models (blue line)

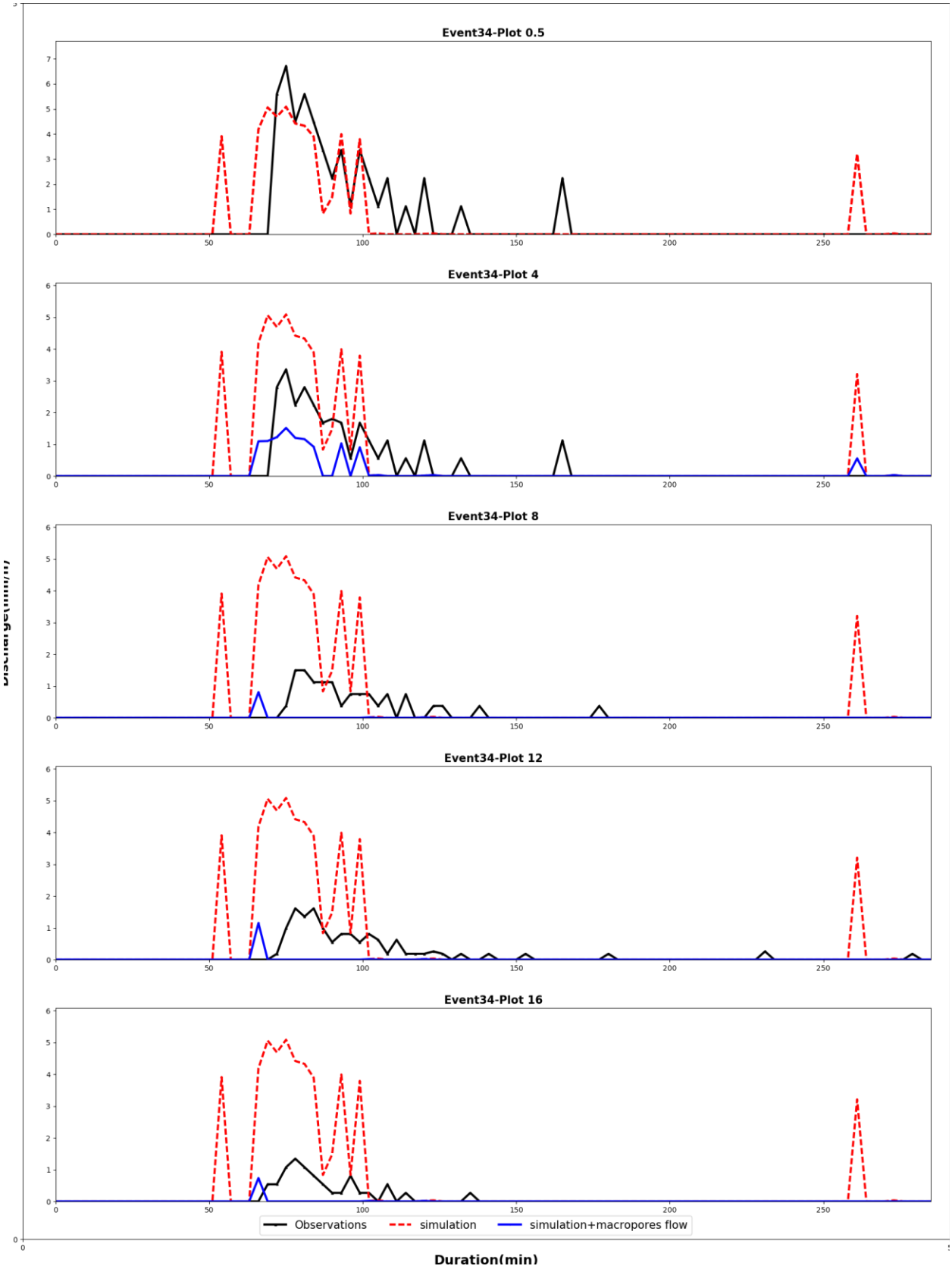

Figure 6.16 Rainfall-runoff simulations at different plot lengths with a) only soil infiltration model (red line) and b) soil infiltration and macropores filling-seeping models (blue line)

Models with macropores simulation captured runoff pulses. Peakflows from simulations with and without macropore flow were plotted against observed peakflow as shown in Figure 6.17. For all events, models with macropore flow resulted in lower peakflows (10%-90%). This trend increased with length as a result of higher macropore flow in longer plots.

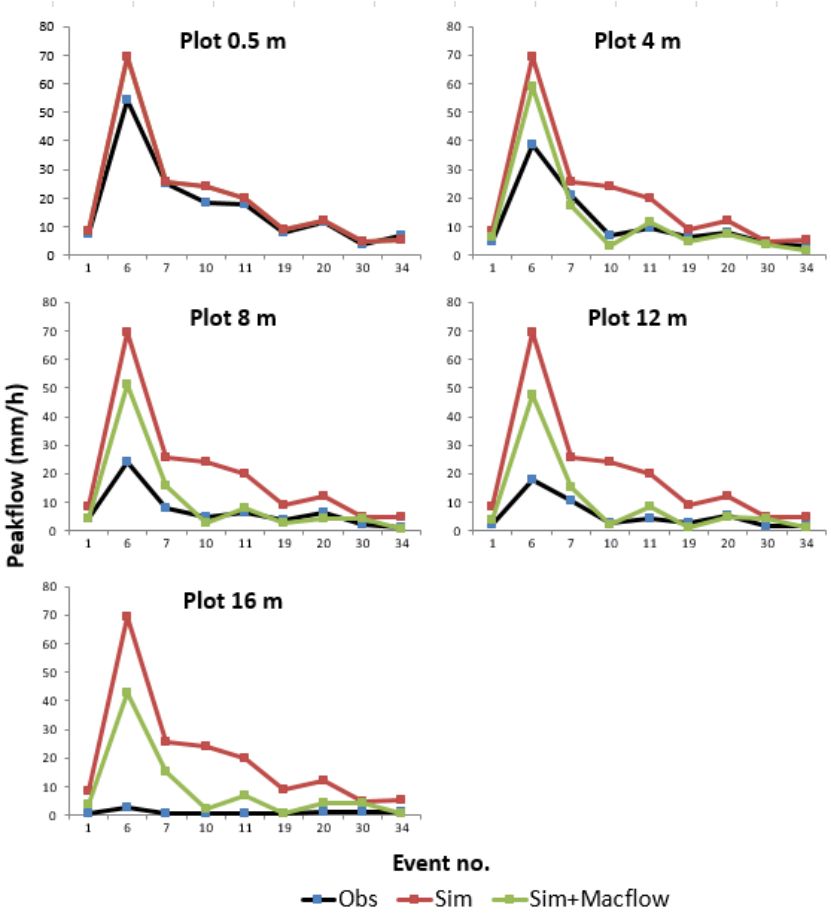

Figure 6.17 Simulated runoff peakflows with and without Macropore flow vs. observations

Models with macropore flow underestimated total runoff depth compared to observations for 4, 8, and 12 m plots (Figure 6.18). For 16 m plots, significant total runoff decrease was mostly explained by macropore flow especially in longer storms, although simulated values are still overestimated.

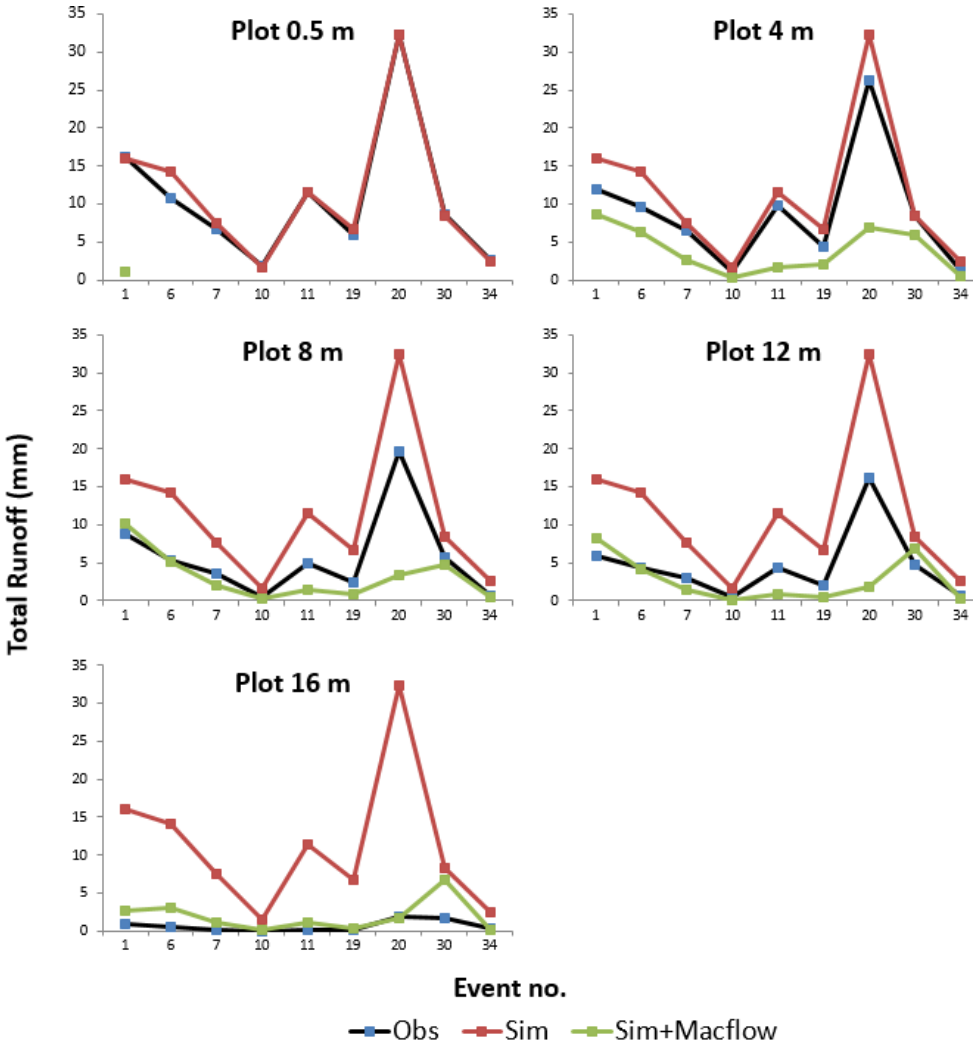

Figure 6.18 Simulated total runoffs with and without Macropore flow vs. observations

Nash–Sutcliffe efficiency coefficient (NSE) obtained from simulations with and without macropore flow were presented in Figure 6.19. Overall, models performance getting worse with plot lengths and the lowest NSE obtained for 16 m plot length. Models with macropore flow obtained higher NSE compared to models without macropore flow.

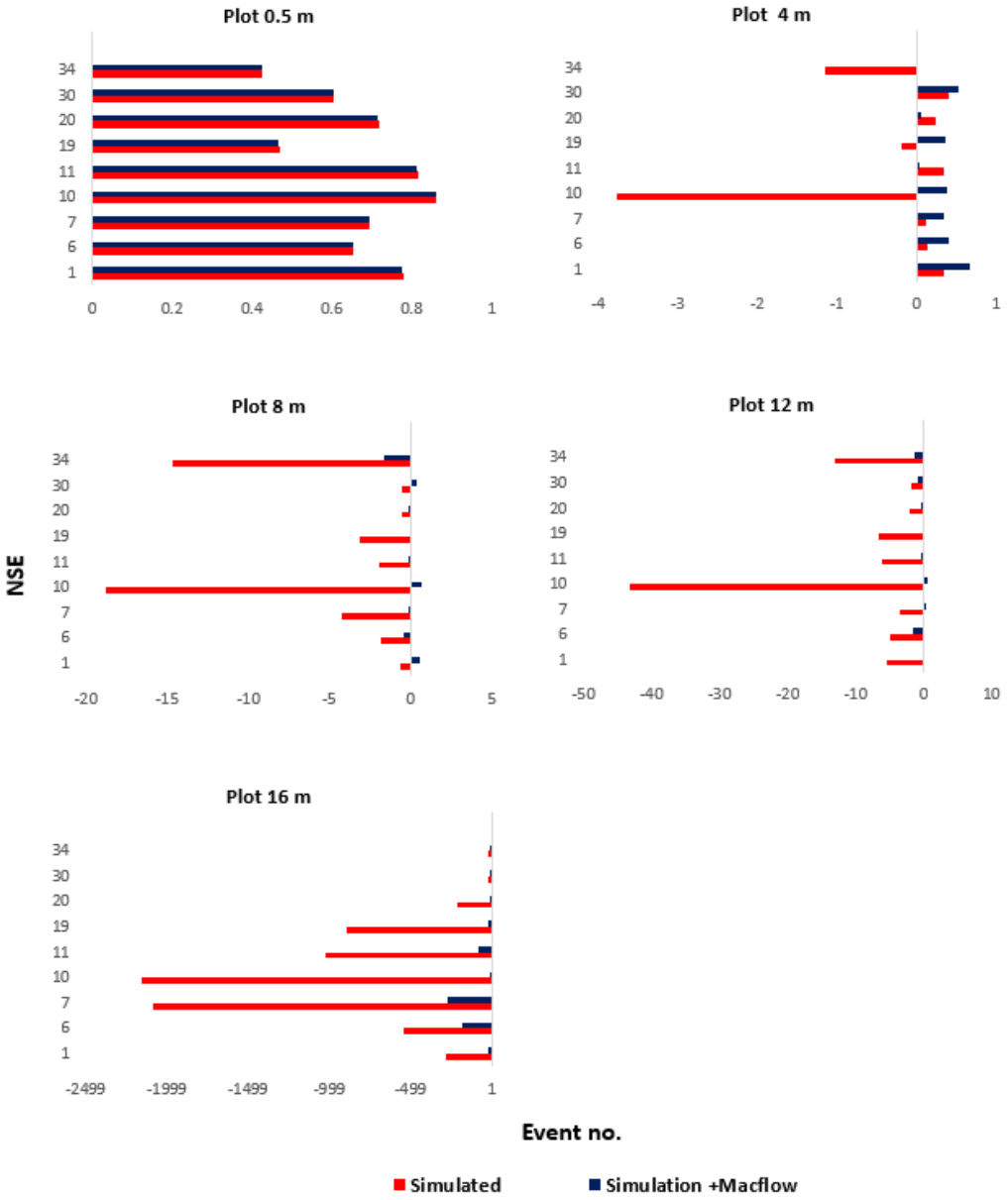

Figure 6.19 Nash–Sutcliffe model efficiency coefficient (NSE) obtained for simulations with and without macropore flow in relation to observations

Scaling behaviours from simulations with and without macropore flow were obtained by plotting total runoffs against plot lengths and compared to observations. As presented in Figure 6.20, models with macropore flow simulations have a better performance in capturing overland flow scaling effects for all events. The Figure shows a sharp scaling decrease for 4 m plot and then flattened for larger plots indicating inconsistence scaling effects captured by models with macropore flow.

Runoff depth scaling coefficients (SC_1) was calculated from simulations with and without macropore flow compared to observations. As shown in Figure 6.21, scaling coefficient (SC_1) from models with macropore flow obtained closer results to observations with a higher

R-squared (R^2=0.93) compared to simulations without macropore flow, but still 2.5 times higher than observations.

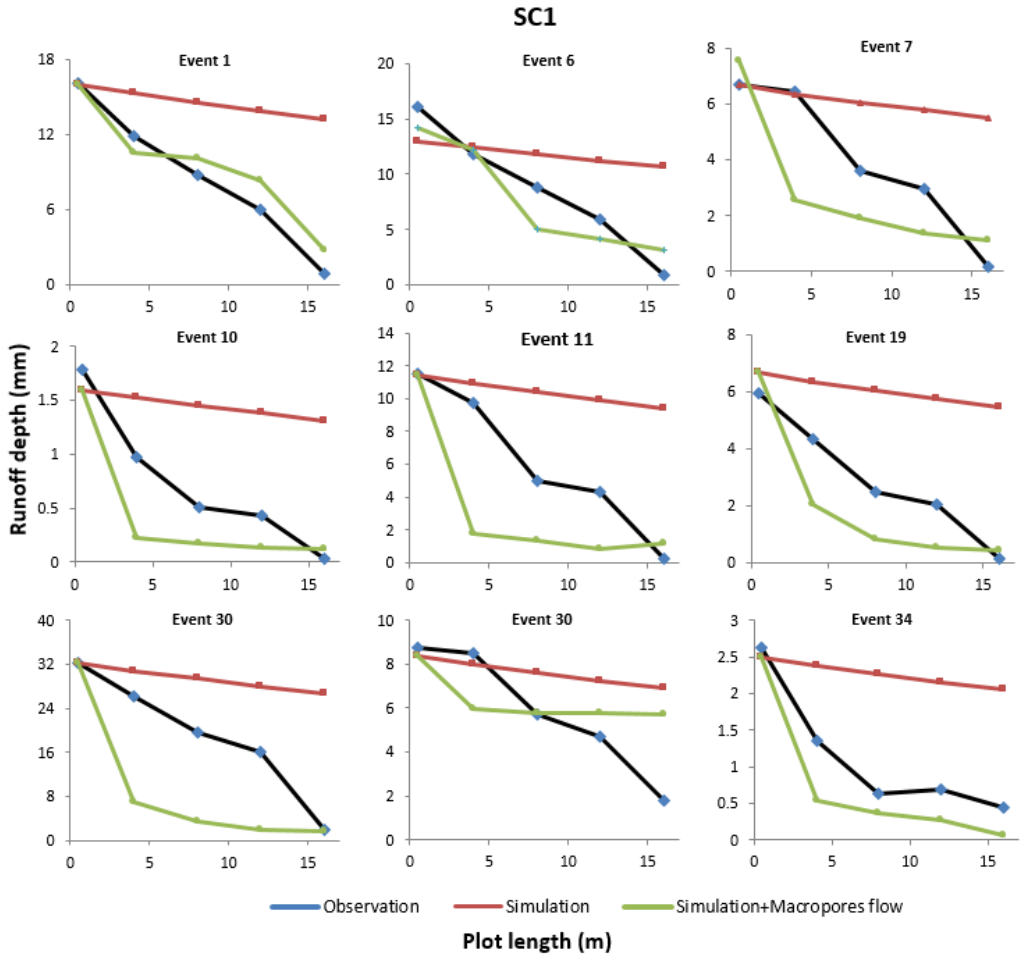

Figure 6.20 Total runoff depth and plot length for simulations with and without macropore flow vs. observation

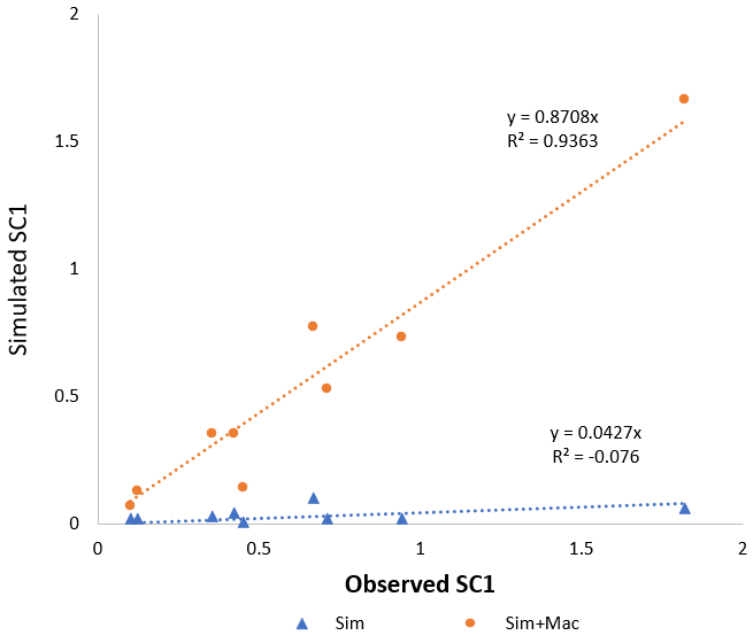

Figure 6.21 Runoff depth scaling coefficient from simulations with and without macropore flow versus observations.

6.4 Discussion and Conclusion

6.4.1 Experiment

The result from blue dye experiment showed that infiltration, both matrix and preferential flows happened 9 to 32 percent of the soil top layer in vertical soil profile across the transects. No increasing trend for blue dyed stains or breakthroughs was found associated with the distance from the uphill to downhill.

Field-based measurement showed that water repellency increased from 1 to 4 cm soil depth, becoming strongly repellent at 4 cm depth. (Ritsema et al., 1993, MacDonald and Huffman, 2004, Van der Sant et al., 2018) found similar patterns for the 4 cm topsoil and then gradual decrease of water repellency obtained from 4 cm downward. Restriction in soil infiltration within depth of 4 cm may result in a bottle neck condition (Bachmann and van der Ploeg, 2002) where vertical infiltration occurs mostly through ponding and macropore flow (Nyman et al., 2010).

Previous literature stating soil hydrophobicity is negatively controlled by soil water control (Hardie et al., 2013, Ritsema et al., 2001, Ritsema and Dekker, 1994) and probably disappears at saturation point (Sheridan et al., 2007, Nyman et al., 2010). However, measurement of soil gravimetric water content (GWC) showed that downhill transects contain lower GWC, with moderate R-squared ($R2 \sim 0.30$).

Together, the results from the proportion of blue dye, water repellency strength and water content of the soil across transects showed no systematic evidence of infiltration increase from the hillslope edge towards downhill, and thereby did not support the Hypothesis I.

6.4.2 Rainfall-runoff Models with Macropore Flow

A potential modelling hypothesis was proposed to simulate macropore flow by calculating pressure entry of the existing pores in relation to the runoff depth at the point, that are exceeded more frequently with distance downslope due to increasing runoff depths. Therefore, longer plots have higher macropore flow during longer events that explains higher scaling coefficients for these events.

Previous preferential flow models are either dual porosity or dual-permeability for preferential flow domain and adjacent soil matrix domain (Gerke, 2006, Šimůnek et al., 2003). In this study, constant hydraulic properties are considered for soil matrix infiltration and macropore flow simulations. Infiltration in the soil happens in four different stages of i) pre-ponding period when only *Ks* contributes to infiltration; ii) filling period during ponding

when runoff depth overcomes pressure entry of pores and macropores filling takes place depending on soil hydrophobicity ($Ks+Mac_{filling}$), iii) filling and seeping period when smaller macropores is still filling and larger pores are full of water and a continuous flow from these pores moving to underneath mineral soil ($Ks+Mac_{filling}+Mac_{seeping}$), and iv) seeping period when all pores are full of water conveying flow to underneath mineral soil.

The simulation results showed that simulated runoff without macropore flow produced overestimated runoffs for all events. Contrast between observations and over-estimated runoffs were pronounced more in longer plots. Thereby, ignoring macropores and preferential flows as dominants factors controlling infiltration in water repellent soil results in overestimation of runoffs where only traditional infiltration theory is considered. Similar conclusion also obtained by (Stoof et al., 2014a, Ritsema et al., 2005). Models with macropore flow simulations had closer peakflows to observations with a better model performance. Although, total runoff was under-estimated (<30%) for all events when macropore flow accounted in these simulations.

Scaling results from simulations with macropore flow were closer to observations with high R-squared (R^2=93), still 2.5 times higher. In summary, the outcome of macropore flow simulations supports Hypothesis II explaining decrease of runoff production per plot length as a result of higher runoff depth providing pressure entry, activating Macropore flow and preferential flow. Macropore flow simulations partly explained sudden decreases in runoff volume per unit width (L/m) in 16 m plot length.

The root of uncertainties associated with macropore flow simulations could be due to assumptions made for pores network, and pores geometry which rarely correspond to the actual macropores geometry. The impact of soil internal air pressure (air entrapment) under ponding condition and lateral preferential flow were also ignored in the macropore flow simulations. Disregarding lateral flow specifically may also contribute to the model uncertainties because hydrophobicity promotes lateral preferential flow at the interface between water repellent soil layer and the mineral layer beneath (Stoof et al., 2014a, Leelamanie and Karube, 2009, Gerke et al., 2015).

Chapter 7: Conclusions

This thesis has investigated overland flow scaling behaviour on a burnt dry hillslope. Methods for conducting the research project are rainfall-runoff monitoring under natural rainfalls, field and laboratory measurements, multiple regression analysis, process-based rainfall-runoff modelling, macropore and water repellency measurement at the site, and macropore flow modelling. A literature review was conducted, and research gaps were identified for overland flow scaling effects in relation to fire-induced water repellency, macropore flow and their interactions with rainfall properties (Chapter 1). The study site was selected on a dry eucalyptus hillslope located in West Gippsland, VIC Australia, severely burnt by bushfire in January 2013 (Chapter 2).

A multi-length monitoring plots were installed at the site and overland flow scaling behaviours was quantified from rainfall-runoff data collected during the second year following the fire. Two scaling coefficient indices were determined by fitting runoff depth and runoff ratio to the logarithm of plot length. These scaling metrics also used to quantify the scaling effects in previous studies (Chapter 3).

The role of rainfall characterises in controlling overland flow behaviours was investigated by conducting stepwise regression analysis for the runoff-generating storms selected from monitoring data (Chapter 4). Simulated scaling effects were obtained from rainfall-runoff models coupling rainfall temporal variations with soil infiltration and runon process (Chapter 5). Vertical pathways of activated macroporose, water repellency strength and soil water content were measured along the longest plots (16 m) to investigate whether infiltration increasing with distance downslope (Chapter 6). A macropore flow model was developed from conceptualised macropores networks generated for runoff plots to simulate macropore flow based on pressure entry of the individual pores in relation to runoff depth. Process-based rainfall-runoff model simulations were combined with macropore modelling to calculate direct infiltration, runon, and macropore flow under temporally varied rainfalls (Chapter 6).

The overall conclusions of the thesis are:

- **Overland flow scaling behaviours in a burned dry hillslope**

Rainfall-runoff data showed strong runoff scaling behaviours at the study site. Runoff depth decreased with plot length for all storm events, seasons and the whole study period. Collected runoff from replicated plots showed good agreement for all storm events, seasonally and the whole study period. Estimated scaling effects were insensitive to inclusion of non-rain intervals during events (2-10% change) and to the details of the event definition.

Scaling effects were calculated using data from previous literature studying scaling effects. The results show that that annual rainfall depth is a strong driver in controlling overland flow scaling.

- **Rainfall characteristics impacting scaling behaviours**

Result from multiple regression analysis showed that rainfall total depth (mm) is the most dominant factor in both overland flow generation and runoff depth scaling effects. Rainfall total depth and other rainfall parameters explained less variation in event runoff production as plot length increased, with R^2 reaching its lowest values at the longest plots (16 m). Similar conclusions were obtained when the relative impact of rainfall factors and soil properties on overland flow scaling were investigated with help of a previous analysis method by (Van de Giesen et al., 2000).

- **Simulated scaling effects from process-based rainfall-runoff models**

KINEROS2 was successfully calibrated to event hydrographs by varying soil and surface parameters to represent fire-induced water repellency. The key soil properties impacting simulated hydrographs were soil hydraulic conductivity (K_s), net capillary drive (G) and surface roughness.

Simulations with calibrated parameters underestimated runoffs in shorter plots and overestimated in longer plots; exhibiting weak scaling behaviour. The scaling effects demonstrated by the model were more than 10 times smaller than observed scaling effects.

The simulated scaling behaviours did not improve when the spatial variability of soil hydraulic conductivity (CV_{Ks}) was accounted in the models, with only slight changes in scaling effects (<3%). Together, these results suggest that models with traditional infiltration coupled with run-on process paradigm and rainfall temporal variability cannot explain the

observed scaling behaviour, even where spatially variability of soil hydraulic conductivity (CV_{Ks}) is considered.

- **Post-fire soil measurements**

Strong hydrophobicity was observed from the field measurements undertaken at the end of the second year following fire. Activated macropores under sprinkler experiments occurred mostly in the 4 cm of the topsoil profile with some finger flows going deeper. The blue dye experiment showed no systematic increase of activated macropore flow or breakthrough with distance. Measurements of soil water repellency and water content showed no systematic changes associated with distance downslope. Thereby, these measurements did not support the hypothesis of runoff scaling behaviour to be a result of infiltration increase with distance from uphill.

- **Models with Macropore Flow**

Macropore flow was modelled in relation to runoff depth satisfying pore entry pressure that is exceeded more frequently with distance downslope due to increased runoff depths. The macropores model was combined with rainfall-runoff model with traditional infiltration theory, runoff-runon, and rainfall temporal variability.

Accounting for macropore flow in the simulations resulted in runoff underestimation (<30%). However, models with macropore flow simulations provided closer predictions of runoff scaling behaviour with a higher R-squared (R^2=0.93), but 2.5 times higher than the observations. The simulations showed that macropore flow occurred more frequently with distance downslope due to increasing runoff depths and thereby longer plots had higher simulated macropore flow resulting in higher scaling effects. The study underpinned that traditional process-based models coupling soil infiltration and run-on process with rainfall temporal variation are not capable of capturing scaling effects while incorporating macropore flow into runoff estimates can improve simulated scaling effects.

Future Study

Overland flow scaling behaviours is mostly measured at different plot scales, while hydrological responses are modelled at catchment scales. The scaling metrics derived from this study was used to quantify scaling effects of runoff-rainfall measurements in the literature. The results showed that show that rainfall total depth impacted scaling effects. Other literature suggests that gradient, soil texture, and vegetation coverage also influence

scaling effects. Very few studies of runoff scaling systematically vary a number of these factors exist further study is required.

Observed runoff from replicated plots showed good agreement for all storm events, seasonally and the whole study period in this study. However, there is some experimental evidence that identical plots behave differently under apparently identical conditions (Wendt et al., 1986). This is not the case here which may indicate that burning attenuates variability between replicates. The level of variance between replicates may also depend on the magnitude of the measured runoff. This could be a topic for future research.

The outcome of this study supports the theory that macropore flow is the dominant factor to explain overland flow scaling behaviours in burnt dry hillslopes where soil is strongly hydrophobic. Therefore, to avoid large bias of simulations due to scaling effects, soil properties, run-on process and representation of macropore flow under high resolution rainfall are the minimum requirements for overland flow models and their parameterization. Furthermore, experiments that directly investigate macropore flow under rainfall event conditions are required.

The largest macropores are known to be highly unstable especially when rainfall heavily disturbs the soils during runoff producing events. More research is required to allow generalization of macropore flow in relation to runoff depth and rainfall characteristics. This will lead to quantitative metrics for runoff scaling behaviours as a function of activated macropores and preferential flow at point scales, soil water repellency, and rainfall patterns. The impact of soil internal air pressure (air entrapment) under ponding condition and lateral preferential flow were ignored in the macropore flow simulations. Disregarding lateral flow specifically contributes to the model uncertainties as hydrophobicity was known to increase lateral preferential flow at the interface between water repellent soil layer and the mineral layer beneath (Stoof et al., 2014a, Gerke et al., 2015). More investigation is required to measure the impact of air pressure and lateral flow in macropore flow.

Appendices

Appendix 3. 1 Primary calibrations of small plots and rain gauges

Gauges	Pre- installation calibration	Tips	Lit per tip	Tips per lit	Field calibration	Tips	Lit per tip	Tips per lit
Tipping buckets		1	0.5	2		1	0.5	2
R1		103	$6.34x10^{-3}$	157.73		103	$6.34x10^{-3}$	157.73
S1		105	$6.22 x10^{-3}$	160.8		104	$6.34x10^{-3}$	159.26
R2		120	$5.44 x10^{-3}$	183.77		95	$6.87x10^{-3}$	145.482
S2		105	$6.22 x10^{-3}$	160.8		113	$5.78x10^{-3}$	173.05
R3		103	$6.34 x10^{-3}$	157.73		152	$4.29 x10^{-3}$	232.77
S3		104	$6.28 x10^{-3}$	159.26		177	$3.69 x10^{-3}$	271.06

Appendix 3. 2 Summary of mean intensity of runoff-generated storms for the whole study period

Event no.	Mean Intensity of Rainfall Pulses (mm/h)							
	I_{3mins}	I_{6mins}	I_{9mins}	I_{15mins}	I_{24mins}	I_{30mins}	I_{45mins}	I_{60mins}
1	2.02	2.10	2.04	2.05	2.06	2.07	2.10	2.15
2	0.30	0.30	0.30	0.31	0.31	0.31	0.32	0.33
3	3.99	4.03	4.06	4.16	4.12	4.41	4.63	4.76
4	2.13	2.34	2.18	2.20	2.23	2.25	2.28	2.35
5	2.53	2.58	2.53	2.54	2.56	2.57	2.61	2.65
6	2.15	2.81	2.02	1.81	1.65	1.59	1.50	1.53
7	2.85	3.69	2.43	2.19	2.04	2.00	1.99	2.17
8	1.08	1.08	1.08	1.08	1.08	1.09	1.09	1.10
9	1.30	1.37	1.31	1.32	1.36	1.39	1.41	1.46
10	1.48	1.46	0.56	0.37	0.27	0.24	0.21	0.44
11	0.86	0.88	0.87	0.87	0.87	0.87	0.84	0.82
12	0.77	0.89	0.78	0.78	0.76	0.75	0.72	0.73
13	0.45	0.45	0.45	0.46	0.46	0.47	0.47	0.46
14	1.89	2.14	1.84	1.82	1.78	1.75	1.68	1.68
15	0.13	3.51	2.12	1.85	1.65	1.54	1.32	1.48
16	0.56	0.57	0.57	0.57	0.57	0.57	0.57	0.58
17	0.06	1.10	1.08	1.08	1.08	1.08	1.07	1.07
18	1.25	1.41	1.27	1.28	1.29	1.29	1.29	1.32
19	1.26	1.36	1.28	1.28	1.28	1.27	1.24	1.25
20	1.90	1.95	1.91	1.91	1.91	1.91	1.90	1.91
21	0.31	0.33	0.31	0.31	0.31	0.30	0.29	0.28
22	0.63	0.66	0.63	0.63	0.63	0.62	0.62	0.63
23	1.47	1.51	1.49	1.50	1.51	1.51	1.52	1.54
24	0.37	0.38	0.37	0.37	0.36	0.36	0.36	0.36
25	1.11	1.11	1.10	1.11	1.11	1.12	1.13	1.14
26	0.97	0.97	0.97	0.98	0.98	0.98	0.98	0.99
27	0.49	0.52	0.49	0.49	0.48	0.48	0.46	0.45
28	0.43	0.45	0.43	0.43	0.43	0.43	0.43	0.43
29	0.52	0.53	0.49	0.49	0.51	0.51	0.46	0.45
30	0.61	0.61	0.62	0.62	0.62	0.62	0.63	0.64
31	0.51	0.51	0.51	0.51	0.51	0.51	0.52	0.53
32	0.47	0.47	0.47	0.47	0.47	0.48	0.48	0.48
33	0.21	0.21	0.21	0.21	0.21	0.22	0.22	0.22
34	0.82	0.88	0.80	0.81	0.81	0.81	0.81	0.84
35	0.54	0.70	0.43	0.39	0.32	0.29	0.23	0.23
36	0.36	0.59	0.37	0.31	0.25	0.22	0.16	0.16
37	0.80	0.90	0.79	0.78	0.76	0.75	0.74	0.75
38	0.31	0.35	0.31	0.30	0.29	0.29	0.28	0.28
39	0.74	0.78	0.75	0.76	0.76	0.77	0.77	0.79
40	0.37	0.37	0.36	0.37	0.37	0.37	0.37	0.38
41	0.29	0.29	0.29	0.29	0.29	0.29	0.29	0.29
Mean	1.01	1.20	1.05	1.03	1.01	1.01	1.00	1.03
Median	0.74	0.88	0.78	0.78	0.76	0.75	0.74	0.75
Minimum	0.06	0.21	0.21	0.21	0.21	0.22	0.16	0.16
Maximum	3.99	4.03	4.06	4.16	4.12	4.41	4.63	4.76

Appendix 3. 3 Summary of maximum intensity of runoff-generated storms for the whole study period

Event no.	Maximum Intensity of Rainfall Pulses (mm/h)							
	I_{3mins}	I_{6mins}	I_{9mins}	I_{15mins}	I_{24mins}	I_{30mins}	I_{45mins}	I_{60mins}
1	8.84	7.76	7.22	6.79	6.88	6.72	6.40	6.15
2	4.51	3.86	3.17	2.51	1.64	1.31	1.07	0.80
3	69.46	43.96	35.18	29.54	23.21	23.34	17.28	14.19
4	9.28	8.54	6.66	6.28	6.20	6.13	5.76	5.42
5	8.94	7.83	6.68	5.98	5.78	5.61	5.35	5.06
6	70.05	85.89	32.85	24.46	17.20	14.52	10.59	9.02
7	26.16	47.77	22.45	16.10	11.05	9.17	6.95	6.06
8	7.61	6.13	5.24	5.21	4.89	4.82	4.43	4.39
9	4.90	4.75	4.14	3.73	3.01	3.11	2.79	2.49
10	24.44	29.61	11.03	6.62	4.14	3.31	2.21	2.30
11	20.38	14.24	11.53	10.25	8.87	8.51	8.05	7.64
12	11.10	10.24	7.24	5.48	3.86	3.21	2.22	1.90
13	6.43	5.34	5.25	4.51	3.93	3.15	2.10	1.60
14	8.99	15.69	8.23	6.98	6.43	6.26	5.93	5.70
15	0.99	38.08	14.95	10.84	9.16	8.04	5.99	5.63
16	12.74	11.00	8.71	6.69	5.22	4.48	3.20	2.77
17	1.60	28.92	22.34	17.83	14.65	12.73	9.87	8.56
18	4.77	5.59	3.57	3.26	2.92	2.90	2.95	2.75
19	9.10	8.78	7.48	7.15	6.36	6.02	5.10	4.76
20	12.32	11.09	11.06	10.59	9.61	9.29	8.44	7.90
21	9.86	7.42	7.61	6.43	5.10	4.56	3.37	2.59
22	9.05	7.51	6.73	5.20	3.47	2.84	2.32	1.99
23	9.23	7.42	6.53	6.11	5.67	5.23	4.99	4.31
24	34.51	17.59	12.43	7.57	4.81	3.91	2.88	2.52
25	5.55	5.05	4.52	3.90	3.42	3.42	3.27	2.99
26	6.21	4.93	4.72	4.21	4.02	4.01	3.75	3.62
27	7.49	10.87	5.75	4.50	3.93	3.39	2.90	2.30
28	4.27	4.00	2.99	2.02	1.48	1.22	1.16	1.07
29	8.40	7.60	5.44	4.25	3.13	2.57	2.04	1.63
30	5.19	4.85	4.74	4.29	3.84	3.72	3.37	3.45
31	4.63	3.42	3.56	2.54	2.38	2.13	1.95	1.68
32	6.15	5.42	5.00	4.00	3.07	2.94	2.67	2.44
33	3.52	2.21	1.84	1.42	1.31	1.09	1.02	0.80
34	5.46	5.26	5.32	5.15	4.54	4.24	3.29	2.72
35	5.33	10.14	4.34	3.89	3.11	2.87	2.32	2.03
36	10.41	14.68	5.26	4.35	3.27	2.71	1.81	1.41
37	5.33	6.71	3.74	3.38	3.20	2.94	2.70	2.33
38	4.33	5.17	2.17	1.98	1.91	1.64	1.42	1.18
39	4.35	4.52	3.59	3.12	2.63	2.33	2.27	2.01
40	3.95	3.78	2.89	2.46	2.09	2.03	1.62	1.48
41	4.11	2.86	2.89	2.27	2.03	1.82	1.60	1.36
Mean	11.71	13.08	8.22	6.68	5.45	4.98	4.13	3.68
Median	7.49	7.51	5.44	5.15	3.93	3.42	2.95	2.59
Minimum	0.99	2.21	1.84	1.42	1.31	1.09	1.02	0.80
Maximum	70.05	85.89	35.18	29.54	23.21	23.34	17.28	14.19

Appendix 3. 4 Scattered *plots* of runoff depths (mm) vs. plot lengths (m) when 16 m plots excluded for 41 events representing runoff depth scaling coefficient (SC1) without 16 m

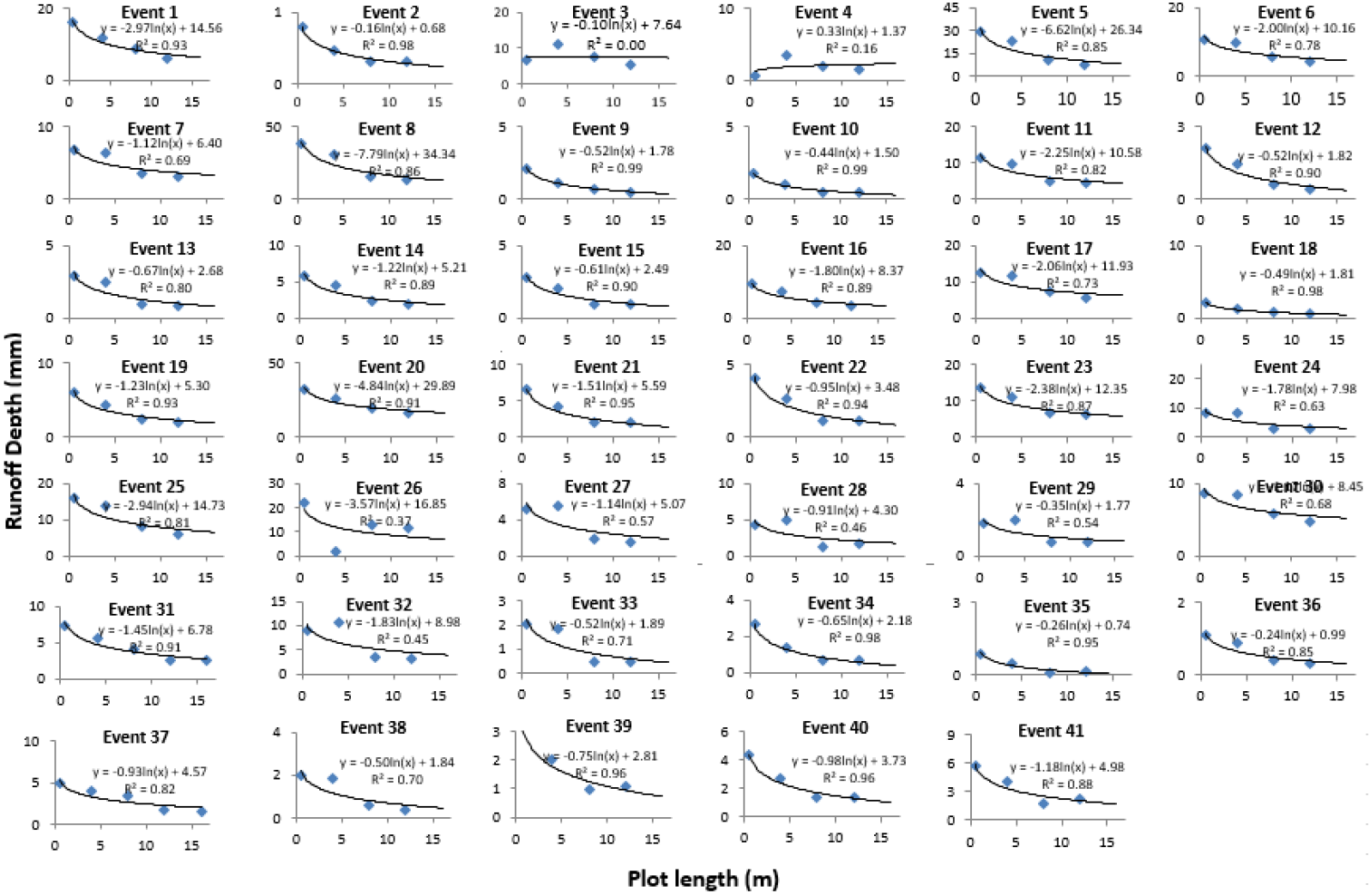

Appendix 3. 5 Scattered plots of runoff ratio (%) vs. plot lengths (m) when 16 m plots excluded for 41 events representing runoff ratio scaling coefficient (SC2) without 16 m plots

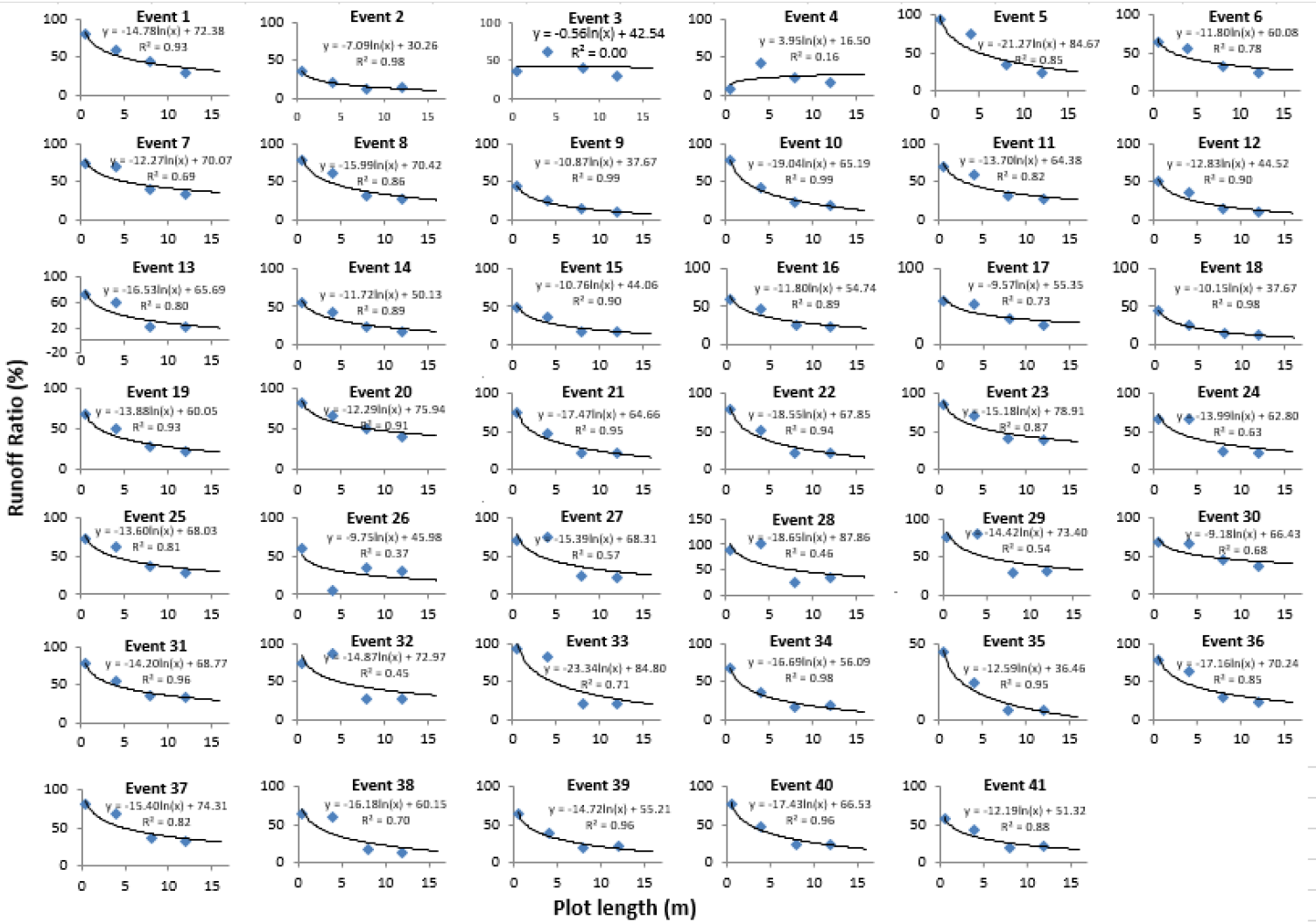

Appendix 3. 6 Volumetric and temporal indices of main pulses of rainfall events and their associated runoff productions for plots with different length

Event No.	Rainfall									Runoff									
	Start	End	Duration	Total	Mean*	peak	CV*	Ř	DT	Plot 0.5m		Plot 4m		Plot 8m		Plot 12m		Plot 16m	
										Depth	Ratio	Depth	Ratio	Depth	Ratio	Depth	Ratio	Depth	Ratio
			hours	mm	mm/h					mm	%	mm	%	mm	%	mm	%	mm	%
1	13/10/2014 20:15	14/10/2014 2:30	6.3	19.6	3.2	8.8	2.9	4.4	6.3	15.5	79.0	11.2	57.2	8.4	42.6	5.6	28.4	0.6	2.9
2	14/10/2014 13:06	14/10/2014 14:54	3.2	1.2	2.2	4.5	14.0	3.0	0.5	0.5	45.0	0.4	32.9	0.3	23.4	0.2	18.5	0.0	1.1
3	27/10/2014 8:48	27/10/2014 11:15	2.5	17.7	8.0	69.5	1.3	25.4	2.1	6.2	35.4	10.8	61.3	7.3	41.2	5.0	28.6	0.6	3.4
4	1/11/2014 6:30	1/11/2014 9:24	3.0	8.3	3.5	9.3	3.3	5.0	2.5	0.5	5.7	3.4	40.5	1.8	21.7	1.3	16.1	0.2	1.9
5	15/11/2014 19:21	16/11/2014 5:54	10.6	31.1	3.3	8.9	3.0	4.3	10.2	29.0	93.1	23.0	73.8	11.0	35.3	7.3	23.6	0.7	2.2
6	24/11/2014 14:15	24/11/2014 16:09	2.0	14.3	7.5	70.1	1.3	25.6	1.7	9.1	63.8	8.4	58.8	4.8	33.6	3.7	26.1	0.4	2.7
7	5/12/2014 8:03	5/12/2014 10:03	2.1	9.1	4.6	26.2	2.2	12.6	1.7	6.7	73.1	6.4	70.4	3.5	38.3	3.0	32.3	0.1	1.6
8a	5/12/2014 20:21	6/12/2014 12:15	16.0	7.7	1.3	7.6	20.7	2.4	3.1	5.1	66.3	3.6	47.1	1.8	23.4	1.6	20.9	0.1	1.4
8b	6/12/2014 22:36	7/12/2014 15:36	17.1	36.4	2.2	5.6	4.3	3.2	13.4	29.2	80.3	24.4	67.0	12.5	34.2	10.3	28.3	0.9	2.5
9	18/12/2014 16:39	18/12/2014 19:21	2.8	4.7	2.1	4.9	5.5	3.0	1.8	2.1	44.3	1.1	24.2	0.6	13.4	0.4	7.7	0.0	0.6
10	8/01/2015 17:30	8/01/2015 17:48	0.4	2.3	11.4	24.4	1.7	17.4	0.3	1.7	75.0	0.9	39.8	0.5	21.4	0.4	16.6	0.0	1.2
11	9/01/2015 15:15	9/01/2015 17:21	2.2	10.7	5.5	20.4	1.9	7.7	2.6	8.2	76.5	6.8	63.4	3.9	36.7	2.9	26.8	0.2	1.9
12	13/01/2015 14:36	13/01/2015 17:03	2.5	4.0	2.2	11.1	6.3	4.9	1.2	2.0	49.5	1.4	35.5	0.6	14.0	0.4	9.0	0.0	0.3
13	13/01/2015 23:06	14/01/2015 2:12	3.2	3.7	2.4	6.4	8.4	3.9	1.3	2.6	69.5	2.2	59.4	0.9	23.4	0.7	19.9	0.0	1.1
14	20/01/2015 23:36	21/01/2015 2:33	3.0	10.4	3.6	9.0	2.6	4.9	3.2	5.7	54.6	4.3	41.1	2.3	22.4	1.7	16.8	0.1	0.5
15	21/01/2015 15:33	21/01/2015 16:33	1.1	5.7	6.0	19.9	1.9	12.6	1.1	2.7	48.1	1.9	34.3	0.9	15.9	0.9	15.7	0.0	0.0
16	29/01/2015 14:24	29/01/2015 19:06	4.8	9.3	2.8	12.7	5.1	4.7	2.9	6.8	73.4	5.8	62.0	3.4	36.6	2.7	29.0	0.2	1.9
17	14/02/2015 7:09	14/02/2015 10:30	13.1	12.4	4.0	32.0	2.6	11.4	2.4	7.3	59.1	8.4	67.3	5.5	44.2	4.1	32.9	0.4	3.2
18	23/02/2015 13:42	23/02/2015 15:48	2.3	4.8	2.3	4.8	4.2	3.3	1.7	1.9	40.1	1.0	21.8	0.7	13.7	0.4	9.3	0.1	1.1
19	28/02/2015 22:30	1/03/2015 1:00	2.6	8.3	3.6	9.1	2.8	4.9	2.6	5.3	63.4	4.0	48.3	2.3	28.2	1.9	22.4	0.1	1.3
20	7/04/2015 5:27	7/04/2015 20:18	14.9	39.3	3.3	12.3	3.6	5.1	11.9	31.7	80.7	25.8	65.5	19.3	49.1	15.8	40.3	1.8	4.7
21	25/04/2015 6:21	25/04/2015 12:39	6.4	3.4	2.1	9.9	18.6	4.6	1.1	2.3	67.1	1.4	42.0	0.7	19.7	0.6	17.1	0.0	0.8
22	5/05/2015 8:21	5/05/2015 15:09	6.9	4.9	2.2	9.0	13.8	4.0	1.7	3.8	77.0	2.5	50.2	1.1	22.7	1.1	22.4	0.1	1.1
23	10/05/2015 4:30	10/05/2015 13:09	8.7	15.6	2.4	9.2	5.4	3.9	5.3	13.4	86.2	10.9	70.0	6.4	41.0	6.0	38.5	0.7	4.2
24	13/05/2015 1:30	14/05/2015 11:48	34.4	12.7	1.5	34.5	23.0	6.5	3.4	8.4	66.0	8.4	66.1	2.9	23.0	2.9	22.5	0.1	1.2
25	21/05/2015 13:12	22/05/2015 8:39	19.5	21.6	1.9	5.5	8.5	2.9	8.3	15.8	73.1	13.6	62.8	8.0	36.8	6.0	27.9	0.3	1.5

26	17/06/2015 17:45	19/06/2015 7:27	37.8	36.6	1.7	6.2	9.6	2.6	14.5	22.3	60.8	2.1	5.8	12.8	34.9	11.4	31.2	1.2	3.4
27	2/07/2015 3:51	2/07/2015 9:24	5.6	6.4	2.1	7.5	8.4	3.1	2.4	4.8	75.3	5.2	81.9	1.8	27.7	1.5	23.6	0.5	7.4
28	11/07/2015 0:12	11/07/2015 10:03	9.9	4.9	1.8	4.3	19.6	2.8	1.9	4.4	89.2	5.0	101.9	1.2	25.3	1.7	35.4	0.4	8.2
29	11/07/2015 14:42	11/07/2015 17:33	2.9	2.4	2.7	8.4	12.1	4.7	0.8	1.8	73.9	1.8	76.6	0.7	29.5	0.7	28.6	0.1	6.1
30	12/07/2015 15:21	12/07/2015 23:24	8.1	11.5	2.2	5.2	6.2	3.0	4.3	8.3	72.7	7.9	69.2	5.5	47.8	4.4	38.5	1.8	15.3
31	13/07/2015 17:36	14/07/2015 2:36	9.1	7.3	1.5	4.6	11.9	2.3	3.0	5.6	77.3	3.9	53.7	2.5	34.8	2.4	33.4	1.0	14.4
32	15/07/2015 22:27	16/07/2015 23:21	25.9	12.1	1.8	6.2	19.8	2.8	4.7	9.0	74.4	10.8	89.0	3.4	27.9	3.2	26.4	1.3	10.5
33	17/07/2015 23:12	18/07/2015 6:48	7.7	2.2	1.3	3.5	33.8	2.1	0.9	2.0	91.5	1.8	83.9	0.4	19.6	0.4	19.7	0.1	6.1
34	22/07/2015 5:45	22/07/2015 8:42	3.0	3.7	2.4	5.5	8.1	4.0	1.2	2.6	71.8	1.3	36.8	0.6	17.4	0.7	18.3	0.4	12.1
35	24/07/2015 17:12	24/07/2015 19:24	2.3	2.0	2.7	5.3	10.4	3.9	0.7	0.9	42.9	0.5	24.0	0.1	5.5	0.1	5.6	0.1	5.3
36	24/07/2015 21:39	24/07/2015 22:54	1.3	1.4	2.6	10.4	9.5	5.7	0.4	1.0	73.3	0.8	54.5	0.4	26.6	0.3	18.6	0.2	12.4
37	25/07/2015 2:39	25/07/2015 6:57	4.4	4.9	2.6	5.3	7.9	3.4	1.7	3.9	79.8	3.3	66.9	1.7	35.4	1.5	31.2	0.9	18.5
38	26/07/2015 1:45	26/07/2015 11:30	9.8	3.1	1.8	4.3	31.7	3.1	1.1	2.0	64.6	1.8	60.4	0.6	18.4	0.4	12.2	0.2	5.7
39	1/08/2015 6:57	1/08/2015 11:00	4.1	5.0	1.8	4.4	8.0	2.9	1.9	3.0	59.7	1.9	37.5	0.9	17.1	1.0	19.7	0.7	13.9
40	3/08/2015 3:09	3/08/2015 18:15	15.2	5.6	1.6	3.9	25.3	2.3	2.3	4.3	77.4	2.7	47.9	1.4	24.4	1.4	24.7	0.8	13.7
41	5/08/2015 3:00	6/08/2015 12:21	33.4	9.7	1.3	4.1	33.8	2.2	4.0	5.6	58.1	4.1	42.1	1.8	18.5	2.2	22.5	1.2	12.1

- *Mean* is mean value of rainfall pulses*
- *CV* is average value of coefficient variable of rainfall pulses*
- *Ř is Depth-weighted rainfall intensity from Van Dijk (2002)*
- *DT rainfall pulses duration from Van Dijk (2002)*

Appendix 3. 7 Main pulse of rainfall events and generated runoffs in plots with different length, left vertical axis is the runoff rate, right vertical axis is the rainfall rate and the horizontal axis is the duration of the rainfall-runoff event (min)

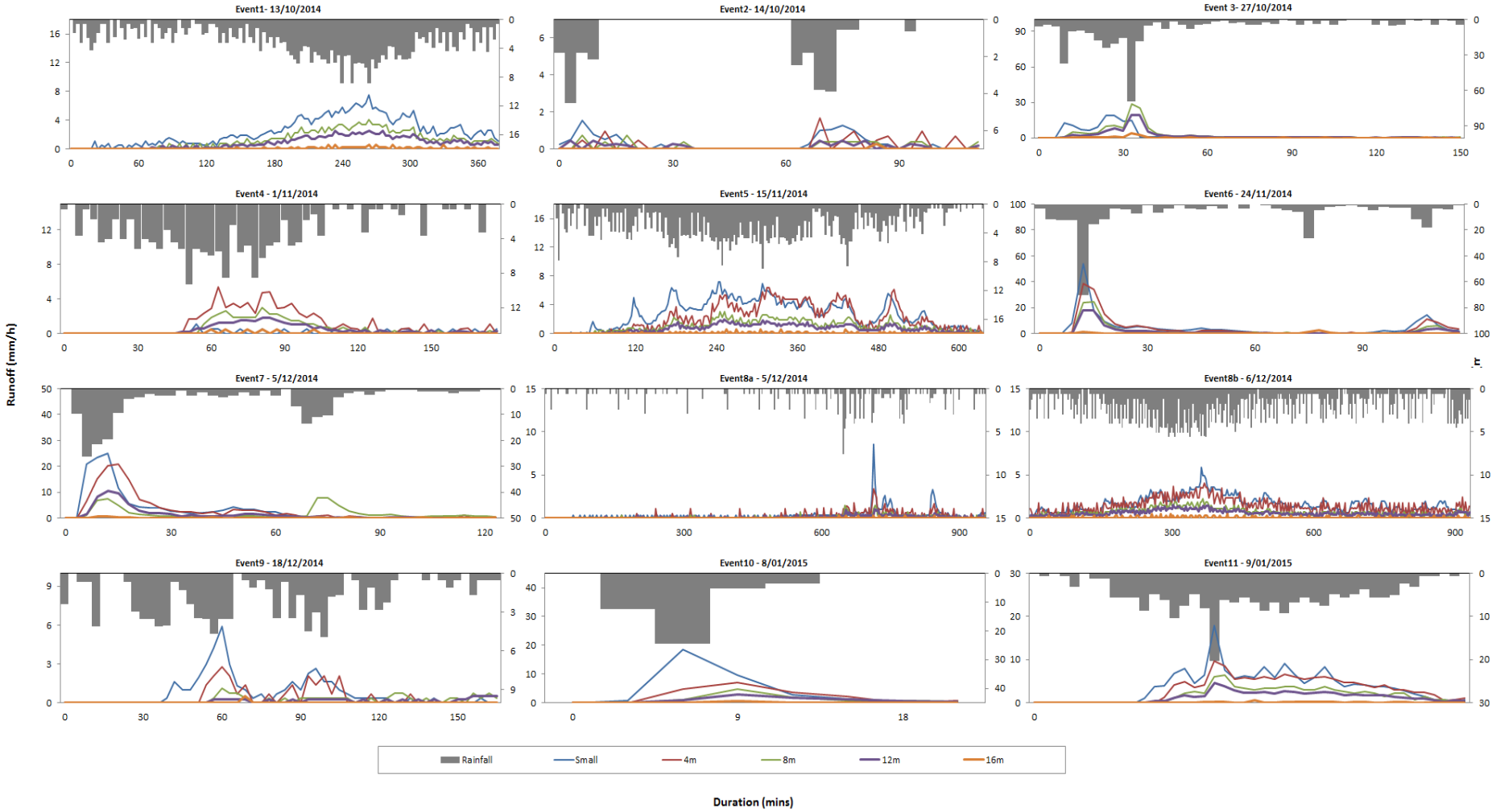

Appendix 3.7. Main pulse of rainfall events and generated runoffs in plots with different length, left vertical axis is the runoff rate, right vertical axis is the rainfall rate and the horizontal axis is the duration of the rainfall-runoff event (min)

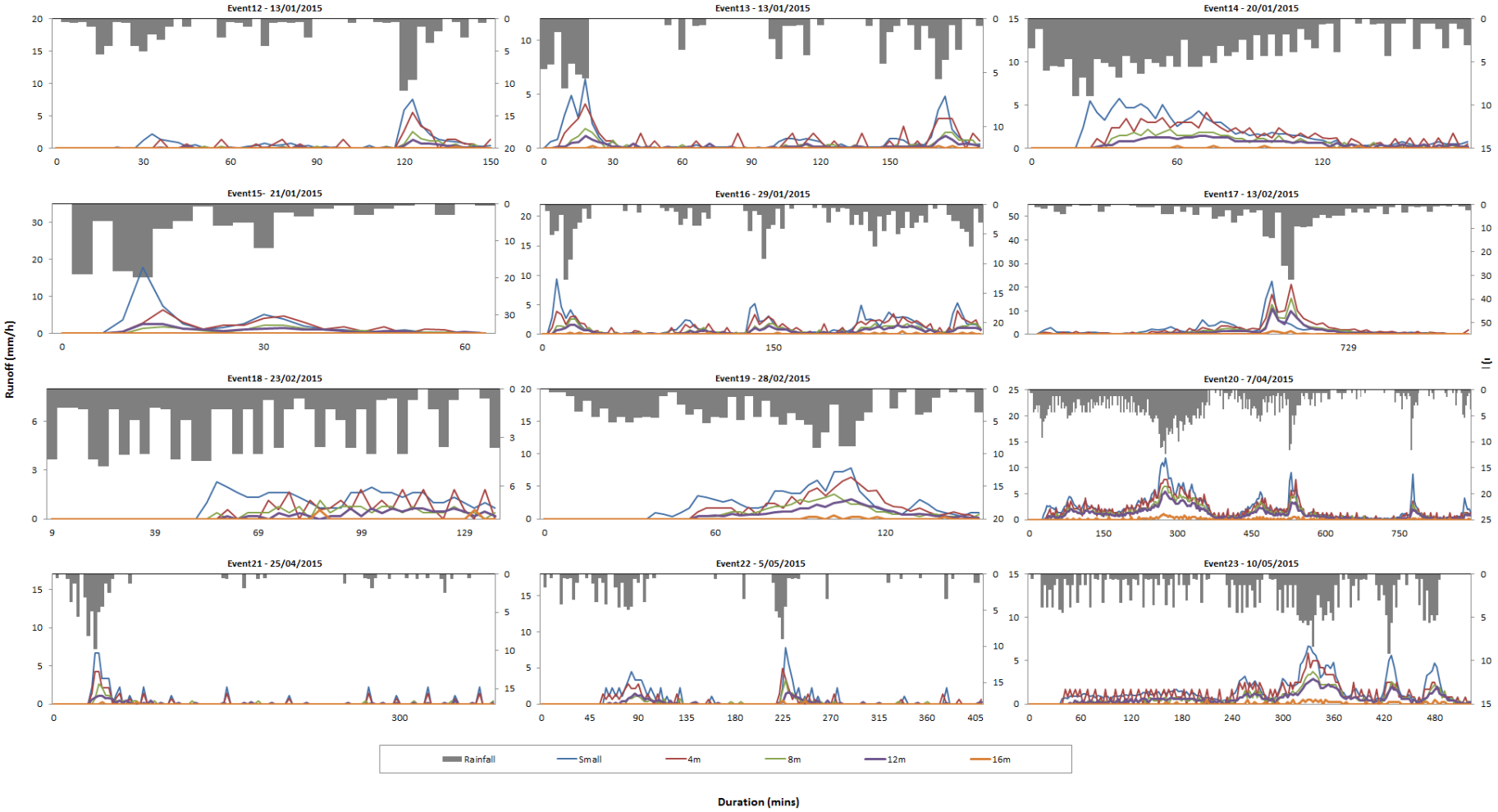

Appendix 3.7. Main pulse of rainfall events and generated runoffs in plots with different length, left vertical axis is the runoff rate, right vertical axis is the rainfall rate and the horizontal axis is the duration of the rainfall-runoff event (min)

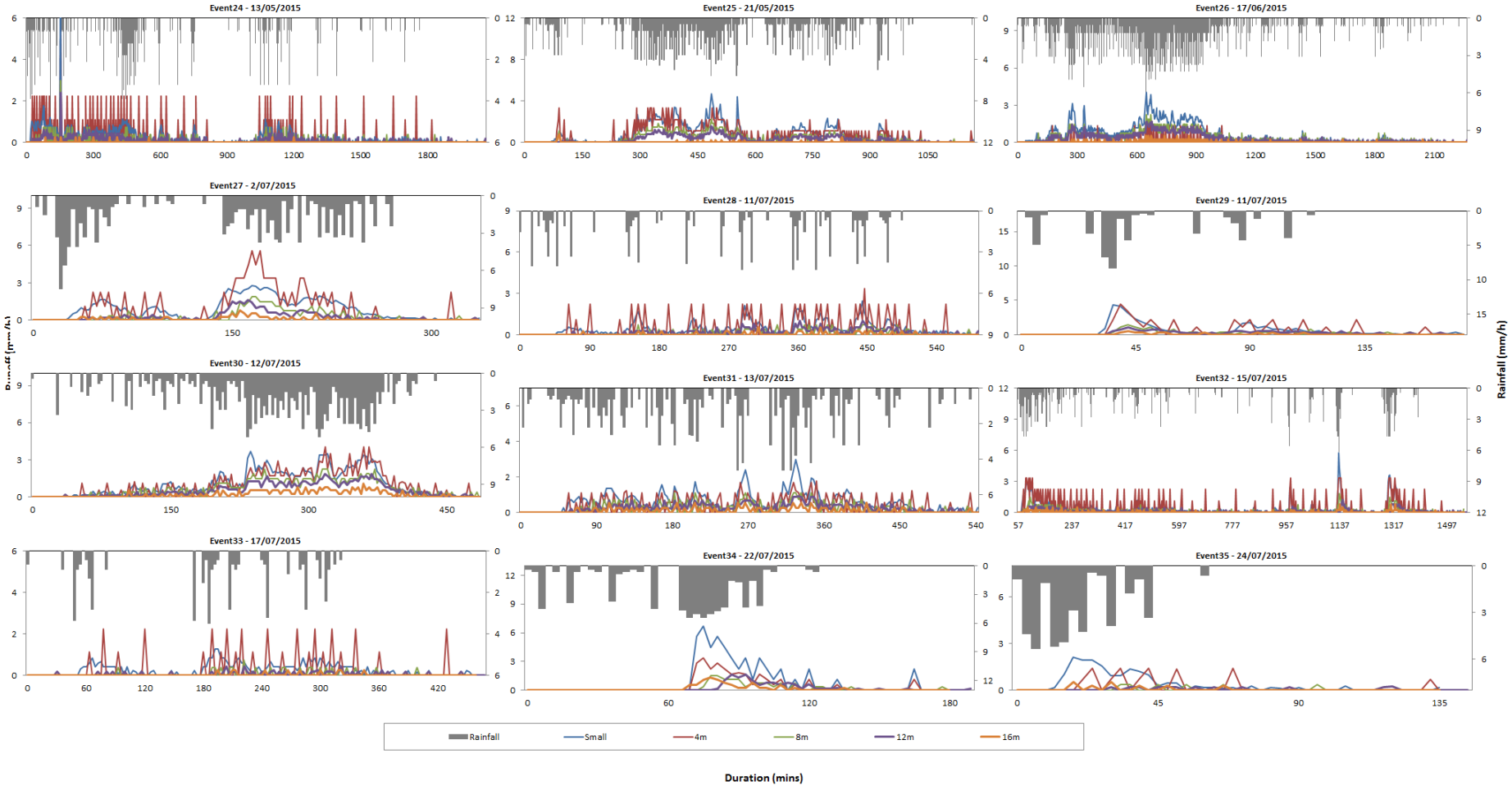

Appendix 3.7. Main pulse of rainfall events and generated runoffs in plots with different length, left vertical axis is the runoff rate, right vertical axis is the rainfall rate and the horizontal axis is the duration of the rainfall-runoff event (min)

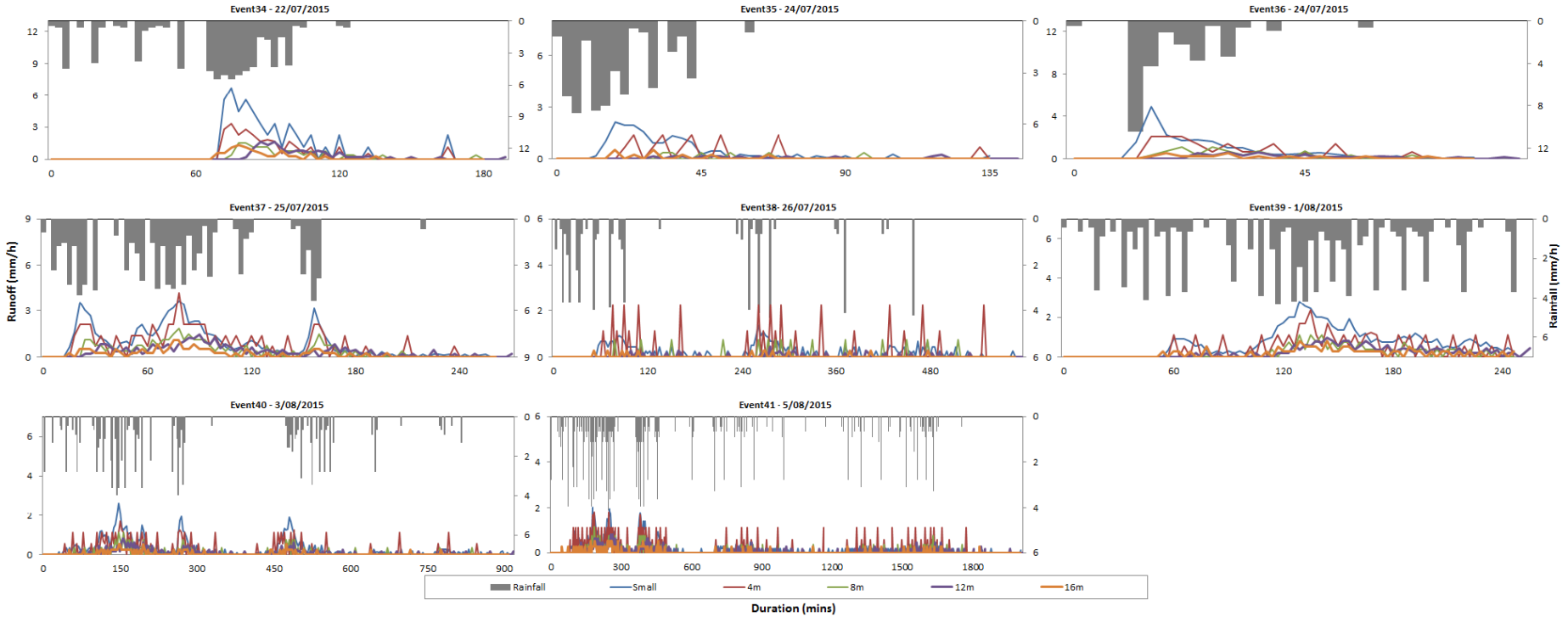

Appendix 3. 8 Scattered plots of runoff depths (mm) vs. plot lengths (m) for main pulses of 41 events representing runoff depth scaling coefficient (SC1)

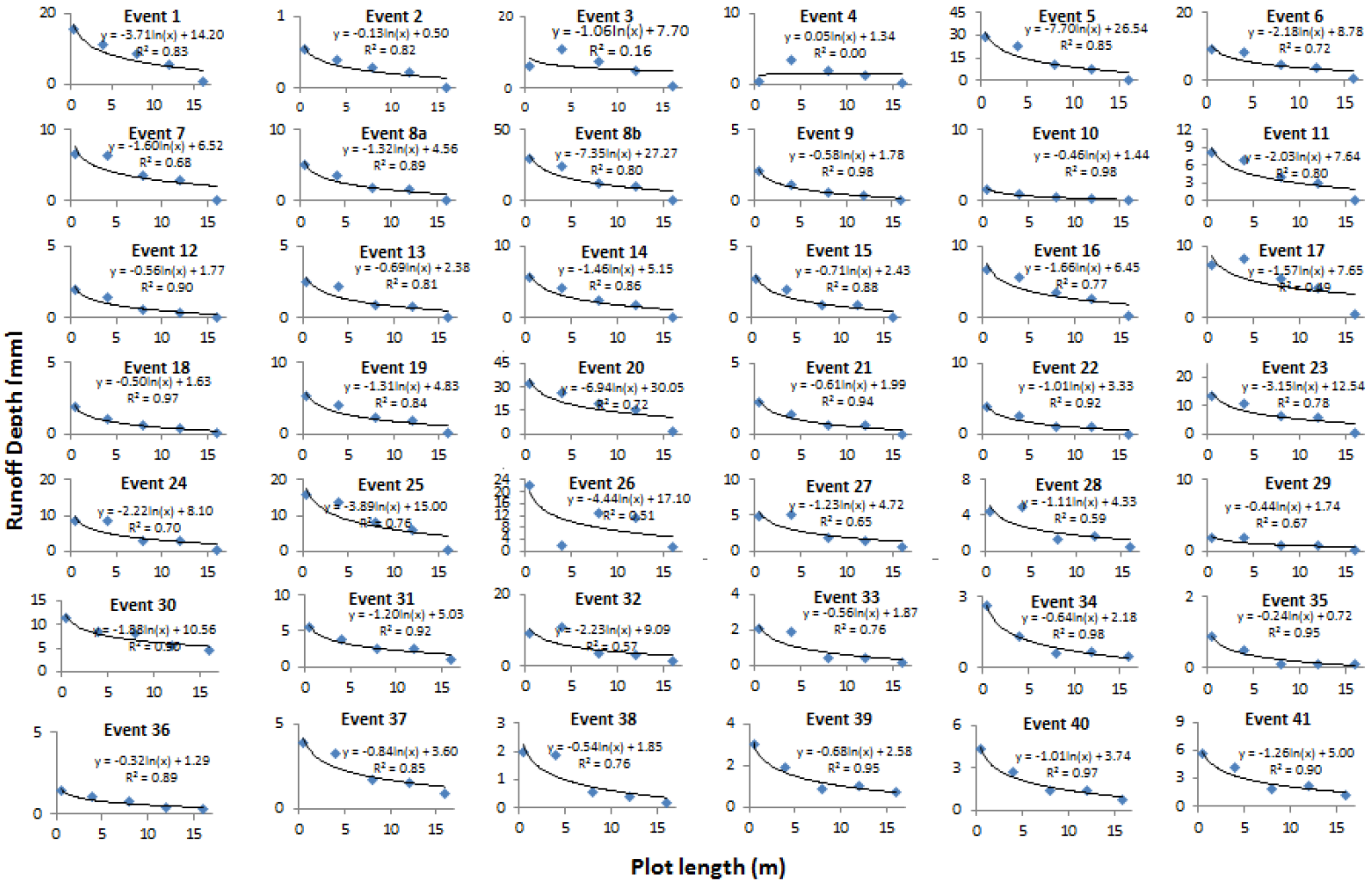

Appendix 3. 9 Scattered plots of runoff ratio (%) vs. plot lengths (m) for main pulses of 41 events representing runoff depth scaling coefficient (SC_2)

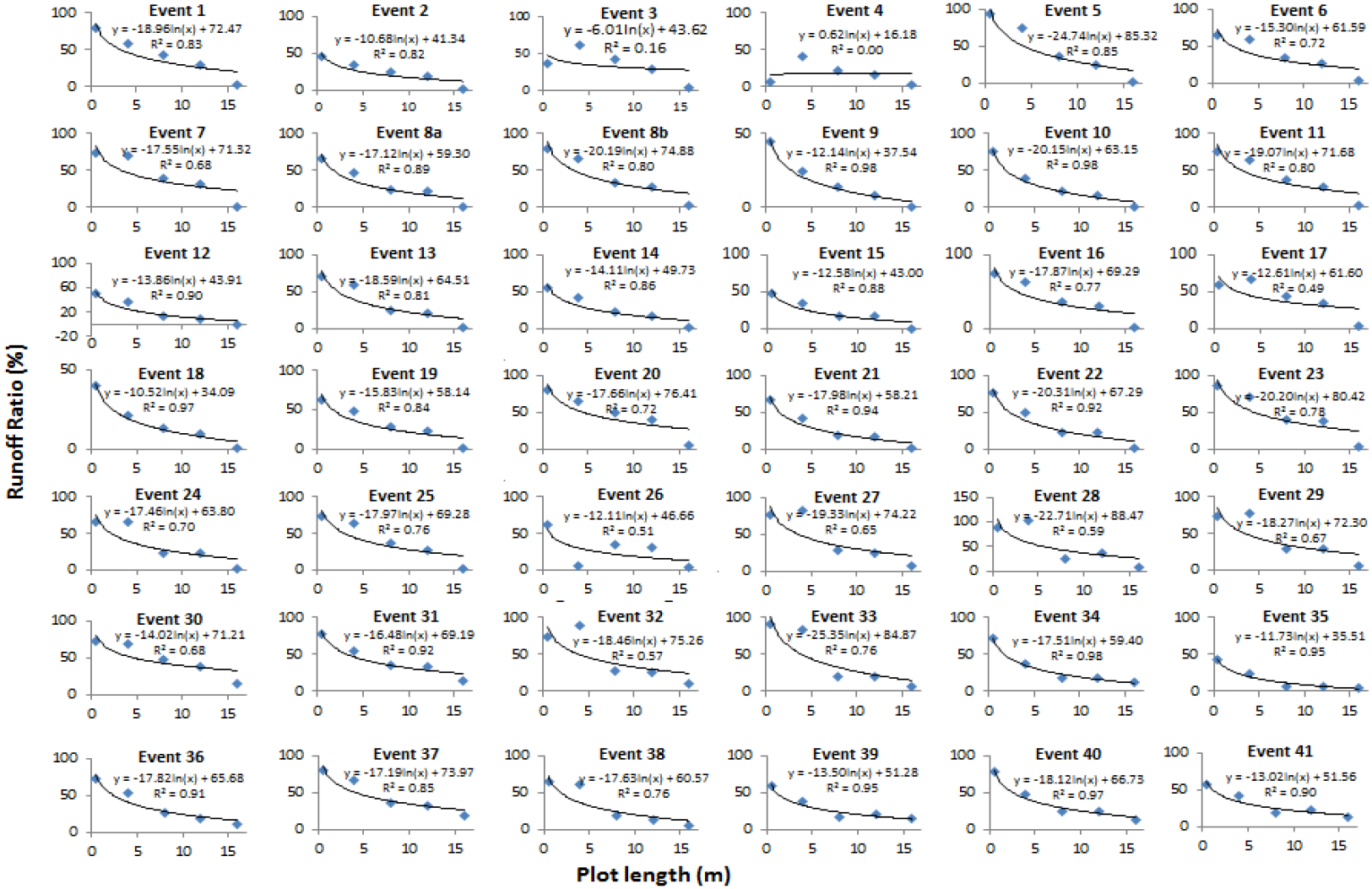

Appendix 4. 1 Total runoff generated from 8m plots correlated with rainfall characteristics; data collected from 8 m plot during the first year following fire (2013-2014) at the study site

8 m plot

Model Summary	S=1.67, R-sq= 85.32%, R-sq(adj) = 84.1%, R-sq(pred)= 77.17 %							
Variable	**β**	**Std Error**	**VIF**	**t value***	**p value***	**Contribution**	**95% CI***	
Total	0.47	0.057	3.86	8.35	0.000	85%	0.35	0.6
Regression Equation = -0.58 + 0.47 total rain								

Appendix 4. 2 Summary of mean intensity of runoff-generated storms during the study period

Event no.	Mean Intensity of Rainfall Pulses (mm/h)							
	I_{3mins}	I_{6mins}	I_{9mins}	I_{15mins}	I_{24mins}	I_{30mins}	I_{45mins}	I_{60mins}
1	2.02	2.10	2.04	2.05	2.06	2.07	2.10	2.15
2	0.30	0.30	0.30	0.31	0.31	0.31	0.32	0.33
3	3.99	4.03	4.06	4.16	4.12	4.41	4.63	4.76
4	2.13	2.34	2.18	2.20	2.23	2.25	2.28	2.35
5	2.53	2.58	2.53	2.54	2.56	2.57	2.61	2.65
6	2.15	2.81	2.02	1.81	1.65	1.59	1.50	1.53
7	2.85	3.69	2.43	2.19	2.04	2.00	1.99	2.17
8	1.08	1.08	1.08	1.08	1.08	1.09	1.09	1.10
9	1.30	1.37	1.31	1.32	1.36	1.39	1.41	1.46
10	1.48	1.46	0.56	0.37	0.27	0.24	0.21	0.44
11	0.86	0.88	0.87	0.87	0.87	0.87	0.84	0.82
12	0.77	0.89	0.78	0.78	0.76	0.75	0.72	0.73
13	0.45	0.45	0.45	0.46	0.46	0.47	0.47	0.46
14	1.89	2.14	1.84	1.82	1.78	1.75	1.68	1.68
15	0.13	3.51	2.12	1.85	1.65	1.54	1.32	1.48
16	0.56	0.57	0.57	0.57	0.57	0.57	0.57	0.58
17	0.06	1.10	1.08	1.08	1.08	1.08	1.07	1.07
18	1.25	1.41	1.27	1.28	1.29	1.29	1.29	1.32
19	1.26	1.36	1.28	1.28	1.28	1.27	1.24	1.25
20	1.90	1.95	1.91	1.91	1.91	1.91	1.90	1.91
21	0.31	0.33	0.31	0.31	0.31	0.30	0.29	0.28
22	0.63	0.66	0.63	0.63	0.63	0.62	0.62	0.63
23	1.47	1.51	1.49	1.50	1.51	1.51	1.52	1.54
24	0.37	0.38	0.37	0.37	0.36	0.36	0.36	0.36
25	1.11	1.11	1.10	1.11	1.11	1.12	1.13	1.14
26	0.97	0.97	0.97	0.98	0.98	0.98	0.98	0.99
27	0.49	0.52	0.49	0.49	0.48	0.48	0.46	0.45
28	0.43	0.45	0.43	0.43	0.43	0.43	0.43	0.43
29	0.52	0.53	0.49	0.49	0.51	0.51	0.46	0.45
30	0.61	0.61	0.62	0.62	0.62	0.62	0.63	0.64
31	0.51	0.51	0.51	0.51	0.51	0.51	0.52	0.53
32	0.47	0.47	0.47	0.47	0.47	0.48	0.48	0.48
33	0.21	0.21	0.21	0.21	0.21	0.22	0.22	0.22
34	0.82	0.88	0.80	0.81	0.81	0.81	0.81	0.84
35	0.54	0.70	0.43	0.39	0.32	0.29	0.23	0.23
36	0.36	0.59	0.37	0.31	0.25	0.22	0.16	0.16
37	0.80	0.90	0.79	0.78	0.76	0.75	0.74	0.75
38	0.31	0.35	0.31	0.30	0.29	0.29	0.28	0.28
39	0.74	0.78	0.75	0.76	0.76	0.77	0.77	0.79
40	0.37	0.37	0.36	0.37	0.37	0.37	0.37	0.38
41	0.29	0.29	0.29	0.29	0.29	0.29	0.29	0.29
Mean	1.01	1.20	1.05	1.03	1.01	1.01	1.00	1.03
Median	0.74	0.88	0.78	0.78	0.76	0.75	0.74	0.75
Minimum	0.06	0.21	0.21	0.21	0.21	0.22	0.16	0.16
Maximum	3.99	4.03	4.06	4.16	4.12	4.41	4.63	4.76

Appendix 4. 3 Summary of maximum intensity of runoff-generated storms during the study period

Event no.	Maximum Intensity of Rainfall Pulses (mm/h)							
	I_{3mins}	I_{6mins}	I_{9mins}	I_{15mins}	I_{24mins}	I_{30mins}	I_{45mins}	I_{60mins}
1	8.84	7.76	7.22	6.79	6.88	6.72	6.40	6.15
2	4.51	3.86	3.17	2.51	1.64	1.31	1.07	0.80
3	69.46	43.96	35.18	29.54	23.21	23.34	17.28	14.19
4	9.28	8.54	6.66	6.28	6.20	6.13	5.76	5.42
5	8.94	7.83	6.68	5.98	5.78	5.61	5.35	5.06
6	70.05	85.89	32.85	24.46	17.20	14.52	10.59	9.02
7	26.16	47.77	22.45	16.10	11.05	9.17	6.95	6.06
8	7.61	6.13	5.24	5.21	4.89	4.82	4.43	4.39
9	4.90	4.75	4.14	3.73	3.01	3.11	2.79	2.49
10	24.44	29.61	11.03	6.62	4.14	3.31	2.21	2.30
11	20.38	14.24	11.53	10.25	8.87	8.51	8.05	7.64
12	11.10	10.24	7.24	5.48	3.86	3.21	2.22	1.90
13	6.43	5.34	5.25	4.51	3.93	3.15	2.10	1.60
14	8.99	15.69	8.23	6.98	6.43	6.26	5.93	5.70
15	0.99	38.08	14.95	10.84	9.16	8.04	5.99	5.63
16	12.74	11.00	8.71	6.69	5.22	4.48	3.20	2.77
17	1.60	28.92	22.34	17.83	14.65	12.73	9.87	8.56
18	4.77	5.59	3.57	3.26	2.92	2.90	2.95	2.75
19	9.10	8.78	7.48	7.15	6.36	6.02	5.10	4.76
20	12.32	11.09	11.06	10.59	9.61	9.29	8.44	7.90
21	9.86	7.42	7.61	6.43	5.10	4.56	3.37	2.59
22	9.05	7.51	6.73	5.20	3.47	2.84	2.32	1.99
23	9.23	7.42	6.53	6.11	5.67	5.23	4.99	4.31
24	34.51	17.59	12.43	7.57	4.81	3.91	2.88	2.52
25	5.55	5.05	4.52	3.90	3.42	3.42	3.27	2.99
26	6.21	4.93	4.72	4.21	4.02	4.01	3.75	3.62
27	7.49	10.87	5.75	4.50	3.93	3.39	2.90	2.30
28	4.27	4.00	2.99	2.02	1.48	1.22	1.16	1.07
29	8.40	7.60	5.44	4.25	3.13	2.57	2.04	1.63
30	5.19	4.85	4.74	4.29	3.84	3.72	3.37	3.45
31	4.63	3.42	3.56	2.54	2.38	2.13	1.95	1.68
32	6.15	5.42	5.00	4.00	3.07	2.94	2.67	2.44
33	3.52	2.21	1.84	1.42	1.31	1.09	1.02	0.80
34	5.46	5.26	5.32	5.15	4.54	4.24	3.29	2.72
35	5.33	10.14	4.34	3.89	3.11	2.87	2.32	2.03
36	10.41	14.68	5.26	4.35	3.27	2.71	1.81	1.41
37	5.33	6.71	3.74	3.38	3.20	2.94	2.70	2.33
38	4.33	5.17	2.17	1.98	1.91	1.64	1.42	1.18
39	4.35	4.52	3.59	3.12	2.63	2.33	2.27	2.01
40	3.95	3.78	2.89	2.46	2.09	2.03	1.62	1.48
41	4.11	2.86	2.89	2.27	2.03	1.82	1.60	1.36
Mean	11.71	13.08	8.22	6.68	5.45	4.98	4.13	3.68
Median	7.49	7.51	5.44	5.15	3.93	3.42	2.95	2.59
Minimum	0.99	2.21	1.84	1.42	1.31	1.09	1.02	0.80
Maximum	70.05	85.89	35.18	29.54	23.21	23.34	17.28	14.19

Appendix 4. 4 Scatter plots of rainfall Imean versus runoff production (mm) at different plot lengths for all runoff generating storms recorded during study period

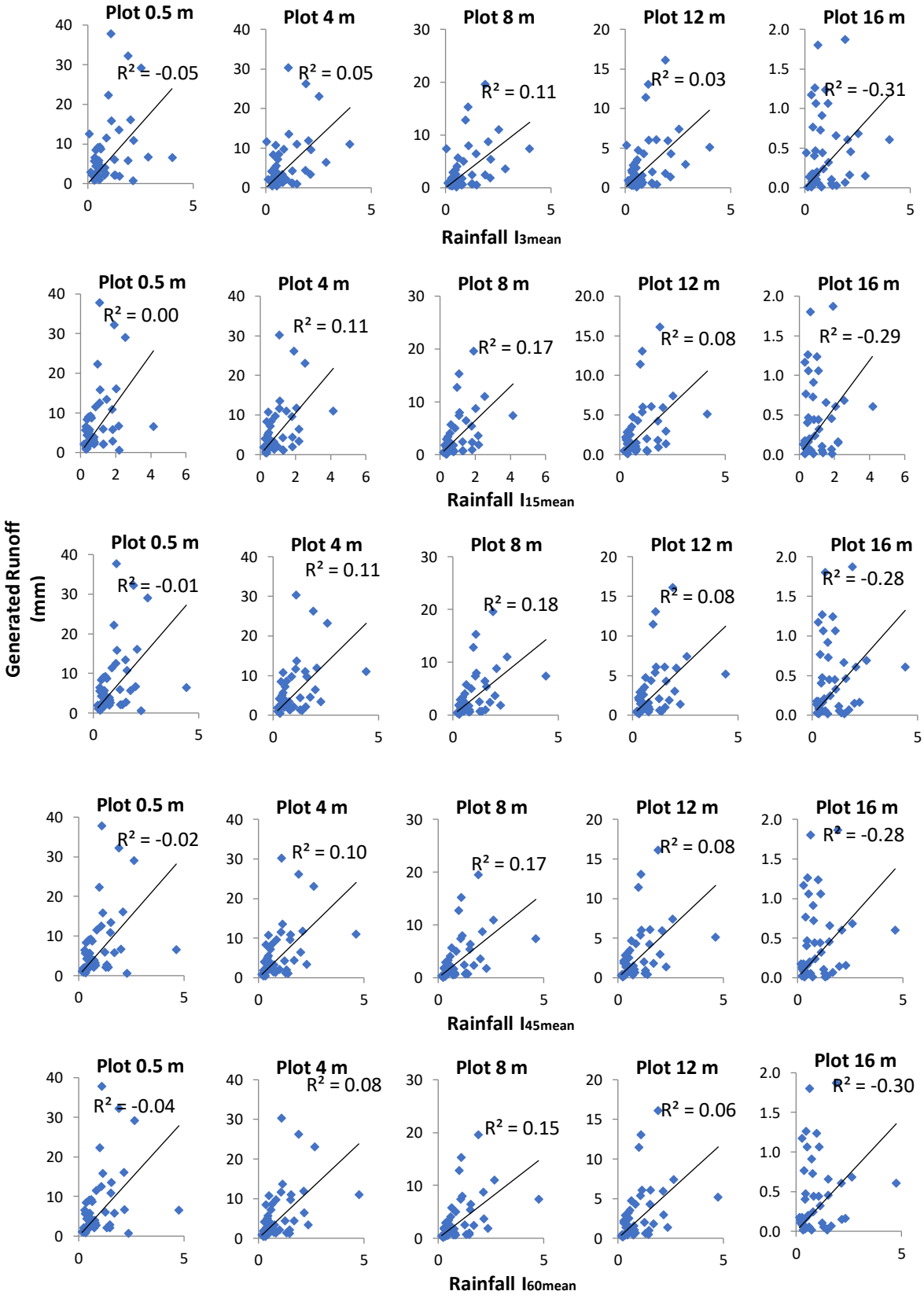

Appendix 4. 5 Scatter plots of rainfall I_{max} versus runoff production (mm) at different plot lengths for all runoff generating storms recorded during study period

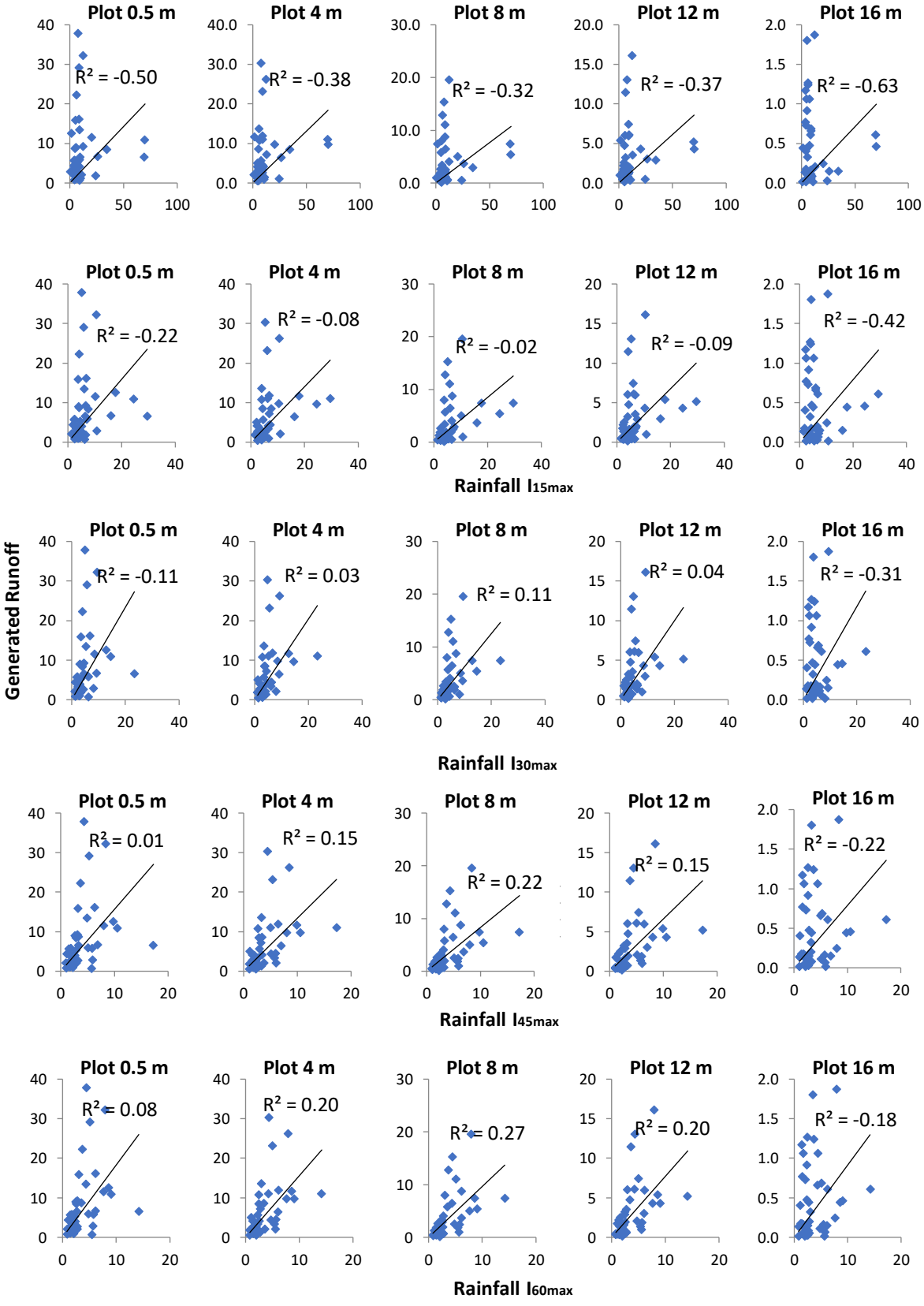

Appendix 4. 6 Averaged mean and maximum rainfall pulses in relation to runoff scaling coefficient (SC1)

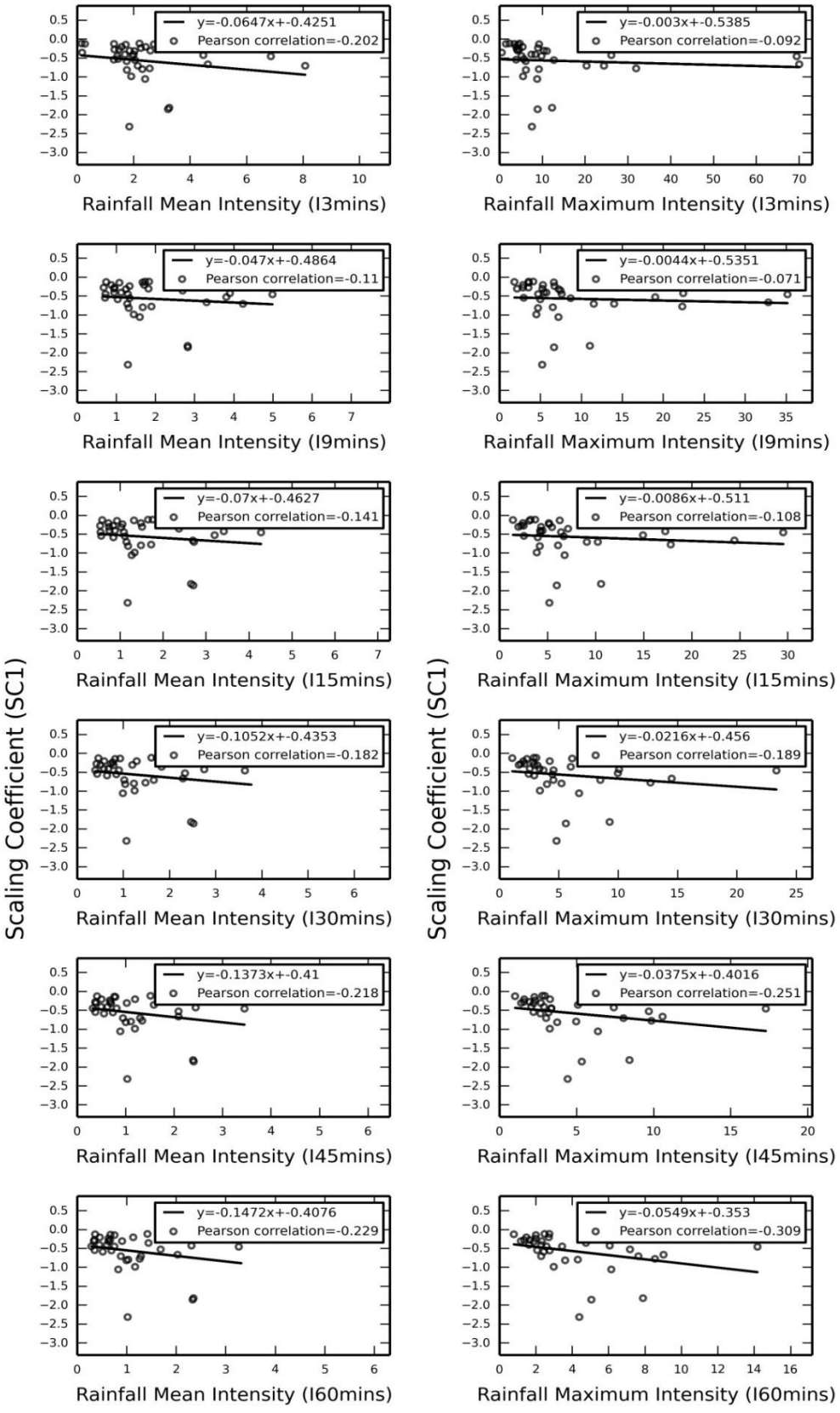

Appendix 5. 1 Volumetric indices of 14 rainfall events from throughfall paired with runoffs collected at two 8 m plots during the first year following fire

Event no.	Date			Throughfall				Runoff plots collected at 8 m plots					
								no.1			no.2		
	Start	End	Length(min)	peak (mm/h)	Mean(mm/h)	Total(mm/m2)	CV between hiatus (%)	peak (mm/h)	Mean(mm/h)	Total(mm/m2)	peak (mm/h)	Mean(mm/h)	Total(mm/m2)
1	18/07/2013 19:09	19/07/2013 2:38	468	16.66	1.85	26.11	41.20	8.33	1.95	15.3	9.16	1.99	15.62
2	28/07/2013 23:15	29/07/2013 3:21	246	11.11	1.49	11.11	32.41	5.83	1.54	6.42	5	1.32	5.5
3	3/08/2013 17:36	3/08/2013 20:06	150	5.56	1.21	5.55	0	4.17	1.06	2.71	2.5	0.68	1.75
4	5/08/2013 16:21	5/08/2013 18:06	105	5.56	0.68	2.2	0	3.33	0.74	1.33	2.5	0.44	0.8
5	14/08/2013 12:33	14/08/2013 17:06	273	11.11	1.01	8.33	24.04	5.83	0.98	4.5	4.16	0.69	3.2
6	28/08/2013 20:06	29/08/2013 21:00	54	11.11	2.11	3.62	26.35	2.5	0.66	0.62	2.5	0.44	0.42
7	15/09/2013 13:08	17/09/2013 7:11	999	5.56	0.55	18.05	0	2.5	0.63	11.41	1.66	0.35	6.92
8	24/09/2013 21:23	26/09/2013 14:59	999	11.11	0.58	18.33	27.77	4.17	0.47	8.37	2.5	0.25	4.37
9	1/10/2013 4:56	1/10/2013 9:14	258	11.11	1.13	8.89	30.94	5.83	0.71	3.08	5	0.49	2.12
10	4/12/2013 9:12	4/12/2013 17:00	468	22.22	2.24	23.61	44.06	7.5	1.48	8.625	6.66	0.98	5.92
11	24/01/2014 8:11	24/01/2014 14:38	387	11.11	2.32	27.22	27.49	5	1.68	10.91	5.83	2.01	13.08
12	19/02/2014 14:19	20/02/2014 2:10	711	22.2	0.7	15	43.03	4.16	0.54	6.37	5	0.65	7.75
13	15/03/2014 20:29	16/03/2014 2:02	333	27.78	1.32	13.33	60.10	8.33	0.97	5.42	7.5	0.91	5.08
14	21/03/2014 15:14	21/03/2014 17:14	120	61.11	2.33	8.61	89.27	43.33	1.69	3.46	46.67	2.13	4.37

Appendix 5. 2 Hyetographs of selected storms (right) and their hydrographs from paired 8 m plots (left)

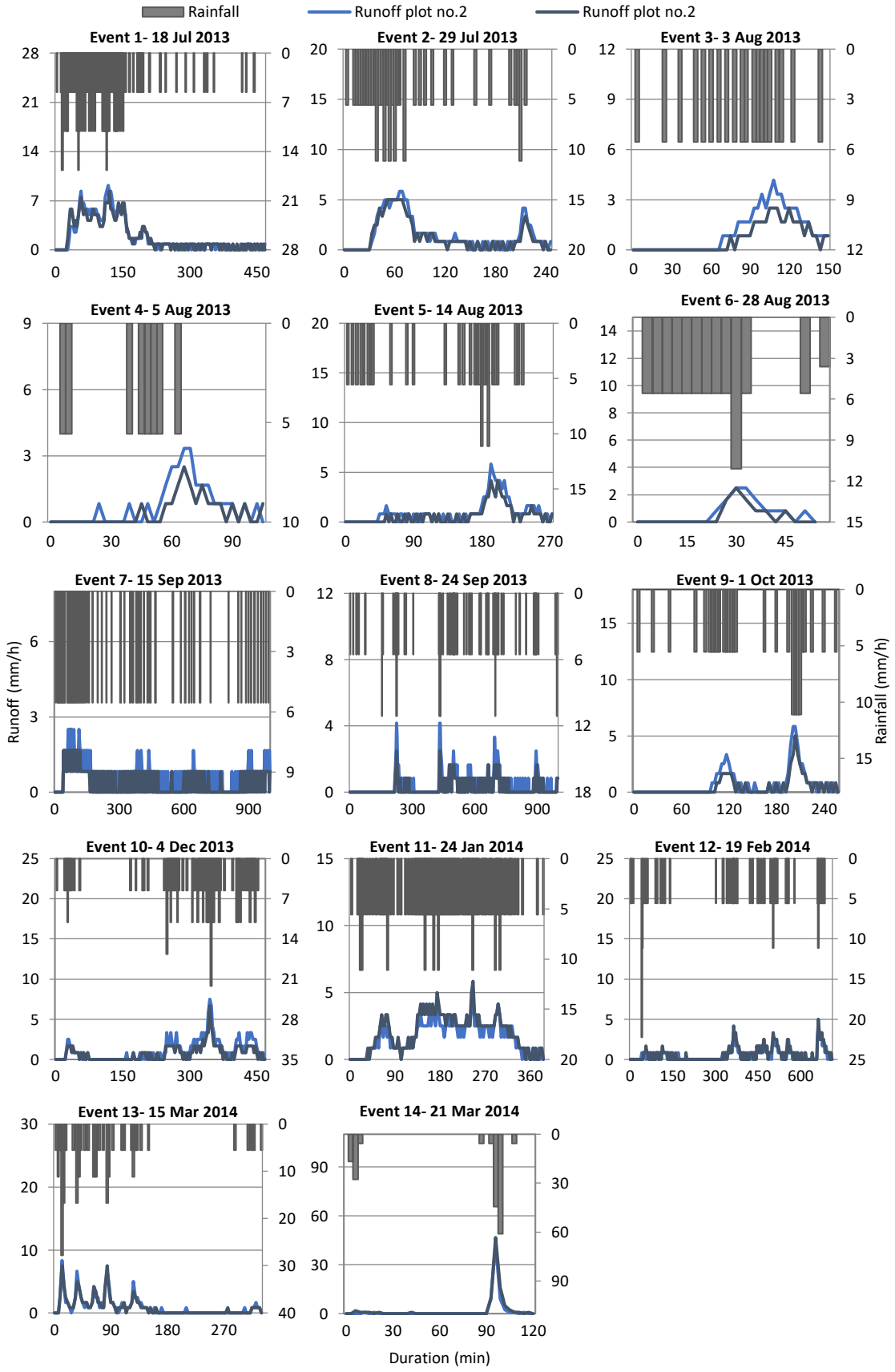

Appendix 5. 3 Downscaling simulations for 0.5 m plot lengths (events 1 to 12)

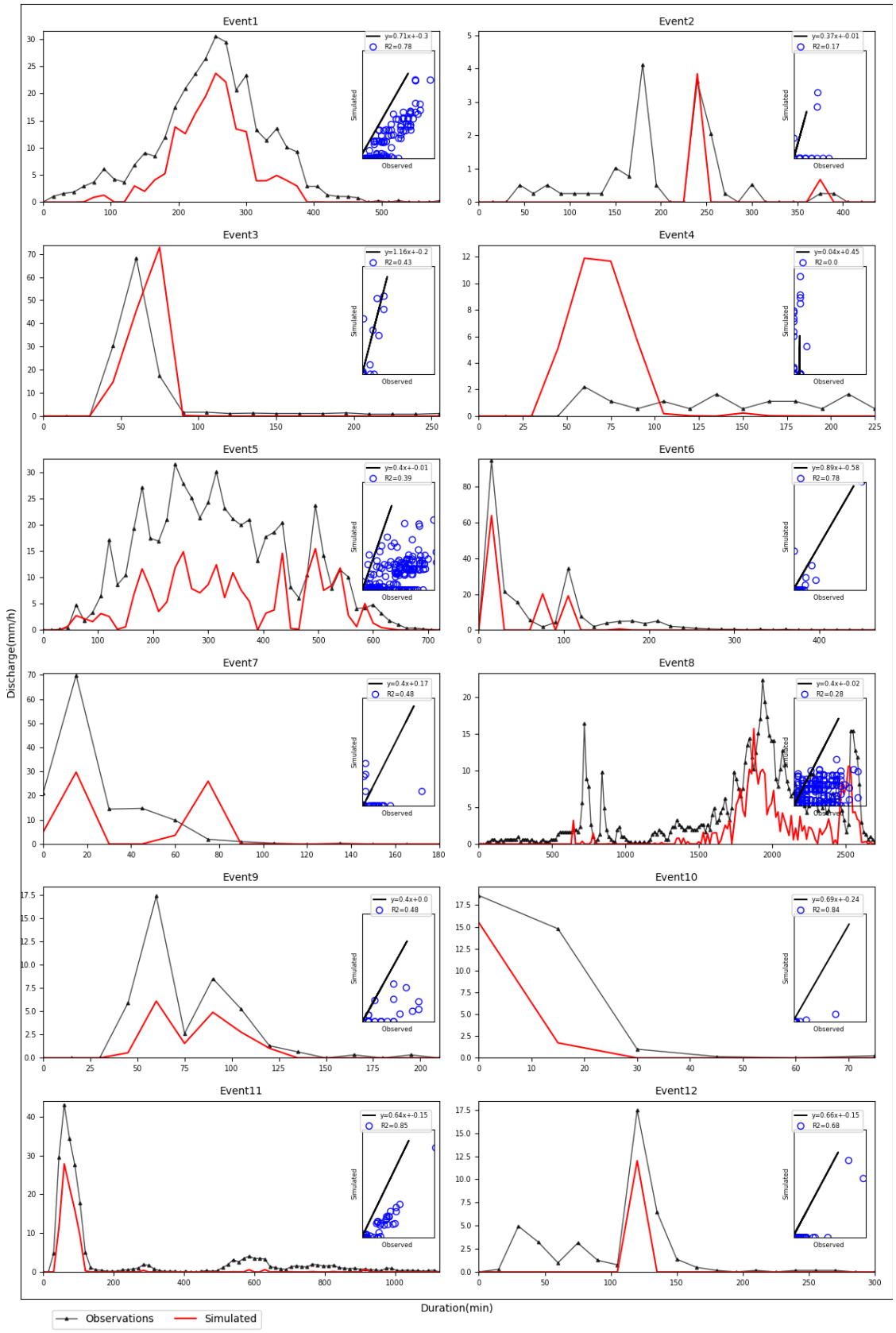

Appendix 5.3. Downscaling simulations for 0.5 m plot lengths (events 13 to 24)

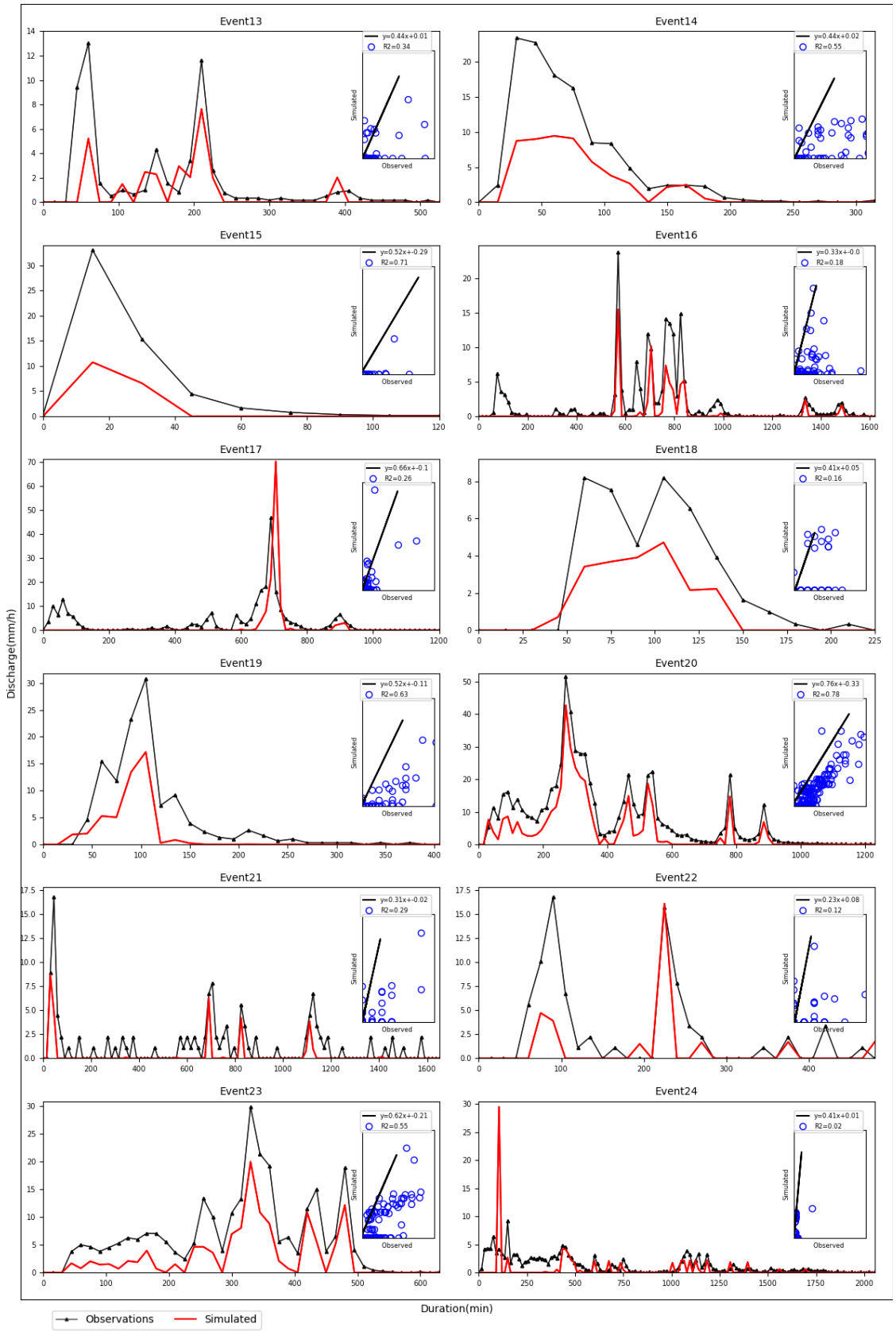

Appendix 5.3. Downscaling simulations for 0.5 m plot lengths (events 25 to 36)

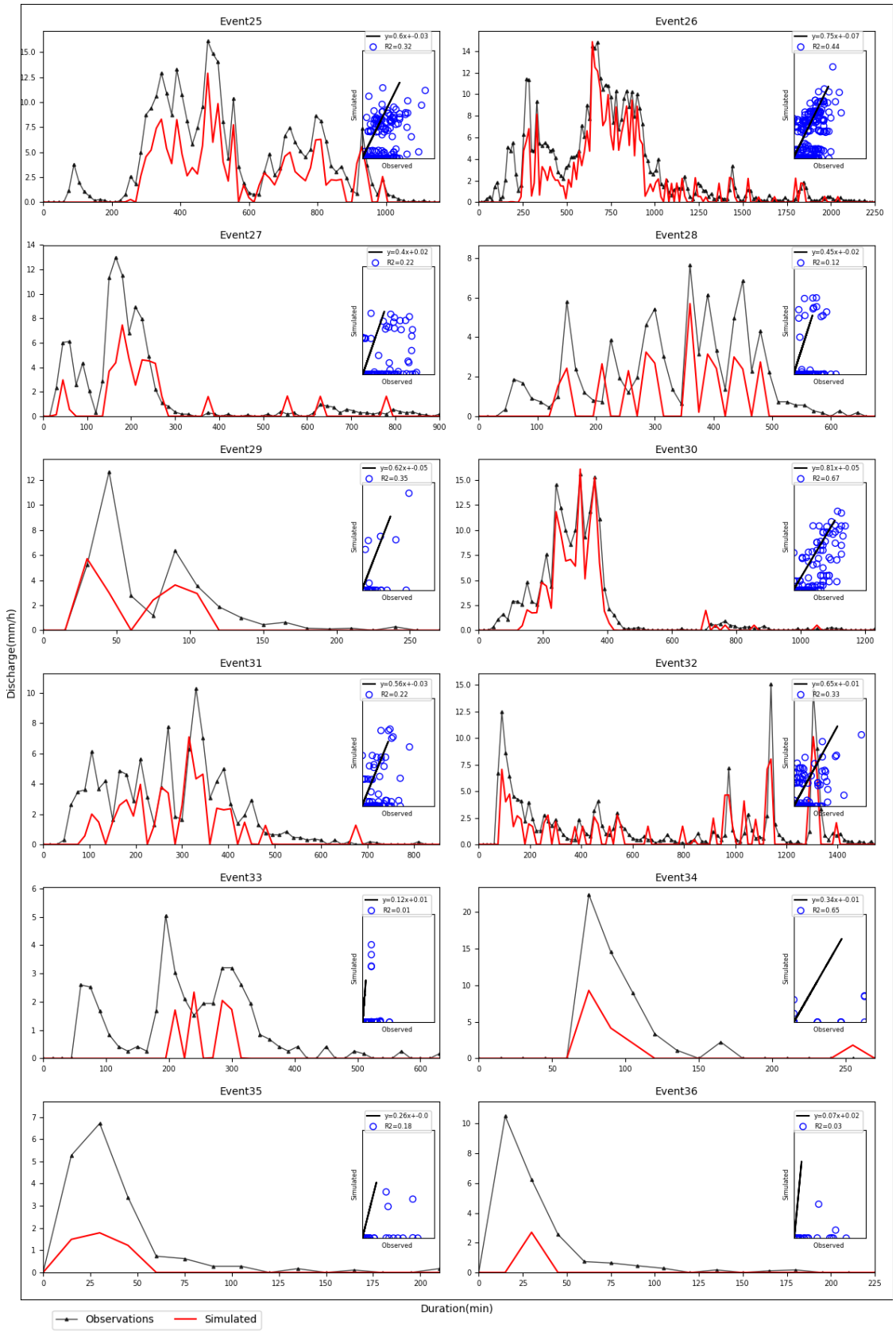

Appendix 5.3. Downscaling simulations for 0.5 m plot lengths (events 37 to 41)

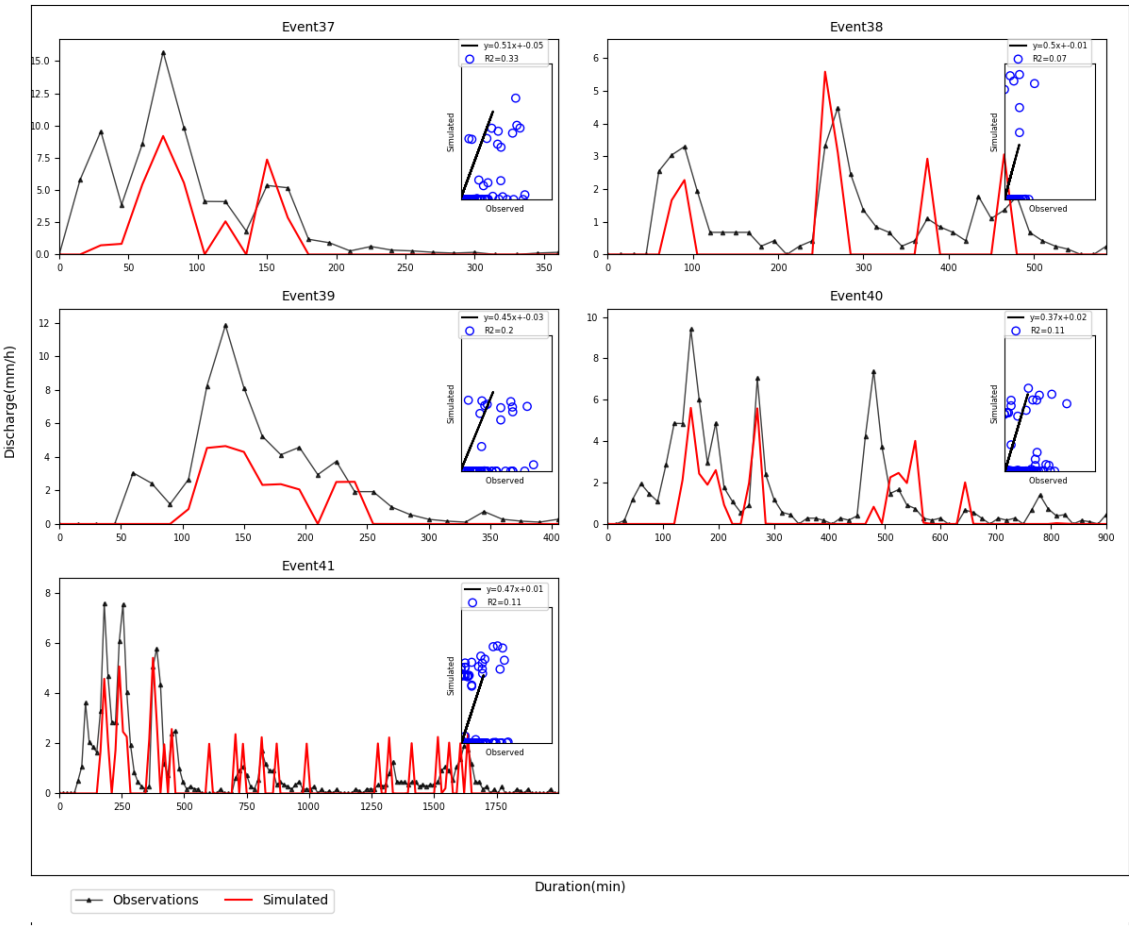

Appendix 5. 4 Downscaling simulations for 4 m plot lengths (events 1 to 12)

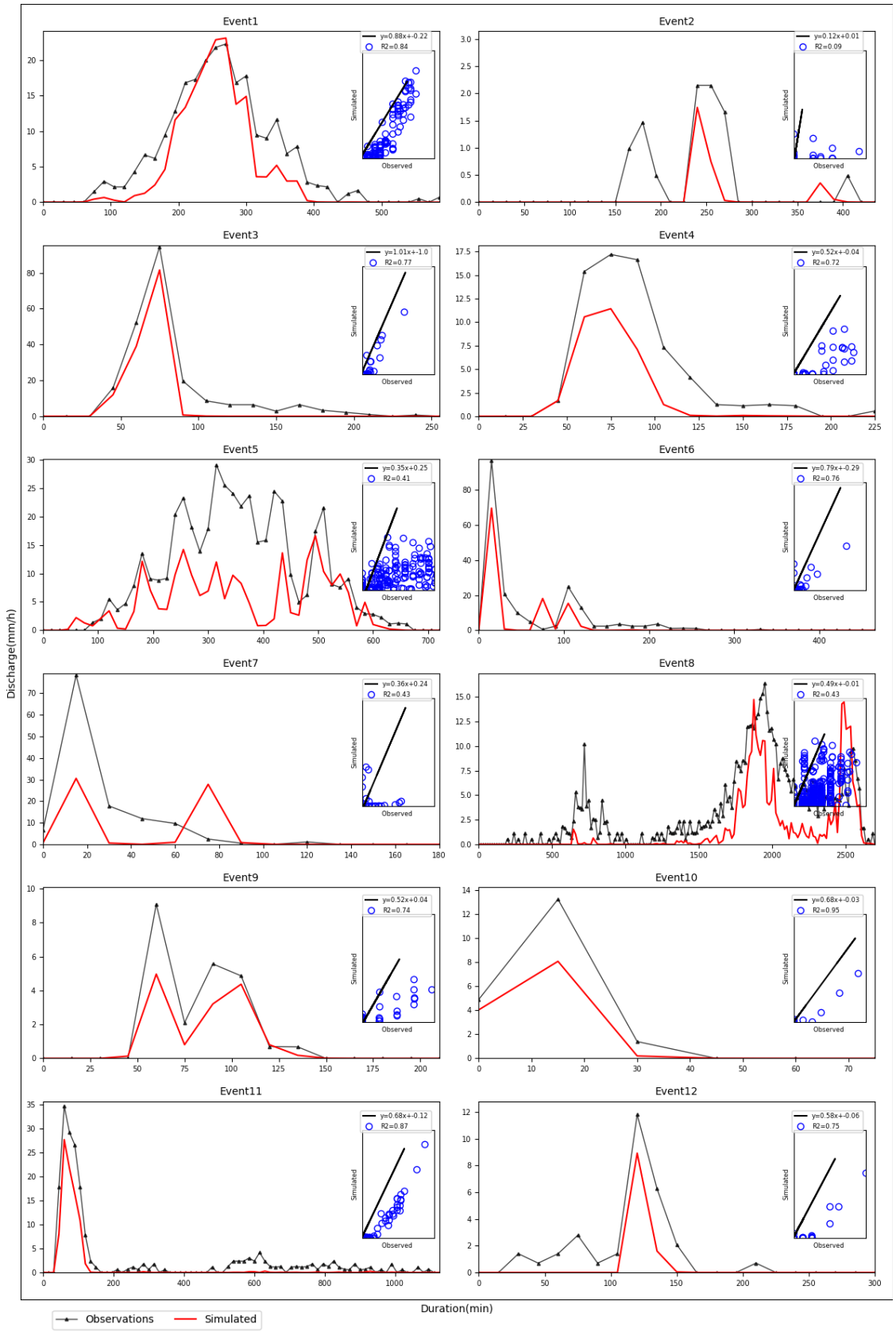

Appendix 5.4. Downscaling simulations for 4 m plot lengths (event 13 to 24)

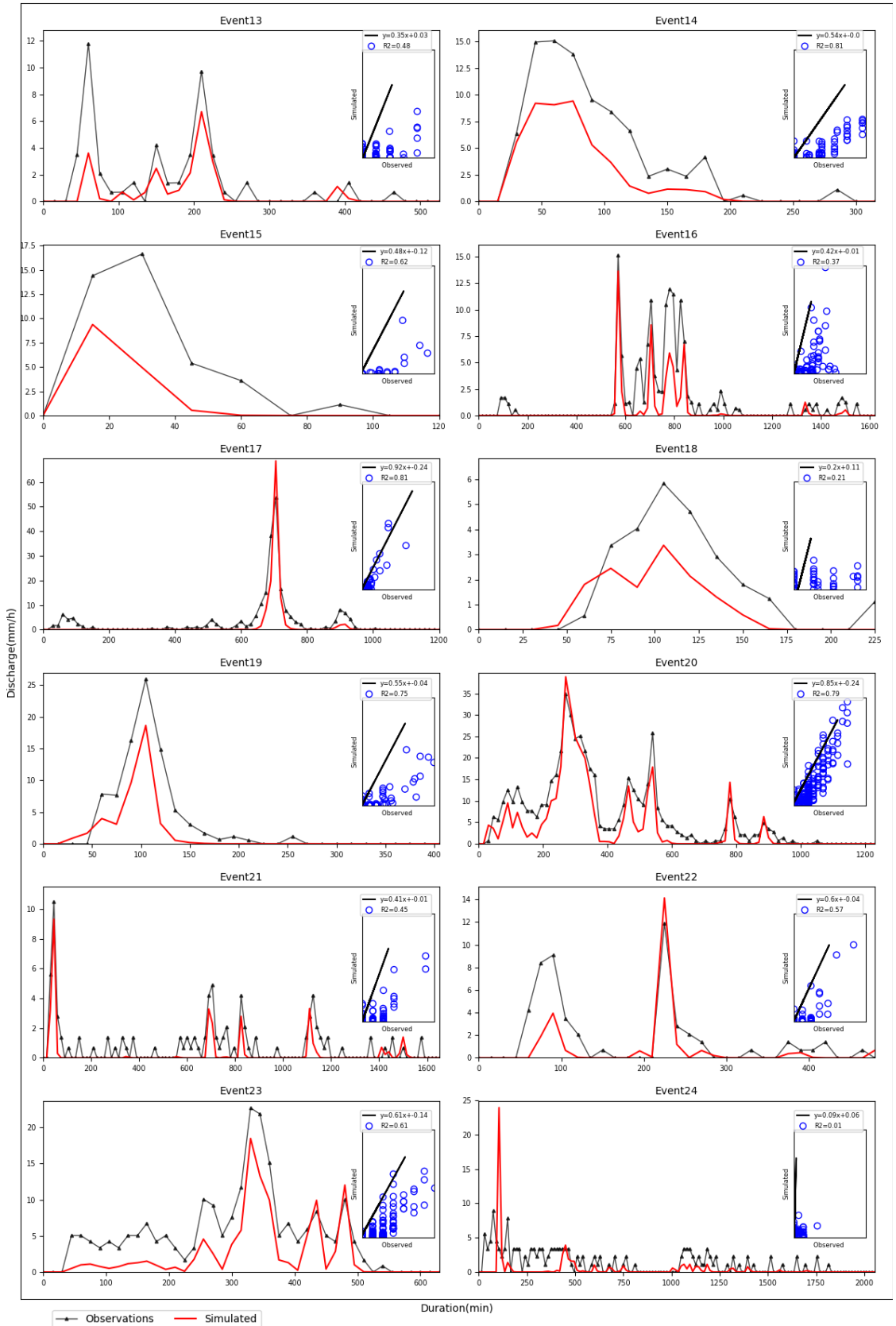

Appendix 5.4. Downscaling simulations for 4 m plot lengths (events 25 to 36)

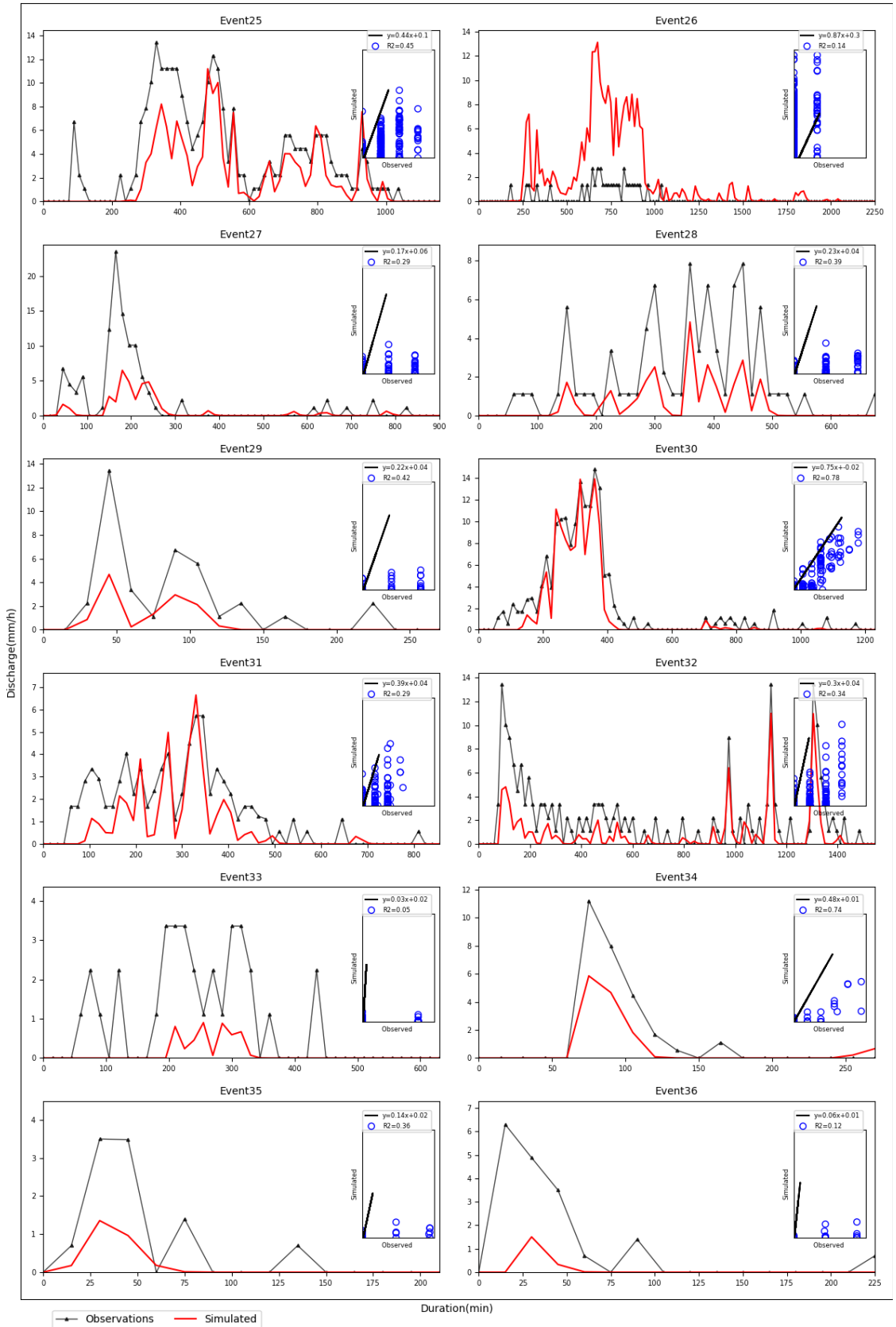

Appendix 5.4. Downscaling simulations for 4 m plot lengths (events 37 to 41)

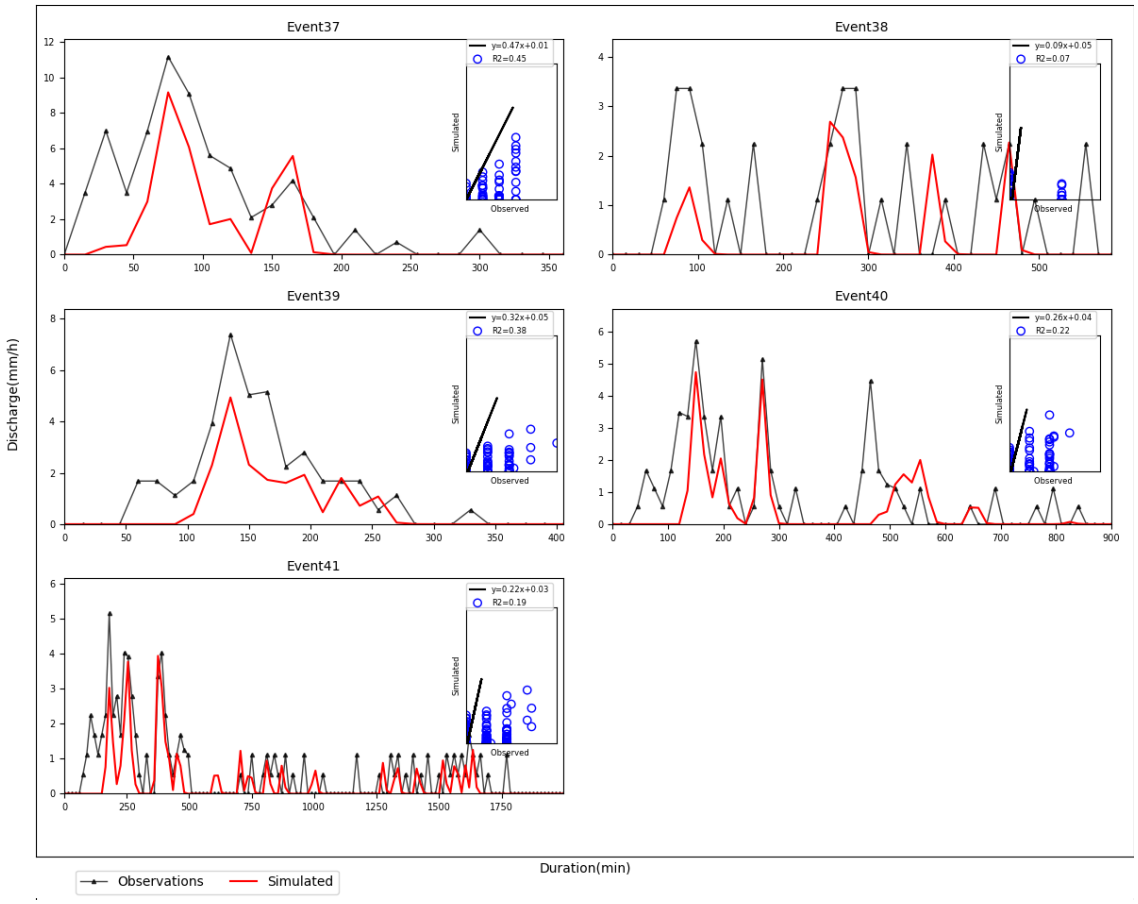

Appendix 5. 5 Upscaling simulations for 12m plot lengths (events 1 to 6)

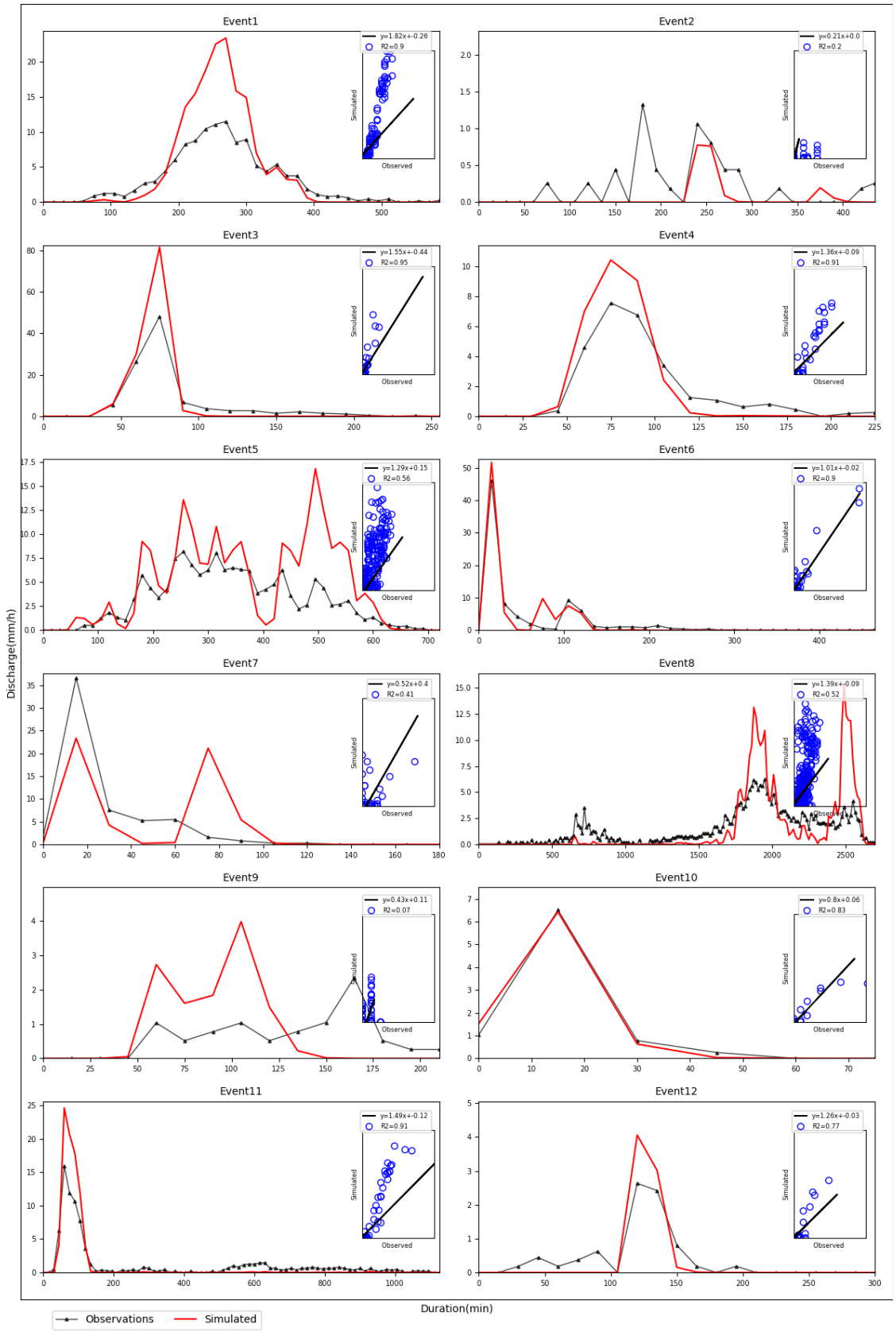

Appendix 5.5. Upscaling simulations for 12m plot lengths (events 13 to 24)

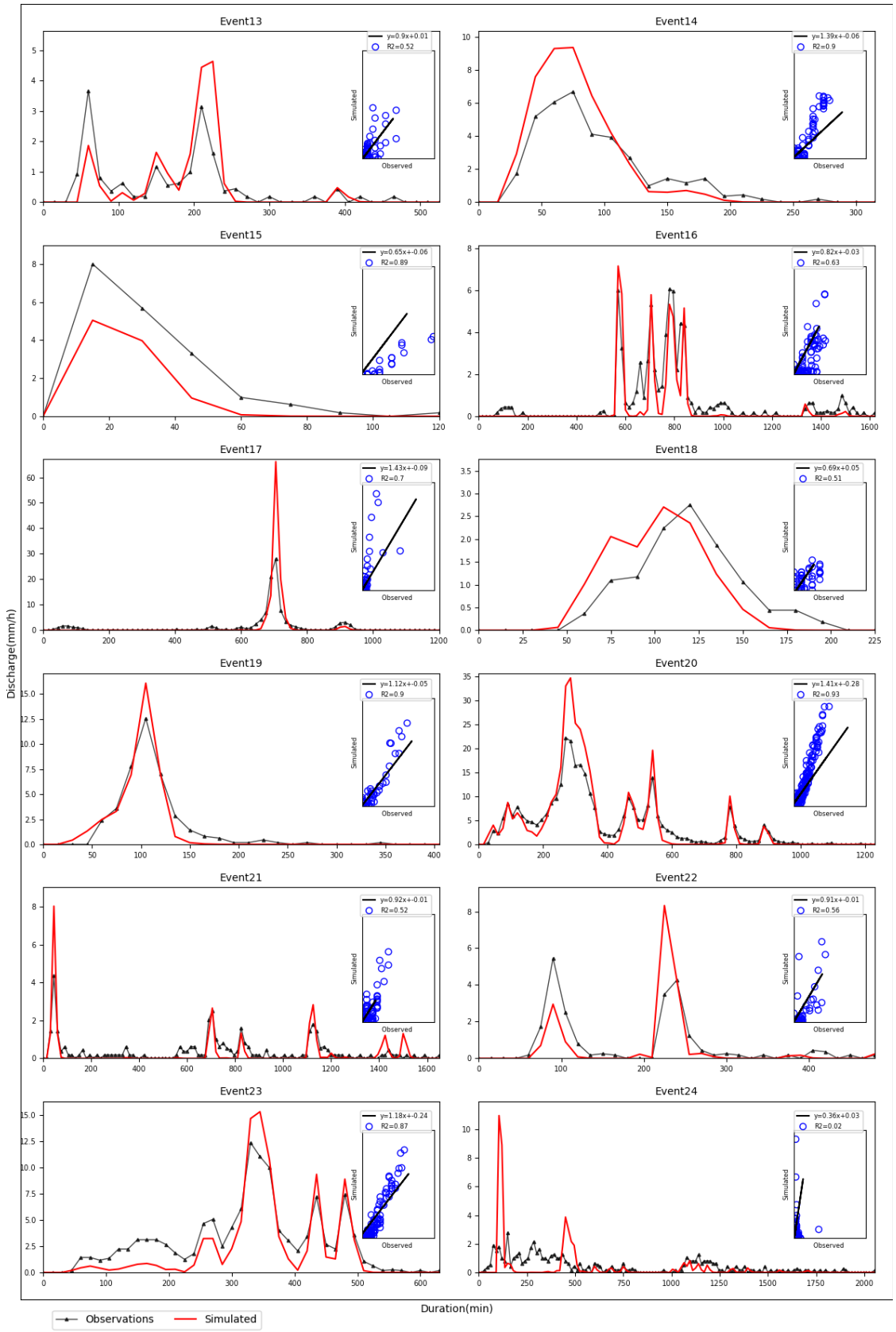

Appendix 5.5. Upscaling simulations for 12m plot lengths (events 25 to 36)

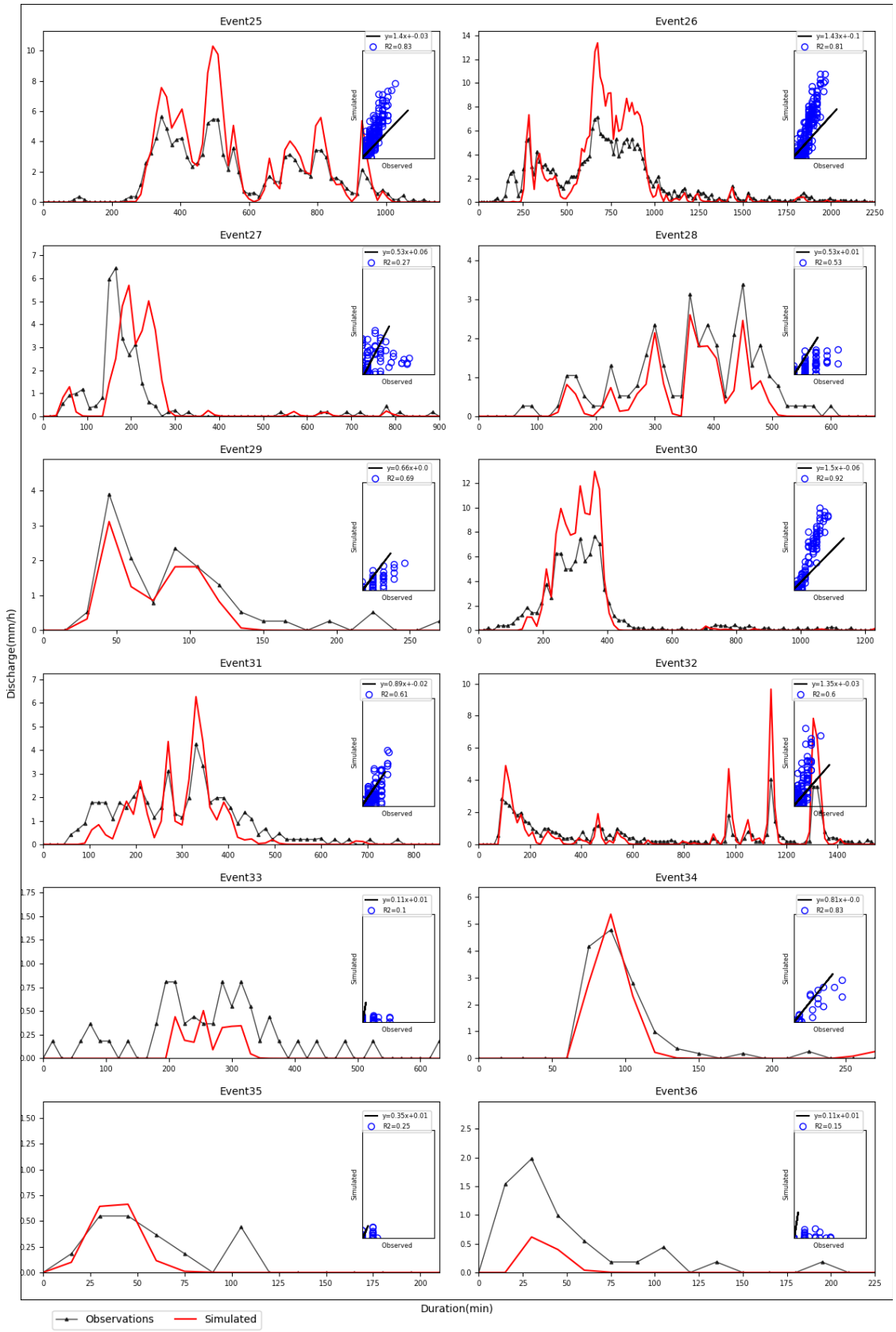

Appendix 5.5. Upscaling simulations for 12m plot lengths (events 37 to 41)

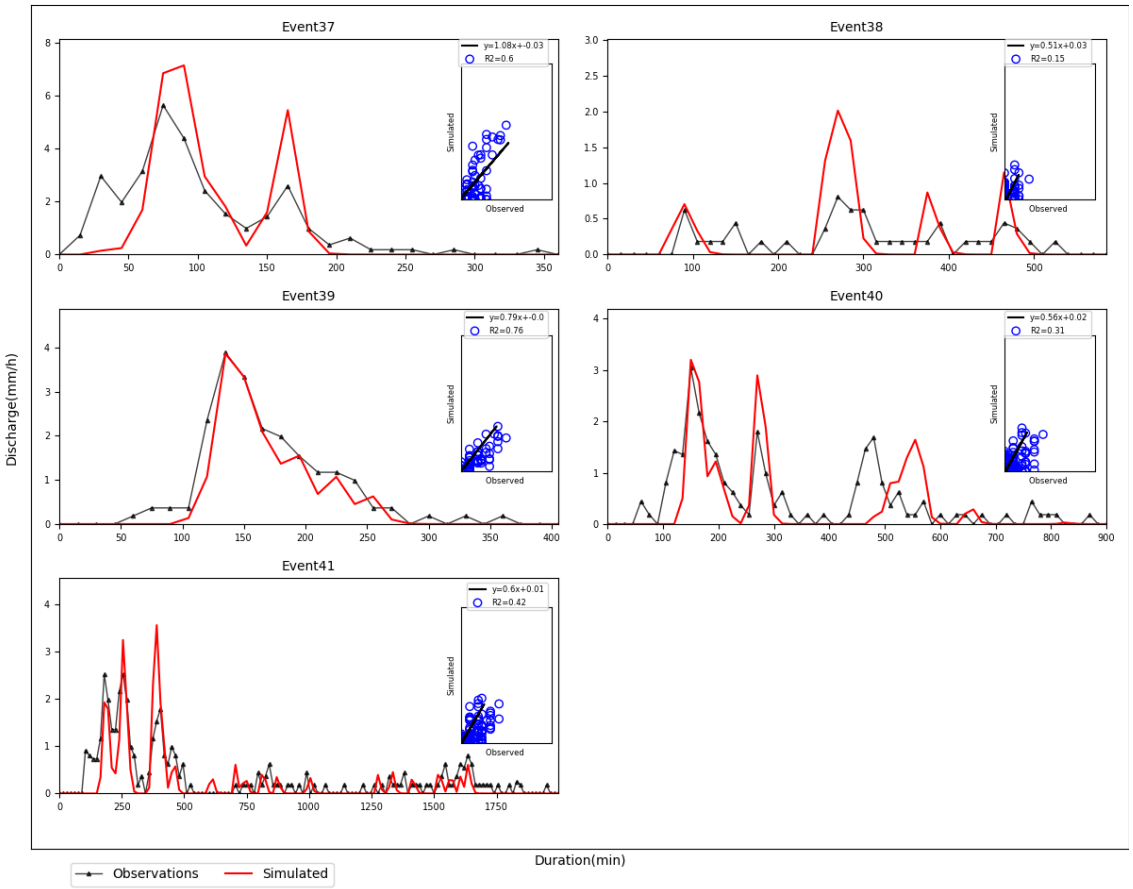

Appendix 5. 6 Upscaling simulations for 16 m plot lengths (events 1 to 12)

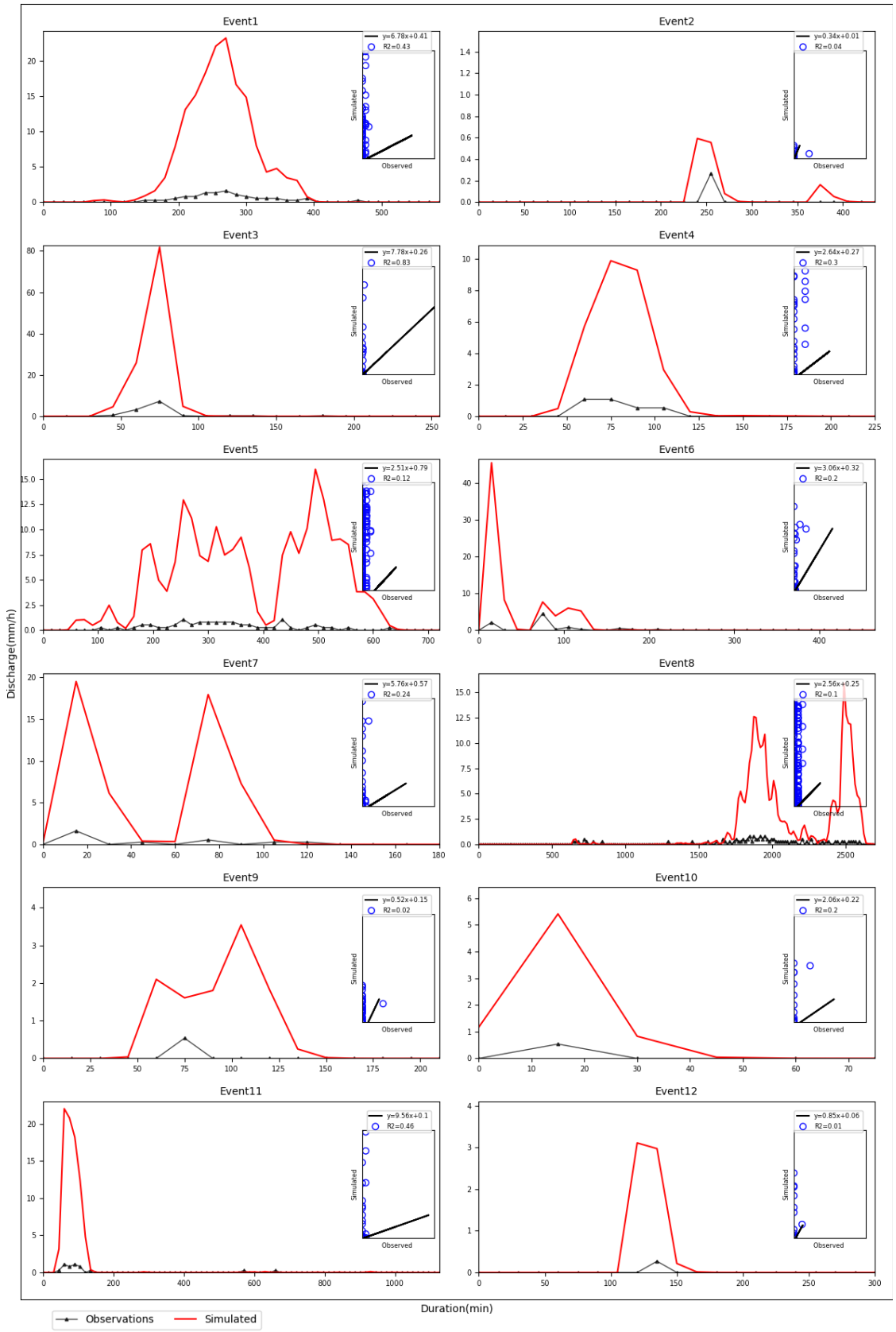

Appendix 5.6 Upscaling simulations for 16 m plot lengths (events 13 to 24)

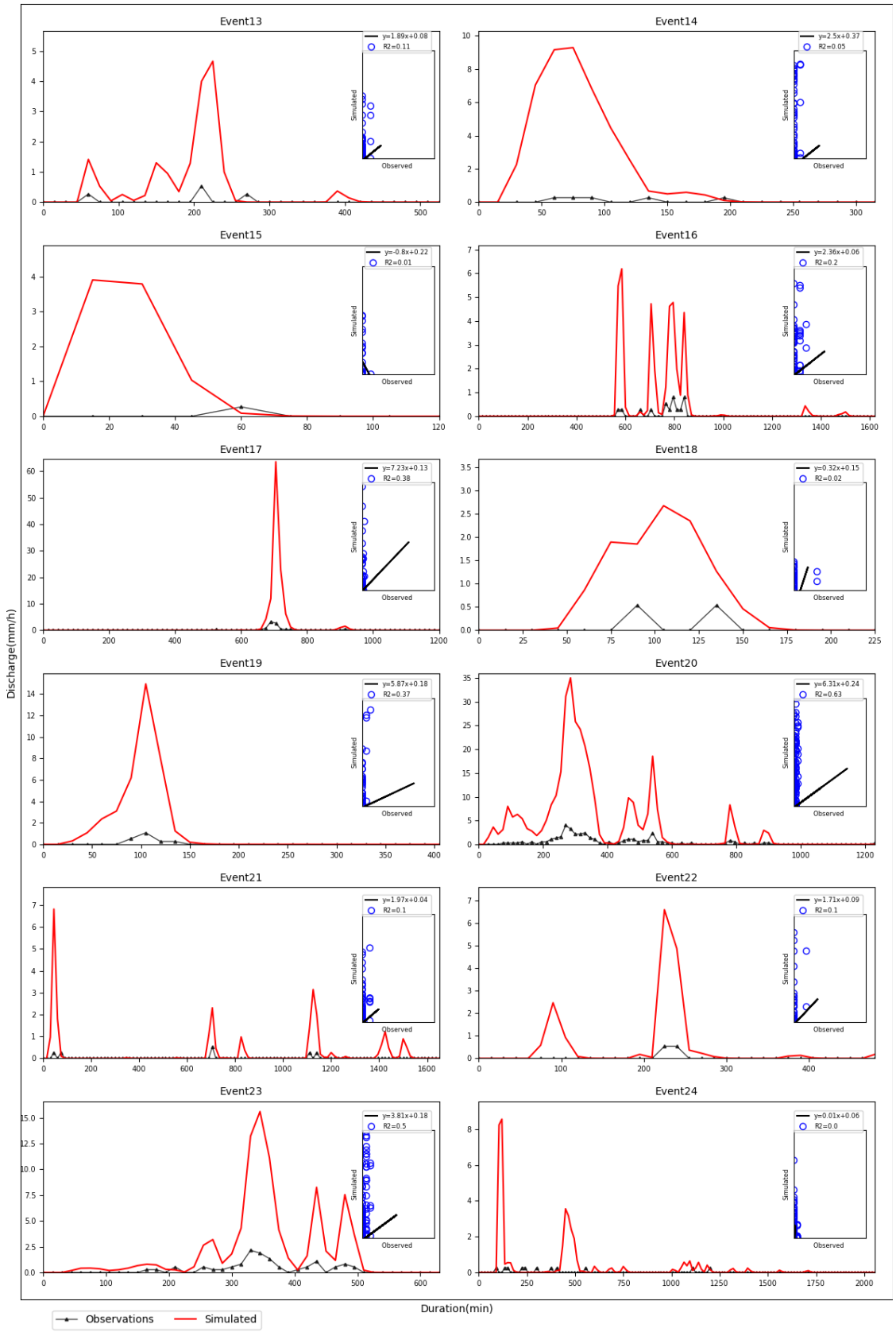

Appendix 5.6 Upscaling simulations for 16 m plot lengths (events 25 to 36)

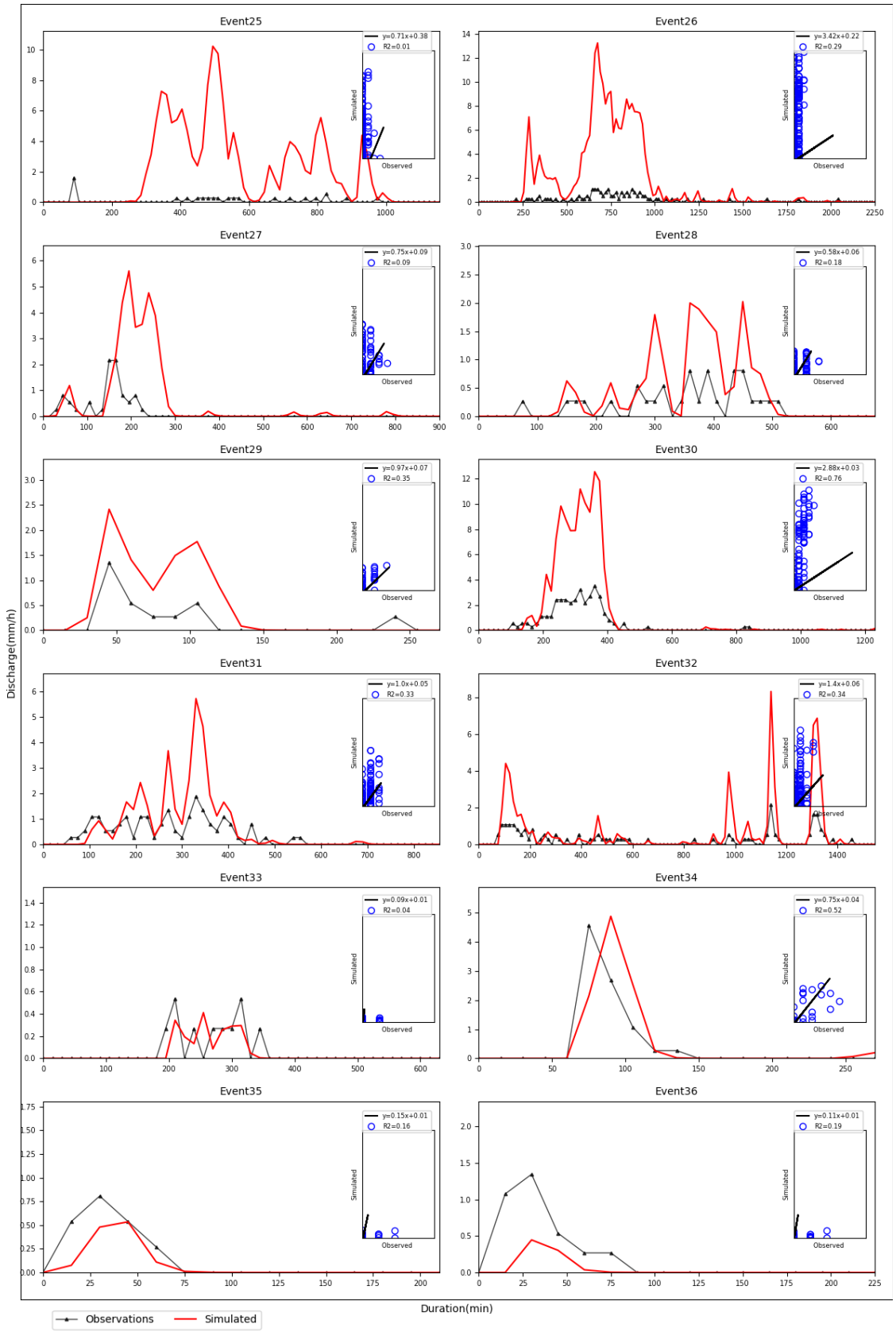

Appendix 5.6. Upscaling simulations for 16 m plot lengths (events 37 to 41)

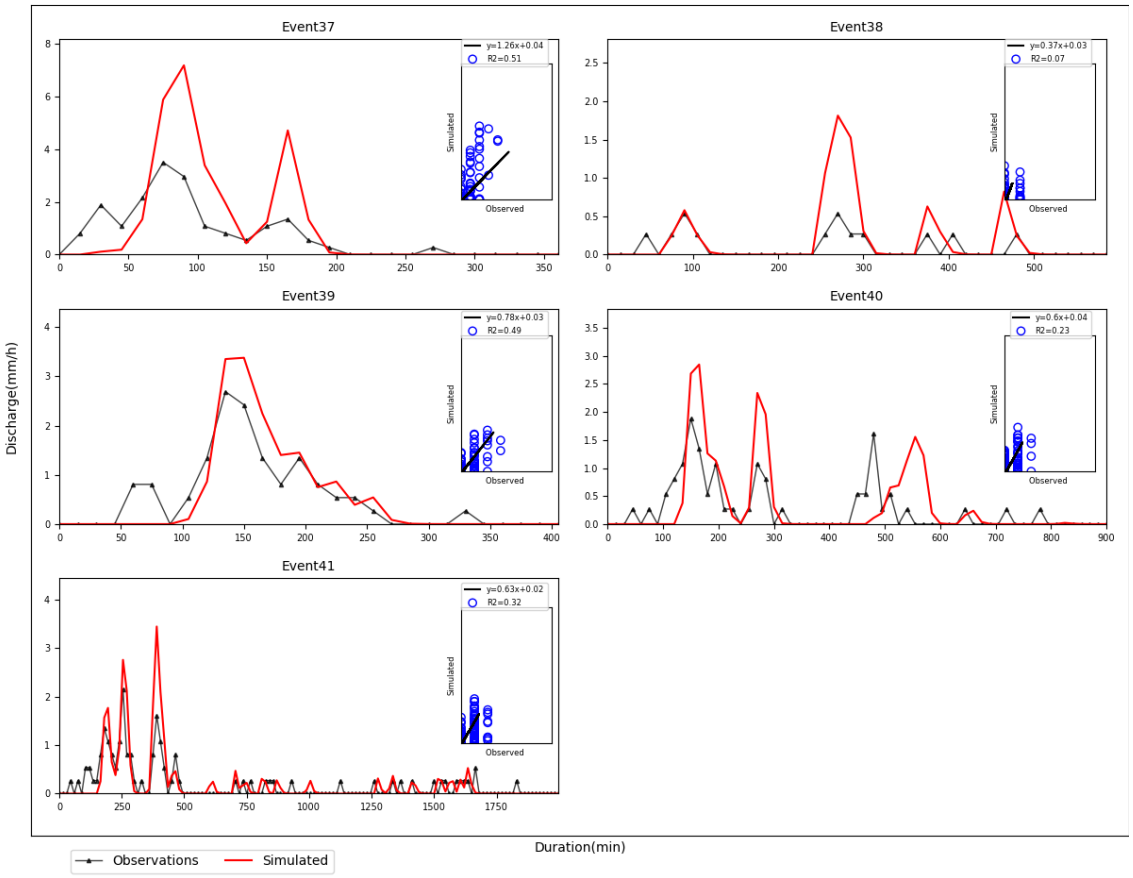

Appendix 6. 1 Shuffled Complex Evolution (SCE) optimization algorithm

```
import numpy as np
import spotpy
from spot_setup_griewank import spot_setup
spot_setup=spot_setup()
def shuffle_complex(row, rep,a,b, BeanSize,Calib_output):
  shuffle=[]
  result_r=[]
  #-------------------------------------------------
  sampler_r=spotpy.algorithms.sceua(spot_setup,a,b, row,dbname=Calib_output+'pores_shffle', dbformat='csv' )
  sampler_r.sample(rep,ngs=BeanSize)
  result_r=(sampler_r.getdata())
  algorithms=['SCEUA']
  for i in result_r:
      shuffle.append(i[1])
  evaluation = spot_setup.evaluation()
  return(shuffle)
```

Appendix 6. 2 Macropores Generator with SCE Optimiser

```
import sys, ast, shutil, os, string, linecache, matplotlib.pyplot as plt, numpy as np
import openpyxl
from openpyxl import Workbook
from pylab import rcParams
import shuffle_function
import math
import copy
import random
from random import shuffle

PoreAttribut = []; xmatrix=[]; ymatrix=[] ; Coordinate = []; PoreAttribut = []
#_____________________________________________________________________________________
     # this function records generated pores info into an excel file including 'radius',
depth, volume, x, y, depth pressure entry

def Poredata_excelfile(length,radius,tube_depth, total_vol, xmatrix,ymatrix, pores_hydro
_depth,pores_hydro_pres):
    filename=Calib_output+'Summary-depth_pressureEntry.xlsx'
    ww = openpyxl.Workbook(filename)
    ww.save(filename)
    wwb = openpyxl.load_workbook(filename=filename, data_only=True)
    wwb.save(filename)
    no=1;i=2
    pw2 = wwb.create_sheet(index=0, title='Pores summary'+ str(length))
    pw2['A1']='no.'
    pw2['B1']='radius'
    pw2['C1']='depth'
    pw2['D1']='volume'
    pw2['F1']='x'
    pw2['G1']='y'
    pw2['H1']='Depth Entry'
    pw2['I1']='Pressure Entry'
    for r in radius:
            pw2['A'+str(i)]=no
            pw2['B'+str(i)]=radius[i-2]
            pw2['C'+str(i)]=tube_depth[i-2]
            pw2['D'+str(i)]=total_vol[i-2]
            pw2['F'+str(i)]=xmatrix[i-2]
            pw2['G'+str(i)]=ymatrix[i-2]
            pw2['H'+str(i)]=pores_hydro_depth[i-2]
            pw2['I'+str(i)]=pores_hydro_pres[i-2]
            no=no+1
            i=i+1
```

```
    wwb.save(filename)
    return []
#_____________________________________________________________________________
     # this function records pores volume and litre per plot in text file

def  Abstractfile():

        Abstractfile=open(Calib_output+'Abstract.txt',"w")
        Abstractfile.write('1. Number of pores in one square metre= '+str (len(radius))+
'\n''\n'+
        '1.1 Pores percentage in surface area (%)= '+str (100*(sum (areamat))/(Area))+'\
n''\n'+
        '2. Total volume of pores (litre)= '+str (sum (total_vol)*1000)+'\n''\n'+  #m3 t
o litre
        '2.1 Pores volume/Area x 0.1 deph m3 soil volume (%)= '+str ((sum (total_vol))*1
00/(Area*0.1))+'\n''\n' +
        '3. Maximum pore pressure depth needed (mm)= '+str (max ( pores_hydro_depth)*100
0)+'\n' '\n'
        '4. Minimum pore pressure depth needed (mm)= '+str (min ( pores_hydro_depth)*100
0)+'\n''\n'
        '5. Minimum pore pressure needed (N/m2)= '+str (min ( pores_hydro_pres))+'\n''\n
'
        '6. Maximum pore pressure needed (N/m2)= '+str (max ( pores_hydro_pres))+'\n''\n
')
        Abstractfile.close()
#_____________________________________________________________________________
     # this function plots 1) pores distribution within the given area, 2) probability
distribution function of pores radius and depth
def graphs(radius, tube_depth):
    L=[radius, tube_depth]
    jj=['pores radius', 'pores depth']
    rcParams['figure.figsize'] = int(float(width)*5),int(float (length)*5)
    plt.figure()
    area = np.pi * (100*np.array(radius))**2
    colors = 1000*np.array(radius)
    plt.scatter(ymatrix,xmatrix,alpha=1,s=area , c=colors,cmap='PuOr')
    plt.colorbar(ticks=range(10), label='radius (mm)')
    plt.clim(0, 10)
    plt.xlabel('Plot Width (cm)', size=12)
    plt.ylabel('Plot length (cm)', size=12)
    plt.xlim(0, float(width)*100)
    plt.ylim(0, float(length)*100)
    plt.savefig(Calib_output+'Macropores graph'+str(length)+'.png',format='png', dpi=200
)
    import pylab as P
    for i, e in enumerate(L):
    # the histogram of the data with histtype='step'
        rcParams['figure.figsize'] = 8,8
        plt.figure()
        n, bins, patches = P.hist([x*1000 for x in e], 50, normed=1, histtype='stepfille
d')
        plt.setp(patches, 'facecolor', 'g', 'alpha', 0.75)
        plt.xlabel(jj[i]+'(mm)', size=12)
        plt.ylabel('PDF', size=12)
        plt.savefig(Calib_output+'PDF'+jj[i]+ str(length)+'.png',format='png', dpi=50)

#_____________________________________________________________________________
   # this function generates pores based on the given plot area
def PoreInfo (Area,row, rep, BeanSize, Calib_output,length, width,x, angle, wr):
#1. call macropores modules (n,h,r), n= numbers of macro-pores, h= depth of macro-
pores, r= radius
    total_vol=[];areamat=[] #total volume matrix
    r=(0.0005, 0.01)      #radius (m)
    td=(0.01,0.10) # tupes depth (m)
    a=r[0];b=r[1] #lower and upper boundary for radius
    radius=(shuffle_function.shuffle_complex(row, rep,a,b, BeanSize, Calib_output))
```

```
    # print str (len(radius))
    for i in radius:
        area=3.14*(i**2)
        areamat.append(area)
    aa=td[0];bb=td[1]
    tube_depth=shuffle_function.shuffle_complex(row, rep,aa,bb, BeanSize,Calib_output )

    # print (len(radius), len (tube_depth))
    if len (radius)!=len(tube_depth):
        dif=abs(len(tube_depth)-len (radius))
        z=(len(tube_depth))-dif
        if len (radius)>len(tube_depth):
            del radius[z:len (radius)]
        if len (radius)<len(tube_depth):
            del tube_depth[z:len (tube_depth)]
    for i in range (0,len (radius)):
            tv=tube_depth[i]*3.14*(radius[i]**2)
            total_vol.append(tv)  #m3
    #_____________________________________________________________________________
 #2. Appointing coordinate
    pointNo= int((float((length))*100)*(float((width))*100))
    # print 'pointNo='+str(pointNo)
    # print 'pores no='+str (len(radius))
    if pointNo < len(radius):
        # print 'pointNo < len(radius)'
        bb= int(float(length)*1000)
        aa=int(float(width)*1000)
    if pointNo >= len(radius):
        # print 'pointNo > len(radius)'
        bb= int(float(length)*100)#cm
        aa=int(float(width)*100) #cm
    for i in range (0,bb):
        for ii in range(0,int(aa)):
                x= i
                xmatrix.append(x) #containing distance from the plot top (cm)
    for j in range (0,aa):
            for jj in range (0,int(bb)):
                y= j
                ymatrix.append(y)
    random.shuffle(xmatrix)
    random.shuffle(ymatrix)
    if len (radius)!=len(xmatrix):
            dif_X=abs(len(xmatrix)-len (radius))
            zx=(len(xmatrix))-dif_X
            dif_Y=abs(len(ymatrix)-len (radius))
            zy=(len(ymatrix))-dif_Y
            if len (xmatrix)>len(radius):
                del xmatrix[zx:len (xmatrix)]
                # print len(xmatrix)
            if len (ymatrix)>len(radius):
                del ymatrix[zy:len (ymatrix)]
                # print len(ymatrix)
#_____________________________________________________________________________
   #3. macro flow
    pores_hydro_depth=[] #critiacal water depth needed to break macropores pressure entr
y
    pores_hydro_pres=[] #pressure entry
    for r in radius:
        hc=abs(2*wr*math.cos(math.radians(angle))/(r*9.8*1000)) # metre
        pores_hydro_depth.append(hc)
        Pc=abs(2*wr*math.cos(math.radians(angle))/(r))
        pores_hydro_pres.append(Pc)
    for i in range (0, len (radius)):
                PoreLoc=(radius[i],tube_depth[i],xmatrix[i],ymatrix[i],pores_hydro_pres[
i] )
                PoreAttribut.append(PoreLoc)
```

```
                pore=(xmatrix[i],ymatrix[i])
                Coordinate.append(pore)
    return [radius,tube_depth,total_vol, xmatrix,ymatrix, pores_hydro_depth,pores_hydro_
pres, areamat]
#-------------------------------------------------------------------------------------
# Above functions can be tested by the below scripts
Calib_output= raw_input("Macropores Output File Address:") +'\\'
i=1
#-------------------------------------------------------------------------------------
length=1;width=1
nn=list(range(0, 1000))
Area=(float (length)*float(width))
x=1 #counter for beansize
angle=105; g=9.8; n=0.65; s=0.51 #S slope
wr=0.043  ##it was 43 milinewton divided by 1000 to convert inot N/m
#-------------------------------------------------------------------------------------
for j in range (1,100):
    n1=(1000*nn[i-1]+1)
    n2=(1000*nn[i])
    row=j #parameter for shuffleComplex-rows of lists
    BeanSize=int(x*(Area+1))
#parameter for shuffleComplex- size distribution of points in list
    rep=int(np.random.uniform (n1*Area,n2*Area)) #point no.
    print 'BeanSize='+str(BeanSize)
    print (n1,n2)
    print "(i,j)="+str((i,j))
    [radius,tube_depth,total_vol, xmatrix,ymatrix, pores_hydro_depth,pores_hydro_pres, a
reamat]=PoreInfo(Area,row, rep, BeanSize, Calib_output,length, width,x, angle, wr)
    VolMeet= 100*(sum (total_vol)/((Area*0.1))) #pores total volume
    print '(r,d)='+str((len(radius), len (tube_depth)))
    print 'total pores volume='+str(VolMeet)
    if VolMeet>5.5:
        x=x-5
    if VolMeet<4:
        x=x+5
    if  VolMeet>=4 and VolMeet<5.5:
         Poredata_excelfile(length,radius,tube_depth, total_vol, xmatrix,ymatrix, pores_
hydro_depth,pores_hydro_pres) #pores info into the excelfile
         graphs(radius, tube_depth) #PDFs for radius and depth, pores locations within t
he given area
         Abstractfile()
         break
    i=i+1
```

The result from the above codes for one 1x1 m plot length:

```
    Number of pores in one square metre = 4620
    Pores percentage in surface area (%) = 10.132255485
    Total volume of pores (litre) = 4.25447747283
    Pores volume/Area x 0.1 deph m3 soil volume (%) = 4.25447747283
```

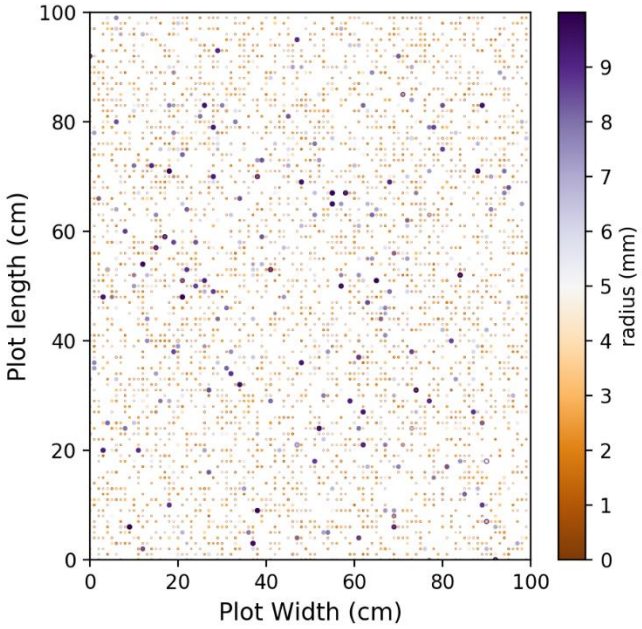

Appendix 6.2.1 Pores coordinates (x,y) within 1x1 m plot

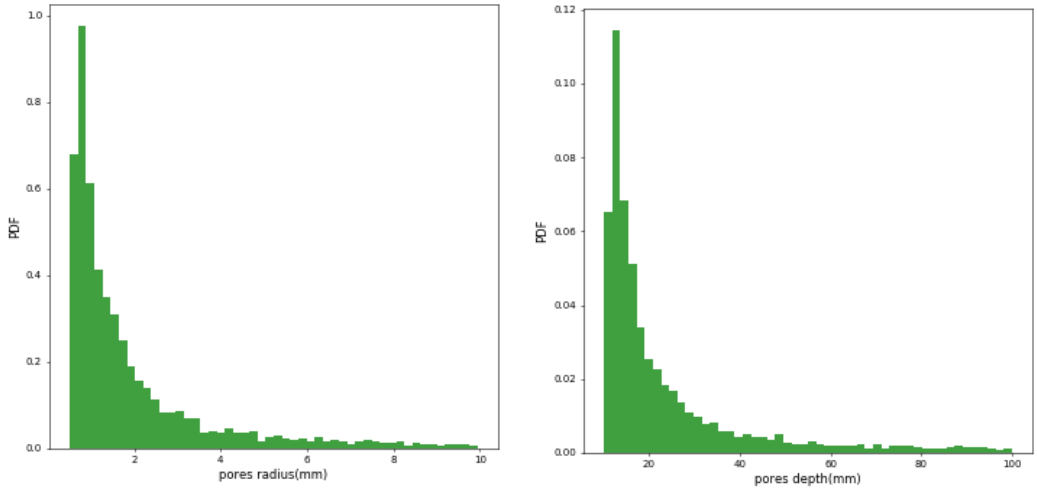

Appendix 6.2.2 Probability distribution function a) pores radius, b) pores depth

Appendix 6. 3 KINEROS2 Simulation for Pre-ponding Infiltration Run

```
# Run Kineros2
os.system("Kineros2 < input.fil")
Output_file=open("Output8.out","r")
discharge_mod=open("DISCHARGE_MOD.OUT", "r")
runoff_Discharge = open('discharge.txt', 'w+')
```

Appendix 6. 4 Pressure Entry at Individual Pores

```
#C:Chezy resistance coefficient (m^1/3/sec), g:gravity (m/s), runoff_mod:simulated runoff
def Flowpressure_gradient (runoff_mod, length, width, g, s, C):
    Area=float (length)*float(width)
    s=0.51 # Plot's slop
    Pwater_list=[]; depth_water=[]
    i=0; h=0;Pwater=0;v=0;
    Constant= 9800+(63.75*(C**2)) #Constant: ρ(g+(C^2 Sf)/8), sf:tan(slope)
    f=((8*9.8)/(C**2)) # number from Moody diagram f:(8g/c^2) or C:√(8g/f) Froude
    re=(96*(C**2))/(8*9.8) #reynold number:(64*(C^2))/(8g) Smith et al., 2007
    if re <2000:
     for q in runoff_mod:
        qq=float(q)*Area/(3600*1000) # mm/h convert to m3/s
        h=((qq/1.5 )/((C)*(s**0.5)))**(0.5) #
m Laminar flow and natural surfaces β:2
        V=((8*g*s*qq)/f)**(0.33333333333333) # m/s Velocity
        Pwater1=1000*((g*h)+(0.5*(V**2)))  # Water pressure (kg/m.S2=N/m2)
        Pwater=0.00010199773339984*1000*((g*h)+(0.5*(V**2)))  # Water head (m)
        Pwater_list.append(Pwater)
        depth_water.append(h)
     if re >2000:
         print 'Reynold number >2000'
    return (Pwater_list,depth_water )
```

Appendix 6. 5 Macropores filling Module

```
# Pwater_list: Simulated water pressure
# flowPressure: water pressure at the plot end m
# filled_Percentage_Timestep: simulation intervals (3 minutes)
# runoff_mod: Simulated runoff from KINEROS(mm/h)
# pores_hydro_depth: Water depth requires to break the pressure entry
# pores_hydro_pres: Pressure enrty requires at pores
# xmatrix: x coordinate of pores location within the plot
# filled_Percentage_Timestep: percentage of pores filled

def Filling (Pwater_list,flowVol,flowPressure, width,length,runoff_mod,depth_water, rai
nInterval, total_vol, pores_hydro_depth,pores_hydro_pres, xmatrix, counter,filled_Perce
ntage_Timestep):

        Area=float (length)*float(width);
        MacfloWVolMatix=[]; Mac_flowPressure=[];New_xmatrix=[]
        Vol_pore_filled=[] #Volume of pores been filled
        pores_vol_pres_kept=[] #Volume of empty pores
        pores_hydro_pres_kept=[]  # pressure entry of empty pores
        for ii in range (0,len(total_vol)):  # for volume of pores m^3
         if flowVol>0:
            vol_abs = ((total_vol[ii])*1000)   # the available volume to be filled in t
his pore   #total_vol[ii])*1000 convert m3 to liter
            Poreloc = xmatrix[ii]
            pore_flowPressure = flowPressure *float(int(float(Poreloc)))/(100*float(len
gth))  # (m) water head or water pressure gradient at each single pore
            MacfloWVol = float(flowVol)*float(Poreloc)/(100*float(length))#### (litre)
volume of water at the pores location in relation to flow depth
            Mac_flowPressure.append(pore_flowPressure)  # (N) water pressure gradient
at each single pore
            MacfloWVolMatix.append(MacfloWVol)   #(litre) volume of pores
#_____________________________________________________________________________
  # 2. applying the filling equation
            if pore_flowPressure>(pores_hydro_depth[ii]): #if water pressure is higher
than pore pressure entry (units are m )
                if MacfloWVol> vol_abs: #if runoff volume is larger than pore volume
and water flow is larger than zero
```

```
                    Vol_pore_filled.append((total_vol[ii])*1000) # fill the pore litre
                    flowVol=flowVol-(total_vol[ii]*1000) #subtract the water went to
pore from runoff volume (litre)
                    counter.append(ii)
            if pore_flowPressure <(pores_hydro_depth[ii]):#if water pressure is smaller
 than pore pressure entry
                pores_hydro_pres_kept.append(pores_hydro_pres[ii])
                pores_vol_pres_kept.append(total_vol[ii])
                New_xmatrix.append(xmatrix[ii])
            ii=ii+1
        Filling_abstract=(sum(Vol_pore_filled)) #volume of water used for filling in th
is time step (litre)
        if sum(total_vol)==0:
            filled_Percentage_Timestep.append(0)
        else:
            filled_Percentage_Timestep.append(float(Filling_abstract/sum(total_vol)))
        # print filled_Percentage_Timestep
        filling_flow= round(((Filling_abstract*60)/(Area*rainInterval)),6) # Filling
abstract in this timestep mm/h
        return [Vol_pore_filled,pores_vol_pres_kept, pores_hydro_pres_kept, New_xmatrix
, filled_Percentage_Timestep, Filling_abstract,filling_flow, total_vol]
```

Appendix 6. 6 Macropores Seeping Module

```
# applying seeping equation
# Spilling_Matrix: pores seeping to underneath mineral soil
# Depth: pores depth; radius: pore radius
# flowVol: pore volume
# Pwater_list: Water pressure at pore
def Spilling(Spilling_Matrix,width,length, Depth,t, flowVol,Pwater_list,depth_water, co
unter,radius,tube_depth, rainInterval, runoff_mod):
      Area=float (length)*float(width)
      Kspilling= 0; runoff_mod_minus_Spilling=[]
      Spilling_Q=[]; constant2=3834960.5 #(1000*9.8*3.14)/(8*0.001) (ρgπ)/8μ;
      Constant=13.9
      if counter!=0 and flowVol>0:
            for v in counter:
                r= radius [v]
                Qii=((r**2)*3.14*tube_depth[v])/(rainInterval*60)   #Q=3.14*r^2*L/t fro
m Podgorney et al., 2008
                Spilling_Q.append(Qii)
            # Kspilling=(sum(Spilling_Q)*0.04/(float(Area)*Pwater_list[t]))*3600000
            if runoff_mod[t]>Kspilling:
                Kspilling= ((sum(Spilling_Q))*Pwater_list[t]/(float(Area)*0.04)) *36000
00   # K_spilling=QΔZ/Ah (mm/h)
            if runoff_mod[t]<Kspilling:
                Kspilling= runoff_mod[t]    #mm/h
            runoff_mod_minus_Spilling.append(runoff_mod[t]-Kspilling)
            Spilling_Matrix.append(Kspilling)
      return [Spilling_Matrix,Kspilling,runoff_mod_minus_Spilling]
```

Reference

AL-QURASHI, A., MCINTYRE, N., WHEATER, H. & UNKRICH, C. 2008. Application of the Kineros2 rainfall–runoff model to an arid catchment in Oman. *Journal of Hydrology,* 355**,** 91-105.

ALLAIRE-LEUNG, S., GUPTA, S. C. & MONCRIEF, J. 2000. Water and solute movement in soil as influenced by macropore characteristics: 1. Macropore continuity. *Journal of Contaminant Hydrology,* 41**,** 283-301.

ALLAIRE, S. E., ROULIER, S. & CESSNA, A. J. 2009. Quantifying preferential flow in soils: A review of different techniques. *Journal of Hydrology,* 378**,** 179-204.

ANDERSON, A., WEILER, M., ALILA, Y. & HUDSON, R. 2008. Dye staining and excavation of a lateral preferential flow network. *Hydrology and Earth System Sciences Discussions,* 5**,** 1043-1065.

BACHMANN, J. & VAN DER PLOEG, R. R. 2002. A review on recent developments in soil water retention theory: interfacial tension and temperature effects. *Journal of Plant Nutrition and Soil Science,* 165**,** 468-478.

BAGARELLO, V. & FERRO, V. 2010. Analysis of soil loss data from plots of differing length for the Sparacia experimental area, Sicily, Italy. *Biosystems Engineering,* 105**,** 411-422.

BAGARELLO, V., FERRO, V. & GIORDANO, G. 2010. Testing alternative erosivity indices to predict event soil loss from bare plots in Southern Italy. *Hydrological processes,* 24**,** 789-797.

BAGARELLO, V., FERRO, V., KEESSTRA, S., COMINO, J. R., PULIDO, M. & CERDÀ, A. 2018. Testing simple scaling in soil erosion processes at plot scale. *Catena,* 167**,** 171-180.

BART, R. R. 2016. A regional estimate of postfire streamflow change in California. *Water Resources Research,* 52**,** 1465-1478.

BAUTERS, T. W., STEENHUIS, T. S., PARLANGE, J. Y. & DICARLO, D. A. 1998. Preferential flow in water-repellent sands. *Soil Science Society of America Journal,* 62**,** 1185-1190.

BERGSTRÖM, S. & GRAHAM, L. P. 1998. On the scale problem in hydrological modelling. *Journal of Hydrology,* 211**,** 253-265.

BERRY, G., JAKOB, C. & REEDER, M. 2011. Recent global trends in atmospheric fronts. *Geophysical Research Letters,* 38.

BEVEN, K. & GERMANN, P. 1982. Macropores and water flow in soils. *Water resources research,* 18**,** 1311-1325.

BEVEN, K. & GERMANN, P. 2013. Macropores and water flow in soils revisited. *Water Resources Research,* 49**,** 3071-3092.

BIRCH, W. D. 2003. Geology of Victoria.

BLÖSCHL, G. & SIVAPALAN, M. 1995. Scale issues in hydrological modelling: a review. *Hydrological processes,* 9**,** 251-290.

BOM 2018. *Bureau of Meterology, 2014. www.bom.gov.au. Commonwealth of Australia, Bureau of Meteorology.*

BOUMA, J., DEKKER, L. & MUILWIJK, C. 1981. A field method for measuring short-circuiting in clay soils. *Journal of Hydrology,* 52**,** 347-354.

BRACKEN, L. J. & CROKE, J. 2007. The concept of hydrological connectivity and its contribution to understanding runoff-dominated geomorphic systems. *Hydrological processes,* 21**,** 1749-1763.

BUTTLE, J. & HOUSE, D. 1997. Spatial variability of saturated hydraulic conductivity in shallow macroporous soils in a forested basin. *Journal of Hydrology,* 203**,** 127-142.

CAI, W., COWAN, T. & SULLIVAN, A. 2009. Recent unprecedented skewness towards positive Indian Ocean Dipole occurrences and its impact on Australian rainfall. *Geophysical Research Letters,* 36.

CAMMERAAT, E. L. 2004. Scale dependent thresholds in hydrological and erosion response of a semi-arid catchment in southeast Spain. *Agriculture, ecosystems & environment,* 104**,** 317-332.

CAMMERAAT, L. 2002. A review of two strongly contrasting geomorphological systems within the context of scale. *Earth Surface Processes and Landforms,* 27**,** 1201-1222.

CANFIELD, H. E., GOODRICH, D. C. & BURNS, I. S. 2005. Selection of parameters values to model post-fire runoff and sediment transport at the watershed scale in southwestern forests. *Managing Watersheds for Human and Natural Impacts: Engineering, Ecological, and Economic Challenges.*

CARRILLO, M., YATES, S. & LETEY, J. 1999. Measurement of initial soil-water contact angle of water repellent soils. *Soil Science Society of America Journal,* 63**,** 433-436.

CATTO, J., JAKOB, C., BERRY, G. & NICHOLLS, N. 2012. Relating global precipitation to atmospheric fronts. *Geophysical Research Letters,* 39.

CAWSON, J., SHERIDAN, G., SMITH, H. & LANE, P. 2012. Surface runoff and erosion after prescribed burning and the effect of different fire regimes in forests and shrublands: a review. *International Journal of Wildland Fire,* 21**,** 857-872.

CAWSON, J., SHERIDAN, G., SMITH, H. & LANE, P. 2013. Effects of fire severity and burn patchiness on hillslope-scale surface runoff, erosion and hydrologic connectivity in a prescribed burn. *Forest Ecology and Management,* 310**,** 219-233.

CERDÁ, A. & DOERR, S. H. 2005. Influence of vegetation recovery on soil hydrology and erodibility following fire: an 11-year investigation. *International Journal of Wildland Fire,* 14**,** 423-437.

CERDÀ, A. & DOERR, S. H. 2008. The effect of ash and needle cover on surface runoff and erosion in the immediate post-fire period. *Catena,* 74**,** 256-263.

CERDAN, O., LE BISSONNAIS, Y., GOVERS, G., LECOMTE, V., VAN OOST, K., COUTURIER, A., KING, C. & DUBREUIL, N. 2004. Scale effect on runoff from experimental plots to catchments in agricultural areas in Normandy. *Journal of hydrology,* 299**,** 4-14.

CHEN, L., BERLI, M. & CHIEF, K. 2013. Examining modeling approaches for the rainfall-runoff process in wildfire-affected watersheds: Using San Dimas Experimental Forest. *JAWRA Journal of the American Water Resources Association,* 49**,** 851-866.

CHEN, L., SELA, S., SVORAY, T. & ASSOULINE, S. 2016a. Scale dependence of Hortonian rainfall-runoff processes in a semiarid environment. *Water Resources Research*.

CHEN, L., SELA, S., SVORAY, T. & ASSOULINE, S. 2016b. Scale dependence of Hortonian rainfall-runoff processes in a semiarid environment. *Water Resources Research,* 52**,** 5149-5166.

CHOW, V., MAIDMENT, D. & MAYS, L. 1988. Applied hydrology (p. 572). *New York (NY): MacGraw-Hill*.

COCHRANE, G., QUICK, G. & SPENCER-JONES, D. 1995. Geological history of Victoria. *Introducing Victorian Geology***,** 97-168.

CORRADINI, C., GOVINDARAJU, R. S. & MORBIDELLI, R. 2002. Simplified modelling of areal average infiltration at the hillslope scale. *Hydrological processes,* 16**,** 1757-1770.

CORRADINI, C., MELONE, F. & SMITH, R. E. 1994. Modeling infiltration during complex rainfall sequences. *Water Resources Research,* 30**,** 2777-2784.

CORRADINI, C., MELONE, F. & SMITH, R. E. 1997. A unified model for infiltration and redistribution during complex rainfall patterns. *Journal of Hydrology,* 192**,** 104-124.

CORRADINI, C., MORBIDELLI, R. & MELONE, F. 1998. On the interaction between infiltration and Hortonian runoff. *Journal of Hydrology,* 204**,** 52-67.

DAGAN, G. & BRESLER, E. 1983. Unsaturated flow in spatially variable fields: 1. Derivation of models of infiltration and redistribution. *Water Resources Research,* 19**,** 413-420.

DE DIOS BENAVIDES-SOLORIO, J. & MACDONALD, L. H. 2005. Measurement and prediction of post-fire erosion at the hillslope scale, Colorado Front Range. *International Journal of Wildland Fire,* 14**,** 457-474.

DEBANO, L. F., NEARY, D. G. & FFOLLIOTT, P. F. 1998. *Fire effects on ecosystems*, John Wiley & Sons.

DEKKER, L. W. & RITSEMA, C. J. 1994. How water moves in a water repellent sandy soil: 1. Potential and actual water repellency. *Water Resources Research,* 30**,** 2507-2517.

DELMAS, M., PAK, L.-T., CERDAN, O., SOUCHÈRE, V., LE BISSONNAIS, Y., COUTURIER, A. & SOREL, L. 2012. Erosion and sediment budget across scale: A case study in a catchment of the European loess belt. *Journal of hydrology,* 420**,** 255-263.

DEPI 2014. *Department of Environment and Primary Industies. http://www.depi.vic.gov.au/fire-and-emergencies/managing-risk-and-learning-about-managing-fire/bushfire-history. Web site accessed August 2014.*

DOERR, S., FERREIRA, A., WALSH, R., SHAKESBY, R., LEIGHTON-BOYCE, G. & COELHO, C. 2003. Soil water repellency as a potential parameter in rainfall-runoff modelling: experimental evidence at point to catchment scales from Portugal. *Hydrological Processes,* 17**,** 363-377.

DOERR, S., SHAKESBY, R. & WALSH, R. 2000. Soil water repellency: its causes, characteristics and hydro-geomorphological significance. *Earth-Science Reviews,* 51**,** 33-65.

DOERR, S. H. 1998. On standardizing the 'water drop penetration time'and the 'molarity of an ethanol droplet'techniques to classify soil hydrophobicity: a case study using medium textured soils. *Earth Surface Processes and Landforms: The Journal of the British Geomorphological Group,* 23**,** 663-668.

DOERR, S. H. & MOODY, J. A. 2004. Hydrological effects of soil water repellency: on spatial and temporal uncertainties. *Hydrological Processes,* 18**,** 829-832.

DOERR, S. H., SHAKESBY, R. A. & MACDONALD, L. H. 2009. Soil water repellency: a key factor in post-fire erosion. *Fire effects on soils and restoration strategies,* 5.

DUNKERLEY, D. 2012. Effects of rainfall intensity fluctuations on infiltration and runoff: rainfall simulation on dryland soils, Fowlers Gap, Australia. *Hydrological Processes,* 26**,** 2211-2224.

DUNNE, T., ZHANG, W. & AUBRY, B. F. 1991. Effects of rainfall, vegetation, and microtopography on infiltration and runoff. *Water Resources Research,* 27**,** 2271-2285.

EBEL, B. A. & MOODY, J. A. 2017. Synthesis of soil-hydraulic properties and infiltration timescales in wildfire-affected soils. *Hydrological processes,* 31**,** 324-340.

FLÜHLER, H., DURNER, W. & FLURY, M. 1996. Lateral solute mixing processes—A key for understanding field-scale transport of water and solutes. *Geoderma,* 70**,** 165-183.

FLURY, M. & FLÜHLER, H. 1994. Brilliant Blue FCF as a dye tracer for solute transport studies—a toxicological overview. *Journal of Environmental Quality,* 23**,** 1108-1112.

FLURY, M. & FLÜHLER, H. 1995. Tracer characteristics of brilliant blue FCF. *Soil Science Society of America Journal,* 59**,** 22-27.

FREE, G. R., BROWNING, G. M. & MUSGRAVE, G. W. 1940. *Relative infiltration and related physical characteristics of certain soils*, US Dept. of Agriculture.

GENTINE, P., TROY, T. J., LINTNER, B. R. & FINDELL, K. L. 2012. Scaling in surface hydrology: Progress and challenges. *Journal of Contemporary Water research & education,* 147**,** 28-40.

GERKE, H. H. 2006. Preferential flow descriptions for structured soils. *Journal of Plant Nutrition and Soil Science,* 169**,** 382-400.

GERKE, H. H., GERMANN, P. & NIEBER, J. 2010. Preferential and unstable flow: From the pore to the catchment scale. *Vadose Zone Journal,* 9**,** 207-212.

GERKE, K. M., SIDLE, R. C. & MALLANTS, D. 2015. Preferential flow mechanisms identified from staining experiments in forested hillslopes. *Hydrological Processes,* 29**,** 4562-4578.

GERMÁN-HEINS, J. & FLURY, M. 2000. Sorption of Brilliant Blue FCF in soils as affected by pH and ionic strength. *Geoderma,* 97**,** 87-101.

GÓMEZ, J., NEARING, M., GIRÁLDEZ, J. & ALBERTS, E. 2001. Analysis of sources of variability of runoff volume in a 40 plot experiment using a numerical model. *Journal of Hydrology,* 248**,** 183-197.

GOMI, T., SIDLE, R. C., MIYATA, S., KOSUGI, K. I. & ONDA, Y. 2008a. Dynamic runoff connectivity of overland flow on steep forested hillslopes: scale effects and runoff transfer. *Water Resources Research,* 44.

GOMI, T., SIDLE, R. C., UENO, M., MIYATA, S. & KOSUGI, K. I. 2008b. Characteristics of overland flow generation on steep forested hillslopes of central Japan. *Journal of Hydrology,* 361**,** 275-290.

GOODRICH, D., BURNS, I., UNKRICH, C., SEMMENS, D. J., GUERTIN, D., HERNANDEZ, M., YATHEENDRADAS, S., KENNEDY, J. R. & LEVICK, L. R. 2012. KINEROS2/AGWA: model use, calibration, and validation. *Transactions of the ASABE,* 55**,** 1561-1574.

GOVINDARAJU, R., KOELLIKER, J., BANKS, M. & SCHWAB, A. 1996. Comparison of spatial variability of infiltration properties at two sites in Konza prairie of East-Central Kansas. *Journal of Hydrologic Engineering,* 1**,** 131-138.

GOVINDARAJU, R., NAHAR, N., CORRADINI, C. & MORBIDELLI, R. 2006. Infiltration and Run-On under Spatially Variable Hydrologic Properties. *The Handbook of Groundwater Engineering, Second Edition.* CRC Press.

GOVINDARAJU, R. S., MORBIDELLI, R. & CORRADINI, C. 2001. Areal infiltration modeling over soils with spatially correlated hydraulic conductivities. *Journal of hydrologic engineering,* 6**,** 150-158.

GRAHAM, M. H. 2003. Confronting multicollinearity in ecological multiple regression. *Ecology,* 84**,** 2809-2815.

GRANGED, A. J., JORDÁN, A., ZAVALA, L. M. & BÁRCENAS, G. 2011. Fire-induced changes in soil water repellency increased fingered flow and runoff rates following the 2004 Huelva wildfire. *Hydrological Processes,* 25**,** 1614-1629.

GREGORICH, E. G. & CARTER, M. R. 2007. *Soil sampling and methods of analysis*, CRC press.

GRIEWANK, A. O. 1981. Generalized descent for global optimization. *Journal of optimization theory and applications,* 34**,** 11-39.

GUO, L. & LIN, H. 2018. Addressing Two Bottlenecks to Advance the Understanding of Preferential Flow in Soils. *Advances in Agronomy.* Elsevier.

HARDIE, M., LISSON, S., DOYLE, R. & COTCHING, W. 2013. Determining the frequency, depth and velocity of preferential flow by high frequency soil moisture monitoring. *Journal of contaminant hydrology,* 144**,** 66-77.

HOPMANS, J. W., NIELSEN, D. R. & BRISTOW, K. L. 2002. How useful are small-scale soil hydraulic property measurements for large-scale vadose zone modeling? *GEOPHYSICAL MONOGRAPH-AMERICAN GEOPHYSICAL UNION,* 129**,** 247-258.

HOUSKA, T., KRAFT, P., CHAMORRO-CHAVEZ, A. & BREUER, L. 2015. SPOTting model parameters using a ready-made python package. *PLoS One,* 10.

IMESON, A., VERSTRATEN, J., VAN MULLIGEN, E. & SEVINK, J. 1992. The effects of fire and water repellency on infiltration and runoff under Mediterranean type forest. *Catena,* 19**,** 345-361.

JARVIS, N. 2007. A review of non-equilibrium water flow and solute transport in soil macropores: Principles, controlling factors and consequences for water quality. *European Journal of Soil Science,* 58**,** 523-546.

JARVIS, N., ETANA, A. & STAGNITTI, F. 2008. Water repellency, near-saturated infiltration and preferential solute transport in a macroporous clay soil. *Geoderma,* 143**,** 223-230.

JARVIS, N., KOESTEL, J. & LARSBO, M. 2016. Understanding preferential flow in the vadose zone: Recent advances and future prospects. *Vadose Zone Journal,* 15.

JOEL, A., MESSING, I., SEGUEL, O. & CASANOVA, M. 2002. Measurement of surface water runoff from plots of two different sizes. *Hydrological Processes,* 16**,** 1467-1478.

JOHANSEN, M. P., HAKONSON, T. E. & BRESHEARS, D. D. 2001. Post-fire runoff and erosion from rainfall simulation: contrasting forests with shrublands and grasslands. *Hydrological processes,* 15**,** 2953-2965.

JOMAA, S., BARRY, D. A., HENG, B., BROVELLI, A., SANDER, G. & PARLANGE, J. Y. 2012. Influence of rock fragment coverage on soil erosion and hydrological response: Laboratory flume experiments and modeling. *Water Resources Research,* 48.

JONES, O., SHERIDAN, G. & LANE, P. A stochastic runoff model incorporating spatial variability. 18th World IMACS Congress and MODSIM09 International Congress on Modelling and Simulation, Anderssen RS, Braddock RD, Newham LTH (eds). Modelling and Simulation Society of Australia and New Zealand and International Association for Mathematics and Computers in Simulation, 2009. 1865-1871.

JORDÁN, A., ZAVALA, L. M., GRANGED, A. J., GORDILLO-RIVERO, Á. J., GARCÍA-MORENO, J., PEREIRA, P., BÁRCENAS-MORENO, G., DE CELIS, R., JIMÉNEZ-COMPÁN, E. & ALANÍS, N. 2016. Wettability

of ash conditions splash erosion and runoff rates in the post-fire. *Science of the Total Environment,* 572**,** 1261-1268.

JULIEN, P. Y. & MOGLEN, G. E. 1990. Similarity and length scale for spatially varied overland flow. *Water Resources Research,* 26**,** 1819-1832.

JULIEN, P. Y., SAGHAFIAN, B. & OGDEN, F. L. 1995. RASTER-BASED HYDROLOGIC MODELING OF SPATIALLY-VARIED SURFACE RUNOFF 1. *JAWRA Journal of the American Water Resources Association,* 31**,** 523-536.

KEAN, J. W., STALEY, D. M. & CANNON, S. H. 2011. In situ measurements of post-fire debris flows in southern California: Comparisons of the timing and magnitude of 24 debris-flow events with rainfall and soil moisture conditions. *Journal of Geophysical Research: Earth Surface,* 116.

KINNER, D. & MOODY, J. 2010. Spatial variability of steady-state infiltration into a two-layer soil system on burned hillslopes. *Journal of Hydrology,* 381**,** 322-332.

KINNER, D. A. & MOODY, J. A. 2008. Infiltration and runoff measurements on steep burned hillslopes using a rainfall simulator with variable rain intensities. U. S. Geological Survey.

KINOSHITA, A. M. & HOGUE, T. S. 2015. Increased dry season water yield in burned watersheds in Southern California. *Environmental Research Letters,* 10**,** 014003.

KIRKBY, M., BRACKEN, L. & SHANNON, J. 2005. The influence of rainfall distribution and morphological factors on runoff delivery from dryland catchments in SE Spain. *Catena,* 62**,** 136-156.

KRAUSE, P., BOYLE, D. & BÄSE, F. 2005. Comparison of different efficiency criteria for hydrological model assessment.

LAL, R. 1983. Effects of slope length on runoff from alfisols in western Nigeria. *Geoderma,* 31**,** 185-193.

LAL, R. 1997. Soil degradative effects of slope length and tillage methods on alfisols in western Nigeria. I. Runoff, erosion and crop response. *Land Degradation & Development,* 8**,** 201-219.

LANE, P. N., FEIKEMA, P. M., SHERWIN, C., PEEL, M. & FREEBAIRN, A. 2010. Modelling the long term water yield impact of wildfire and other forest disturbance in Eucalypt forests. *Environmental Modelling & Software,* 25**,** 467-478.

LANE, P. N., SHERIDAN, G. J. & NOSKE, P. J. 2006. Changes in sediment loads and discharge from small mountain catchments following wildfire in south eastern Australia. *Journal of Hydrology,* 331**,** 495-510.

LANGHANS, C., GOVERS, G. & DIELS, J. 2013. Development and parameterization of an infiltration model accounting for water depth and rainfall intensity. *Hydrological Processes,* 27**,** 3777-3790.

LANGHANS, C., GOVERS, G., DIELS, J., STONE, J. J. & NEARING, M. A. 2014. Modeling scale-dependent runoff generation in a small semi-arid watershed accounting for rainfall intensity and water depth. *Advances in water resources,* 69**,** 65-78.

LANGHANS, C., LANE, P. N., NYMAN, P., NOSKE, P. J., CAWSON, J. G., OONO, A. & SHERIDAN, G. J. 2016. Scale dependency of effective hydraulic conductivity on fire-affected hillslopes. *Water Resources Research*.

LARSEN, I. J., MACDONALD, L. H., BROWN, E., ROUGH, D., WELSH, M. J., PIETRASZEK, J. H., LIBOHOVA, Z., DE DIOS BENAVIDES-SOLORIO, J. & SCHAFFRATH, K. 2009. Causes of post-fire runoff and erosion: water repellency, cover, or soil sealing? *Soil Science Society of America Journal,* 73**,** 1393-1407.

LE BISSONNAIS, Y., BENKHADRA, H., CHAPLOT, V., FOX, D., KING, D. & DAROUSSIN, J. 1998. Crusting, runoff and sheet erosion on silty loamy soils at various scales and upscaling from m2 to small catchments. *Soil and Tillage Research,* 46**,** 69-80.

LEELAMANIE, D. & KARUBE, J. 2009. Effects of hydrophobic and hydrophilic organic matter on the water repellency of model sandy soils. *Soil Science and Plant Nutrition,* 55**,** 462-467.

LEELAMANIE, D., KARUBE, J. & YOSHIDA, A. 2008. Characterizing water repellency indices: Contact angle and water drop penetration time of hydrophobized sand. *Soil Science & Plant Nutrition,* 54**,** 179-187.

LEIGHTON-BOYCE, G., DOERR, S. H., SHAKESBY, R. A., WALSH, R. P., FERREIRA, A. J., BOULET, A.-K. & COELHO, C. O. 2005. Temporal dynamics of water repellency and soil moisture in eucalypt plantations, Portugal. *Soil Research,* 43**,** 269-280.

LEIGHTON-BOYCE, G., DOERR, S. H., WALSH, R. P., SHAKESBY, R. A., FERREIRA, A., BOULET, A. & COELHO, C. 2003. Spatio-temporal patterns of soil water repellency in Portuguese eucalyptus forests and implications for slope hydrology. *International Association of Hydrological Sciences, Publication***,** 111-116.

LETEY, J., CARRILLO, M. & PANG, X. 2000. Approaches to characterize the degree of water repellency. *Journal of Hydrology,* 231**,** 61-65.

LI, H. & SIVAPALAN, M. 2011. Effect of spatial heterogeneity of runoff generation mechanisms on the scaling behavior of event runoff responses in a natural river basin. *Water Resources Research,* 47.

LIN, H. 2010. Linking principles of soil formation and flow regimes. *Journal of Hydrology,* 393**,** 3-19.

LIU, B., NEARING, M., SHI, P. & JIA, Z. 2000. Slope length effects on soil loss for steep slopes. *Soil Science Society of America Journal,* 64**,** 1759-1763.

LOAGUE, K. & GANDER, G. A. 1990. R-5 revisited: 1. Spatial variability of infiltration on a small rangeland catchment. *Water Resources Research,* 26**,** 957-971.

MACDONALD, L. H. & HUFFMAN, E. L. 2004. Post-fire soil water repellency. *Soil Science Society of America Journal,* 68**,** 1729-1734.

MARTIN, Y., VALEO, C. & TAIT, M. 2008. Centimetre-scale digital representations of terrain and impacts on depression storage and runoff. *Catena,* 75**,** 223-233.

MAYNORD, S. T. 1991. Flow resistance of riprap. *Journal of Hydraulic Engineering,* 117**,** 687-696.

MAYOR, Á. G., BAUTISTA, S. & BELLOT, J. 2011. Scale-dependent variation in runoff and sediment yield in a semiarid Mediterranean catchment. *Journal of Hydrology,* 397**,** 128-135.

MAYOR, Á. G., BAUTISTA, S., SMALL, E. E., DIXON, M. & BELLOT, J. 2008. Measurement of the connectivity of runoff source areas as determined by vegetation pattern and topography: A tool for assessing potential water and soil losses in drylands. *Water Resources Research,* 44.

MCDONALD, R. C., ISBELL, R., SPEIGHT, J. G., WALKER, J. & HOPKINS, M. 1998. *Australian soil and land survey: field handbook*, CSIRO publishing.

MCLIN, S. G., SPRINGER, E. P. & LANE, L. J. 2001. Predicting floodplain boundary changes following the Cerro Grande wildfire. *Hydrological Processes,* 15**,** 2967-2980.

MERINO, A., FONTURBEL, M. T., FERNÁNDEZ, C., CHÁVEZ-VERGARA, B., GARCÍA-OLIVA, F. & VEGA, J. A. 2018. Inferring changes in soil organic matter in post-wildfire soil burn severity levels in a temperate climate. *Science of the Total Environment,* 627**,** 622-632.

MIYATA, S., KOSUGI, K. I., NISHI, Y., GOMI, T., SIDLE, R. C. & MIZUYAMA, T. 2010a. Spatial pattern of infiltration rate and its effect on hydrological processes in a small headwater catchment. *Hydrological Processes,* 24**,** 535-549.

MIYATA, S., KOSUGI, K. I., NISHI, Y., GOMI, T., SIDLE, R. C. & MIZUYAMA, T. 2010b. Spatial pattern of infiltration rate and its effect on hydrological processes in a small headwater catchment. *Hydrological Processes: An International Journal,* 24**,** 535-549.

MOODY, D. R. & SCHLOSSBERG, M. J. 2010. Soil water repellency index prediction using the molarity of ethanol droplet test. *Vadose Zone Journal,* 9**,** 1046-1051.

MOODY, J. A. 2012. An analytical method for predicting postwildfire peak discharges.

MOODY, J. A. & EBEL, B. A. 2014. Infiltration and runoff generation processes in fire-affected soils. *Hydrological Processes,* 28**,** 3432-3453.

MOODY, J. A., KINNER, D. A. & ÚBEDA, X. 2009. Linking hydraulic properties of fire-affected soils to infiltration and water repellency. *Journal of Hydrology,* 379**,** 291-303.

MOODY, J. A., SHAKESBY, R. A., ROBICHAUD, P. R., CANNON, S. H. & MARTIN, D. A. 2013. Current research issues related to post-wildfire runoff and erosion processes. *Earth-Science Reviews,* 122**,** 10-37.

MORBIDELLI, R., CORRADINI, C. & GOVINDARAJU, R. S. 2006a. A field-scale infiltration model accounting for spatial heterogeneity of rainfall and soil saturated hydraulic conductivity. *Hydrological Processes,* 20**,** 1465-1481.

MORBIDELLI, R., CORRADINI, C. & GOVINDARAJU, R. S. 2006b. A field-scale infiltration model accounting for spatial heterogeneity of rainfall and soil saturated hydraulic conductivity. *Hydrological Processes: An International Journal,* 20**,** 1465-1481.

MORBIDELLI, R., CORRADINI, C., SALTALIPPI, C. & GOVINDARAJU, R. S. 2008. Laboratory experimental investigation of infiltration by the run-on process. *Journal of Hydrologic Engineering,* 13**,** 1187-1192.

MORENO-DE LAS HERAS, M., NICOLAU, J. M., MERINO-MARTÍN, L. & WILCOX, B. P. 2010. Plot-scale effects on runoff and erosion along a slope degradation gradient. *Water Resources Research,* 46.

MÜLLER, K., MASON, K., STROZZI, A. G., SIMPSON, R., KOMATSU, T., KAWAMOTO, K. & CLOTHIER, B. 2018. Runoff and nutrient loss from a water-repellent soil. *Geoderma,* 322**,** 28-37.

MURPHY, B. F. & TIMBAL, B. 2008. A review of recent climate variability and climate change in southeastern Australia. *International Journal of Climatology: A Journal of the Royal Meteorological Society,* 28**,** 859-879.

NAHAR, N., GOVINDARAJU, R., CORRADINI, C. & MORBIDELLI, R. 2004. Role of run-on for describing field-scale infiltration and overland flow over spatially variable soils. *Journal of Hydrology,* 286**,** 36-51.

NATHANS, L. L., OSWALD, F. L. & NIMON, K. 2012. Interpreting multiple linear regression: A guidebook of variable importance. *Practical Assessment, Research & Evaluation,* 17.

NEARY, D. G., GOTTFRIED, G. J. & FFOLLIOTT, P. F. Post-wildfire watershed flood responses. Proceedings of the 2nd International Fire Ecology Conference, American Meteorological Society, Orlando FL, Paper, 2003.

NEARY, D. G., KLOPATEK, C. C., DEBANO, L. F. & FFOLLIOTT, P. F. 1999. Fire effects on belowground sustainability: a review and synthesis. *Forest ecology and management,* 122**,** 51-71.

NEARY, D. G., RYAN, K. C. & DEBANO, L. F. 2005. Wildland fire in ecosystems: effects of fire on soils and water. *Gen. Tech. Rep. RMRS-GTR-42-vol. 4. Ogden, UT: US Department of Agriculture, Forest Service, Rocky Mountain Research Station. 250 p.,* 42.

NIMMO, J. R. 2004. Porosity and pore size distribution. *Encyclopedia of Soils in the Environment,* 3**,** 295-303.

NIMMO, J. R. 2012. Preferential flow occurs in unsaturated conditions. *Hydrological Processes,* 26**,** 786-789.

NYMAN, P., SHERIDAN, G. & LANE, P. N. 2010. Synergistic effects of water repellency and macropore flow on the hydraulic conductivity of a burned forest soil, south-east Australia. *Hydrological Processes,* 24**,** 2871-2887.

NYMAN, P., SHERIDAN, G. J., SMITH, H. G. & LANE, P. N. 2011. Evidence of debris flow occurrence after wildfire in upland catchments of south-east Australia. *Geomorphology,* 125**,** 383-401.

NYMAN, P., SHERIDAN, G. J., SMITH, H. G. & LANE, P. N. 2014. Modeling the effects of surface storage, macropore flow and water repellency on infiltration after wildfire. *Journal of Hydrology,* 513**,** 301-313.

NYMAN, P., SHERWIN, C., SHERIDAN, G. & LANE, P. Landscape aridity, fire severity and rainfall intensity as controls on debris flow frequency after the 2009 Black Saturday Wildfires in Victoria. EGU General Assembly Conference Abstracts, 2015.

NYQUIST, J. E., TORAN, L., PITMAN, L., GUO, L. & LIN, H. 2018. Testing the fill-and-spill model of subsurface lateral flow using ground-penetrating radar and dye tracing. *Vadose Zone Journal,* 17.

OATES, A. & TARANTO, M. 2001. *Vegetation mapping of the Port Phillip & Westernport region*, Department of Natural Resources and Environment Melbourne.

ONDA, Y., DIETRICH, W. E. & BOOKER, F. 2008. Evolution of overland flow after a severe forest fire, Point Reyes, California. *Catena,* 72**,** 13-20.

OSSOLA, A. & NYMAN, P. Aridity and decomposition processes in complex landscapes. EGU General Assembly Conference Abstracts, 2015.

PARLANGE, J.-Y. & HAVERKAMP, R. 1989. Infiltration and ponding time. *Unsaturated Flow in Hydrologic Modeling.* Springer.

PARLANGE, J.-Y., LISLE, I., BRADDOCK, R. & SMITH, R. 1982. The three-parameter infiltration equation. *Soil Science,* 133**,** 337-341.

PARLANGE, J.-Y., ROSE, C. & SANDER, G. 1981. Kinematic flow approximation of runoff on a plane: an exact analytical solution. *Journal of Hydrology,* 52**,** 171-176.

PASCUAL GRANGED, A. J., MARTÍNEZ ZAVALA, L. M., JORDÁN LÓPEZ, A., GIL TORRES, J., BELLINFANTE CROCCI, N., ESCALANTE, E., SEGOVIA, B. & SÁNCHEZ, R. 2010. Changes in soil water repellency increased preferential flow and soil erosion risk after intense wildfire (Huelva, 2004). *Fuegored 2010: Jornadas Internacionales: Investigación y gestión para la protección del suelo y restauración de los ecosistemas forestales afectados por incendios forestales***,** 187-190.

PEEL, M. C., FINLAYSON, B. L. & MCMAHON, T. A. 2007. Updated world map of the Köppen-Geiger climate classification. *Hydrology and earth system sciences discussions,* 4**,** 439-473.

PENMAN, T., KAVANAGH, R., BINNS, D. & MELICK, D. 2007. Patchiness of prescribed burns in dry sclerophyll eucalypt forests in south-eastern Australia. *Forest Ecology and Management,* 252**,** 24-32.

PERSSON, M. 2005. Accurate dye tracer concentration estimations using image analysis. *Soil Science Society of America Journal,* 69**,** 967-975.

PHILIP, J. R. 1957. The theory of infiltration: 4. Sorptivity and algebraic infiltration equations. *Soil science,* 84**,** 257-264.

PODGORNEY, R. K. & FAIRLEY, J. P. 2008. Investigation of episodic flow from unsaturated porous media into a macropore. *Vadose Zone Journal,* 7**,** 332-339.

POON, P. K. & KINOSHITA, A. M. 2018. Spatial and temporal evapotranspiration trends after wildfire in semi-arid landscapes. *Journal of Hydrology,* 559**,** 71-83.

RAWLS, W. J., BRAKENSIEK, D. L. & SAXTONN, K. 1982. Estimation of soil water properties. *Transactions of the ASAE,* 25**,** 1316-1320.

READING, L. P., BAUMGARTL, T., BRISTOW, K. L. & LOCKINGTON, D. A. 2012. Hydraulic conductivity increases in a sodic clay soil in response to gypsum applications: Impacts of bulk density and cation exchange. *Soil Science,* 177**,** 165-171.

REANEY, S., BRACKEN, L. & KIRKBY, M. 2007. Use of the connectivity of runoff model (CRUM) to investigate the influence of storm characteristics on runoff generation and connectivity in semi-arid areas. *Hydrological Processes,* 21**,** 894-906.

REANEY, S., BRACKEN, L. & KIRKBY, M. 2014. The importance of surface controls on overland flow connectivity in semi-arid environments: Results from a numerical experimental approach. *Hydrological Processes,* 28**,** 2116-2128.

RITSEMA, C. J. & DEKKER, L. 2000. Preferential flow in water repellent sandy soils: principles and modeling implications. *Journal of Hydrology,* 231**,** 308-319.

RITSEMA, C. J. & DEKKER, L. W. 1994. How water moves in a water repellent sandy soil: 2. Dynamics of fingered flow. *Water resources research,* 30**,** 2519-2531.

RITSEMA, C. J. & DEKKER, L. W. 1995. Distribution flow: A general process in the top layer of water repellent soils. *Water Resources Research,* 31**,** 1187-1200.

RITSEMA, C. J., DEKKER, L. W., HENDRICKX, J. & HAMMINGA, W. 1993. Preferential flow mechanism in a water repellent sandy soil. *Water Resources Research,* 29**,** 2183-2193.

RITSEMA, C. J., VAN DAM, J. C., DEKKER, L. W. & OOSTINDIE, K. 2005. A new modelling approach to simulate preferential flow and transport in water repellent porous media: Model structure and validation. *Soil Research,* 43**,** 361-369.

RITSEMA, C. J., VAN DAM, J. C., NIEBER, J. L., DEKKER, L. W., OOSTINDIE, K. & STEENHUIS, T. S. Preferential flow in water repellent sandy soils: principles and modeling approaches. Preferential Flow: Water Movement and Chemical Transport in the Environment, 2001. American Society of Agricultural and Biological Engineers, 129.

ROBICHAUD, P. R. 2000. Fire and erosion: evaluating the effectiveness of a post-fire rehabilitation treatment, contour-felled logs. *Watershed Management and Operations Management 2000.*

ROBICHAUD, P. R., BEYERS, J. L. & NEARY, D. G. 2000. Evaluating the effectiveness of postfire rehabilitation treatments. *Gen. Tech. Rep. RMRS-GTR-63. Fort Collins: US Department of Agriculture, Forest Service, Rocky Mountain Research Station. 85 p.,* 63.

ROBICHAUD, P. R., WAGENBRENNER, J. W., PIERSON, F. B., SPAETH, K. E., ASHMUN, L. E. & MOFFET, C. A. 2016. Infiltration and interrill erosion rates after a wildfire in western Montana, USA. *Catena,* 142**,** 77-88.

ROBINET, J. C., SARDINI, P., COELHO, D., PARNEIX, J. C., PRÊT, D., SAMMARTINO, S., BOLLER, E. & ALTMANN, S. 2012. Effects of mineral distribution at mesoscopic scale on solute diffusion in a clay-rich rock: Example of the Callovo-Oxfordian mudstone (Bure, France). *Water Resources Research,* 48.

RYE, C. & SMETTEM, K. 2015. Seasonal and interannual variability of the effective flow cross-sectional area in a water-repellent soil. *Vadose Zone Journal,* 14.

RYE, C. & SMETTEM, K. 2017. The effect of water repellent soil surface layers on preferential flow and bare soil evaporation. *Geoderma,* 289**,** 142-149.

SAGHAFIAN, B. 1993. Hydrologic analysis of watershed response to spatially varied infiltration.

SAGHAFIAN, B. & JULIEN, P. 1995. Time to equilibrium for spatially variable watersheds. *Journal of Hydrology(Amsterdam),* 172**,** 231-245.

SAGHAFIAN, B., JULIEN, P. Y. & OGDEN, F. L. 1995. Similarity in catchment response: 1. Stationary rainstorms. *Water Resources Research,* 31**,** 1533-1541.

SAMEC, M., SANTIAGO, A., CÁRDENAS, J., BENITO, R., TARQUIS, A., MOONEY, S. & KOROŠAK, D. 2013. Quantifying soil complexity using network models of soil porous structure. *Nonlinear Processes in Geophysics,* 20**,** 41-45.

SAMMARTINO, S., LISSY, A.-S., BOGNER, C., VAN DEN BOGAERT, R., CAPOWIEZ, Y., RUY, S. & CORNU, S. 2015. Identifying the functional macropore network related to preferential flow in structured soils. *Vadose Zone Journal,* 14.

SAMMARTINO, S., MICHEL, E. & CAPOWIEZ, Y. 2012. A novel method to visualize and characterize preferential flow in undisturbed soil cores by using multislice helical CT. *Vadose Zone Journal,* 11.

SANDERS, E. C., ABOU NAJM, M. R., MOHTAR, R. H., KLADIVKO, E. & SCHULZE, D. 2012. Field method for separating the contribution of surface-connected preferential flow pathways from flow through the soil matrix. *Water Resources Research,* 48.

SANTÍN, C. & DOERR, S. H. 2016. Fire effects on soils: the human dimension. *Phil. Trans. R. Soc. B,* 371**,** 20150171.

SHAKESBY, R. 2011. Post-wildfire soil erosion in the Mediterranean: review and future research directions. *Earth-Science Reviews,* 105**,** 71-100.

SHAKESBY, R. & DOERR, S. 2006. Wildfire as a hydrological and geomorphological agent. *Earth-Science Reviews,* 74**,** 269-307.

SHARMA, K., PAREEK, O. & SINGH, H. 1986. Microcatchment water harvesting for raising Jujube orchards in an arid climate. *Transactions of the ASAE,* 29**,** 112-0118.

SHEIN, E. 2010. Soil hydrology: stages of development, current state, and nearest prospects. *Eurasian Soil Science,* 43**,** 158-167.

SHERIDAN, G. J., LANE, P. N. & NOSKE, P. J. 2007. Quantification of hillslope runoff and erosion processes before and after wildfire in a wet Eucalyptus forest. *Journal of Hydrology,* 343**,** 12-28.

SHERIDAN, G. J., NOSKE, P. J., LANE, P. N., JONES, O. D. & SHERWIN, C. B. 2014. A simple two-parameter model for scaling hillslope surface runoff. *Earth Surface Processes and Landforms,* 39**,** 1049-1061.

ŠIMŮNEK, J., JARVIS, N. J., VAN GENUCHTEN, M. T. & GÄRDENÄS, A. 2003. Review and comparison of models for describing non-equilibrium and preferential flow and transport in the vadose zone. *Journal of hydrology,* 272**,** 14-35.

SITTERSON, J., KNIGHTES, C., PARMAR, R., WOLFE, K., MUCHE, M. & AVANT, B. 2017. An overview of rainfall-runoff model types. *United States Environmental protection Agency: Washington, DC, USA*.

SIVAPALAN, M. & WOOD, E. 1986. Spatial heterogeneity and scale in the infiltration response of catchments. *Scale problems in hydrology.* Springer.

SMITH, H. G., SHERIDAN, G. J., LANE, P. N. & BREN, L. J. 2011a. Wildfire and salvage harvesting effects on runoff generation and sediment exports from radiata pine and eucalypt forest catchments, south-eastern Australia. *Forest Ecology and Management,* 261**,** 570-581.

SMITH, H. G., SHERIDAN, G. J., LANE, P. N., NOSKE, P. J. & HEIJNIS, H. 2011b. Changes to sediment sources following wildfire in a forested upland catchment, southeastern Australia. *Hydrological Processes,* 25**,** 2878-2889.

SMITH, M. W., COX, N. J. & BRACKEN, L. J. 2007. Applying flow resistance equations to overland flows. *Progress in Physical Geography,* 31**,** 363-387.

SMITH, R. & PARLANGE, J. Y. 1978. A parameter-efficient hydrologic infiltration model. *Water Resources Research,* 14**,** 533-538.

SMITH, R. E. 1972. The infiltration envelope: results from a theoretical infiltrometer. *Journal of Hydrology,* 17**,** 1-22.

SMITH, R. E., CORRADINI, C. & MELONE, F. 1993. Modeling infiltration for multistorm runoff events. *Water Resources Research,* 29**,** 133-144.

SPIGEL, K. M. & ROBICHAUD, P. R. 2007. First-year post-fire erosion rates in Bitterroot National Forest, Montana. *Hydrological Processes,* 21**,** 998-1005.

STERN, H., DE HOEDT, G. & ERNST, J. 2000. Objective classification of Australian climates. *Australian Meteorological Magazine,* 49**,** 87-96.

STOKES, A., ATGER, C., BENGOUGH, A. G., FOURCAUD, T. & SIDLE, R. C. 2009. Desirable plant root traits for protecting natural and engineered slopes against landslides. *Plant and soil,* 324**,** 1-30.

STOMPH, T., DE RIDDER, N., STEENHUIS, T. & VAN DE GIESEN, N. 2002. Scale effects of Hortonian overland flow and rainfall-runoff dynamics: Laboratory validation of a process-based model. *Earth Surface Processes and Landforms,* 27**,** 847-855.

STOMPH, T. J. & DE RIDDERN, N., STEENHUIS T. S. AND VAN DE GIESEN, N. C. 2002. SCALE EFFECTS OF HORTONIAN OVERLAND FLOW AND RAINFALL-RUNOFF DYNAMICS: LABORATORY VALIDATION OF A PROCESS-BASED MODEL. *Earth Surface Processes and Landforms,* 27**,** 8.

STOOF, C., SLINGERLAND, E., MOL, W., BERG, J., VERMEULEN, P., FERREIRA, A., RITSEMA, C., PARLANGE, J. Y. & STEENHUIS, T. 2014a. Preferential flow as a potential mechanism for fire-induced increase in streamflow. *Water Resources Research,* 50**,** 1840-1845.

STOOF, C., SLINGERLAND, E., MOL, W., VAN DEN BERG, J., VERMEULEN, P., FERREIRA, A., RITSEMA, C., PARLANGE, J. Y. & STEENHUIS, T. 2014b. Preferential flow as a potential mechanism for fire-induced increase in streamflow. *Water Resources Research,* 50**,** 1840-1845.

STOOF, C. R., VERVOORT, R., IWEMA, J., ELSEN, E., FERREIRA, A. & RITSEMA, C. 2012. Hydrological response of a small catchment burned by experimental fire. *Hydrology and Earth System Sciences,* 16**,** 267-285.

STRICKLER, A. 1923. Some contributions to the problems of the velocity tomula and roughness factor to rivers, canals and closed conduits. *Mitteilungen des Eidgenossischer Amtes fur Wasserwirtschaft, Bern, Switzerland*.

TOFTENG, C., HANSEN, S. & JENSEN, H. E. 2002. Film and pulse flow in artificial macropores. *Hydrology Research,* 33**,** 263-274.

VAN DE GIESEN, N., STOMPH, T.-J., AJAYI, A. E. & BAGAYOKO, F. 2011. Scale effects in Hortonian surface runoff on agricultural slopes in West Africa: Field data and models. *Agriculture, ecosystems & environment,* 142**,** 95-101.

VAN DE GIESEN, N., STOMPH, T. & DE RIDDER, N. 2000. Scale effects of Hortonian overland flow and rainfall–runoff dynamics in a West African catena landscape. *Hydrological Processes,* 14**,** 165-175.

VAN DE GIESEN, N., STOMPH, T. J. & DE RIDDER, N. 2005. Surface runoff scale effects in West African watersheds: modeling and management options. *Agricultural water management,* 72**,** 109-130.

VAN DER SANT, R. 2016. Aridity as a predictor of the hydrogeomorphic response of burnt landscapes. *PhD thesis*.

VAN DER SANT, R. E., NYMAN, P., NOSKE, P. J., LANGHANS, C., LANE, P. N. & SHERIDAN, G. J. 2018. Quantifying relations between surface runoff and aridity after wildfire. *Earth Surface Processes and Landforms*.

VAN DIJK, A. I. J. M. 2002. *Water and sediment dynamics in bench-terraced agricultural steeplands in West Java, Indonesia*, AIJM van Dijk.

VIEIRA, D., FERNÁNDEZ, C., VEGA, J. & KEIZER, J. 2015. Does soil burn severity affect the post-fire runoff and interrill erosion response? A review based on meta-analysis of field rainfall simulation data. *Journal of Hydrology,* 523**,** 452-464.

WAINWRIGHT, J. & PARSONS, A. J. 2002. The effect of temporal variations in rainfall on scale dependency in runoff coefficients. *Water Resources Research,* 38.

WEILER, M. & FLÜHLER, H. 2004. Inferring flow types from dye patterns in macroporous soils. *Geoderma,* 120**,** 137-153.

WELLS, W. I. 1981. Some effects of brushfires on erosion process in coastal Southern California. *International Association of Hydrological Sciences,* 132**,** 305-342.

WENDT, R., ALBERTS, E. & HJELMFELT JR, A. 1986. Variability of runoff and soil loss from fallow experimental plots. *Soil Science Society of America Journal,* 50**,** 730-736.

WESSOLEK, G., STOFFREGEN, H. & TÄUMER, K. 2009. Persistency of flow patterns in a water repellent sandy soil–Conclusions of TDR readings and a time-delayed double tracer experiment. *Journal of hydrology,* 375**,** 524-535.

WHITE, A. M., LOCKINGTON, D. A. & GIBBES, B. 2017. Does fire alter soil water repellency in subtropical coastal sandy environments? *Hydrological processes,* 31**,** 341-348.

WIETING, C., EBEL, B. A. & SINGHA, K. 2017. Quantifying the effects of wildfire on changes in soil properties by surface burning of soils from the Boulder Creek Critical Zone Observatory. *Journal of Hydrology: Regional Studies,* 13**,** 43-57.

WILCOX, B. P., BRESHEARS, D. D. & ALLEN, C. D. 2003. Ecohydrology of a resource-conserving semiarid woodland: Effects of scale and disturbance. *Ecological Monographs,* 73**,** 223-239.

WILCOX, B. P., NEWMAN, B. D., BRANDES, D., DAVENPORT, D. W. & REID, K. 1997. Runoff from a semiarid ponderosa pine hillslope in New Mexico. *Water Resources Research,* 33**,** 2301-2314.

WINE, M. & CADOL, D. 2016. Hydrologic effects of large southwestern USA wildfires significantly increase regional water supply: fact or fiction? *Environmental Research Letters,* 11**,** 085006.

WOHL, E. 2018. Introduction to the themed issue: Wildfire and Geomorphic Systems. *Earth Surface Processes and Landforms*.

WONG, M. & PARKER, G. 2006. Reanalysis and correction of bed-load relation of Meyer-Peter and Müller using their own database. *Journal of Hydraulic Engineering,* 132**,** 1159-1168.

WOODS, S. W. & BALFOUR, V. N. 2010. The effects of soil texture and ash thickness on the post-fire hydrological response from ash-covered soils. *Journal of Hydrology,* 393**,** 274-286.

WOOLHISER, D., SMITH, R. & GIRALDEZ, J. V. 1996. Effects of spatial variability of saturated hydraulic conductivity on Hortonian overland flow. *Water Resources Research,* 32**,** 671-678.

WOOLHISER, D., SMITH, R. & GOODRICH, D. 1990. KINEROS: A Kinematic Runoff and Erosion Model: Documentation and User Manual, ARS-77. *US Department of Agriculture, Agricultural Research Service,* 130.

XU, X.-L., LIU, W., KONG, Y.-P., ZHANG, K.-L., YU, B. & CHEN, J.-D. 2009. Runoff and water erosion on road side-slopes: Effects of rainfall characteristics and slope length. *Transportation research part D: transport and environment,* 14**,** 497-501.

YATHEENDRADAS, S., WAGENER, T., GUPTA, H., UNKRICH, C., GOODRICH, D., SCHAFFNER, M. & STEWART, A. 2008. Understanding uncertainty in distributed flash flood forecasting for semiarid regions. *Water Resources Research,* 44.

ZHANG, B. & GOVINDARAJU, R. S. 2000. Spatial Interpolation of Hydraulic Conductivity using Radial-Basis Function Networks. *Building Partnerships.*

ZHANG, Y., ZHANG, M., NIU, J. & ZHENG, H. 2016. The preferential flow of soil: A widespread phenomenon in pedological perspectives. *Eurasian soil science,* 49**,** 661-672.

ZHANG, Z., PENG, X., ZHOU, H., LIN, H. & SUN, H. 2015. Characterizing preferential flow in cracked paddy soils using computed tomography and breakthrough curve. *Soil and Tillage Research,* 146**,** 53-65.

ZUUR, A. F., IENO, E. N. & ELPHICK, C. S. 2010. A protocol for data exploration to avoid common statistical problems. *Methods in ecology and evolution,* 1**,** 3-14.